KAUNAS UNIVERSITY OF TECHNOLOGY

VYKINTAS SAMAITIS

ULTRASONIC METHODS FOR STRUCTURAL HEALTH MONITORING OF COMPOSITE OBJECTS

Doctoral dissertation
Technological sciences, Electrical and Electronics Engineering (01T)

2016, Kaunas

UDK 620.179.16 (043.3)

This research was accomplished during the period of 2012 – 2016 at Prof. Kazimieras Baršauskas Ultrasound Research Institute of Kaunas University of Technology. The research was granted by Research Council of Lithuania.

Scientific supervisor
Prof. Dr Liudas MAŽEIKA (Kaunas University of Technology, Technological Sciences, Electrical and Electronics Engineering – 01T)

English Language Editor:
UAB “Synergium”

Doctoral dissertation has been published in:
http://ktu.edu

ISBN 978-609-02-1242-4

NOMENCLATURE AND ABBREVIATIONS

A_i	Asymmetrical mode (where $i = 0, 1, 2, \ldots$)
Al	Aluminium alloy
CFRP	Carbon Fibre Reinforced Plastic
CT	Chirplet Transform
CWT	Continuous Wavelet Transform
DC	Dispersion Curves
DI	Damage Index
DWT	Discrete Wavelet Transform
EMD	Empirical Mode Decomposition
EUSR	Embedded Ultrasonic Structural Radar
FE	Finite Element Method
FFT	Fast Fourier Transform
GFRP	Glass Fibre Reinforced Plastic
GW	Guided Waves
HHT	Hilbert Huang Transform
HT	Hilbert Transform
IDT	InterDigital Transducers
IFFT	Inverse Fast Fourier Transform
IMF	Intrinsic Mode Functions
LDR	Local Defect Resonance
LDV	Lased Doppler Vibrometer
MFC	Macro-fibre composite transducer
MP	Matching Pursuit
MRD	Minimum Resolvable Distance
MTMR	Multiple Transmitters Multiple Receivers
NDT	Non-Destructive Testing
PAA	Phased Addition Algorithm
PVDF	PolyVinyliDene Fluoride
PZT	Lead (P) Zirconate (Z) Titanate (T)
SAFE	Semi Analytical Finite Element
SH_i	Shear Horizontal mode (where $i = 0, 1, 2, \ldots$)
SHM	Structural Health Monitoring
S_i	Symmetrical mode (where $i = 0, 1, 2, \ldots$)
SNR	Signal to Noise Ratio
STD	Standard deviation
STFT	Short Time Fourier Transform
STMR	Single Transmitter Multiple Receivers
TFR	Time Frequency Representation
ToF	Time of Flight
WT	Wavelet Transform
WVD	Wigner Ville Distribution

TABLE OF CONTENTS

INTRODUCTION

Relevance of the work

The integrity assessment is critical to maintain the safe, reliable and optimal performance of ageing in-service engineering structures (1). The use of non-destructive testing (NDT) techniques in the areas of nuclear and green energy, aerospace and civil infrastructure allows the structural integrity to be assessed, to estimate and prolong the expected life-cycle, to minimize the risk of catastrophic failures or any other unexpected incidents (2, 3, 4, 5, 6, 7). However, the conventional NDT techniques are not optimized in terms of periodicity, usually require disassembly (to have access to parts), are quite operator dependent, and are slow and costly, especially for large engineering structures (8). Various studies reveal that up to 27% of an aircraft life-cycle cost is spent on conventional inspection and repair routines (9). As an alternative for conventional NDT, a structural health monitoring (SHM) systems may be used, which provides an on-demand health inspection through embedded sensors (10, 11). It enables the periodic maintenance with condition-based maintenance to be changed, to minimize downtime and human involvement, to avoid dismounting parts and to ensure constant reliability and maintenance costs during the whole life-cycle of the structure (12). According to different sources, an effective SHM reduces the maintenance costs and inspection time from 30% to 40% (13, 14).

One of the most promising inspection techniques for SHM in terms of sensitivity to damage and propagation range is ultrasonic guided waves (GW) (10, 15). The GW are sensitive to the change in elastic modulus of the material and possess minor amplitude damping, which enables large structures to be inspected using only a few measurement positions and to detect both surface and internal defects (16, 17, 18). GW based SHM provides fast, low-cost inspection with good spatial coverage and the ability to inspect structures under water, ground, coatings or insulation (19, 20, 21). Many studies have been carried out on the application of guided waves (GW) for damage detection in pipes (22, 23, 24, 25, 26, 27, 28, 29, 30), concrete structures (31, 32, 33), steel strands (34, 35, 36, 37, 38), rails (39, 40, 41), pressure vessels (42, 43), metallic structures (44, 45), composites (46, 47, 48, 49, 50, 51) and other aircraft components (52, 53, 54).

The application of GW in such a wide variety of areas, looking for different kinds of defects, shows huge potential for GW inspection, unfortunately there is still a lack of practical applications due to its complicated propagation physics. The GW possess multiple wave modes, each with different dispersive and directional properties. This leads to many distorted wave packets traveling in the structure with a different frequency and direction dependent velocities (55). Moreover, mode conversion occurs after the interaction of the GW with an object’s boundaries or with other reflectors, such as defects (18, 56). As a result, the signals captured from the structure are distorted and overlapped, while the damage-scattered components are concealed within. All these challenges require the development of an advanced signal analysis methods that would help to analyse, interpret and predict the complex behaviour of the GW and to extract the information about the presence of damage.

The current success of the SHM systems relies on the comparison between two system states, the current and the baseline (10, 57, 58). Typically, when the transducers are permanently attached to the surface of the structure, the initial time traces between all the possible transducer pairs are recorded and referred as baseline data. Then in order to detect the damage, the algebraic difference is calculated between the current time trace and the baseline, which represents the structure without the damage. As a result, the residual signal ideally should contain the information only about the damage (59, 60), removing all possible boundary reflections. From the NDT technique development point of view, this approach is not attractive due to difficulties in verification and calibration of the monitoring system. Moreover, such approach gives an indication about the presence of damage only, however, it does not say anything about the features (type, size, depth, location) of the defect.

In order to verify that a certain type of defect has been detected, the appropriate database of the experiments on the reference samples with artificial defects possessing known parameters (size, depth, position) is required. Then the residual signal captured during the operational life of the structure can be compared to the residuals from the defective reference sample database, looking for the best match. However, considering the variety of possible defects and the fact that there are no two identical structures, such database of the reference experiments becomes very large, impractical and unreliable, especially for complex structures. Moreover, the defects are usually weak reflectors whereas the amplitude of the residual can be significantly affected by the environmental and operational conditions, such as temperature and loads (59, 61, 62, 63). Therefore, currently the baseline comparison can only give an indication about the changes in the structure, but unfortunately cannot be used for reliable damage detection and feature extraction. This leads to the **scientific hypothesis** that special signal processing methods exist, which would allow the guided wave interaction within the analysed structure to be understood and to be able distinguish changes that are caused by the originating defects.

Objective and tasks

The **objective of the thesis** is to develop ultrasonic guided wave methods for structural health monitoring of plate-like structures, enabling the feature extraction of detected damage, and techniques for the validation of the monitoring system.

In order to achieve the objectives, the following tasks were foreseen:

1. To investigate and explain the mechanism of GW generation, and to develop mathematical methods to analyse and predict the spectral characteristics of separate GW mode packets.
2. To develop and verify an analytical model that simplifies the analysis and interpretation of the complex propagation of GW in plate-like anisotropic structures.
3. To create and validate the methods for GW phase velocity estimation in multimodal, overlapped signals captured by spatially distributed sensors, which can be used for the identification of unpredicted modes and modal decomposition purposes.

4. To propose and investigate methods for the detection of the delamination type defects and extraction of its features such as the size and the depth.
5. To create and validate methods suitable for the verification and calibration of the monitoring system, without using the database of the reference samples, that describe different states of the damage.

Scientific novelty

1. The novel mathematical approach for GW data analysis was proposed, which allow the frequency response of GW modes on any structure under any excitation conditions to be analysed and predicted if input parameters are known. The method relates the frequency response of a single generated GW mode to the spatial particle velocity distribution at the excitation area, dimensions of the transducer and dispersive properties of the material.
2. The analytical model was developed for the rapid analysis of the propagation of GW signals. The model allows the propagation of separate GW mode packets in the plate-like rectangular anisotropic structures to be analysed, to calculate the arrival times after multiple reflections at virtual receivers positioned anywhere on the object and to retrace the wave propagation paths at specific time intervals.
3. The method for the GW phase velocity estimation was introduced, which is based on the phase spectrum method. The method requires only two time-series measured at different locations and enables the segment of the dispersion curve of the phase velocity to be reconstructed within the –20 dB level frequency bandwidth of the transducer, thus identify the unpredicted modes in the multimodal signals.
4. The novel method was proposed for the detection and description of delamination type defects in composite structures. The method exploits the frequency sweep excitation and combines the set of analytically calculated dependencies to detect the damage and to extract its features, such as size and depth.
5. The novel technique was proposed for the verification and calibration of the monitoring system, which is based on the non-destructive imitation of signal trapping behaviour within the delamination, which is commonly observed in the presence of such defect. The technique enables to get the similar response in terms of time-of-flight as the structural delamination type defects.

Practical value of the work

1. The proposed signal analysis methods can be used as a framework to predict the complex mechanism of guided wave generation, to analyse multi-modal propagation and to decompose the GW signals captured on plate-like anisotropic structures.
2. The developed ultrasonic measurement methods can be used as a tool to detect and extract the size and depth of the delamination type defects situated across the path of permanently attached sensors.

3. The presented ideas related to the verification and calibration of SHM systems can be used as a basis for development of novel non-destructive structural defect imitation techniques, which can be further used to solve the issues related to the estimation of sensitivity to certain types of defects, minimum detectable defect size and etc.
4. Most of the methods presented in this research are designed in a way not to be attached to the particular structure and exploits the dispersive properties of composite materials, which can be easily modified. Thus the proposed methods can be applied to different types of materials with different properties and other parameters. Only a few of the proposed methods rely on the geometrical shape of the investigated object.

Some parts of this work were used in the reports of the following international projects:

- European Union Framework Programme 7 (FP7) project (SME-2012-1-315207) "In-situ Wireless Monitoring of on an Offshore Wind Turbine Blades Using Energy Harvesting Technology – Demonstration/ Wintur Demo".
- European Union Framework Programme 7 (FP7) project (SME-2011-1-286989) "Demonstration of a Condition Monitoring System for Tidal Stream Generators / TidalSense Demo".
- European Social Fund (ESF) programme project (VP1-3.1-ŠMM-08-K-01-015) "Micro sensors, Microprocessors and Microcontrollers for Mechatronic Systems / Go-Smart".

Approbation

The scientific results obtained during the period of the dissertation were published in 7 publications: 4 articles were published in international journals referred in Thomson Reuters ISI Web of Science, while the other 3 publications were accepted to the reviewed proceedings of international conferences. The results were also presented in 15 international conferences held in Kaunas, Vilnius, Palanga, Singapore, Portoroz, Prague, Krakow, Lublin, Manchester, Dresden, Brussels and Munich. In 2014-2016, a doctoral scholarship, provided by the research council of Lithuania, was received. In 2016, the research was granted an international student grant by the Committee for International Research and Education (CIRE) of the Acoustical Society of America (ASA).

Results presented in defence of the thesis

1. The excitability function estimation technique, which enables the frequency response of separate guided wave modes to be predicted, based on the material properties of the structure, size of source and type of excitation.
2. The analytical model for analysis and interpretation of GW propagation in plate-like anisotropic structures, which provides the arrival times of separate wave packets after multiple reflections and enables wave propagation paths to be retraced.

3. Enhanced phase velocity estimation techniques, based on the phase spectrum method, which enables the accuracy of the conventional method to be improved and to effectively use it in SHM applications.
4. The method to detect and evaluate the size and depth of delamination type defects in composite structures, based on the arrival time estimation and constructive/destructive interference of the A_0 mode.
5. The structural damage imitation technique, which enables the reproduction of the delamination type defect in terms of ToF of the “trapped” wave without intervention into the structure.

Structure and coverage of the thesis

The thesis consists of an introduction, six chapters, conclusions, list of references and authors scientific publications. Overall the dissertation is composed of 152 pages, including 74 figures, 147 equations, 5 tables and 260 bibliographic references. The contents of the thesis are organized as follows:

1. In the first chapter, the extensive review of available literature is presented, which reveals the existing gaps and open areas, where the new SHM methods and signal processing techniques are required. The current state of the art in different SHM areas, such as means of guided wave simulation, selective mode excitation, signal processing and damage detection is presented as well as the tasks of the research are anticipated.
2. The second chapter presents the study on the source influence to the excitation of GW. The developed excitability function estimation technique is introduced, theoretically formulated and verified with the numerical simulations and experiments on glass fibre reinforced plastic (GFRP) and aluminium samples.
3. The third chapter reveals the concept of the developed analytical model for analysis and interpretation of GW propagation in plate-like structures. The major benefits and limitations of the proposed technique are discussed, using the numerical finite element (FE) method as a reference.
4. In the fourth chapter the developed guided wave phase velocity estimation technique is formulated, followed by numerical and experimental validation. The accuracy of the proposed technique is discussed, by comparing the extracted phase velocities of direct and reflected/converted modes with the theoretical predictions.
5. The fifth chapter presents the method to detect and describe the delamination type damage in composite structures. The physics of general GW interaction with a delamination type defect is presented and the theoretical foundation of the proposed technique is introduced. The operation of developed method is verified detecting defects of different sizes situated at different depths.
6. In the sixth chapter, the approach to non-destructively imitate the delamination type defect is briefly introduced. The adequacy of the proposed set-up in terms of ToF of the repetitive A_0 mode transmissions is mathematically proved and demonstrated by numerical modelling on a GFRP composite sample.

1. STRUCTURAL HEALTH MONITORING OF COMPOSITES BY MEANS OF ULTRASONIC GUIDED WAVES

1.1 Basic features of ultrasonic guided waves in plate-like structures

This section introduces the main physical features of ultrasonic guided waves in plate-like structures and the most important challenges that currently complicates the development of GW based monitoring systems. Guided waves are the waves that propagate along the boundary of the structure, which has the thickness considerably lower than the wavelength λ_w. In general, the guided waves are the result of interference between the longitudinal and shear waves, which are reflecting back and forth and converting to each another inside the structure (64, 65).

One of the types of the guided waves that propagate in a plate-like structure with stress-free boundaries are called Lamb waves (66). Both bulk and Lamb waves mathematically are governed by the same partial differential wave equations, however in the case of guided waves an additional boundary conditions must be satisfied. The formulation of the Lamb waves in the isotropic, homogenous plate can be derived from the general form of the Navier equation of motion (67, 68, 69):

$$\mu \cdot u_{i,jj} + (\lambda + \mu) \cdot u_{j,ji} + \rho \cdot f_i = \rho \cdot \ddot{u}_i \ (i, j = 1,2,3\ldots), \tag{1.1.1}$$

where u_i and f_i are the displacement and body force in the x_i direction; ρ and μ are the density and the shear modulus; λ is the Lame constant ($\lambda = \frac{2\mu \cdot \upsilon}{1-2\upsilon}$, where υ denotes the Poisson ratio). Using the Helmholtz decomposition (70) and the method of potentials, eq. 1.1.1 can be decomposed into two independent equations, which describe the longitudinal and the shear waves (14, 67, 69):

$$\frac{\partial^2 \phi}{\partial x_1^2} + \frac{\partial^2 \phi}{\partial x_3^2} = \frac{1}{c_L^2} \frac{\partial^2 \phi}{\partial t^2}, \tag{1.1.2}$$

$$\frac{\partial^2 \psi}{\partial x_1^2} + \frac{\partial^2 \psi}{\partial x_3^2} = \frac{1}{c_T^2} \frac{\partial^2 \psi}{\partial t^2}, \tag{1.1.3}$$

where:

$$\phi = \Phi(x_3)\exp[i(kx_1 - \omega t)] = [A_1 \sin(px_3) + A_2 \cos(px_3)]\exp[i(kx_1 - \omega t)], \tag{1.1.4}$$

$$\psi = \Psi(x_3)\exp[i(kx_1 - \omega t)] = [B_1 \sin(qx_3) + B_2 \cos(qx_3)]\exp[i(kx_1 - \omega t)], \tag{1.1.5}$$

and $p^2 = \frac{\omega^2}{c_L^2} - k^2$, $q^2 = \frac{\omega^2}{c_T^2} - k^2$, $k = \frac{2\pi}{\lambda_w}$, where A_1, A_2, B_1, B_2 are the constants describing the boundary conditions; k, ω and λ_w are the wavenumber, circular frequency and wavelength of the wave respectively; c_L and c_T are the velocities of the longitudinal and shear wave ($c_L = \sqrt{\frac{2\mu(1-\upsilon)}{\rho(1-2\upsilon)}}$, $c_T = \sqrt{\frac{\mu}{\rho}}$), x_1 and x_3 denotes the coordinate of along the length and across width of the free analysed plate respectively (x_1 is the direction of wave propagation). If the term $\exp[i(kx_1 - \omega t)]$ is omitted in eq. 1.1.4 and eq. 1.1.5, according to the method of potentials the displacements u and the stresses σ can be written as (67, 69, 71):

$$u_1 = \frac{\partial \phi}{\partial x_1} + \frac{\partial \psi}{\partial x_3} = \left[ik\Phi + \frac{d\Psi}{dx_3} \right], \;\; u_2 = 0, \;\; u_3 = \frac{\partial \phi}{\partial x_3} + \frac{\partial \psi}{\partial x_1} = \left[\frac{d\Phi}{dx_3} + ik\Psi \right], \tag{1.1.6}$$

$$\begin{gathered} \sigma_{31} = \mu\left(\frac{\partial u_3}{\partial x_1} + \frac{\partial u_1}{\partial x_3} \right) = \mu\left(2ik\frac{d\Phi}{dx_3} + k^2\Psi + \frac{d^2\Psi}{dx_3^2} \right), \\ \sigma_{33} = \lambda\left(\frac{\partial u_1}{\partial x_1} + \frac{\partial u_3}{\partial x_3} \right) + 2\mu\frac{\partial u_3}{\partial x_3} = \lambda\left(-k^2\Phi + \frac{d^2\Phi}{dx_3^2} \right) + 2\mu\left(\frac{d^2\Phi}{dx_3^2} - ik\frac{d^2\Psi}{dx_3} \right). \end{gathered} \tag{1.1.7}$$

At this point the solution is divided into two separate sets: one for the symmetric mode (eq. 1.1.8) and another one for the antisymmetric mode (eq. 1.1.9) (67, 69, 72):

$$\begin{gathered} \Phi = A_2\cos(px_3), \;\; \Psi = B_1\sin(qx_3), \\ u = u_1 = ikA_2\cos(px_3) + qB_1\cos(qx_3), \\ w = u_3 = -pA_2\sin(px_3) + ikB_1\sin(qx_3), \\ \sigma_{31} = \mu\left(-2ikpA_2\sin(px_3) + \left(k^2 - q^2\right)B_1\sin(qx_3)\right), \\ \sigma_{33} = -\lambda\left(k^2 + p^2\right)A_2\cos(px_3) - 2\mu\left(p^2A_2\cos(px_3) + ikqB_1\cos(qx_3)\right), \end{gathered} \tag{1.1.8}$$

$$\begin{gathered} \Phi = A_1\sin(px_3), \;\; \Psi = B_2\cos(qx_3), \\ u = u_1 = ikA_1\sin(px_3) + qB_2\sin(qx_3), \\ w = u_3 = -pA_1\cos(px_3) + ikB_2\cos(qx_3), \\ \sigma_{31} = \mu\left(2ikpA_1\cos(px_3) \div \left(k^2 - q^2\right)B_2\cos(qx_3)\right), \\ \sigma_{33} = -\lambda\left(k^2 + p^2\right)A_1\sin(px_3) - 2\mu\left(p^2A_1\sin(px_3) + ikqB_2\sin(qx_3)\right). \end{gathered} \tag{1.1.9}$$

In the equations above, u describes the motion in the x_1 direction (along wave propagation), while w deals with the motion in the x_3 direction (across the thickness). Since the guided waves propagate in the finite domain, the following traction free boundary conditions can be applied at both surfaces (14, 67, 69):

$$\sigma_{31} = \sigma_{33} = 0, \text{ at } x_3 = \pm d/2 = \pm h, \tag{1.1.10}$$

where d and h are the full and the half thickness of the plate respectively. Then the general equation, describing the Lamb waves at the isotropic-homogenous plate can be written from eq. 1.1.6 as (69):

$$\frac{\left(k^2 - q\right)\sin(qh)}{2ikp(\sin(ph))} = \frac{-2\mu ikq(\cos(qh))}{\left(\lambda k^2 + \lambda p^2 + 2\mu p^2\right)\cos(ph)}, \tag{1.1.11}$$

Considering the p and q values presented above and the definitions of the Lame constant ($\lambda = \frac{2\mu \cdot \upsilon}{1 - 2\upsilon} = c_L^2\rho - 2$) and wave velocities ($c_L$, c_T), the Rayleigh-Lamb equations for the symmetric and antisymmetric modes can be obtained (69, 71, 73):

$$\frac{\tan(qh)}{\tan(ph)} = \frac{4k^2 qp}{\left(q^2 - k^2\right)^2}, \quad \frac{\tan(qh)}{\tan(ph)} = \frac{\left(q^2 - k^2\right)^2}{4k^2 qp}. \tag{1.1.12}$$

The last two equations above can be used to calculate the phase velocity (c_p) of the guided waves in plate-like structures at the particular frequency-thickness (*fd*) product. The relation between phase and group velocity (c_g) can be written as (66, 69):

$$c_\mathrm{g} = c_\mathrm{p}^2 \left[c_\mathrm{p} - (fd) \frac{dc_\mathrm{p}}{d(fd)} \right]^{-1}. \tag{1.1.13}$$

Unlike the bulk waves, Lamb waves possess an infinite number of modes that can propagate in the structure. It means that for any frequency-thickness product (*fd*) there is an infinite number of wavenumbers *k*, which satisfy eq. 1.1.12. The most basic modes of the Lamb waves, which can propagate in the plate-like structures, are called symmetrical (S_i), asymmetrical (A_i) and shear (SH_i), where subscript (i = 0, 1…∞) denotes the order of the particular mode. Symmetrical and asymmetrical modes of the guided waves have both in-plane (x_1) and out-of-plane (x_3) displacements, while the shear mode is confined in one plane. The S_i modes have dominant radial in-plane displacements, whereas the A_i modes have a dominant out-of-plane displacement. However, as the frequency-thickness product (*fd*) increases, the ratio between in-plane and out-of-plane-displacement changes within the same mode (see Fig. 1.1.1) (14, 69).

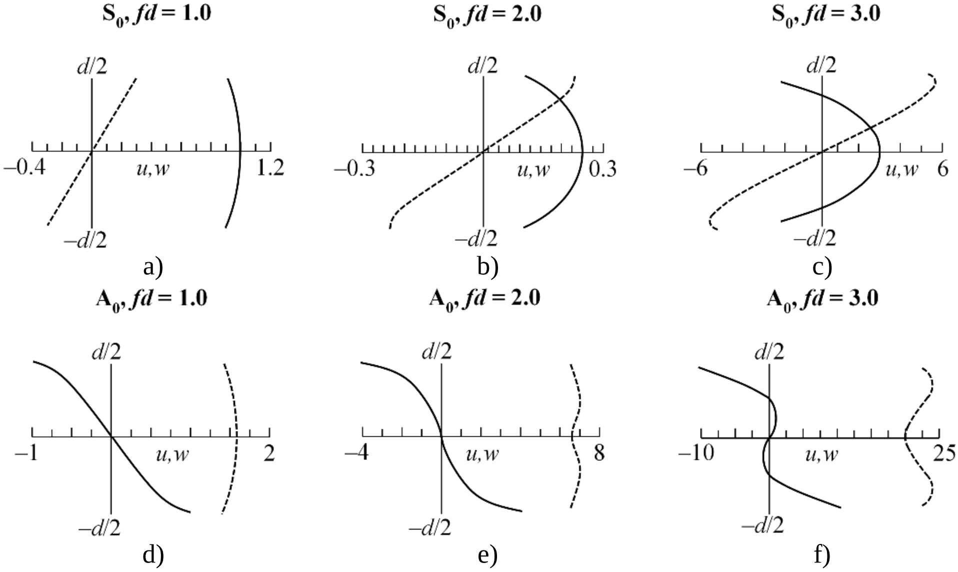

Fig. 1.1.1. The in-plane (*u*, solid line) and out-of-plane (*w*, dashed line) displacement profiles across the thickness of the aluminium plate (c_T = 3.1 mm/μs; c_L = 6.3 mm/μs) for the S_0 (a, b, c) and A_0 (d, e, f) modes at various frequency-thickness (*fd*) values (9, 67, 69)

The results in the picture above (Fig. 1.1.1) show that the S_0 mode has almost constant in-plane displacement at low frequencies, which becomes concentrated at the centre of the plate as the (*fd*) increases (Fig. 1.1.1a, b, c). Similar observations can be made for the A_0 mode, where the out-of-plane displacement starts to dominate at the outside surfaces at higher (*fd*) values (Fig. 1.1.1d, e, f).

The shear mode of the guided waves possesses the particle vibration orthogonal to the direction of wave propagation (x_2). The SH_i modes can also be either symmetrical (shear-horizontal) or asymmetrical (shear-vertical). In the case of ($u_1 = u_3 = 0$), the general equation for the SH_i mode can be written as (14, 70):

$$\frac{\partial^2 u_2}{\partial x_1^2}+\frac{\partial^2 u_2}{\partial x_3^2}=\frac{1}{c_T^2}\frac{\partial^2 u^2}{\partial t^2}. \tag{1.1.14}$$

With the appropriate boundary conditions ($\frac{\partial u_2}{\partial x_3}=0, x_3 = 0$) the solution to eq. 1.1.15 can be written as (14):

$$u_2(x_1,x_3,t)=Ae^{-bx_3}\exp[i(kx_1-\omega t)], \tag{1.1.15}$$

where A is the constant, $b=k\left[1-\left(\frac{\omega}{k\cdot c_T}\right)^2\right]^{1/2}$.

Each mode of the Lamb wave propagates with different a velocity, which depends on frequency, thickness, density and elasticity of the material (14, 74). This phenomenon is called dispersion and for the symmetric and the antisymmetric modes can be described by eq. 1.1.12. The real part of the numerical solution of these Rayleigh-Lamb equations enables the dispersion curves (DC) to be obtained, which graphically describe the relationship between the phase and group velocity of the guided wave modes and the product of the frequency and thickness. To obtain the numerical solution of the Rayleigh-Lamb equations, various methods, such as semi-analytical finite element (SAFE) (75, 76, 77, 78), transfer matrix (79, 80, 81) or global matrix (82, 83) can be used. The example of the phase c_p and group c_g velocity dispersion curves for the traction-free aluminium plate are presented in Fig. 1.1.2.

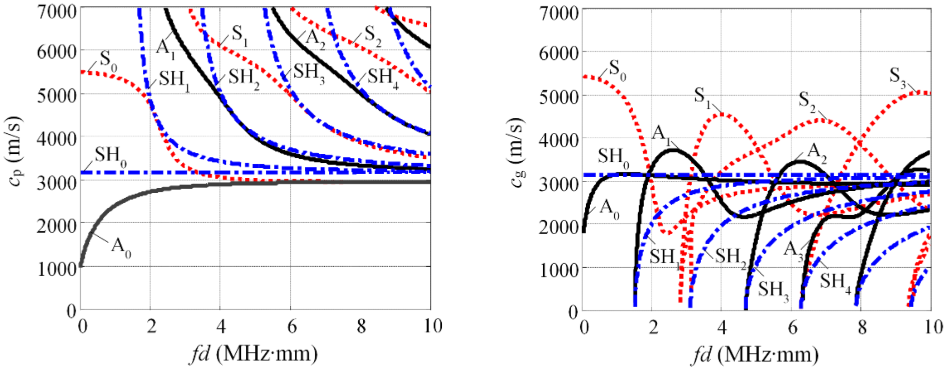

a) b)

Fig. 1.1.2. The phase (a) and group (b) velocity dispersion curves for a traction-free aluminium plate with a thickness of 1 mm (dashed line – symmetric modes; solid line – antisymmetric modes; dash-dot line – shear horizontal modes)

Due to the dispersion the higher-frequency parts of the waveform travel at different a velocity compared to the lower-frequency parts (66, 84). Therefore, each dispersive wave can be decomposed into the set of individual waves, which travel at different a velocity compared to the overall wave. The phase velocity c_p of the guided waves describe the speed of the individual waves within the single wave-packet, while the group velocity c_g is the velocity of an envelope or an overall wave (14, 66). Typically for the S_0 mode the lower-frequency parts move faster, so the trail of the waveform becomes contracted (see Fig. 1.1.3a). Conversely, the waveform of the A_0 mode becomes stretched-out, as the high frequency components move faster (see Fig. 1.1.3b). The results in Fig. 1.1.3 show that due to the dispersion the wave-packets become spread out in time domain and contracted in amplitude. Those factors limit the resolution and sensitivity to damage, especially in long range inspection. The intensity of the dispersion depends on the number of counts in the waveform. The waves with many cycles are less dispersive since the frequency spectra is quite narrow. However, if the waveform has only one or a few cycles it becomes highly dispersive due to the wide frequency band. For example, a continuous infinite harmonic wave is non-dispersive since its spectrum in the ideal case contains only one carrier frequency (66). However, if the signal duration is finite, it will be more or less dispersive.

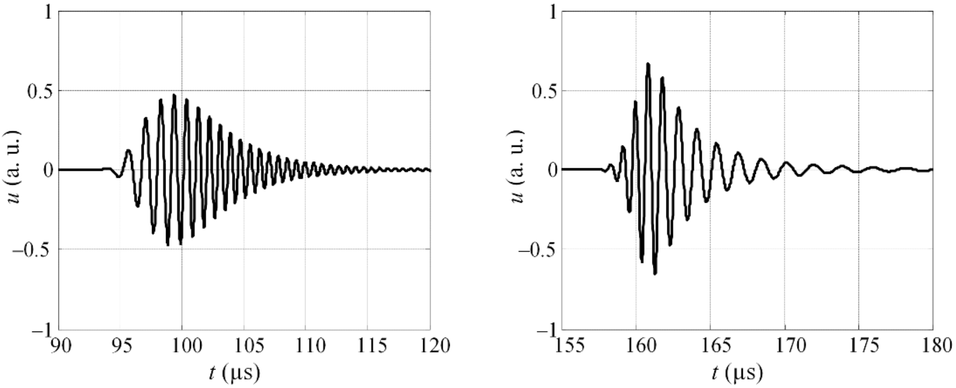

a) b)

Fig. 1.1.3. The 1 MHz waveforms of 3 cycles after traveling 0.5 m in 1 mm thickness aluminium plate: the S_0 mode (a) and the A_0 mode (b)

As the guided wave propagates in the material it encounters some obstacles, such as the defects or the waveguide boundaries. At the interface of the two medium, the ultrasonic wave undergoes reflection, refraction, scattering and mode conversion. The simplest case is a normal incidence to the planar boundary, when due to the difference in the acoustic impedances, there is a partial reflection and partial transmission. In addition to this, the waves that reflect from the medium with a lower acoustical impedance, will be reversed in phase (85). At the oblique incidence the part of the energy is refracted while the rest is reflected and converts into another mode. Wave scattering occurs in porous materials or at curved defects and causes loss in wave energy. The mechanism of the mode conversion and wave scattering can be described by Snell’s law, which relates the incidence angle and the wave velocity in the medium (69, 86). The phenomenon of the mode conversion and scattering has received great interest from various researchers while developing new methods for the detection of voids (87), grooves (88), notches (49, 89, 90, 91), corrosion (92, 93) and delaminations (94, 95, 96).

When the guided waves propagate in multi-layered laminated composite the symmetric and antisymmetric mode dispersion equations can be written as (97):

$$\begin{aligned}&\left(C_{33}R_{-}k_{\mathrm{z}-}+C_{13}k_{\mathrm{x}}\right)\left(R_{+}k_{\mathrm{x}}+k_{\mathrm{z}+}\right)\sin\left(k_{\mathrm{z}+}h\right)\cos\left(k_{\mathrm{z}-}h\right)-\\&-\left(C_{33}R_{+}k_{\mathrm{z}+}+C_{13}k_{\mathrm{x}}\right)\left(R_{-}k_{\mathrm{x}}+k_{\mathrm{z}-}\right)\sin\left(k_{\mathrm{z}-}h\right)\cos\left(k_{\mathrm{z}+}h\right)=0,\end{aligned}\tag{1.1.16}$$

$$\begin{aligned}&\left(C_{33}R_{+}k_{z+}+C_{13}k_{x}\right)\left(R_{-}k_{x}+k_{z-}\right)\sin\left(k_{z+}h\right)\cos\left(k_{z-}h\right)-\\&-\left(C_{33}R_{-}k_{z-}+C_{13}k_{x}\right)\left(R_{+}k_{x}+k_{z+}\right)\sin\left(k_{z-}h\right)\cos\left(k_{z+}h\right)=0,\end{aligned}\tag{1.1.17}$$

$$\begin{gathered}R_{\pm}=\frac{\left(\rho\omega-C_{11}k_x^2-C_{55}k_{z\pm}^2\right)}{\left(C_{55}+C_{13}\right)k_xk_{z\pm}},\ k_{z\pm}=\left[\frac{-M\pm\sqrt{M^2-4N}}{2}\right]k_x^2,\\ M=\frac{\left\{\frac{C_{11}C_{33}}{\rho^2}-\frac{1}{\rho}\left(2C_{55}C_{13}\right)+\left(C_{13}\right)^2-\frac{\omega^2}{\rho k_x^2}\left(C_{33}+C_{55}\right)\right\}}{\frac{C_{33}C_{55}}{\rho^2}},\\ N=\frac{\left\{\left(\frac{\omega^2}{k_x^2}-\frac{C_{11}}{\rho}\right)\left(\frac{\omega^2}{k_x^2}-\frac{C_{55}}{\rho}\right)\right\}}{\frac{C_{33}C_{55}}{\rho^2}},\end{gathered}\tag{1.1.18}$$

where C$_{iklm}$ is the stiffness matrix; k_x and k_z are the wavenumber of x and z direction, x, z represents the wave propagation and the plate thickness direction respectively.

The nature of the multi-layered anisotropic materials introduces such phenomena as reflection and refraction between the internal layers and the directional dependence of the wave velocity. It means that in the anisotropic composites there are no pure modes anymore, since the wave-front is not omnidirectional (98, 99). Moreover, the directional dependencies for the phase and the group velocities are different. The graphic representation of the directional dependence of the phase velocity $1/c_\mathrm{p}(\theta)$ is called the slowness profile, where θ – is the angle of wave propagation (Fig. 1.1.4a) (14, 69). The slowness profile can be calculated by solving the Christoffel equation (69):

$$\left(\rho\omega^2\delta_{im}-C_{iklm}k_\mathrm{k}k_\mathrm{l}\right)\cdot u_m=0,\tag{1.1.19}$$

where δ_{im} is Kronecker's delta; k_k and k_l represents the wave-front propagation direction and u_m are the displacements. From Fig. 1.1.4a it follows that the group velocity vector $\vec{c}_\mathrm{g}$ is perpendicular to the tangent of the slowness profile, while the direction of the wave-vector $\vec{k}$ or the phase velocity vector $\vec{c}_\mathrm{p}$ is different. The angle between the vectors $\vec{c}_\mathrm{g}$ and $\vec{k}$ is called the skew angle ϕ (97, 99). The plot of the group velocity $c_\mathrm{g}(\psi)$, where ψ is the combination of θ and the skew angle ϕ, is called the wave-front curve (Fig. 1.1.4b). The results in Fig. 1.1.4b show that in this case the wave-vector $\vec{k}$ is perpendicular to the tangent of the wave-front curve (97, 99).

The analysis of the basic guided wave features shows that there are many factors that complicate the use of guided waves for non-destructive inspection, especially for multi-layered anisotropic composites. Since all the waves propagate at a different frequency and direction dependent velocities, after multiple reflections, scattering and mode conversions, the receiver captures the interfered and diffused ultrasonic field. Moreover, those features vary going from one structure to another and depend on the type of excitation. To illustrate the complexity of the problem, the example of a typical waveform captured from the rectangular anisotropic composite is presented in Fig. 1.1.5. To be able to analyse such signals and to detect the damage, there is a need for a deep understanding of the mechanism of guided wave generation, propagation and interaction with the medium as well as with the likely defects.

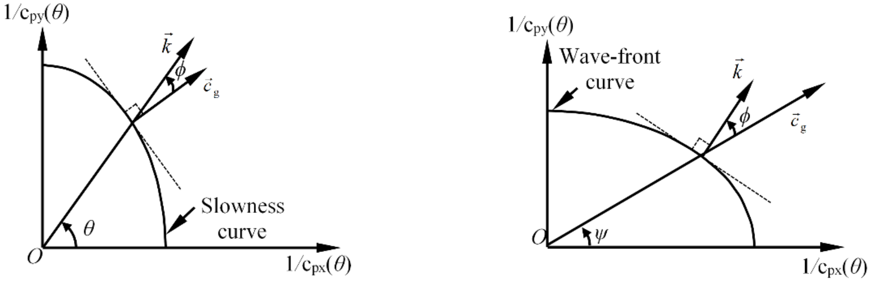

a) b)

Fig. 1.1.4. The relation between the wave vector and the group velocity vector: the slowness profile $1/c_p(\theta)$ (a) and the wave-front curve (b) (97, 99)

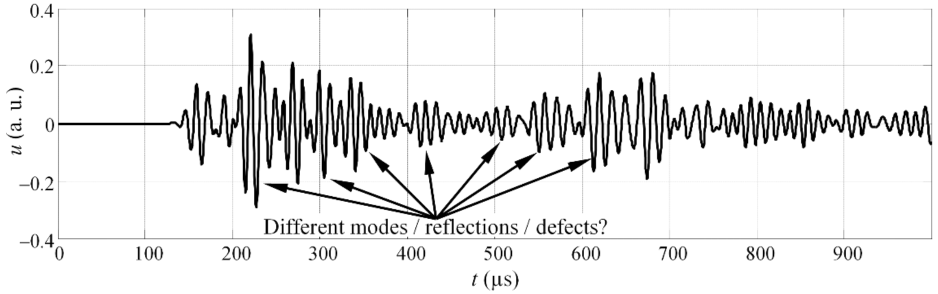

Fig. 1.1.5. An example of the multimodal, dispersive and interfered waveform captured on 4 mm thickness glass fibre reinforced plastic

There are a few main trends in the field of guided wave inspection that attracts the most attention among various researchers. These are related to the most relevant problems and the current state of the art. Three major topics or trends can be outlined as follows: the investigations on the mechanism of guided wave generation and mode tuning to produce single mode signals and to make the analysis of the acquired waveforms easier (100, 101, 102); the development of guided wave mode decomposition methods to extract the information from the overlapped signals (103, 104, 105); the investigations on the interaction between the guided waves and the defects, to detect the damage and to extract its features (106, 107, 108, 109).

1.2 Means of ultrasonic guided wave generation, mode selection and tuning

The following chapter discusses the main issues that have to be addressed in order to properly select the GW mode for inspection as well as the existing means to generate it, supressing the displacements of the other modes. Additionally, an advantage of using multi-modal inspection over the single mode approach is considered and the existing gaps for new signal analysis methods in case of multimode inspection are revealed. Prior to development of any SHM technique, the appropriate mode should be considered, which satisfies the system requirements. In the ideal case the Lamb wave mode that most suits the defect detection should feature: no dispersion, low attenuation, high sensitivity to the damage, easy excitability and detectability (55). Some of these features, like dispersion, attenuation and sensitivity depend on the material under inspection, while the rest of them rely on the scheme of the excitation (110). As it was mentioned in Chapter 1.1, the dispersion can limit the spatial resolution, the sensitivity to the damage as well as the distance of propagation. The effect of dispersion can be reduced by using the narrow band tone-bursts for guided wave excitation. The relation between the frequency band [$f_{\min}$, $f_{\max}$] of the tone-burst, the central frequency f_0 and the number of cycles n can be expressed as (110):

$$f_{\min} = f_0\left(1-\frac{k}{n}\right),\quad f_{\max} = f_0\left(1+\frac{k}{n}\right), \tag{1.2.1}$$

where k is the constant depending on the bandwidth being used. From the equation above it follows that when the number of cycles n increases, the bandwidth [$f_{\min}$, $f_{\max}$] reduces. However, the narrowband signals possess a long duration in the time domain and can overlap with other modes or structural reflections. For each guided wave mode there is the point on the dispersion curve, where the best compromise between the propagation distance, number of cycles, wavelength and resolution can be achieved. This can be determined by the minimum resolvable distance MRD (111):

$$\mathrm{MRD} = \frac{c_0}{d}\left[l\left(\frac{1}{c_{\min}} - \frac{1}{c_{\max}}\right) + T_{\mathrm{in}} \right]\Bigg|_{\min}, \tag{1.2.2}$$

where l and d are the wave propagation distance and the plate thickness; $c_{\min}$, $c_{\max}$ are the minimum and maximum velocities through the distance l; c_0 is the velocity at the central frequency; T_{in} is the initial time duration of the wave-packet. In general, the MRD value show the best possible spatial resolution for the particular frequency and propagation distance, which can be achieved if the number cycles are optimised in the input signal. For the fundamental modes A_0 and S_0 the MRD values varies at low frequencies and tends to monotonically reduce at higher frequencies. However even at low frequencies local minima can be found, which represents a good resolution point. Typically, the fundamental modes possess lower local MRD values and require less cycles to obtain a good resolution (55, 110, 111).

The attenuation is another factor which has to be considered while selecting an appropriate guided wave mode for inspection. The guided waves are mainly attenuated due to (110, 112): dispersion, beam divergence, material damping, scattering and leakage into the adjacent media. One of the most dominant among the abovementioned factors is the leakage of the acoustic energy into the surrounding media (30, 113). The leaking amount of energy is a function of frequency, which depends on the coupling between the modes in the structure and the bulk waves that can exist in the embedded media. For example, if the metal plate is surrounded by air, there will be no leakage due to the huge mismatch between the acoustic impedances of the two mediums. On the other hand, for metals submersed in water, the leakage losses can be significant for some of the modes (110). The bulk waves in the embedded media can only be excited if the phase velocity of the guided waves in the structure is above the bulk wave velocity in the surroundings ($c_{\mathrm{p}}>c_{\mathrm{L}}$ or $c_{\mathrm{p}}>c_{\mathrm{T}}$). Otherwise if the phase velocity is less than the velocity of any bulk wave ($c_{\mathrm{p}}<c_{\mathrm{L}}$ or $c_{\mathrm{p}}<c_{\mathrm{T}}$), there will be no leakage of wave energy (114). It should be considered, that the A_0 mode is more attenuated, however, it has a shorter wavelength and is more sensitive to the delaminations, surface and sub-surface defects. In contrast, the S_0 mode is almost non-dispersive at low frequencies and is highly effective at detecting the damage anywhere in the thickness of the plate (14, 56). In most of the cases, it is preferred to excite a single mode of the guided waves, because it makes the analysis of the signals much easier (115). However, the generation of multiple modes at the same time makes the inspection system more versatile, since the different modes possess different properties. In the few following paragraphs, the approaches to excite the single desired mode of the guided waves will be reviewed. Subsequently the chapter is concluded with short discussion of the advantages of multi-mode excitation.

Since the most suitable mode of the guided waves is selected for the inspection, it has to be excited in the structure by some means. The simplest solution is to apply the excitation force to the surface of the specimen, with the same direction as the dominant displacements of the preferred mode. In other words, the tangential force is used to excite the symmetrical modes S_i, while the normal force is used for the asymmetrical one A_i. However, under such excitation conditions, multiple modes are generated anyway (116). The selective guided wave mode generation is usually achieved by using either simple piezoelectric lead zirconate titanate wafers (PZT), interdigital or phased array transducers (117, 118, 119, 120, 121).

The basic piezoelectric wafers are usually made from the lead zirconium titanate ($\mathrm{Pb(Zr\text{–}Ti)O_3}$) or polyvinylidene fluoride films (PVDF). Although the PVDF transducers are thin, flexible and durable, the PZT patches are preferred. The major drawbacks of PVDF are the poor inverse piezoelectric effect and electromechanical coupling, large temperature dependency and limited applications at frequencies lower than 500 kHz (122, 123). The single mode excitation with the PZT wafers can be achieved by selecting the appropriate size of an element. For the PZT wafer the strain $\varepsilon(x,t)$ and displacement $u(x,t)$ wave solutions can be written as (100, 124):

$$\begin{aligned} \varepsilon_x(x,t)\big|_{y=d} &= -i\frac{a\tau_0}{\mu}\sum_{k^{\mathrm{S}}}\left(\sin k^{\mathrm{S}} a\right)\frac{N_{\mathrm{S}}\left(k^{\mathrm{S}}\right)}{D_{\mathrm{S}}'\left(k^{\mathrm{S}}\right)}e^{-i\left(k^{\mathrm{S}}x-\omega t\right)} - \\ &-i\frac{a\tau_0}{\mu}\sum_{k^{\mathrm{A}}}\left(\sin k^{\mathrm{A}} a\right)\frac{N_{\mathrm{A}}\left(k^{\mathrm{A}}\right)}{D_{\mathrm{A}}'\left(k^{\mathrm{A}}\right)}e^{-i\left(k^{\mathrm{A}}x-\omega t\right)}, \end{aligned} \tag{1.2.3}$$

$$u_x(x,t)\big|_{y=d} = -i\frac{a\tau_0}{\mu}\sum_{k^{\mathrm{S}}}\frac{\sin k^{\mathrm{S}}a}{k^{\mathrm{S}}}\frac{N_{\mathrm{S}}\left(k^{\mathrm{S}}\right)}{D'_{\mathrm{S}}\left(k^{\mathrm{S}}\right)}e^{-i\left(k^{\mathrm{S}}x-\omega t\right)} - \\ -i\frac{a\tau_0}{\mu}\sum_{k^{\mathrm{A}}}\frac{\sin k^{\mathrm{A}}a}{k^{\mathrm{A}}}\frac{N_{\mathrm{A}}\left(k^{\mathrm{A}}\right)}{D'_{\mathrm{A}}\left(k^{\mathrm{A}}\right)}e^{-i\left(k^{\mathrm{A}}x-\omega t\right)}, \tag{1.2.4}$$

where

$$\begin{gathered} D_{\mathrm{S}} = \left(k^2-q^2\right)^2\cos(ph)\sin(qh) + 4k^2pq\sin(ph)\cos(qh), \\ N_{\mathrm{S}} = kq\left(k^2+q^2\right)\cos(ph)\cos(qh), \\ D_{\mathrm{A}} = \left(k^2-q^2\right)^2\sin(ph)\cos(qh) + 4k^2pq\cos(ph)\sin(qh), \\ N_{\mathrm{A}} = kq\left(k^2+q^2\right)\sin(ph)\sin(qh), \end{gathered} \tag{1.2.5}$$

a is the lateral width of the transducer; the notations S and A at the subscript or the superscript denotes the variables corresponding either to the symmetric or the asymmetric motion. From eq. 1.2.3 and eq. 1.2.4 it follows that the maxima of the function $\sin(ka)$ will occur, when $ka=((2n–1)\pi)/2$. It means that the function exceeds the maximum value when the width of the transducer $2a$ is equal to the odd multiple of half wavelengths $\lambda/2$. In the same fashion, the minima of the function $\sin(ka)$ occurs when $ka = n\pi$ or the width of the transducer is equal to the even number of half wavelengths $\lambda/2$. In such a way the selection of the size of PZT wafers enables the frequencies at which only the single mode is dominant to be found (124, 125, 126). However, the PZT wafers have a few disadvantages, which led the researchers to continue investigating the capabilities of single mode generation. Since the size of the PZT wafer depends on the wavelength, the set of the PZT patches are required to be tuned for different modes or at different frequencies. Moreover, the size of the PZT transducer should become quite large at lower frequencies, leading to poor surface conformability (123, 127).

The other way to excite the single guided wave mode is to use interdigital transducers (IDT) (78, 115, 127, 128, 129, 130). Such kind of transducers consists of two sets of electrodes that are driven by an opposite phase electrical field. The top view of the conventional IDT transducer is presented in Fig. 1.2.1a. The main transducer parameters are: the quantity (*n*), the pitch (*S*), the width (*W*) and the length (*L*) of the electrode. The width of the electrode (*W*) sets the effective area of the transducer, while the length (*L*) influences the directivity. The other parameters, such as the number of electrodes (*n*) is related to the resolution and mode selectivity. In order to excite the single mode with the interdigital transducer, the pitch (*S*) between the electrodes must be equal to half the wavelength $\lambda/2$ of the desired mode (129). There are many approaches to design and improve the interdigital transducers. Salas and Cesnik (123) introduced sectorial IDT's, which enables an angular scan of an object to be performed. Jin et al. (130) developed a double sided IDT with strong excitation efficiency and spatial focusing. Finally, Jeong et al. (127) designed and investigated a single element, paired IDT transducer, which is optimised for Rayleigh wave generation at 3 MHz on a 1.27 cm thickness aluminium plate.

Since the IDT transducers are quite robust, the more convenient approach is to use the phased arrays, or a pair of separately driven actuators. By selecting the appropriate distance between the elements, the displacements for the particular mode can be optimized (120). Grondel et al. (131) showed, that the predominant A_0 mode can be efficiently generated by using dual elements and in-phase excitation (see Fig. 1.2.1b). He showed that the normal amplitude of the mode is a function of the inter-element distance p:

$$a_{\{m\}}(x_1, p)=\left(\sum_{n=0}^{N-1} e^{jk_{\{m\}}np}\right)a_{\{m\}}(x_1), \tag{1.2.6}$$

where $a_{\{m\}}(x_1)$ is the normal amplitude of the mode along the x_1 direction; N is the number of elements excited in phase. Using this approach both single A_0 and single S_0 modes can be generated, depending on the inter-element distance p, which is equal to two wavelengths of the desired mode 2λ. The pair of elements can also be mounted on the opposite surfaces of the specimen. In that case, depending on the poling direction, both pure A_0 and S_0 modes can be produced with the same configuration (see Fig. 1.2.1c). For the S_0 mode out-of-phase generation is required, while the A_0 mode is efficiently generated using in-phase excitation (132).

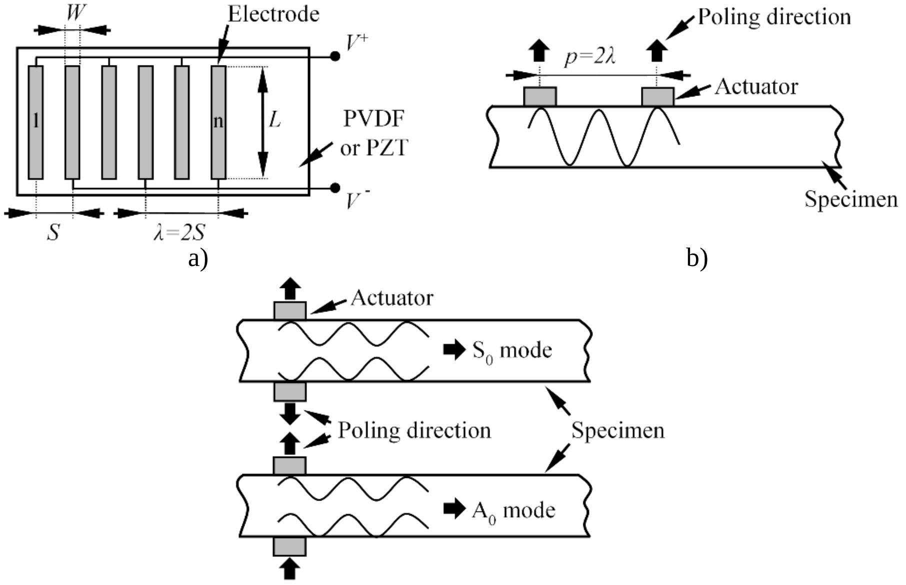

a) b)

c)

Fig. 1.2.1. The basic configuration of an IDT transducer (a) and the basic principle for generation of the single guided wave modes in case of one-side (b) and two-side (c) access (129, 131, 132)

There is plenty of research focusing on single guided wave mode generation using either the phased arrays or separately driven actuators. Fromme et al. (133) used a ring shaped array to perform a circular B-scan imaging of the structure. Borigo et al. (134) investigated the omnidirectional single mode generation using the annular arrays. Special attention was also made to the use of phased delays to control the mode selection (120, 135, 136).

The single mode excitation techniques can be an attractive way to make the analysis of the acquired signals easier. However, it is only a partial and usually not sufficient solution, because other modes with significantly lower displacements are also excited. It means that with the methods described above it is possible to get one dominant mode, but most likely it will not be single in the entire structure. Moreover, after the mode conversion and multiple reflections, the interpretation of such results will be complicated anyway. The example of the simulated single S_0 mode signal, after multiple reflections in the basic rectangular defect-free GFRP plate (70 mm × 670 mm) is presented in Fig. 1.2.2 (the mode conversion and the attenuation is neglected). From the results presented in Fig. 1.2.2 follows, that despite the use of a single mode excitation scheme, several wave-packets still exist due to omnidirectional wave propagation. The inclusion of the defects and mode conversion, would make the resulting signal even more complicated. Therefore, the methods to analyse such waveforms and to identify/trace wave-packets are required.

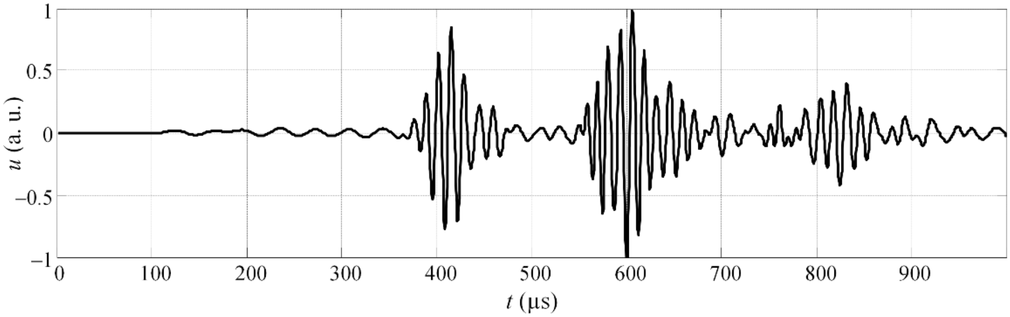

Fig. 1.2.2. A simulated time representation of the S_0 mode after propagation in a rectangular defect free GFRP plate with dimensions of 70 mm × 670 mm

The single mode excitation can also be robust, since in all cases the sets of transducers are mandatory if excitation of various modes at different frequencies are required. In addition, at low frequencies, such actuators become bulky, as the inter-element distance depends on the wavelength. On the other hand, the multimode excitation makes the inspection system more versatile. As mentioned above, different modes possess different properties and each of them is more sensitive to a different kind of defect due to distinct displacement profiles. This leads to the conclusion that single-mode excitation might not always be the solution for the reliable monitoring system. The techniques for single mode excitation are mainly developed for simplification purposes. In order to have a both reliable and versatile SHM system, a multi-modal excitation might be used along with the sophisticated signal processing methods for analysis of guided wave generation and propagation. One of the most important factor in this case is to understand the mechanism that generates the guided waves within the structure and what parameters determine the spectral characteristics of each mode. This initial information is crucial for further analysis of the dynamical behaviour of GW and for the development of other signal processing methods, which rely on the initial data.

1.3 Existing numerical and analytical methods for the simulation of guided wave propagation

Prior to the investigation of any structure or development of any NDT method it is essential to know and predict what kind of modes can propagate in the structure under certain excitation and how it interacts with structural features such as object boundaries and defects. This leads to the proper development of inspection techniques, based on the initial simulation data. The aim of this chapter is to review the existing numerical and analytical methods for simulation of guided wave propagation and to identify the needs for development of new methods adapted to the special requirements of SMH systems. There are few commonly available predictive modelling techniques for simulation and analysis of guided wave propagation in anisotropic plate-like structures. Two major groups can be outlined: methods for calculation of dispersion relations, which in general allows the type of modes and its corresponding velocities at particular frequency band to be identified and tools for simulation of guided wave propagation over long distances, which enables the complex dynamic guided wave behaviour to be calculated and analysed.

The numerical solution of the Rayleigh-Lamb equations, which in general gives the dispersion relationship, can be obtained using either the transfer matrix (79, 80, 81), global matrix (82, 83) or semi-analytical finite element (75, 76, 77, 78) methods. In the subsequent paragraphs the basics of each method will be reviewed followed by a short discussion about the existing merits and demerits.

In the transfer matrix method, the multi-layered structure is condensed into a set of four equations that relates the boundary conditions of the first and the last interface eliminating the equations for the intermediate interfaces (82). Let's consider a structure, which consist of *N* layers (Fig. 1.3.1a). The transfer matrix method assumes that in the case of an isotropic structure four waves exist at each layer: the direct longitudinal L^+ and shear S^+ propagating down from the upper interface and reflected longitudinal L^- and shear S^- coming up from the lower interface. In the case of an anisotropic structure, six partial waves exist: longitudinal (L^+, L^-), shear horizontal (SH^+, SH^-) and shear vertical (SV^+, SV^-). The superposition of these four to six partial waves can describe any field in the case of the linear system (137). Then the displacements $\mathbf{u}_{j\text{-}1}$ and stresses $\boldsymbol{\sigma}_{j\text{-}1}$ on the upper surface ($z=z_j$) of the j^{th} layer can be expressed in the matrix form as (79, 81):

$$\begin{bmatrix} \mathbf{u}_{j-1} \\ \boldsymbol{\sigma}_{j-1} \end{bmatrix} = \begin{bmatrix} \mathbf{P}^- & \mathbf{P}^+\mathbf{H}^+ \\ \mathbf{D}^- & \mathbf{D}^+\mathbf{H}^+ \end{bmatrix}_j \begin{bmatrix} \mathbf{A}_j^- \\ \mathbf{A}_j^+ \end{bmatrix}, \tag{1.3.1}$$

$$\mathbf{P}^\pm = \left[\mathbf{p}_1^\pm \quad \mathbf{p}_2^\pm \quad \mathbf{p}_3^\pm\right], \; \mathbf{D}^\pm = \left[\mathbf{d}_1^\pm \quad \mathbf{d}_2^\pm \quad \mathbf{d}_3^\pm\right], \; \mathbf{A}_j^\pm = \left[\mathbf{a}_1^\pm \quad \mathbf{a}_2^\pm \quad \mathbf{a}_3^\pm\right]_j^{\mathrm{T}},$$

$$\mathbf{H}^+ = \mathrm{Diag}\left[e^{-ik_z^{+1}h_j} \quad e^{-ik_z^{+2}h_j} \quad e^{-ik_z^{+3}h_j}\right], \; h_j = z_{j-1} - z_j, \tag{1.3.2}$$

where positive and negative superscripts represent the wave propagation in *z*+ or *z*– directions; $\mathbf{p}_i^\pm$ are the displacement polarization vectors (*i* – denotes i^{th} partial wave, $i = 1, 2, 3$); T – represents transpose; Diag – denotes the diagonal matrix; h_j is the thickness of the j^{th} layer; k_z is the wave vector; **A** is the wave amplitude vector.

Analogically for the bottom surface ($z = z_j$) the displacements $\mathbf{u}_{j\text{-}1}$ and stresses $\boldsymbol{\sigma}_{j\text{-}1}$ are formulated as (79, 81):

$$\begin{bmatrix} \mathbf{u}_j \\ \boldsymbol{\sigma}_j \end{bmatrix} = \begin{bmatrix} \mathbf{P}^{-}\mathbf{H}^{-} & \mathbf{P}^{+} \\ \mathbf{D}^{-}\mathbf{H}^{-} & \mathbf{D}^{+} \end{bmatrix}_j \begin{bmatrix} \mathbf{A}_j^{-} \\ \mathbf{A}_j^{+} \end{bmatrix}, \tag{1.3.3}$$

$$\mathbf{H}^{-} = \mathrm{Diag}\begin{bmatrix} e^{-ik_z^{-1}h_j} & e^{-ik_z^{-2}h_j} & e^{-ik_z^{-3}h_j} \end{bmatrix}. \tag{1.3.4}$$

Combining eq.1.3.1 and eq.1.3.3 leads to the expression of the layer transfer matrix $\mathbf{B}_j$, which relates the displacements and stresses at the top and bottom of the j^{th} layer (79, 81):

$$\begin{bmatrix} \mathbf{u}_j \\ \boldsymbol{\sigma}_j \end{bmatrix} = \begin{bmatrix} \mathbf{P}^{-}\mathbf{H}^{-} & \mathbf{P}^{+} \\ \mathbf{D}^{-}\mathbf{H}^{-} & \mathbf{D}^{+} \end{bmatrix}_j \begin{bmatrix} \mathbf{P}^{-}\mathbf{H}^{-} & \mathbf{P}^{+} \\ \mathbf{D}^{-}\mathbf{H}^{-} & \mathbf{D}^{+} \end{bmatrix}_j^{-1} \begin{bmatrix} \mathbf{u}_{j-1} \\ \boldsymbol{\sigma}_{j-1} \end{bmatrix} = \mathbf{B}_j \begin{bmatrix} \mathbf{u}_{j-1} \\ \boldsymbol{\sigma}_{j-1} \end{bmatrix}. \tag{1.3.5}$$

The transfer matrix $\mathbf{B}_J$ for the whole structure can then be obtained by the multiplication of each layer's transfer matrix $\mathbf{B}_j$ (81):

$$\mathbf{B}_J = \mathbf{B}_j \mathbf{B}_{J-1}, \tag{1.3.6}$$

$$\mathbf{B}_{J-1} = \prod_{i=1}^{J-1} \mathbf{B}_i,$$

where $\mathbf{B}_{J\text{–}1}$ – is the total transfer matrix for the top J–1 layers, capital indices indicate the total number of layers. From the formulation above it follows that the transfer matrix method condenses the dispersion equations of individual layers, thus the external boundary conditions are considered only (14). The major drawback of the transfer matrix method is that it becomes numerically unstable for the waves at oblique incidence above the critical angle and if the thickness of the plate or the frequency increases to infinity. In such case both matrices in eq. 1.3.5 have zero columns, thus become singular, which is the cause of the instability. There are some available approaches to solve the instability problem by reformulating the recursive algorithm with the calculation of the layer stiffness matrix (79, 81). However, the alternative methods, such as global matrix and SAFE, are mostly used instead.

The global matrix method describes the whole system with the single matrix **G**, which consists of 4(n–1) equations (n – is the total number of layers) (82, 83, 138):

$$G = \begin{bmatrix} \mathbf{D}_{1hb} & \mathbf{D}_{2t} & & & & \\ & \mathbf{D}_{2b} & \mathbf{D}_{3t} & & & \\ & & \mathbf{D}_{3b} & \cdots & & \\ & & & \cdots & \mathbf{D}_{(n-1)t} & \\ & & & & \mathbf{D}_{(n-1)b} & \mathbf{D}_{htn} \end{bmatrix}, \tag{1.3.7}$$

where $\mathbf{D}_{1hb}$, $\mathbf{D}_{htn}$ – bottom and top half space matrices respectively, which denotes the acoustic loading conditions of the analysed multi-layered structure, $\mathbf{D}_{jt}$, $\mathbf{D}_{jb}$ – top and bottom matrices of the j^{th} layer, which describes the wave reflection and transmission at the top and bottom of the considered layer. In this case the complete matrix **G** is used for the solution, instead of the recursive approach. The global matrix method enables different loading conditions to be simulated as well as the influence of the structural defects such as a kissing bond or delaminations. On the other hand, for some structures the matrix **G** can become quite bulky, leading to the slow solution.

In contrast to the matrix techniques, in the SAFE method the 2D cross-section of the analysed structure is meshed into the grid of points and the displacement field is expressed by nodal displacements with an interpolation function across the whole cross-section of the structure. The displacement distribution along the direction of wave propagation (z) is described by orthogonal functions $e^{i\xi z}$, where ξ is the wavenumber (see Fig. 1.3.1b). The governing equation for the SAFE method can be written as (139):

$$\bar{\mathbf{f}} = \left(\mathbf{K}_1 + i\xi\mathbf{K}_2 + \xi^2\mathbf{K}_3\right)\bar{\mathbf{U}} - \omega^2\mathbf{M}\bar{\mathbf{U}}, \tag{1.3.8}$$

where $\bar{\mathbf{f}}$ and $\bar{\mathbf{U}}$ are the Fourier transform of the nodal force vector **f** and displacement vector **U**; $\mathbf{K}_1$, $\mathbf{K}_2$, and $\mathbf{K}_3$ are the matrices obtained from material properties; **M** is the mass matrix; ω is the angular frequency. The governing equations (eq. 1.3.8) of the SAFE method can be expressed as the first order Eigen system, which can be solved with respect to the wavenumber ξ at a certain frequency (76):

$$(\mathbf{A} - \xi\mathbf{B})\mathbf{Q} = \mathbf{p}, \tag{1.3.9}$$

$$\mathbf{A} = \begin{bmatrix} 0 & \mathbf{K}_1 - \omega^2\mathbf{M} \\ \mathbf{K}_1 - \omega^2\mathbf{M} & i\mathbf{K}_2 \end{bmatrix}, \mathbf{B} = \begin{bmatrix} \mathbf{K}_1 - \omega^2\mathbf{M} & 0 \\ 0 & -\mathbf{K}_3 \end{bmatrix}, \mathbf{Q} = \begin{bmatrix} \bar{\mathbf{U}} \\ \xi\bar{\mathbf{U}} \end{bmatrix}, \mathbf{p} = \begin{bmatrix} 0 \\ \bar{\mathbf{f}} \end{bmatrix}. \tag{1.3.10}$$

Consequently, the m^{th} solution ξ_{m} of the Eigen system gives the wavenumber of m^{th} resonance mode at the certain frequency. The phase and group velocities of m^{th} mode at angular frequency ω are then expressed as (75):

$$c_{\text{p}} = \frac{\omega}{\xi_m},\ c_{\text{g}} = \frac{\text{d}\omega}{\text{d}\xi_m}. \tag{1.3.11}$$

The SAFE method is easily applicable to the geometries with complicated cross-sections (rails, spar, longeron etc.), unlike the conventional matrix techniques. On the other hand, since the method only takes into the account the cross-section of the material it can only be used for the structures uniform in the longitudinal direction. Moreover, the SAFE method experiences some issues with the mode sorting and differentiation in case multiple modes with similar velocities exist at the same frequency (140). Loveday et al. (141) addressed the latter issue and proposed to exploit modal orthogonality for sorting of guided wave modes in rails. Additionally, Mu and Rose (78) developed orthogonality for the multi-layered structures possessing any combination of elastic and viscoelastic materials.

The methods described above are the most popular tools for the analysis of dispersion relationships of the GW. It gives the very important initial knowledge, in general what type of modes can propagate in the considered structure in the particular frequency band and under the certain excitation conditions. Moreover, some of those methods enables the in-plane and out-of-plane displacement profiles to be analysed, even for the multi-layered structures. However, this initial knowledge is usually not sufficient for the complete understanding of the mechanism of the guided wave generation, long range propagation and interaction with the structural features. In order to have a full understanding of guided wave behaviour, the finite element (FE) (142), boundary element (143) or spectral element (144) methods are additionally used for the simulation of the dynamic behaviour of the GW.

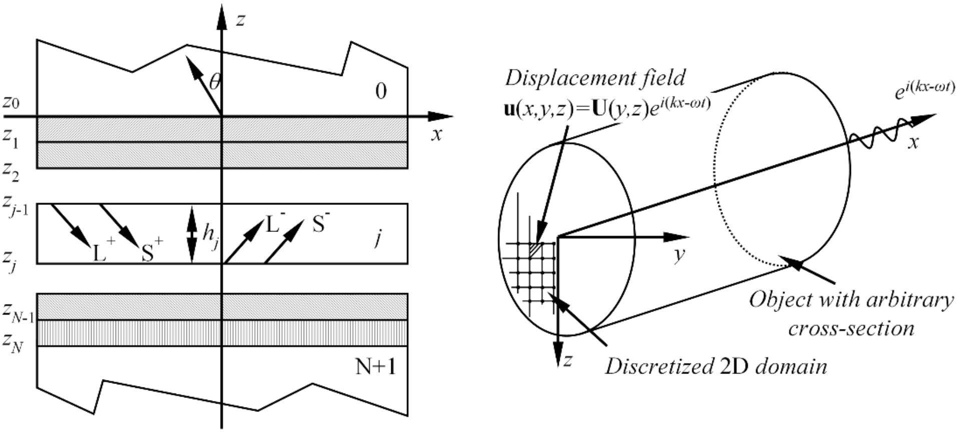

a) b)

Fig. 1.3.1. A sketch of the multi-layered structure with four partial waves at jth layer for principle demonstration of the transfer matrix method (a) a mesh of the cross-section of an analysed structure and calculation of displacement field for principle demonstration of SAFE method (75, 81)

The idea of the conventional finite element method lies on the approximate numerical solution of the governing equations of motion and associated boundary conditions. The solution is obtained by meshing the entire structure into the finite elements and calculating the values of the field variables at each node of the mesh. In the case of a 2D solid body under plane stress, the displacement vector having two components (degrees of freedom) is calculated as the field variable at each node of the finite element. The solutions for the non-nodal points within the element are then obtained using the interpolation of the elements nodal values. The general equation of motion in the matrix form, which is solved in the FE method, can be written as (142):

$$[\mathbf{M}]\ddot{\mathbf{u}} + [\mathbf{C}]\dot{\mathbf{u}} + [\mathbf{K}]\mathbf{u} = \{\mathbf{F}(t)\}, \qquad (1.3.12)$$

where [**M**], [**C**], and [**K**] are the mass, damping and stiffness matrices respectively; **u** is the displacement vector and its time derivatives. The dynamic solution of eq. 1.3.12 can be obtained using different time integration methods, such as implicit Newmark or explicit Central difference (145). In order to obtain reliable results, the finite element method requires the proper selection of the time integration step Δt and size of the finite element l_e. If the time step Δt is too long, the higher frequency components are not resolved properly, while too small time step leads to a high computation time. For the Newmark time integration scheme, the best compromise between the accuracy and calculation time is achieved when Δt is 20 points per cycle of the highest frequency of interest $f_{\max}$ (146):

$$\Delta t = \frac{1}{20 f_{\max}}. \tag{1.3.13}$$

Similarly, the size of the element l_e should be at least 10 ÷ 20 nodes per wavelength of the shortest wave $\lambda_{\min}$ (147):

$$l_e = \frac{\lambda_{\min}}{20}. \tag{1.3.14}$$

The finite element analysis can give a quite accurate dynamical representation of guided wave propagation. However, the high frequency 3D solutions require a fine mesh and small integration time step, which leads to a huge demand on computational resources and time. The following example gives an idea of this problem. Consider the guided wave propagation is simulated in the 10 cm × 1 cm 2D plate for the $t = 50$ μs, up to frequency $f_{\max} = 2$ MHz ($\lambda_{\min} = 2$ mm). Then according to eq.1.3.13 and eq.1.3.14 $\Delta t = 0.025$ μs and $l_e = 0.1$ mm. The meshed 2D structure will then have 100,000 elements and 2,000 time integration steps. The real matrix equation for the 2D case will be twice the number of elements, because of the degrees of freedom and it has to be solved 2,000 times to obtain the final result (146). In structural health monitoring applications, the wavelengths are small compared to the dimensions of the object, therefore it requires a high number of elements and degrees of freedom if the structure is discretized according to eq.1.3.14. If some defects are introduced within the structure, in some cases it requires even finer mesh at the sharp edges such as the tip of the crack. There are some available approaches to decrease the calculation time of the FE method. The most common and easiest way is to use the explicit time integration schemes, such as central difference method, which bypasses the inversion of the stiffness matrix **[K]** during the solution of eq. 1.3.12, thus provide a faster result. On the other hand, the explicit methods are conditionally stable and require small time integration steps to give reliable results. Implicit methods, such as Newmark, are unconditionally stable, because the solution in this case is based on the quantities calculated in the previous time step. However, the implicit methods are slow and require the computationally intensive stiffness matrix inversion (145). There are some existing hybrid methods that have the general purpose of obtaining the faster solution. In the hybrid methods the semi-infinite, uniform and defect free regions are calculated using the analytical solutions, while defective areas are described by FE (143, 148). For example, Terrien et al. (149) used a combination of the FE and a modal decomposition method to study Lamb wave interactions with micro defects. The authors proposed to calculate the modal decomposition of the wave before and after the defect, while the finite element mesh was used in the regions around the defects. Similarly, Benmeddour et al. (150) coupled the classic FE with SAFE method to study the interaction of guided waves with cracks in cylinders. The authors used a semi-infinite waveguide with arbitrary cross-section before and after the volume with the crack. A slightly different approach was used by Gravenkamp et al. (143) who used a semi-analytical scaled boundary finite element method, which only requires the discretization of the object boundary with the surface finite elements.

All the methods described above can give the substantial information required for a better understanding of the behaviour of GW. However, the FE models cannot provide very fast results directly with the information most important in SHM applications. For example, in the case of SHM it is important to extract the information about the propagation of separate mode packets, to analyse the time of flight (ToF) and interaction between modes as well as to retrace wave propagation paths. This information is essential in order to understand how the guided waves behave in the structure, which modes are passing the defective area, what the sample spatial coverage is etc. Therefore, there is still a gap for rapid models that would allow the propagation of each guided wave mode to be analysed separately, to determine the propagation paths and ToF of each wave after multiple reflections. Such tool would be beneficial for prompt analysis and modelling of various real time situations as well as for the mode decomposition and could be further used as an advisory instrument in real-world SHM systems.

1.4 Techniques for time and frequency domain analysis and mode decomposition of ultrasonic guided waves

Since the few chapters above were discussing a possible demand for tools to improve the understanding of the guided wave generation and propagation, this chapter deals with the review of the existing methods to decompose the guided wave signals and to extract the information about the damage from the data, which is measured at distinct positions on the object. The conventional solutions to the complicated guided wave signal analysis can be divided into three major groups: time domain, frequency domain and integrated time-frequency domain analysis. The techniques of integrated time-frequency domain representation (TFR), such as short-time Fourier transform (STFT) (151), two-dimensional fast Fourier transform (2D-FFT) (152), Hilbert transform (HT) (153), Hilbert-Huang transform (HHT) (154), Wigner-Ville distribution (WVD) (155), wavelet transform (WT) (156) and Chirplet transform (CT) (157) are currently dominant among others. The general purpose of such analysis is to represent a complicated, non-stationary signal in the time-frequency domain where the modes are separated and can be identified based on comparison with theoretical calculations.

Most of the techniques mentioned above are more or less based on the discrete Fourier transform and hence suffers from its limitations, such as aliasing, leakage and Gibbs, or the edge effect. The 2D-FFT is one of the oldest approaches to analyse guided wave signals. It transforms the discrete amplitude-time measurements to the amplitude-wavenumber records at discrete frequencies (152). The 2D-FFT of the dataset $u(x,t)$ can be expressed as (158):

$$H(k, f) = \int\int u(x,t) e^{-j(\omega t + kx)} dx dt, \tag{1.4.1}$$

where x is the direction of wave propagation; k is the wavenumber; $\omega = 2\pi f$ is the angular frequency; $u(x,t)$ represents the displacements on the surface of the plate

$u(x,t) = A(\omega)e^{j(\omega t-kx-\theta)}$; θ is the initial phase. The different Lamb wave modes possess different k and f values, that leads to different results of the $H(k,f)$. Hence, it enables the guided wave modes to be identified by comparing the calculated $H(k,f)$ with Lamb wave dispersion curves (158). On the other hand, the 2D-FFT requires a sufficient number of equally spaced waveforms that makes it unsuitable for SHM applications. In contrast, the other TFR's, such as STFT, WT, CT, WVD or HHT uses only a single signal for time-frequency analysis (151).

According to the equation of the discrete Fourier transform, the time representation of the signal $x(t)$ is assumed to be a periodic and stationary function. If the function is non-stationary, the special methods, such as the STFT, are required to properly analyse the signals and to extract the frequency variation over time (71). The basic idea of the STFT method relies on cutting the signal $x(t)$ into short time segments with the sliding window. On each window position, the energy spectrum of the quasi-stationary signal can be calculated. As a result of this moving time window, the energy spectrum as a function of time can be obtained (159, 160). Mathematically, STFT can be expressed as (159):

$$STFT_x(t,f) = \int_{-\infty}^{\infty} x(\tau)w(\tau - t)\exp(-j2\pi f\tau)d\tau, \tag{1.4.2}$$

where $x(t)$ is the time representation of the signal; $w(\tau-t)$ is the window function, centred at t; τ is the time variable. Since symmetrical and asymmetrical modes possess different time-frequency regularities, STFT can be used as one of the tools for guided wave signal analysis and mode decomposition. The major drawback of the STFT method is that it cannot provide a good time and frequency resolution at the same time, due to the Heisenberg's uncertainty principle (161). To solve this limitation, Kotte et al. (162) proposed a differential reassignment method, which enables the background noise to be reduced, while preserving the edge information in STFT. Additionally, Hong et al. (163) introduced a dispersion based on STFT, where each time-frequency atom of STFT is rotated based on the dispersion properties of the particular wave, thus improving the time-frequency localization. Finally, Le Touze et al. (164) used time-varying filters to efficiently separate the non-linear guided wave modes. However, the conventional STFT is mainly suitable for the signals with well-defined frequencies and does not work so well on signals with fluctuations or discontinuities (165).

In contrast to the fixed sliding window and sine approximation in the conventional STFT, the wavelet transform (WT) decomposes a signal into the wavelet components or atoms, which can be stretched, compressed or shifted (165). In WT the width of the sliding window is variable and depends on the frequency of the analysed signal. There are two common forms of WT, called continuous wavelet transform (CWT) and discrete wavelet transform (DWT). The CWT of a function $x(t)$ can be written as the integral of the product of $x(t)$ and the time translated and amplitude dilated mother wavelet (161, 166):

$$S(a,b)=\frac{1}{\sqrt{a}}\int_{-\infty}^{\infty}x(t)\psi\left(\frac{t-b}{a}\right)dt, \tag{1.4.3}$$

where *a* and *b* are the dilation or scale (compression/expansion) and the translation or the time shift respectively; ψ is the wavelet function or the mother wavelet. From eq. 1.4.3 it follows that the wavelet coefficients $S(a,b)$ relies on the mother wavelet ψ. There are plenty of different available mother wavelets, however Gabor and Morlet are one of the most popular as they're based on the Gaussian envelope and provides good time-frequency resolution. Since the mother wavelet is selected, wavelet atoms $S(a,b)$ are obtained by dilation and translation of the mother wavelet. The Gabor and Morlet mother wavelets can be defined as (167, 168):

$$\psi_G(t)=\frac{1}{\sqrt[4]{\pi}}\sqrt{\frac{\omega_0}{\gamma}}\exp\left[-\frac{(\omega_0/\gamma)^2}{2}t^2\right]\exp(i\omega_0 t), \tag{1.4.4}$$

$$\psi_M(t)=\frac{1}{\sqrt[4]{\pi}}\exp\left(-\frac{1}{2}t^2\right)\exp(i\omega_0 t), \tag{1.4.5}$$

where $\psi_G(t)$ and $\psi_M(t)$ denotes the Gabor and Morlet mother wavelet respectively; γ modifies the width of the Gaussian envelope; ω is the angular frequency. The time-frequency resolution is determined from the duration Δt and the bandwidth Δf of the mother wavelet (169):

$$\Delta t = a\Delta t_{\psi},\ \Delta f = \frac{\Delta f_{\psi}}{a}, \tag{1.4.6}$$

$$\Delta t_{\psi} = \frac{1}{\|\psi\|_2}\sqrt{\int_{-\infty}^{\infty}(t-t_{\psi})^2|\psi(t)|^2dt},\quad \Delta f_{\psi} = \frac{1}{\|\hat{\psi}\|_2}\sqrt{\int_{-\infty}^{\infty}(\omega-\omega_{\psi})^2|\hat{\psi}(\omega)|^2d\omega}, \tag{1.4.7}$$

where $\hat{\psi}(\omega)$ is the Fourier transform of $\psi(t)$. According to eq. 1.4.6 and eq. 1.4.7, the Gabor wavelet has a higher time resolution, while the Morlet wavelet provides a better frequency resolution (168). In general, the CWT is computationally expensive, because it continuously translates and dilates the mother wavelet in time and frequency domain. For simplification, DWT can be employed, where the dilation *a* and translation *b* can be set as (170):

$$a=a_0^{-j},\ b=a_0^{-j}kb_0,$$
$$j,k\in Z,\ a_0>1,\ b_0>0. \tag{1.4.8}$$

Then the mother wavelet is scaled in powers of 2 and translated at each level. Hence, the expression of the wavelet function can be written as (165, 170):

$$\psi_{j,k}(t)=2^{-\frac{j}{2}}\psi\left(2^{-j}t-k\right) \tag{1.4.9}$$

Finally, the DWT wavelet coefficients are expressed by (170):

$$W(a,b)=2^{-\frac{j}{2}}\int_{-\infty}^{\infty}f(t)\psi\left(2^{-j}t-k\right)dt, \tag{1.4.10}$$
$$f(t)=\sum_{k}\sum_{j}W\left(2^{-j},2^{-j}\right)\psi\left(2^{-j}t-k\right).$$

WT as well as the other time-frequency representation methods, enables the amplitudes, frequency content, arrival time and other useful information about the guided waves to be extracted. There are plenty of applications of WT for damage detection in various structures. Liu et al. (167) used a CWT and Gabor mother wavelet to detect the radial cracks in pipes. Siqueira et al. (165) used a bandpass filtering along with DWT to increase the signal-to-noise ratio (SNR) and to detect the notch type defects in carbon steel pipes. Grabowska et al. (171) demonstrated the application of WT to detect fatigue cracks in aluminium rods. Rizzo et al. (172) used a combination of DWT and outlier analysis to detect notches in the multi wire steel-strand. Another application was demonstrated by Lee et al. (173), who used WT to detect the damage of various ratios in rock bolts. They demonstrated that the high frequency components appear when the defect ratio of the bolt increases.

WT is a powerful and widely used tool for analysis and decomposition of non-stationary guided wave signals. The major drawback of using WT arises from the selection of the mother wavelet, which fits most for the analysed signal. This selection is essential, to obtain reliable results with adequate resolution. As there are plenty of available mother wavelet options (Daubechies, Haar, Morlet, Gabor, Cauchy, Harmonic, Laplace, Hermit etc.), the methodologies for selecting the appropriate one are still missing. Moreover, the use of one particular mother wavelet for signal decomposition leads to the limited effectiveness analysing dissimilar or non-fractal signals (159).

CT is a combination of fast Fourier transform, STFT and WT. The time-frequency atom in this case is obtained by translating, scaling and shearing the time window function (157). Instead of three dimensions in WT, the CT is using five operations to represent the signal in the time-frequency domain. The general form of the CT for signal $x(t)$ can be written as (155, 157, 174):

$$\begin{aligned}C_x^{\mathrm{ct}}(t_0,\omega_0,s,q,p)&=\int_{-\infty}^{\infty}x(t)\cdot g^{*}_{t_0,\omega_0,s,q,p}(t)dt=\\&=\frac{1}{2\pi}\int_{-\infty}^{\infty}X(\omega)\cdot G^{*}_{t_0,\omega_0,s,q,p}(\omega)d\omega,\\g^{*}_{t_0,\omega_0,s,q,p}(t)&=\mathrm{T}_{t_0}\mathrm{F}_{\omega_0}\mathrm{S}_{s}\mathrm{Q}_{q}\mathrm{P}_{p}h(t),\\G^{*}_{t_0,\omega_0,s,q,p}(\omega)&=\mathrm{T}_{t_0}\mathrm{F}_{\omega_0}\mathrm{S}_{s}\mathrm{Q}_{q}\mathrm{P}_{p}H(\omega),\end{aligned} \tag{1.4.11}$$

where T_{t_0} and F_{ω_0} are the time and frequency shift operators; S_s is the scale operator; Q_q and P_p are the frequency shear and the time shear operators respectively; $g(t)$ and

$G(\omega)$ are the basis function and its Fourier transform; $h(t)$ and $H(\omega)$ are the window function and its Fourier transform; * denotes the complex conjugate.

In general, CT offers some advantages over the conventional STFT and WT, however it uses five-dimensional space, which is difficult to visualize. Therefore, usually two of five parameters are considered for TFR as in the conventional STFT (160). CT has been used in various fields by different researchers. For example, Yang et al. (175) used a polynomial chirplet transform for non-linear group delay estimation of the guided waves, while Hu (176) proposed an improved and inverse CT for detection of voltage harmonics.

Wigner-Ville distribution (WVD) is the bilinear time-frequency representation, which also uses the Fourier transform (155, 159):

$$WVD(t,\omega)=\int_{-\infty}^{\infty} x\left(t+\frac{\tau}{2}\right)\cdot x^{*}\left(t-\frac{\tau}{2}\right)e^{-j\omega t}d\tau, \tag{1.4.12}$$

where $x^*(t)$ is the complex conjugate of $x(t)$. In general, WVD measures the local time-frequency energy and does not use the time window. Hence it provides the best time-frequency resolution among other TFR’s. However, WVD can usually produce negative values and suffers from cross-interference. When the signal contains the sum of two components, WVD is expressed as (155):

$$WVD_{x+y}(t,\omega)=WVD_x(t,\omega)+2\mathrm{RE}\left[WVD_{x,y}(t,\omega)\right]+WVD_y(t,\omega), \tag{1.4.13}$$

where $2\mathrm{RE}[WVD_{x,y}(t,\omega)]$ is the cross-term, which can cause overlapping and reduces time-frequency resolution. It means that if the signal contains two components $x(t)+y(t)$, it will be decomposed into two separate components $x(t)$, $y(t)$ and the additional cross-term. The number of cross-terms is defined by (159):

$$C_n^2=\frac{n(n-1)}{2}, \tag{1.4.14}$$

where n is the number of signal components. A couple of solutions are available to overcome the limitations of the conventional WVD, like pseudo Wigner-Ville distribution (p-WVD), which calculates the convolution, between the conventional WVD and Gaussian window function. The other approach to remove the cross-terms is to use the Cohens class distribution, which smooths WVD with kernel function (Rihaczek, Choi-Williams, Born-Jordan etc.). However, the smoothed WVD is no longer sensitive to the sinusoids and Dirac impulses (177, 178). Recently, Chen et al. (155) proposed a Chirplet WVD, which removes the cross-term by transforming the non-linear and non-stationary signal into several intermittent mono-frequency signals. Pachori and Nishad (179) used a tunable Q-WT for cross-term suppression, which simultaneously designs the mother wavelet according to the quality factors Q. Despite some limitations, WVD still attracts plenty of attention in damage detection and signal processing due to its high time-frequency resolution. Zeng et al. (180) used laser imaging and WVD to detect a surface notch in aluminium plate. Tang et al. (181) proposed to use a combination of the Morlet wavelet de-noising, auto-terms windowing and WVD to detect the fault in wind turbines. Finally, Rodriguez et al.

(182) used WT and WVD to process the signals with coherent noise obtained from highly scattering materials.

Another approach to decompose the guided wave signals was proposed by Mallat and Zhang (183), who introduced matching pursuits (MP). It is an iterative approximation algorithm, which seeks for the best match between the atom in the dictionary and the part of the waveform. In other words, the algorithm decomposes the complex, non-stationary signal into the elementary stationary functions and uses an atom dictionary instead of the single basis function (159). MP decomposition of the signal $x(t)$ into m atoms can be summarized as follows (159, 184):

- The dictionary D is defined, which contains all possible atoms: $D=\{k_i\}$, where k_i belongs to the Hilbert space $L^2(R)$ (R is a set of real numbers);
- The atom that fits the signal best $x(t)$ is selected from the dictionary D (103):

$$k_{i_m} = \arg\max_{k_i \in D} \left| \left\langle R^{m-1}x, k_i \right\rangle \right|. \tag{1.4.15}$$

- The best atom is subtracted from the signal $x(t)$, leading to the residual (103):

$$R^m x = R^{m-1}x - \left\langle R^{m-1}x, k_{i_m} \right\rangle k_{i_m}. \tag{1.4.16}$$

- The steps described above are iteratively repeated until the defined residual tolerance or the maximum number of iterations is exceeded.

The major advantage of the MP algorithm is that it can be fully automated and it does not require an additional post-processing to remove the cross-terms etc. On the other hand, MP strongly depends on the quality of the signals and on the selection of the right dictionary. The noise and selection of the wrong initial atoms can lead to increased computation time and unpredictable results (159). The Gabor and Chirplet functions are the most popular atoms, to construct the dictionary D. Analogically to eq. 1.4.3, the Gabor atoms can be defined as (103):

$$k_{(l,u,\omega)}(t) = \frac{1}{\sqrt{a}}\, g\left(\frac{t-u}{a}\right) \exp\left(i\omega(t-u)\right), \tag{1.4.17}$$
$$g(t) = 2^{1/4}\exp\left(-\pi t^2\right),$$

where t is the time centre of the atom. The Gabor atoms are stationary and possess symmetrical time domain representation due to the Gaussian envelope. Thus the Gabor atoms are not suitable for the dispersive and non-stationary wave analysis. To decompose such signals, Gaussian modulated Chirplet atoms can be used (184):

$$k_{(l,u,\omega,c_r)}(t) = \frac{1}{\sqrt{a}}\, g\left(\frac{t-u}{a}\right) \exp\left[i\left(\omega(t-u) + \frac{c_r}{2}(t-u)^2 \right) \right], \tag{1.4.18}$$

where c_r is the chirp rate of the atom. Chirplet atoms are computationally efficient and can be used even for the guided wave mode classification. Xu et al. (184) found that the positive chirp rate ($c_r>0$) corresponds to the S_0 mode while negative ($c_r<0$) chirp rate denotes the A_0 mode. Hence MP is suitable in a wide variety of applications. Liu et al. (185) used a matching pursuit with Gabor atoms to detect the bearing vibration and to extract the information about the damage. Similarly, Yang et al. (186) used a basis matching pursuit to post-process the data obtained from faulty rolling bearings. Finally, Yuemin et al. (187) applied MP to detect a 10 mm diameter hole in stainless steel pipe and compared the results with the reference data.

Huang et al. (188) proposed another approach to decompose the guided wave data, which is based on the local properties of the signal and called Hilbert-Huang transform (HHT). This method uses empirical mode decomposition (EMD), which extracts a zero-mean signal harmonics, thus generating a finite set of intrinsic mode functions (IMF). The EMD decomposition of the signal $x(t)$ into n IMF's can be written as (71):

$$x(t)=\sum_{i=1}^{n}c_i(t)+r_n(t), \tag{1.4.19}$$

where $c_i(t)$ is the intrinsic mode function; $r_n(t)$ is the remaining signal. In general, HHT searches for the local maxima and local minima of the signal $x(t)$. Then it connects all the local maxima and local minima with a cubic spline to obtain the upper and lower envelope. The mean of the upper and lower envelope $m(t)$ is then subtracted from the signal $x(t)$ and IMF candidate $h_1(t)$ is obtained (151):

$$h_1(t)=x(t)-m(t). \tag{1.4.20}$$

$h_1(t)$ is considered as IMF if the number of zero crosses matches the number of extrema and the mean value of $h_1(t)$ is equal to zero. Once the correct IMF $h_1(t)$ is obtained, it is subtracted from the signal $x(t)$ to obtain the residual. The whole procedure is then repeated, treating the residual as a new signal. The procedure is stopped when the required number of IMF is achieved or $r_n(t)$ becomes a monotonic function (189).

Each IMF has its own frequency bandwidth going from high to low frequencies. The first IMF contains the highest frequency component of the signal, while the frequency of the subsequent IMFs decrease. For each of the IMF $c_i(t)$, the Hilbert transform can be calculated $d_i(t)$. Then from eq. 1.4.19 follows (190):

$$z_i(t)=c_i(t)+jd_i(t)=A_i e^{j\theta_i},\ A_i\equiv\sqrt{c_i^2+d_i^2},\ \theta_i=\tan^{-1}\left(\frac{d_i}{c_i}\right), \tag{1.4.21}$$

$$u(t)=r_n+\mathrm{RE}\sum_{i=1}^{n}A_i(t)e^{j\theta_i(t)}.$$

The plot of the amplitudes of IMF analytical signals $A_i(t)$ as a function of frequency and time represents a Hilbert spectrum (189, 191). HHT suffers from the edge effect and cannot accurately decompose the signals at the data ends. To avoid this problem, slope based methods were introduced, which partially solve the problem (192). Moreover, HHT requires a sufficient sampling rate, which is at least 10 samples per cycle and cannot efficiently separate the mode if it exist only over a segment of time (190).

There are also some other not so common methods to analyse and decompose the guided wave signals, such as: adaptive optimal kernel method (193), Wigner higher order spectrum (194), auto-regressive moving average analysis (195), local mean decomposition (196) or the Teager energy separation algorithm (197). This basic review shows that various time and frequency analysis methods have been developed in the past few decades to decompose the complex guided wave signals and to extract the information about the damage. Unfortunately, almost all of them possess some resolution and cross-term issues. For example, STFT and WT use a pre-defined basis function, therefore such methods cannot be used for adaptive time frequency analysis and does not provide good time and frequency resolution simultaneously. WVD suffers from the cross-terms, while HHT has some issues with the signal edges and cannot separate the signals consisting of two or more non-synchronous regular harmonics. Therefore, it has been shown that the best results are achieved when a combination of two or more methods is used. For example, WVD can be smoothed with the kernel function to avoid the cross-terms, whereas HHT uses a slope based method to reduce the data end effect. On the other hand, most of the methods described in this chapter are based on the analysis of the real part of the Fourier spectra. Schumacher et al. (198) proposed the analysis of the phase spectrum of the signals to accurately measure the phase velocity of guided waves. Later this approach was used by Prosser (199) to measure the phase velocity of the extensional and flexural modes on anisotropic graphite/epoxy plates. Analogically, Anastasi (200) measured phase velocities to assess the structural integrity of the aging wire insulation. The improvement and re-emerge of such phase spectrum examination methods, along with some *a-priori* analytical knowledge, could be further used for the precise wave velocity measurements and guided wave mode identification. Moreover, there are only a few attempts to combine a special transducer placement or special type of excitation, i.e. frequency sweep, along with guided wave signal processing. This leads to a conclusion that the existing methods still need to be improved or combined together to introduce accurate advanced techniques to distinguish the modes of guided waves from the multimodal signals.

1.5 Existing approaches for detection, localisation and feature extraction of structural damage in plate-like structures

The following chapter deals with the review of existing approaches to detect, localise and describe the damage in plate-like structures. Only the most common techniques are described and the demand for the implementation of new methods is considered. The simplest approach to detect the presence of damage in SHM relies on the baseline subtraction. The signal is introduced into the structure through the bonded transducer and captured with the receiver at a different location. If there is any damage in the structure, the guided waves will be reflected or scattered by it, thus some changes will appear somewhere within the signal. Subtracting this signal from the defect-free baseline will give the residual, which indicates the presence of damage. However, such approach only indicates the changes in the structure and suffers from the influence of the environmental and operational conditions, such as temperature, loads etc. Konstantinidis et al. (60) proposed to use a database of optimal baselines, to compensate the changes of temperature and to improve the signal to a coherent noise ratio compared with the single baseline subtraction. The proposed optimal database consists of time traces recorded at discrete temperatures ΔT and mean square deviation is used to find the best match to the current time trace. Once the best match is found on the database, the signals are subtracted leaving the influence caused only by the structural changes. Alternatively, Lu and Michaels (62) introduced a baseline signal stretch method, which compensates the influence of the temperature by stretching the time axis of the single baseline. This method assumes that the changes in temperature mainly affect the arrival time of the wave packet. However, some investigations show that if the magnitude of the reflection from the defect is approximately –30 dB compared to the first arrival, then the temperature change of at least 10 °C can conceal the defect even if the compensation techniques are used (59, 201).

In contrast to the baseline subtraction, many authors have used a time-reversal acoustics for baseline-free damage detection. According to the concept of the time reversal acoustics, for a defect free structure the input signal should match the reconstructed signal, which is captured with the receiver at some location, reversed in time and reemitted back to the transmitter (202). In other words, the wave is introduced into the structure by applying the voltage $V_A(\omega)$ for transducer A. The wave then propagates in the structure and sensor B captures the signal $V_B(\omega)$. The signal $V_B(\omega)$ is reversed in time and reemitted back to transducer A. Finally, transducer A receives the signal $V_{BA}(\omega)$ and compares it with the original input $V_A(\omega)$. For the defect free structure, the two signals $V_{BA}(t)$ and $V_A(t)$ should match in time domain, while any mismatch indicates some changes in the structure (47, 203). The match can be measured using the simple correlation function as follows (47):

$$p_{ab}(t) = \frac{n\sum a_i b_i - \sum a_i \sum b_i}{\sqrt{\left[n\sum a_i^2 - \left(\sum a_i\right)^2\right]\left[n\sum b_i^2 - \left(\sum b_i\right)^2\right]}}, \qquad (1.5.1)$$

where a_i and b_i are the sample values of the signals $V_A(t)$ and $V_{BA}(t)$ respectively. The measurement of signal match by using a correlation function is sensitive to the selection of the moving time window. Therefore, signals must be lined up according to some reference prior to any comparison. Moreover, the probability of detecting the damage depends on its position and possessing the normal spatial distribution. It means that the damage must lie somewhere across the pathway of the wave in order to have sufficient sensitivity (47). Furthermore, Gangadharan (204) showed that the notch type defects do not affect the shape of time reversed Lamb wave in metallic structures. Thus, the time-reversal cannot actually be used as a reference free technique for damage detection.

The methods described above are commonly used for the detection of structural changes. Unfortunately, in order to localise the damage and to extract its features further signal analysis is required. In general, the defect localisation is mostly based on the certain transducer arrangement and measurement of the time-of-flight (ToF) of the reflection or the residual. The basic principle for damage localization in 1D space is presented in Fig.1.5.1a. Suppose that the damage scattered signal $x_D(t)$ is obtained using a subtraction as follows (201):

$$x_D(t) = x_B^{damage}(t) - x_B^{health}(t), \tag{1.5.2}$$

where $x_B^{health}(t)$ and $x_B^{damage}(t)$ represents the signals obtained from an undamaged and damaged state of the object. According to Fig.1.5.1a, the initial distance l_0 and the arrival time T_0 between the transmitter and the receiver are fixed and known. T_1 represents the time interval from the signal received by transducer *B* and the reflection obtained from the damage *D*. The value of *x* is unknown, but can be calculated using the simple following proportion (201):

$$\frac{l_0}{T_0} = \frac{2x}{T_1}. \tag{1.5.3}$$

In case of 2D space and *N* piezoelectric transducers, it is more convenient to create a defect map that shows an exact location of a flaw. Let's assume that the transmitter, receiver and the flaw are located at the following coordinates: (x_t,y_t), (x_r,y_r), (x_f,y_f) (see Fig.1.5.1b). Then the receiver will capture the direct signal from the transmitter and the one scattered by the flaw. If only a single mode propagates in the structure, the group velocity c_g of that mode can be estimated from the direct arrival between the transmitter and the receiver (205):

$$c_g = \frac{\sqrt{(x_t - x_r)^2 + (y_t - y_r)^2}}{t_{tr}}, \tag{1.5.4}$$

where t_{tr} is the direct ToF between the transmitter and the receiver. Then, in case of an isotropic structure, the ToF of the signal going from transmitter to the receiver through the flaw can be estimated as (206):

$$t_{tr}^f = \frac{\sqrt{(x_t - x_f)^2 + (y_t - y_f)^2} + \sqrt{(x_r - x_f)^2 + (y_r - y_f)^2}}{c_g}. \tag{1.5.5}$$

If there are *N* piezoelectric transducers attached to the structure, the scattered signals will arrive at different time instances t_{tr}^f for each transmitter-receiver pair, yielding the $N(N-1)/2$ different paths. Consequently, the received signals or the residuals for each transmitter-receiver pair can be time shifted by t_{tr}^f and added to yield an average signal at the potential flaw location (206):

$$s_{xy}(t) = \sum_{t=1}^{N-1} \sum_{r=1}^{N} r_{tr}\left(t - t_{tr}^{\mathbf{f}}\right) w\left(t - t_{tr}^{\mathbf{f}}\right), \tag{1.5.6}$$

where r_{tr} – is the residual signal of transducer pair (*t*-*r*) shifted by t_{tr}^f, *w* – is the windowing function. Finally, the defect map can be created by repeating this procedure at different imaging positions in a 2D plane. At the points where the reflectors actually exist, the constructive interference possessing high amplitude will be obtained.

There are plenty of available transducer configurations and imaging approaches, which are based on the idea described above. For example, Giurgiutiu et al. (207) and Purekar et al. (208) used a linear piezoelectric wafer active array and embedded ultrasonic structural radar (EUSR) method to detect the damage in thin-wall structures. The use of arrays offers some advantages over the conventional single transmitter-receiver measurements, such as sectorial steering and focusing of ultrasonic beam by an electronical sweep of the array elements. Thus, the large area of the sample can be examined with sufficient resolution. In the EUSR, one transducer is excited at a time and then switched to another to generate a virtual sweep beam. At the reception, all elements of the array are used to record a response from the structure. Because of the array spacing, the distances between the array elements and the target *P* will be different. For the m^{th} element of the array, the distance to the target *P* will be shorter by: $\Delta_m(\phi) = m(d\cos(\phi))/c_\mathrm{g}$ (207). Hence, if the array elements are fired with delays, the signals at target $P(r,\phi_0)$ can be expressed as (209, 210):

$$s_\mathrm{p}(t) = \frac{1}{\sqrt{r}} \sum_{m=0}^{M-1} s_\mathrm{T}\left(t - \frac{r}{c_\mathrm{g}} + \frac{r - r_m}{c_\mathrm{g}} + \Delta_m(\phi) \right), \tag{1.5.7}$$

where $1/\sqrt{r_m}$ represents the decay of oscillation due to wave radiation; r/c_g is the time for the wave to travel from origin to the target; $(r–r_m)/c_\mathrm{g}$ is the time for the wave to travel from target *P* to the m^{th} array element; $\Delta_m(\phi)$ is the individual delay applied to array elements. In such way the beamforming with the array can be implemented by using different delays $\Delta_m(\phi)$ in array excitation. If the target exists at the azimuth ϕ_0 and the distance *R* with respect to the array, the beam needs to be swept, until the azimuth of the wave $\phi = \phi_0$. Eventually, at the reception all the received signals have to be synchronized using the reciprocal delays $\Delta_m(\phi)$. The beamforming at the reception can be expressed as (207):

$$s_\mathrm{R}(t) = \left(\sum_{m=0}^{M} w_m^{'} \frac{1}{\sqrt{r_m}} \right) s_\mathrm{T}\left(t - \frac{r}{c_\mathrm{g}} \right) A \sum_{m=0}^{M} w_m \frac{1}{\sqrt{r_m}}, \tag{1.5.8}$$

where *A* is the backscatter coefficient; w_m and $w_m^{'}$ are the weight functions for the transmission and reception respectively. In general, to obtain the target direction the EUSR method uses an angle sweep and tracks for the maximum received energy $E_\mathrm{R}(\phi_0)$ (210):

$$E_R(\phi_0) = \int_{t_p}^{t_p + t_a} \left| s_\mathrm{R}(t) \right|^2 dt. \tag{1.5.9}$$

Once the target direction ϕ_0 is obtained, the ToF to the target can be estimated by calculating the cross-correlation between the transmitted and received signals (207):

$$y(\tau)=\int_{t_p}^{t_p+t_a} s_{\mathrm{R}}(t)s_{\mathrm{T}}(t-\tau)dt, \tag{1.5.10}$$

$$\tau_{\mathrm{ToF}}=\frac{2R}{c_{\mathrm{g}}},\quad R=\frac{c_{\mathrm{g}}\tau_{\mathrm{ToF}}}{2}, \tag{1.5.11}$$

where τ_{ToF} corresponds to τ where the cross-correlation function indicates the best coincidence.

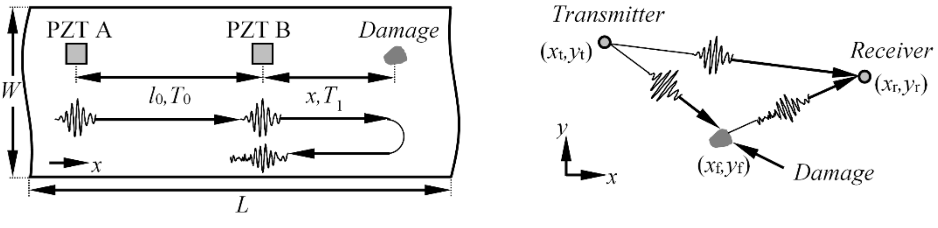

a) b)

Fig. 1.5.1. The concept of damage localization in 1D (a) and 2D (b) case scenario (201, 205)

A slightly different approach to localise the damage was used by Wilcox et al. (211) and Vishnuvardhan et al. (212), who used a circular omni-directional array along with the phased addition algorithm (PAA). The PAA is implemented in wavenumber k domain with the purpose of determining the angles of the reflected waves. To achieve this goal, the time domain signals are recorded for each transmitter receiver pair within the circular array to matrix **T**, where the columns represents the time domain signals for each of the receivers ($\mathbf{T}(t)$ = [T_1, T_2, … T_n]). Each column in matrix **T** is transferred to the frequency ω domain using the one dimensional Fourier transform to obtain the complex matrix **S** ($\mathbf{S}(\omega)$ = [S_1, S_2, … S_n]). Eventually, the phased addition is performed for the matrix **S** in ω domain for all reconstruction angles θ_p, leading to the matrix **A** ($\mathbf{A}(\omega,\theta_p)$ = [A_1, A_2, … A_n]). Each element in the matrix **A** can be expressed mathematically as (213):

$$A_{\omega P}=\sum_{j=1}^{N} S_j(f)\exp\left(-i2\pi k\left(\omega_k,\theta_p\right)x_{pj}\right), \tag{1.5.12}$$

where $S_j(f)$ is the complex spectra of the signal received by the j^{th} receiver; x_{pj} is the change in path related to the signal received by the j^{th} transducer to be coherent with steering angle θ_p (213):

$$x_{pj}=R_j\cos\left(\Phi_j-\theta_p\right), \tag{1.5.13}$$

where R_j and Φ_j are the polar coordinates of the j^{th} receiver. By knowing the slowness relationship, it is possible to compensate the effect of dispersion through interpolation of matrix **A**. The result of interpolation leads to matrix **W** ($\mathbf{W}(k,\theta_p)$ = [W_1, W_2, … W_n]), consisting of spectra in k domain. The final image matrix **E** in polar domain ($\mathbf{E}(r,\theta_p)$=[E_1, E_2, … E_n])) is obtained by applying an inverse Fourier transform to the columns of matrix **A**. The results can be visualized by plotting the amplitudes with corresponding polar position (213, 214). The PAA can be used as the imaging technique with any transducer configuration: single transmitter-multiple receivers (STMR), multiple transmitters-multiple receivers (MTMR) or linear arrays. The discretization of the imaging plane can be implemented using either a polar or Cartesian coordinate system. On the other hand, this algorithm has some shortcomings. The resolution of the PAA is poor in the near field, which is equal from 2 to 3 diameters of the whole circular array set. In contrast, the larger array diameter gives an increased resolution at the far field, thus resulting in an increased area of the near field. Moreover, in order to localise the defects in anisotropic structures, the initial knowledge of the directional dependencies of the phase and group velocities is required (213).

Kudela et al. (215) also used the same circular transducer arrangement, however the authors proposed the creation of a damage influence map, based on the match between the excitation and reflected signals. They assumed that the excitation signal and the signal reflected from the defects has some matching features. Therefore, the idea to arbitrary place the excitation signal on the received time series with some time shift and to measure the match was proposed. The time shift is then equal to the ToF from the transmitter to the receiver through the point of possible damage location. When the received signal contains the information about the damage, the measure of the match possesses significant values, which can be associated with coordinates of the imaging point (216). According to the proposed technique, the match between the two time series is mathematically expressed as (215):

$$e_k(x,y)=\int_{t_0}^{t_0+\Delta t^*}\hat{S}_{\mathrm{T}}(t)\left[F(t)G(x,y)\hat{S}_{\mathrm{R},k}(t)\right]dt, \tag{1.5.14}$$

where t_0 and Δt^* are the start and the width of the time window; $\hat{S}_{\mathrm{T}}(t)=S_{\mathrm{T}}\left(t_0,t_0+\Delta t^*\right)$ is the windowed excitation signal; $\hat{S}_{\mathrm{R},k}(t)=S_{\mathrm{R},k}\left(t_0+\Delta t,t_0+\Delta t^*\right)$is the signal registered with the k^{th} receiver, $F(t)$ is the window function (Gauss, Hann etc.); $G(x,y)=e^{\alpha(d_{0\mathrm{P}}+d_{\mathrm{P}k})}$ is the function dependent on the attenuation; α is the attenuation coefficient; $d_{0\mathrm{P}}$ and d_{Pk} represents the distances between the transmitter-imaging point and imaging point-receiver; Δt is the signal time shift, which depends on the x, y coordinates of the imaging point and the group velocities $c_{0\mathrm{P}}$ and c_{Pk}. The final image is constructed from signals received by all sensors over each discrete point at the imaging plane (215):

$$E=\sum_{k}\int_{S}e_k(x,y)dS\approx\sum_{k}\sum_{i,j}e_k\left(x_i,y_j\right), \tag{1.5.15}$$

where S is the area of the imaging plane; $i = 1\dots N$, $j = 1\dots M$, where N and M denotes the total number of nodes located on the imaging plane. It should be noted that the proposed measurement of the match works well for non-dispersive tone-burst type signals. In the case of dispersive modes, quality of the damage influence map is limited to the amount of the dispersion (216). Wandowski et al. (217) used the same idea described above, except the authors proposed to calculate the damage index (DI) at the imaging points. The portion of the DI (PDI_k) at the imaging point P is calculated for N transmitter-receiver pairs from the amplitude of the carrier frequency f_c peak as follows (217):

$$\mathrm{PDI}_k(P)=\sum_{i=1}^{N}\hat{S}_i(f)\Big|_{f_\mathrm{c}}, \tag{1.5.16}$$

where $\hat{S}_i(f)$ is the frequency spectra of the signal at the carrier frequency f_c. Then the normalized DI can be expressed as (217, 218):

$$\mathrm{DI}(P)=\log\left(\frac{\mathrm{PDI}_k(P)}{\max(\mathrm{PDI}_k(P))}\right). \tag{1.5.17}$$

In this case, the DI is calculated taking into the account the information related to the carrier frequency f_c only. Michaels (206) used an extended approach along with the broadband excitation. After collecting the data, the authors propose to use the bandpass filters with various central frequencies to obtain an extra set of bandlimited signals for each transmitter-receiver pair. Each bandlimited signal is then subjected to the imaging techniques to generate the defect map at particular central frequency of the filter f_m. Eventually, the individual images are fused, leading to the improved final image with minimized influence of the phasing artefacts, unwanted extra modes and other distortions, such as variation of temperature. The fusion is performed pixel by pixel taking the minimum pixel value from all of the corresponding images.

Giridhara et al. (219) implemented a damage localization technique based on a radial segmentation and triangulation method. The authors used a circular STMR array and divided the area of the plate into the circumferential segments. Then the signals from neighbouring transducers are compared to rapidly determine the location of the damage with respect to the transmitter position. If the flaw is positioned along x axis (see Fig.1.5.2a), then the comparison between the sensor signals (S_2 and S_8; S_2 and S_1; S_1 and S_8) will indicate some changes in the structure. If the signals from the sensors S_2 and S_8 match, it means that the damage lies in front of the sensor S_1, otherwise the damage is located either on one side of sensor S_1 or another (the damage is in the segment S_1 and S_2 or in the segment S_1 and S_8). The side of the damage is determined by measuring the ToF of the reflection from the flaw back to the sensor S_2 and sensor S_8. The implementation of the procedure described above enables the segment where the damage is actually located to be determined (45). For exact damage positioning the triangulation method is used which requires the coordinates of the transmitter $T(0,0)$ and two adjacent receivers $S_i(x_i,y_i)$, $S_{i+1}(x_{i+1},y_{i+1})$ within the selected segment as input data (see Fig.1.5.2b). According to this technique, the angle of the flaw θ in respect to the x axis can be determined using the relations (219):

$$\theta=\phi+\cos^{-1}K;\ \phi=\tan^{-1}\left(\frac{py_{i+1}-qy_i}{px_{i+1}-qx_i}\right);\ K=\cos(\theta-\phi). \tag{1.5.18}$$

Consequently, the radial distance r_d between the transmitter $T(0,0)$ and damage $P(x,y)$ can be written as (219):

$$r_d = \frac{p}{2\left(x_i \cos\theta + y_i \sin\theta - d_i\right)} = \frac{q}{2\left(x_{i+1} \cos\theta + y_{i+1} \sin\theta - d_{i+1}\right)}, \tag{1.5.19}$$

where $p = x_i^2 + y_i^2 + d_i^2$, $q = x_{i+1}^2 + y_{i+1}^2 + d_{i+1}^2$, d_i and d_{i+1} are the total travel path from the transmitter through the flaw to the sensors S_i and S_{i+1} respectively ($d_i = r_d + a$, $d_{i+1} = r_d + b$, $r_d = x^2 + y^2$); a and b are the distances of the sensors $S_i(x_i,y_i)$, $S_{i+1}(x_{i+1},y_{i+1})$ to the damage P ($a^2 = (x–x_i)^2 + (y–y_i)^2$, $b^2 = (x–x_{i+1})^2 + (y–y_{i+1})^2$).

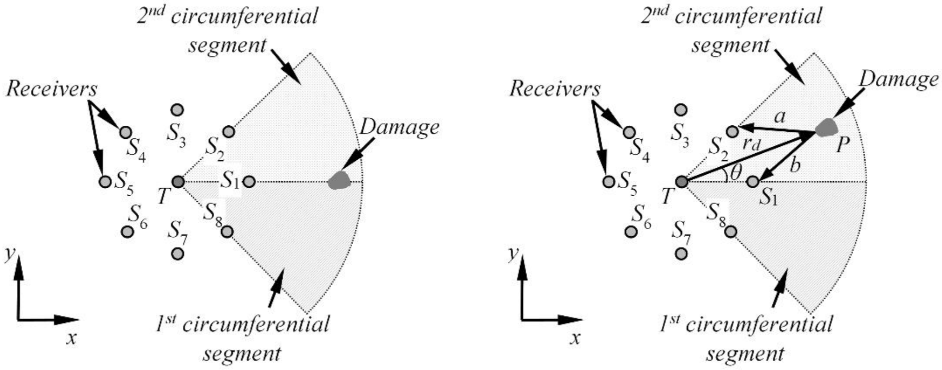

a) b)

Fig. 1.5.2. The concept to determine the radial segment of the damage location (a) and the idea of exact damage positioning using the triangulation method (b) (219)

The methods for damage detection and localisation described above are based on the linear reflection, transmission and scattering of ultrasonic guided waves. However, for the certain type of defects the contrast of the acoustical impedances might be not sufficient for the reliable defect detection. Recently Solodov (220) and Delrue (16) demonstrated that under the use of high energy Lamb wave excitation, the defects such as cracks or early stage closed delaminations possess “clapping” behaviour leading to the generation of the local nonlinear frequency harmonics. This led to the development of the nonlinear ultrasonic detection of delamination and crack type defects, which is based on analysis of the harmonics (2*f*, 3*f*, …) and subharmonics (*f*/2, *f*/3, …) resulting from the “clapping” behaviour. In order to provide maximum wave-defect interaction, Solodov used a concept of local defect resonance (LDR), which is based on the fact that the defects drop the local stiffness of the material. Thus the characteristic frequency f_0 of the defect can be found which enhances the defect response. As the energy of excitation overcome the activation threshold and some generated nonlinear harmonics match the resonant frequency of the defect f_0, the higher harmonics are solely generated in the defective area and the defect location and its shape can be clearly seen in the radiation pattern. Those higher order harmonics create the Chladni-type figures, which can be easily observed by using the laser vibrometry or thermosonic imaging (221, 222). The fundamental resonance frequency of the sub-surface delamination type defect can be calculated using the expression (220):

$$f_0 \cong \frac{3.2D}{2a^2}\sqrt{\frac{E}{12\rho\left(1-\sigma^2\right)}}, \qquad (1.5.20)$$

where a and D are the radius and the depth of the delamination; E is the Young's modulus; σ is the Poisson ratio; ρ is the density.

As it appears from the brief review above, there are numerous available techniques for damage detection and localisation. However, their success is strongly influenced by dispersion, environmental conditions and complicated multimodal propagation of the guided waves. Moreover, the defects are mostly weak reflectors, while the monitoring system tends to detect and locate them in a large structure using a small number of sensors. This leads to the low SNR which complicates the signal analysis and the estimation of the ToF. The reconstruction techniques, which are based on multiple measurements can be used as an attractive approach for the damage localisation, nevertheless it also requires sufficient measurement positions to provide the adequate resolution.

Since the presence and location of damage can be determined with more or less accuracy, the damage feature extraction is even more complicated and open task. For example, Tua (223) et al. used HHT to detect the crack and to determine its size and orientation by analysing the energy spectrum at different transducer angles and spatial positions. The authors concluded that the angle of the crack can be determined from the analysis of the amplitude of the peak, reflected from the flaw, while the size can be evaluated analysing the spatial shift of the transducer at which the reflection peak vanishes from the spectrum. Similarly, Paget et al. (224) and Douka et al. (225) used wavelet coefficients to evaluate the size and the depth of the crack using the pre-described relationship between the defect parameters and coefficients of WT. Despite the few available approaches to extract the damage features, it is still a relatively new and open area. Hence new guided wave SHM techniques have to be developed to extract the size and the depth of the damage leading to the further estimation of the severity of damage and a prognosis of the life time of the structure.

1.6 Brief review of the guided wave application on structural health monitoring of composite structures

In this chapter, a brief review of the guided wave application on structural health monitoring of composites is presented. The aim of this review is to identify the possible guided wave application areas in the field of structural assessment of composites and to estimate the existing open questions, which can be addressed later in this research. The application of GW to the structural assessment of the composite materials has received significant attention during the past few years. On one hand the composite materials are light weight and provide good mechanical properties, but on the other the composites are susceptible to various defects that may occur both during manufacturing and the life cycle. Since the variety of available composites is limitless, some part of present research is focused on the analysis of the material properties, while the others deal with damage detection. Recently Baid et al. (226) measured a group velocity of GW in aluminium, woven composite and honeycomb sandwich samples, and compared the results with the developed theoretical models. Similarly, Moreno et al. (227) demonstrated a simple technique to measure the phase velocity of guided waves in quasi-isotropic carbon fibre samples. The authors extracted the phase velocity from the time-distance measurements of the constant phase point in a received pulse. The phase and group velocity measurements in general can be used not only for the material characterization, but also for the mode decomposition if the dispersion relationships in the material are known in advance. Another work in the field of material characterization was accomplished by Sreekumar et al. (228), who investigated the attenuation of the A_0 mode as a function of the amount of nanofillers. The authors concluded that the nanofillers affect the attenuation of guided waves especially at higher frequencies and the attenuation itself depends on the type of nanomaterials. It was also demonstrated that the attenuation was more significant in glass fibre reinforced plastic composites (GFRP) regardless of the amount of nanomaterials. Yu et al. (229) analysed the propagation of guided waves in functionally graded viscoelastic plates. They showed the viscous effect to the dispersion curves and attenuation of different GW modes.

Among the research, focusing on the structural assessment, significant attention has been paid to the ultrasonic health monitoring of the bonded joints, composite repairs, aerospace components and composites with impact damage and delaminations. Ren and colleagues (230) investigated the carbon fibre reinforced plastic (CFRP) skin and flange stinger joint with artificial defects using GW. The authors used an angle beam transducer in pitch-catch configuration and selected higher order modes that are mostly sensitive to disbond defects. The special effectiveness index was proposed for mode-frequency selection, based on the sensitivity and mode conversion features. Sherafat et al. (231) analysed almost the same structure, however they proposed to use non-contact measurements using the 3D laser Doppler vibrometer (LDV). The authors compared the measurements in defect free and defective skin-stinger joints and analysed a reflection, transmission and scattering of the A_0 and S_0 modes. It was observed that a 10% increase in the transmission can be observed for the A_0 mode at frequencies below 350 kHz, while for the S_0 mode an increase of scattering by 60% can be noticed at the same frequency band in the presence of damage. Deng et al. (51) studied the propagation of GW in composite structures with a tapered adhesive layer. The authors demonstrated the influence of the thickness of the adhesive layer to the dispersive properties of GW. An interesting work was presented by Castaings et al. (232) who investigated a joint between a concrete block and composite plate. The authors analysed the dispersion relationship in such structure and selected a specific mode for inspection based on its through-thickness displacements. Then the changes of the dispersion relationship as a function of the bond quality is studied for that particular mode. A few years later Castaings et al. (233) presented research on the application of air-coupled ultrasonic inspection of high-pressure composite tanks made from carbon composite wound around a titanium liner. It was shown that the longitudinal mode has higher sensitivity to moisture content while the circumferential mode was more sensitive to micro-cracking. Therefore, the authors proposed to measure the amplitude of longitudinal waves to indicate the moisture content and the arrival time of the circumferential mode to detect micro cracking.

Some interesting research can be found on damage detection in adhesively bonded composite repairs. Caminero and colleagues (234) investigated the performance of the bonded repair in CFRP laminates under axial tensile loading and compared the Lamb wave measurements with digital image correlation. The authors demonstrated that the Lamb waves possess sufficient sensitivity in the propagation paths with high strains. Pavlopoulou et al. (235) monitored a helicopter stabilizer with a CFRP patch on top of the crack using GW. The sample was tested under bending fatigue along with the outlier and principal component analysis of Lamb waves. Habib et al. (236) compared a Lamb wave testing with a surface mounted crack sensor approach detecting the damage in carbon fibre samples with boron patches. The authors concluded that the Lamb wave SHM still requires optimization of the transducer placement for each sample, which is critical in order to reliably detect the damage. In this case it was proposed to attach the sensors at the low strain areas of the sample to avoid the transducer disbonding from the substrate. The authors also state, that the analysis of Lamb wave data is usually confusing and still requires an experienced operator as well as the development of some methods for damage quantification.

Another group of authors demonstrated an effort in detecting the impact and delamination type damage in composites. For example, Staszewski et al. (237) studied a carbon/epoxy composite plate with a series of drop weight induced impact damage in a single position. The area of the defect was scanned using 3D LDV and the results demonstrated that at the position of the impact an increase in the out-of-plane component can be detected. Similarly, Sohn et al. (238) investigated a carbon composite sample with delamination using the 1D LDV, measuring the out-of-plane velocity field. Sohn noticed that the standing waves appear at the delamination so the special signal processing technique was proposed to isolate them from the rest of the wave field. Grondel et al. (239) performed research on a composite wingbox structure trying to detect the impact and disbond damage. The presence of defects and their growth in this case were detected by measuring the changes in the amplitude of S_0, S_1 and A_0, A_1 modes. Rogge and colleagues (240) investigated the possibilities of determining the depth of delamination type defects by estimating the spatially dependent wavenumber values using the Fourier domain analysis. The local wavenumber values were extracted from the velocity field obtained using LDV and immersion scanning of the defective area. Su et al. (241) presented work which uses the artificial neural networks to locate the delaminations in carbon epoxy quasi-isotropic sample. The authors proposed an intelligent signal processing and pattern recognition package by which the digital damage fingerprints are constructed from wavelet transform and further used to train the neural network. Ramadas et al. (242) studied the possibilities of detecting the delamination type defects in quasi-isotropic laminates using air-coupled excitation of Lamb waves. In this work the transducers were adjusted to 18° to excite the A_0 mode and the B-scan and D-scan images were created by moving both transducers over the delaminated area. Taking into account the probe separation and the probe diameter, the width and length of the delamination was extracted from the measurements.

The research described above mainly focuses on the detection of the presence of the defect or monitoring its growth during mechanical tests. In most cases, the location, size and other defect parameters are obtained by scanning the defective area. Since the contact scanning requires the special scanners and complicated set-ups, usually non-contact laser vibrometers or air-coupled ultrasonics are used to measure the velocity or displacement field. None of the work presented above are proposing some methods for damage feature extraction using permanently attached transducers without scanning. Another issue which unifies all the presented research is that none of them are discussing the problems related to the verification and calibration of the monitoring system. In real world environments, it is very important to prove and to be sure that a certain defect is detected, prior to making any decision based on that data. One of the possible ways to accomplish this is to have a large database of real world situations and compare them to those obtained during the operational life of the structure. However, such database is almost impossible to implement. Therefore, some methods can be created which would enable the experimental imitation of the influence of real defects without actually destroying the structure of the object. This is the task which is barely accomplished and artificial defect imitation maybe would never give the same response as the real defects, however it would definitely be a step towards more reliable and effective monitoring systems. Such tools could also be beneficial in the calibration of the monitoring system, since the development of any NDT technique requires evidence that it is sensitive to certain types and sizes of the defects.

1.7 Conclusions of Chapter 1 and following tasks of the research

1. Structural health monitoring based on ultrasonic guided waves can be used in a wide variety of applications, and offers many advantages over other existing techniques, such as sufficient propagation distance and sensitivity to defects of a different nature. However, advanced techniques are still required to deal with dispersion, mode conversion, multi-modal propagation and anisotropy of wave velocity.
2. The provided survey demonstrated that there are some developments in the field of single GW mode excitation. However, usually this is not a sufficient solution because other modes possessing lower displacements are also excited and the set of transducers for different frequencies are required. The multi-mode approach offers a more versatile SHM systems, sensitive to multiple type of defects at the same time. On the other hand, the multi-modal systems accordingly require special methods to understand the wave generation and propagation.
3. Research on existing methods for the simulation of guided wave propagation revealed, that despite the available advantages, the FE methods are relatively slow and cannot provide fast results directly with the information most desirable for SHM systems. Therefore, some development possibilities for

rapid analytical models, which would allow the analysis of the propagation of separate mode packets, to determine the paths and ToF's were identified.

4. The investigations on the available guided wave signal analysis and decomposition methods showed that the most reliable results are obtained when the combination of a few methods are used. Since methods based on analysis of the real part of the Fourier spectra has been widely investigated, there is still a lack of current work relying on the analysis of imaginary parts. Such methods have a potential in measuring a phase velocity of guided waves and along with some *a-priori* analytical knowledge and various excitation schemes could be further used for guided wave mode decomposition.
5. The brief review of the existing means for damage localisation and feature extraction revealed that there are some reliable and widely investigated methods to locate damage using guided waves, mostly based on phased addition and triangulation, however there are almost no studies focusing on damage feature extraction using embedded transducers, which is very important for the prognosis of the life time of structures.
6. The general review of the application of GW to SHM of composites demonstrated that the focus is mainly on the detection of the presence of damage, however there is no available research trying to create a framework suitable for verification and calibration of monitoring systems, without the introduction of destructive artificial defects. Such framework could be used as a reference-free and non-destructive basis to verify and calibrate distinct SHM systems in different real-world situations.

According to the key findings in the review of literature the following **tasks of the research** were anticipated:

1. To investigate and explain the mechanism of GW generation, and to develop mathematical methods to analyse and predict the spectral characteristics of separate GW mode packets.
2. To develop and verify an analytical model that simplifies the analysis and interpretation of the complex propagation of GW in plate-like anisotropic structures.
3. To create and validate the methods for GW phase velocity estimation in multimodal, overlapped signals captured by spatially distributed sensors, which can be used for the identification of unpredicted modes and modal decomposition purposes.
4. To propose and investigate methods for the detection of the delamination type defects and extraction of its features such as the size and the depth.
5. To create and validate methods suitable for the verification and calibration of the monitoring system, without using the database of the reference samples, that describe different states of the damage.

In the above chapter, the current state of the art in the field of guided wave structural health monitoring was briefly presented. Each of the reviewed methods has its own advantages and drawbacks, which for the convenience of the reader are briefly summarized in table 1.7.1.

Table 1.7.1. The summarized pros and cons of the currently used methods in different research areas related to the GW SHM

Pros:	*Cons*:	*Suggested solution*:
Techniques for selective guided wave mode excitation		
• Dominant GW mode can be generated by selecting either the size of the PZT wafer, the pitch between the electrodes of the IDT transducer or the inter-element distance of separately driven transducer array. • PZT wafers and arrays of separately driven actuators are relatively cheap and simple. • Separately driven actuators can be adjusted for selective GW excitation at various frequencies.	• Enables the generation of one dominant mode, however, other modes are generated anyway. • The set of PZT patches or the IDT transducers are required for selective GW mode excitation at different frequencies and materials. • The SHM system becomes restricted to detection of the certain type of defects only. • At low frequencies, the PZT wafers and IDT transducers become bulky.	• A multimodal excitation would make the SHM system more reliable and sensitive to a variety of defects. However, in such case the signal processing methods for analysis of guided wave generation and propagation are required. • Hence, the appropriate methods for GW signal analysis could be developed, which would allow the use of multi-modal signals and to avoid the selective GW excitation.
Methods for simulation of guided wave propagation		
• The SAFE and matrix techniques enable the identification of modes which exist in the structure and to analyse the displacement profiles in the cross-section. • The FE technique enables the analysis of dynamical wave propagation and can be reliably used for verification purposes.	• Transfer matrix method possess stability problems, while SAFE has mode sorting issues and is applicable only to uniform objects. • The reliable FE solution requires a fine mesh and integration time step which leads to a slow solution. Besides, the FE method provides a lot of surplus information in case of SHM.	• For the proper analysis of GW propagation in SHM systems it is most important to estimate the ToF of separate modes and to retrace wave propagation paths. The conventional FE method cannot directly provide such information; hence rapid analytical models could be developed especially for SHM.
Methods for time and frequency domain analysis		
• TFR methods enables to identify GW modes which are present in the structure, to estimate their magnitude, frequency content and to help detecting defects of different kinds.	• Most of the methods cannot provide good time and frequency resolution simultaneously. • The WT and MP has difficulties in selecting the right mother wavelet and dictionary. • The WVD has cross-term problems, while HHT possess issues with signal ends.	• As the most present methods are based on analysis of the real part of the signal spectrum, some decomposition techniques can still be proposed, which would be based on estimation of phase velocities of GW from the imaginary part of the Fourier spectrum.
Approaches for defect detection and localisation		
• The reconstruction methods based on the constructive interference can be efficiently used both to detect and to localise the damage. • The existing image fusion and DI approach offers increased resolution of reconstructions.	• The baseline subtraction or time reversal technique can indicate structural changes only. • The resolution of the mapping methods depends on the number of transducers. Besides, they do not estimate defect size and depth.	• New guided wave SHM techniques can be developed which would allow the gap in damage size and depth estimation methods with embedded sensors to be filled. Such methods are crucial for the prognosis of the life-time of the structure.

2. METHOD TO PREDICT THE FREQUENCY RESPONSE OF GUIDED WAVES

2.1 Motivation and demand of the proposed method

Prior to the development of any reliable technique for signal processing and defect detection, the initial step is to understand the mechanism of the wave generation and to be able to predict the parameters of each guided wave mode upon its introduction into the structure. Hence, in the upcoming chapter, the main attention will be paid to the development of the methods to explain and predict the source influence on the excitation of different GW modes.

The generation of GW is in general different compared to the bulk wave case. For the sake of better understanding, in the following paragraph the main differences between the nature of bulk and guided waves will be briefly discussed. Despite that both bulk and guided waves may be generated employing the same principle (for example angle-beam excitation), whether the bulk or guided wave is generated mainly depends on frequency. To excite the GW, the wavelength has to be greater than the thickness of the material, meanwhile the bulk waves in general are propagating in the infinite medium, where the boundaries have no influence on wave propagation. Due to this reason, in the case of bulk waves, mostly there is one or two desired non-dispersive waves (longitudinal or shear), propagating at constant phase velocity. In contrast, the GW is a superposition of longitudinal and shear waves, which reflects back and forth, and converts to other modes. At a given frequency, the result of such wave interaction may be either constructive, destructive or intermediate. As a consequence different GW modes are produced simultaneously, each having its own frequency-thickness dependent velocity and particle velocity vibration across the thickness of the sample. There are a few available techniques to produce the single desired mode of guided waves in the structure, which were briefly introduced in Chapter 1. However, in most cases, more than one mode is present in the structure at a time, thus the proper understanding of properties of each mode becomes critical for the development of high accuracy inspection systems and techniques.

2.2 State of the art and theoretical formulation of proposed method

One of the most important and versatile features, which can be used to describe the modes of guided waves, is the frequency response. The frequency response of guided wave modes depends both on the geometrical, structural properties of the investigated medium and the parameters of the source, such as size and type of excitation. For simplicity, in most theoretical models, it is presumed that the conditions are ideal possessing the uniform loading and continuous plane wave excitation. However, in reality, the transducers possess limited size and frequency bandwidth. Hence, the type of excitation determines the mode, which is introduced into the structure, whereas the amplitude of vibrations depend on the size-wavelength ratio of the source.

There are several existing approaches to predict the source influence on guided wave generation, namely normal mode expansion and integral transform (69). These techniques enable the partial differential equations to be solved, which were presented in Chapter 1, section 1.1 with appropriate symmetric and asymmetric boundary conditions and to obtain the mode excitability (response amplitude) as a function of frequency separately for each mode. Such excitability functions are commonly used to implement the single mode excitation (so called mode tuning), since they provide information about the response amplitude oscillation of particular modes at distinct frequencies. The application of the integral transform method was demonstrated by Giurgiutiu et al. (124), who used this technique to estimate the frequencies at which the desired modes can be either enhanced or suppressed using the piezoelectric wafers. Similarly, Grondel et al. (131) implemented a normal mode expansion method during the design of the comb transducer, which produces the single A_0 mode. Finally, di Scalea et al. (243) calculated the response of rectangular piezoelectric sensors to different type of excitation fields. However, these excitability functions are mostly used during the design of so called single mode transducers. On the other hand, this function can be used as a tool to predict the frequency response of each mode and to explain the filtering phenomenon due to the source influence as well, which usually can be observed if the wideband excitation is applied. Such filtering phenomenon is usually neglected in most of the available GW signal processing methods. However, taking into the account the excitability function may significantly increase the reliability and accuracy of signal processing techniques.

It can be proved that the magnitude spectrum of each guided wave mode $U(f)$ can be described as a product of the spectrum of excitation pulse $U_{\mathrm{ref}}(f)$ and excitability function H, which itself depends on type of excitation (particle velocity distribution on the surface of structure, u) and size of source (l):

$$U(f)=U_{\mathrm{ref}}(f)\cdot H(f,u,l). \tag{2.2.1}$$

Thus, the goal of this study, in contrast to the work done by others, is to develop a technique, which would allow the frequency response $U(f)$ for each guided wave mode to be predicted upon its introduction into the structure under any type of excitation. For this purpose, the complete solution for the forced guided wave excitation will be proposed, which enables the excitability function $H(f,u,l)$ to be estimated. The estimated excitability functions H will be used as the bandpass filter to describe the change of spectrum of excitation pulse for each mode. In this study the generation of GW with a surface mounted macro-fibre composite (MFC) transducer, subjected to the tone burst excitation and operating in d_{33} mode will be analysed (244). The working principle of the considered transducer is revealed in the reference cited above. In the remaining part of this section, the principle and routine of the proposed technique to predict the excitability function $H(f,u,l)$ will be briefly revealed.

The method proposed in this study is based on Fourier analysis of the particle velocity distribution (u) on the excitation surface at the initial instant of excitation. Such particle velocity distribution is related to the excitation force, which is required to introduce the desired mode into the structure. Let’s assume that the virtual MFC transducer is mounted on the surface of the sample and excites the A_0 and S_0 modes simultaneously. Consider that the spatial distribution of the particle velocity is like that presented on Fig. 2.2.1. Note, that the presented spatial distribution of particle velocity was selected according to the working principle of the MFC transducer. Hence, it is presumed that the particle velocity at the excitation surface has to be exclusively concentrated at the edges of the transducer to introduce the A_0 mode (Fig. 2.2.1a). Similarly, the saw tooth like particle velocity distribution is required to excite the S_0 mode (Fig.2.2.1b). Mathematically for the A_0 and S_0 modes it can be expressed as follows:

$$u_{A_0}(z) = \begin{cases} 1 & z = z_1 \text{ or } z = z_2 \\ 0 & \text{other case} \end{cases}, \tag{2.2.2}$$

$$u_{S_0}(z) = \begin{cases} \dfrac{2z - l}{l} & z_1 < z < z_2 \\ 0 & \text{other case} \end{cases}, \tag{2.2.3}$$

where z_1 and z_2 are the coordinates of the front and back edge of the MFC transducer; $l=z_2-z_1$ is the width of source.

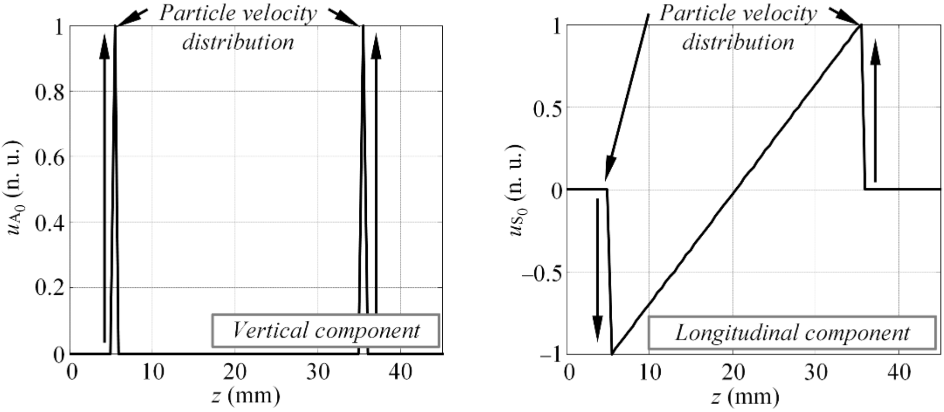

a) b)

Fig. 2.2.1. The presumed spatial distribution of the particle velocity of the MFC transducer on the excitation surface: the vertical or normal component, which generates the A_0 mode (a) and the longitudinal or tangential component, which produces the S_0 mode (b)

It can be proved that the spatial distribution of the particle velocity on the excitation surface at the initial instant of excitation surface actually depends on the structural properties of the material, which can be described by the phase velocity. As a consequence, for the non-dispersive wave the particle velocity distribution can be represented in the particle velocity-time domain as $u(t)$, using the simple relation $t=z/c_p$, where c_p is the phase velocity. For the dispersive wave, the phase velocity is the function of frequency $c_p(f)$, hence the particle velocity distribution depends on the frequency as well ($u(z/c_p(f))$).

The excitability function at the given frequency f_k can be expressed as the magnitude of the Fourier representation of particle velocity distribution $u(z/c_p(f_k))$. The same procedure can be repeated over the bandwidth of the transducer, to collect the whole set of magnitude values of excitability function:

$$H_{\mathrm{A}_0}(f_k)=U'_{\mathrm{A}_0}(f)\Big|_{f=f_k},\ U'_{\mathrm{A}_0}(f)=\left|\mathrm{FT}\left[u_{\mathrm{A}_0}\left(\frac{z}{c_{\mathrm{pA}_0}(f_k)}\right)\right]\right|, \tag{2.2.4}$$

$$H_{\mathrm{S}_0}(f_k)=U'_{\mathrm{S}_0}(f)\Big|_{f=f_k},\ U'_{\mathrm{S}_0}(f)=\left|\mathrm{FT}\left[u_{\mathrm{S}_0}\left(\frac{z}{c_{\mathrm{pS}_0}(f_k)}\right)\right]\right|, \tag{2.2.5}$$

where $H_{\mathrm{A}_0}(f_k)$ and $H_{\mathrm{S}_0}(f_k)$ are the analytical excitability functions for the A_0 and S_0 modes; u_{A_0} and u_{S_0} are the particle velocity distributions for A_0 and S_0 modes at particular frequency f_k; FT denotes the Fourier transform. According to eq. 2.2.4 and eq. 2.2.5 the excitability functions, which show the response amplitude oscillation versus frequency, can be obtained. The proposed method is not limited to particular geometries or types of materials and can be used to predict the excitability function on any structure, under any type of excitation. To get the proper results, the method requires the phase velocity dispersion curve of the analysed structure and the principle of operation of the investigated transducer (particle velocity distribution for the analysed mode) as input data.

To illustrate the excitability function versus frequency, let's consider the 4 mm thick glass fibre reinforced plastic (GFRP) plate as an investigated sample, with the material properties as follows: the Young's modulus: $E_x = 10$ GPa, $E_z = 35.7$ GPa; the Poisson's ratio: $\upsilon_{xz} = 0.325$, $\upsilon_{zx} = 0.091$, $\upsilon_{yx} = 0.35$; Shear modulus: $G_{xz} = 2.8$ GPa; density: $\rho = 1{,}800$ kg/m^3. Then the analytically obtained excitability functions for the A_0 and S_0 modes will look like that presented on Fig. 2.2.2a and Fig. 2.2.2b. Note, that the excitability functions were estimated considering the same particle velocity distribution as it was defined by eq. 2.2.2 and eq. 2.2.3.

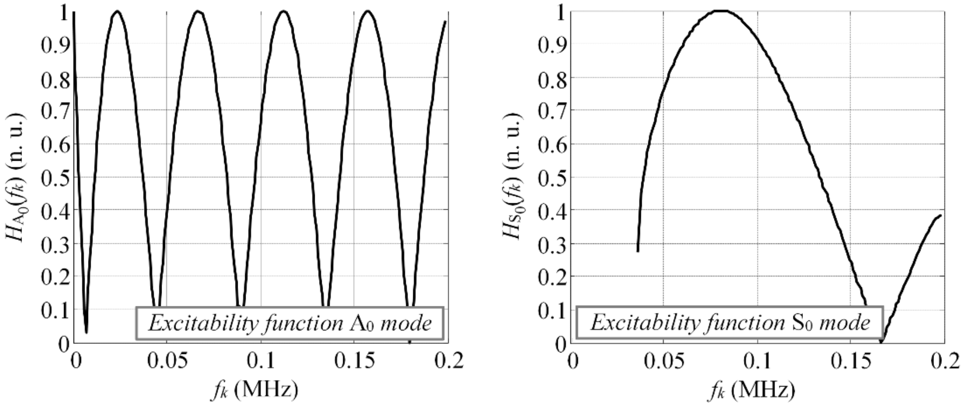

a) b)

Fig. 2.2.2. The excitability functions on 4 mm thick GFRP plate for the A_0 (a) and S_0 (b) modes, calculated according to the vertical and longitudinal component of particle velocity

The results presented in Fig. 2.2.2 indicate, that in both cases the response amplitude of excitability function oscillates with an increase of frequency. The zero values of the excitability function can be found at some frequency components, thus the filtering phenomenon will be introduced, if the spectrum of broadband excitation signal overlap with the cut-off frequencies of excitability function. The periodicity of response amplitude oscillation is higher for the A0 mode, meaning that the modes possessing smaller wavelengths (i.e. A0) will likely be more distorted in comparison to the symmetrical S0 mode. These excitability curves can be used to enhance or supress the excitation of the desired mode. For example, at a frequency of 160 kHz, the response amplitude for the A0 mode is high, meanwhile the S0 mode will be supressed (see Fig. 2.2.2). However, as the relatively broadband excitation is usually used to drive the transducer, both modes will be generated anyway. Depending on the frequency and the bandwidth of the excitation pulse, it will be more or less distorted due to the influence of excitability function.

To illustrate the filtering effect due to such type of excitation and size of source, let's consider that the transducer is driven by a tone-burst with a Gaussian envelope of 3 periods and central frequency of 80 kHz. Then the magnitude spectrum of the excitation pulse will look like that presented by a solid line on Fig. 2.2.3. The excitability function and its product with the magnitude spectrum of excitation pulse can also be seen on the same Fig. 2.2.3 (dash-dot and dashed lines respectively). It can be observed, that under such type of excitation and the size of source, some significant distortions are present in the spectrum of the A0 mode (Fig. 2.2.3a). In order to correctly interpret the guided wave propagation, mode interference and interaction with defects, the likely filtering effects has to be taken into the account, although in most research such filtering phenomenon is usually still neglected.

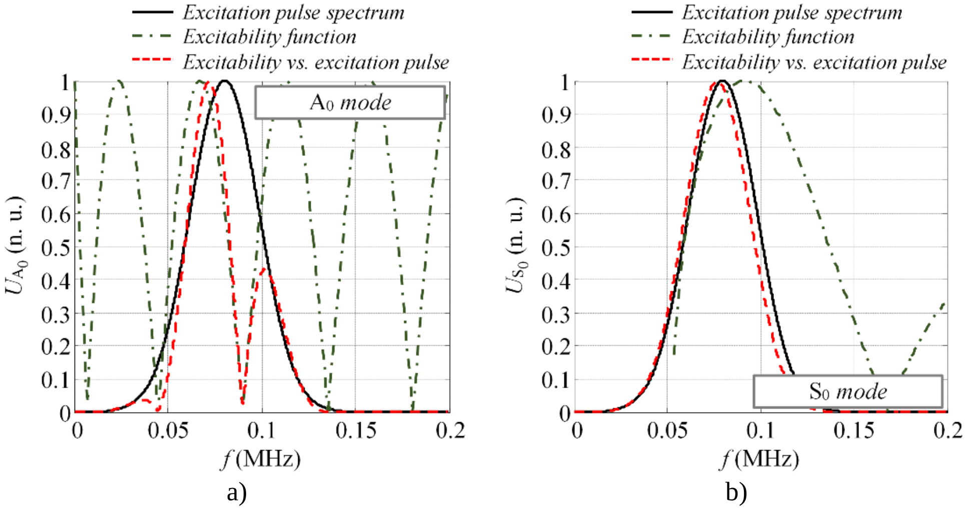

Fig. 2.2.3. The influence of the excitability function to the frequency response of the guided waves for the asymmetric A0 (a) and symmetric S0 (b) modes (solid line – spectrum of the excitation pulse, dash-dot line – excitability function, dashed line – product of excitation pulse and excitability function)

2.3 Validation of the proposed technique employing FE method

The goal of this section is to validate the excitability function estimation technique presented above and to prove that the magnitude spectrum of each guided wave mode present in the structure is a product of the frequency spectrum of the excitation pulse and the excitability function. For this purpose, the 3D finite element (FE) model of the transient wave propagation was employed for a complex shaped GFRP plate with dimensions of 800 mm × 70 mm × 4 mm. Then the frequency spectrum of the fundamental A_0 and S_0 modes were extracted from the FE simulation data and compared to the analytically predicted excitability functions. In a few upcoming paragraphs, the numerical model of the GFRP sample will be briefly described, followed by the procedure used to extract the spectrum of A_0 and S_0 modes.

Description of the GFRP FE model. The graphic representation of the model used in FE simulations can be seen in Fig. 2.3.1a. The geometrical shape and dimensions of the simulated sample were deliberately selected to correspond to the real mock-up specimen, which will be used later for the experimental verification. In the numerical model, the operation of MFC (M-2814-P1) actuator, with an active area of 28 mm × 14 mm, working in the elongation d_{33} mode was simulated. The distance along z axis between the centre of the virtual transducer and the nearest end of the sample was set to 165 mm. The excitation area was aligned to the centre of the sample in respect to the x axis. The thin layer of wax (Young's modulus: E = 1.81 GPa, Poisson's ratio: υ = 0.49; density: ρ = 951 kg/m^3) was used as a coupler between the specimen and the transducer. To simulate the operation of the MFC transducer in the elongation d_{33} mode, the active surface of the actuator was divided into two separate areas referred as: "zone A" and "zone B", each with dimensions of 14 mm × 14 mm (see Fig. 2.3.1b). Then the excitation of guided waves was simulated by applying the monotonically increasing excitation force of the opposite phase to nodal points in "zone A" and "zone B" as illustrated in Fig. 2.3.1b. In such a way the waves generated in "zone A" propagate along the positive direction of the z axis, meanwhile the waves introduced in "zone B" propagates backwards. Under such type of excitation, typically both fundamental asymmetrical and symmetrical modes are generated. The waveform of the excitation force was a burst with a Gaussian envelope of 3 periods, a central frequency of 80 kHz and a bandwidth of 42.9 kHz at –6 dB.

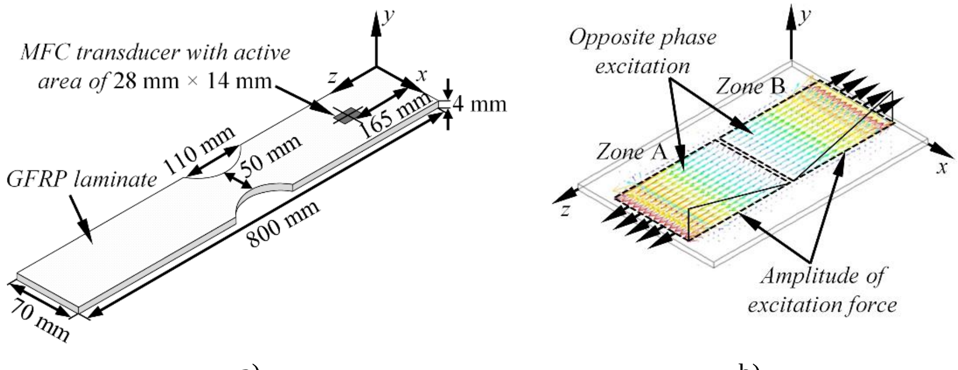

a) b)

Fig. 2.3.1. The schematic view of the GFRP plate used in FE simulations (a), the principle of guided wave generation in FE model, simulating the d_{33} mode of MFC transducer (b)

For transient simulation the Newmark time integration scheme was applied. The integration step in time domain was 0.625 μs, which is 1/20 of the period at 80 kHz central frequency. The sample was meshed using SOLID64 elements, which has eight nodes each with three degrees of freedom. The average spatial size of the element was equal to 1 mm possessing 14 nodes per wavelength for the slowest A_0 mode at 80 kHz frequency. The finite elements of the regular areas were created using the mapped mesh, whereas for the regions close to cut-outs the free sweep mesh was implemented. Material properties were selected to be the same as those presented in the previous section. The variable monitored in this study was a vertical (y) and longitudinal (z) component of particle velocity at the nodal points situated along the centreline of the sample. The B-scan image of vertical and longitudinal component of particle velocity can be seen on Fig. 2.3.2.

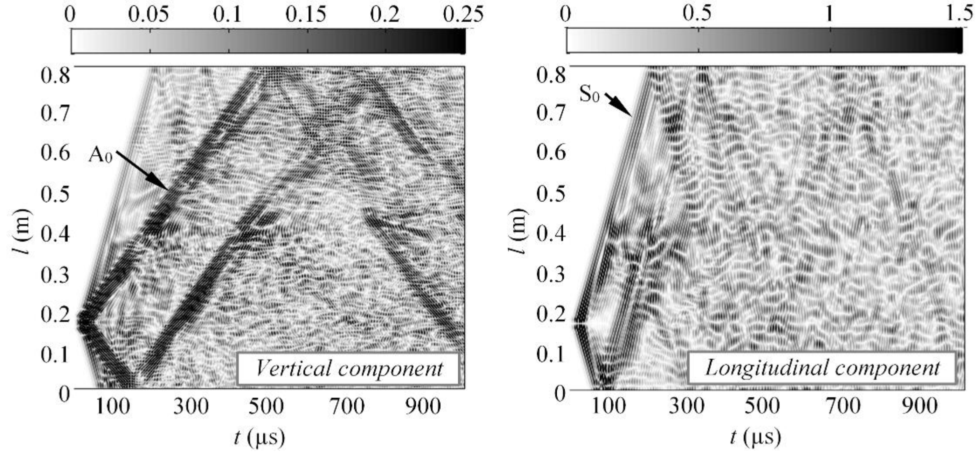

a) b)

Fig. 2.3.2. The simulated B-scan images of the vertical (a) and longitudinal (b) component of guided waves along the centreline of the GFRP sample

At the end of the simulation routine, the frequency spectrum of fundamental A_0 and S_0 modes, which are present in the structure was extracted from the B-scan data of vertical and longitudinal component of particle velocity. For this purpose, the B-scan data $u(t,x)$ was transferred to the frequency-wavenumber domain $u(f,\xi)$ using the 2DFFT. The frequency-wavenumber representation of the B-scan show the wavenumber DC for all modes available in the structure. As the fundamental A_0 and S_0 waves were the modes of interest, the appropriate DC were filtered from $u(f,\xi)$, employing the Gaussian filter, which mathematically can be described by an equation:

$$F(f,\xi)=e^{-A(\xi-\xi_0(f))^2}, \tag{2.3.1}$$

where A is the coefficient which determines the width of the Gaussian filter along wavenumber axis; $\xi_0(f)=a_k \cdot f+b_k$; a_k and b_k are the coefficients of the linear equation; $k = 1\ldots K$; K is the total number of linear points; $f\in[f_k, f_{k+1}]$; f_k, f_{k+1} defines the frequency bandwidth under investigation. The Gaussian filter was adjusted to fit the DC of each mode of interest, meaning that each mode was approximated by a set of linear segments in the frequency-wavenumber domain, which were selected manually. As the consequence, the filtered A_0 and S_0 modes can be described by the equations:

$$U_{A_0}(f,\xi)=u(f,\xi)\cdot F_{A_0}(f,\xi), \tag{2.3.2}$$

$$U_{S_0}(f,\xi)=u(f,\xi)\cdot F_{S_0}(f,\xi), \tag{2.3.3}$$

where $u(f,\xi)$ are the wavenumber dispersion curves obtained from the B-scan data using the 2D FFT approach; $F(f, \xi)$ are the Gaussian filters for A_0 and S_0 modes. As the result of the filtering the wavenumber dispersion curves have been obtained separately for the A_0 and S_0 modes. Then the frequency spectra of these modes was calculated using the following expressions:

$$U_{A_0\max}(f)=\max_{\xi}\left(U_{A_0}(f,\xi)\right), \tag{2.3.4}$$

$$U_{A_0N}(f)=\frac{U_{A_0\max}(f)}{\max\limits_{f}\left(U_{A_0\max}(f)\right)}, \tag{2.3.5}$$

$$U_{S_0\max}(f)=\max_{\xi}\left(U_{S_0}(f,\xi)\right), \tag{2.3.6}$$

$$U_{S_0N}(f)=\frac{U_{S_0\max}(f)}{\max\limits_{f}\left(U_{S_0\max}(f)\right)}. \tag{2.3.7}$$

As the goal of this study is to compare the simulated spectrum of A_0 and S_0 modes ($U_{A_0N}(f)$, $U_{S_0N}(f)$) with the analytically predicted excitability functions ($U_{A_0an}(f_k)$, $U_{S_0an}(f_k)$), in the following few paragraphs, their estimation will be briefly described.

Estimation of the excitability functions for the considered problem. In order to estimate the excitability functions using the technique described in section 2.2.1, the spatial distribution of the particle velocity for the A_0 and S_0 modes has to be defined first. In this case it is presumed that the particle velocity of the vertical component (y) on the active area of the transducer at the first time instant of the modelling represents the excitation of A_0 mode (see Fig. 2.3.3a). Similarly, the particle velocity of longitudinal component (z) at the first time instant may be used to describe the generation of the S_0 mode (see Fig. 2.3.3b).

The spatial particle velocity distributions presented in Fig. 2.3.3 were used in the calculation of the excitability functions. For the sake of better understanding, let's denote such type of wave generation as "case A" excitation. The same material properties, described in the previous section, were used to define the DC for a 4 mm GFRP plate as well. The excitability functions in this case were estimated in a frequency band up to 200 kHz. Once the calculations were finished, the excitability functions $U_{A_0}(f_k)$ and $U_{S_0}(f_k)$ were compared to the magnitude spectra of appropriate mode $U_{A_0N}(f)$ and $U_{S_0N}(f)$, estimated by eq. 2.3.5 and eq. 2.3.7. The comparison of the analytical and numerical results can be seen in Fig. 2.3.4.

The results presented in Fig. 2.3.4 show a good agreement between the numerical calculations and analytical estimation. The results may lead to the conclusion, that the magnitude spectrum of each guided wave mode is actually the product of excitation pulse spectrum $U_{\mathrm{ref}}(f)$ and the excitability function $H(f,u,l)$, which itself depends on the properties of material, type of excitation and size of source. If at least one of the abovementioned parameters is changing, the spectrum of the mode present in the structure will vary as well.

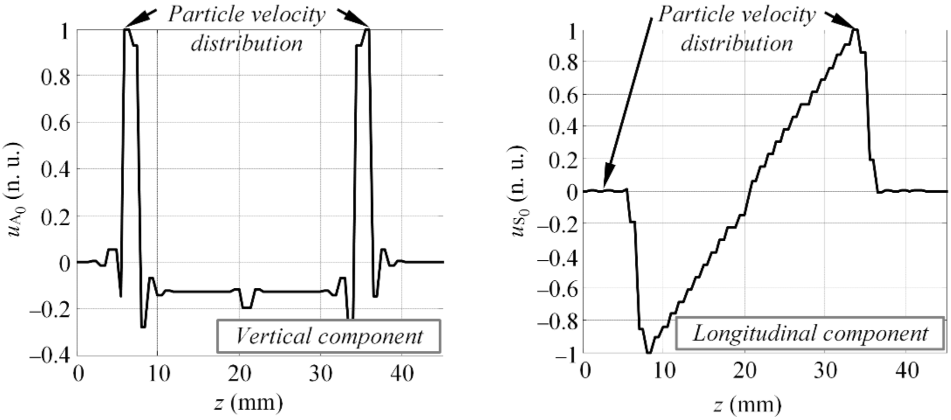

a) b)

Fig. 2.3.3. The vertical (a) and longitudinal (b) component of particle velocity at the excitation surface at the first time instant of the modelling

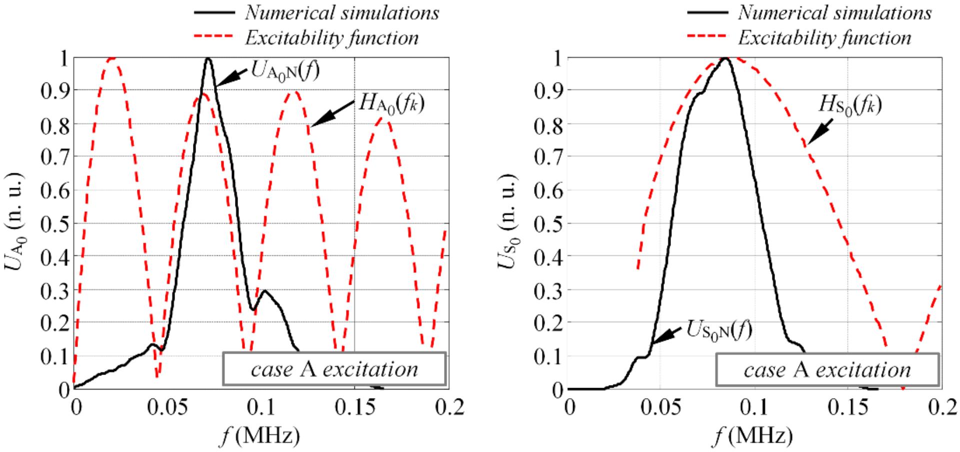

a) b)

Fig. 2.3.4. The numerically estimated frequency spectra of the pure A_0 (a) and S_0 (b) mode on 4 mm GFRP sample (solid line) along with analytically predicted excitability functions (dashed line)

To illustrate the influence of excitation type on the excitability function, another numerical experiment was carried out, retaining the same set-up, yet at different particle velocity distribution, which will be referred as “case B” excitation. In this numerical experiment, the particle velocity distribution was the only parameter which has been changed in all the calculations (material properties and size of source were the same as in the previous case) (see Fig. 2.3.5). It means that the velocity distribution does not correspond to the working principle of MFC transducer anymore.

The particle velocity distribution presented in Fig. 2.3.5 was simulated by applying the same phase excitation to “zone A” and “zone B” in the numerical model with the excitation force increasing towards the edge of each zone along the z axis. The comparison between the magnitude spectra of appropriate mode $U_{\mathrm{A_0 N}}(f)$ and $U_{\mathrm{S_0 N}}(f)$ with the analytical excitability functions $U_{\mathrm{A_0}}(f_k)$ and $U_{\mathrm{S_0}}(f_k)$ is presented in Fig. 2.3.6. The results demonstrate, that in both cases the spectrum of symmetrical $\mathrm{S_0}$ mode remains unchanged, as the excitability function is relatively wideband (see Fig. 2.3.4b and Fig. 2.3.6b). Meanwhile the magnitude spectrum of the asymmetrical $\mathrm{A_0}$ mode has changed upon the change of type of excitation. It can be observed, that the excitability function is related to the wavelength of the guided waves, therefore the filter of the $\mathrm{A_0}$ mode has the more zero harmonics compared to $\mathrm{S_0}$ mode.

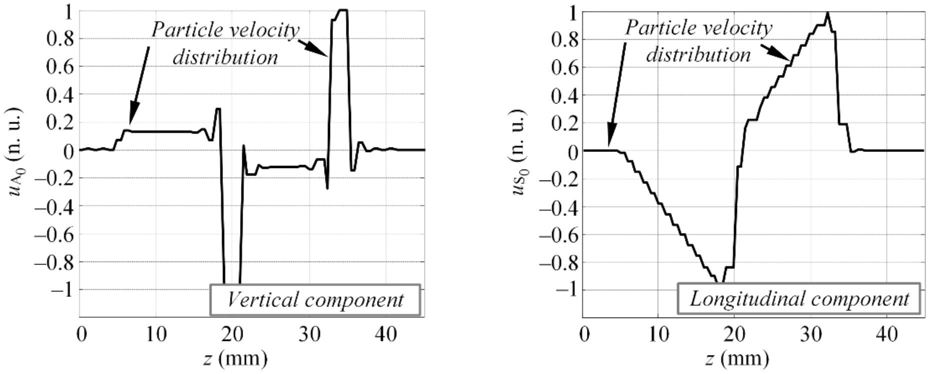

a) b)

Fig. 2.3.5. The vertical (a) and longitudinal (b) component of particle velocity at the excitation surface at first time instant of the modelling, referred to as “case B” excitation

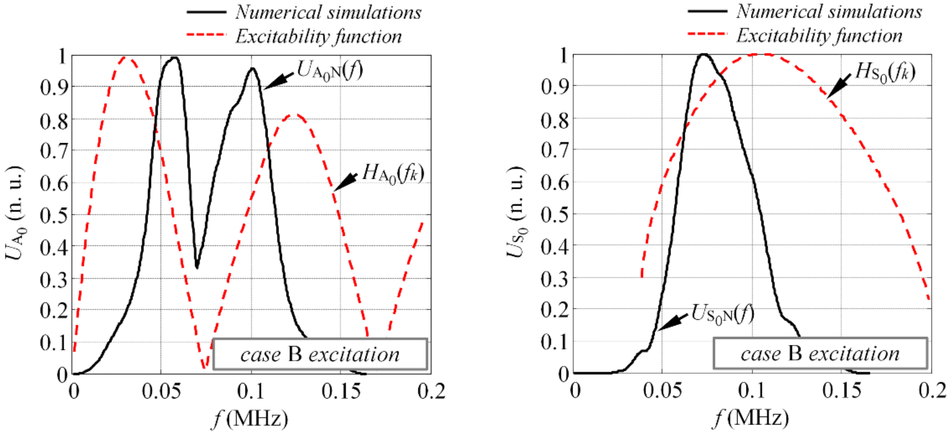

a) b)

Fig. 2.3.6. The numerically estimated frequency spectra of the pure $\mathrm{A_0}$ (a) and $\mathrm{S_0}$ (b) mode on 4 mm GFRP sample (solid line) along with the excitability functions calculated considering the “case B” excitation (dashed line)

As it was mentioned previously, it can be proved, that the spectrum of each mode is a product of input signal spectrum $U_{\mathrm{ref}}(f)$ and the excitability function $H(f,u,l)$. To illustrate that, the product of input signal spectrum ($U_{\mathrm{ref}}(f)$) and the excitability function H in case of "case A" and "case B" excitation of A_0 mode is calculated and then compared to the numerically estimated spectra of A_0 mode, which were presented in Fig. 2.3.4a and Fig. 2.3.6a. The comparison was done for the A_0 mode only, since the spectrum of S_0 mode remains almost the same input for any of the investigated type of excitation. The results of comparison can be seen in Fig. 2.3.7. The left hand side of the figure show the results for "case A" excitation, meanwhile the right hand side is devoted for the "case B" excitation.

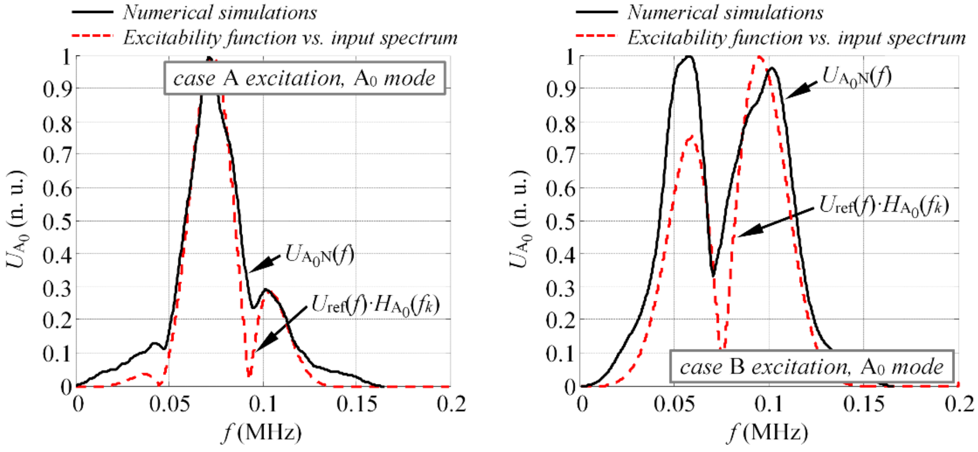

a) b)

Fig. 2.3.7. The comparison between numerically obtained spectrum of A_0 mode for the case A (a) and case B (b) excitation with the product of input signal spectrum and appropriate analytically estimated excitability function

2.4 Experimental verification on the anisotropic GFRP plate

To further investigate the feasibility of proposed excitability function estimation technique, the experiments have been carried out on GFRP samples, possessing the same geometry, mechanical properties and sensor allocation, as described in section 2.3. The goal of this study was to compare the experimentally obtained frequency response of asymmetrical A_0 mode with the analytically predicted excitability function. Thus, to fulfil the scope of the study, the experiments, which are described in the following paragraph were carried out.

The MFC actuator of type M-2814-P1 was mounted on top of the sample, using a thin layer of wax for coupling as shown in Fig. 2.3.1. The actuator was driven with a 1 cycle, 50 V square pulse with a central frequency of 80 kHz, to generate multiple modes in wide frequency bandwidth. To collect the experimental data, the custom made low frequency thickness mode transducer (central frequency 240 kHz; bandwidth of the transducer at –6 dB level 340 kHz) was attached perpendicularly to the surface of the sample and scanned along the wave path of guided waves. The receiver was moving away from the transmitter up to 380 mm with a step increment of 1 mm. The initial spacing between the actuator and sensor was equal to 5 mm. To get the reliable acoustic contact between the sensor and the specimen, the glass textolite protector with a contact area of 3 mm^2 was used. The waveforms were recorded using a 25 MHz sampling frequency. The response signals were measured 8 times and averaged to ensure better signal to noise ratio. In such way, the B-scan dataset of out-of-plane component was collected at the centreline of the sample. The experimental set-up is graphically illustrated at Fig. 2.4.1.

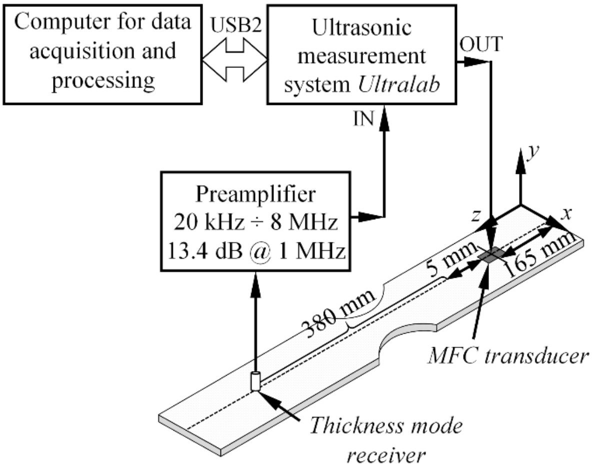

Fig. 2.4.1. The experimental set-up for investigation of source influence on guided wave generation

The experimentally obtained raw B-scan $u(t,x)$ image of the out-of-plane component of guided waves is presented in Fig. 2.4.2a. Analogically, the frequency-wavenumber representation of the B-scan data $u(f,\xi)$, showing the modes available in the structure can be seen in Fig. 2.4.2b. The results in Fig. 2.4.2a,b show that mainly two modes are present in the structure, while the A_0 is a dominant one.

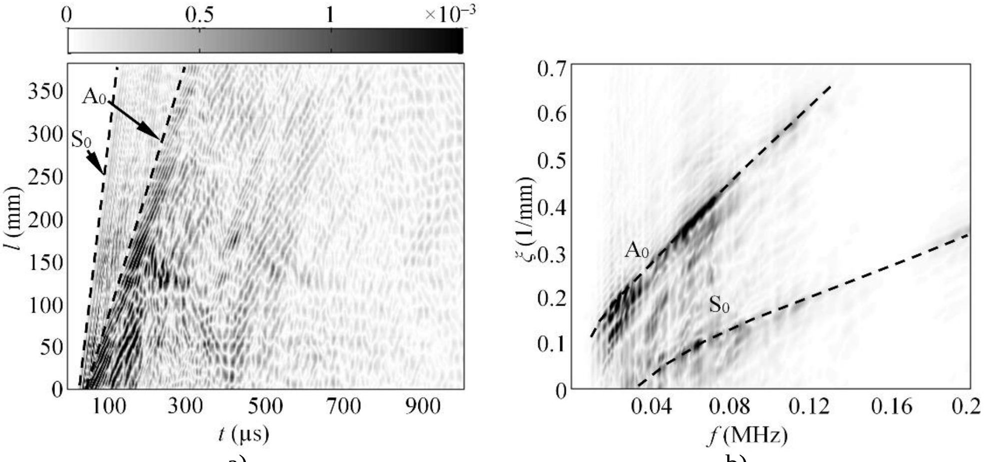

a) b)

Fig. 2.4.2. The experimental B-scan of the out-of-plane component of GW along the 4 mm thick GFRP sample (a), the frequency-wavenumber representation of the B-scan data (b)

To fulfil the scope of the experiment, the spectrum of the A_0 mode was extracted from the frequency-wavenumber $u(f,\xi)$ data (Fig. 2.4.2b) implementing the procedure, described in section 2.3. For the calculation of excitability function, it was presumed, that the loading distribution, required to introduce the A_0 mode is the same as presented in Fig. 2.3.3a. Then the excitability function of the A_0 mode $U_{A_0\mathrm{exp}}(f)$ was calculated according to eq. 2.2.4 in a frequency band up to 200 kHz, assuming that the material properties of the investigated GFRP sample are the same as it was listed in section 2.2. The comparison between the experimentally obtained spectrum of A_0 mode and the analytical excitability function $H_{A_0}(f_k)$ can be seen in Fig. 2.4.3. The results show quite a good agreement between the analytical predictions and experiments. Note, that in this case, the transducer was driven by a square pulse of 1 cycle. It means that there might be additional zero harmonics in the frequency spectrum of the A_0 mode, due to the type of input signal. This can be observed from Fig. 2.4.3 where a local minimum is present at the frequency slightly above 100 kHz. Thus, it is important to bear in mind that some distortions in the frequency spectrum of a particular mode might be caused by a type of input signal and not necessarily due to the source influence.

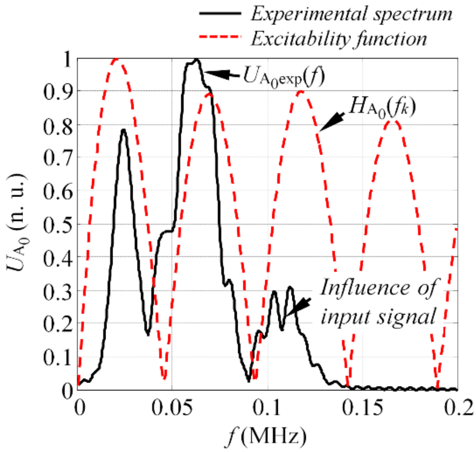

Fig. 2.4.3. The comparison between the experimental spectrum of A_0 mode and the analytical excitability function

2.5 Experimental verification employing the linear array with variable aperture

In previous sections, the excitability function estimation technique was introduced and verified. It was demonstrated with the numerical simulations and validated with experiments, that the type of excitation influences the spectrum of each GW mode. In this chapter, the influence of source size on the forced guided wave excitation will be demonstrated and validated as well. For this purpose, the experiments were carried out on 0.5 mm thick aluminium plate with dimensions of 1,250 mm × 700 mm. The material with well-known properties was deliberately selected for this study, to simplify the analysis of GW signals. It was estimated, that for such type of material, only the fundamental modes (A_0 and S_0) exist in the frequency band up to 3 MHz. To fulfil the scope of the study, the 2.25 MHz, 128 elements phased array (Olympus 2.25L128-96x12-I3-P-2.5HY) was used as an actuator and attached to the surface of the plate using oil for acoustic coupling. The array was positioned along the centreline of the sample at a distance of 425 mm to the closest edge of the plate. In total four independent experiments were carried out (referred as experiment #1, experiment #2 and so on) to get the response from the structure at different actuator sizes. In the first experiment, only the single element of an array was excited. In each of the subsequent experiment, the active aperture of an array was incremented by adding one neighbouring array element to an active aperture. It means that in the second experiment, two array elements were excited at once and so on. In each of the experiments, the array was driven by a tone burst of 1 cycle and 200 V with central frequency of 2.25 MHz. To collect the experimental data, the thickness mode transducer with a point type protector was attached perpendicularly to the surface of the plate and scanned along the wave path of the sample. The initial distance between the array and the receiver was equal to 100 mm, while in each case the receiver was scanned away from the transmitter up to 300 mm with step increment of 0.1 mm. All the waveforms were recorded using the 100 MHz sampling frequency and averaged 8 times. The experimental set-up and aperture configurations are presented in Fig. 2.5.1.

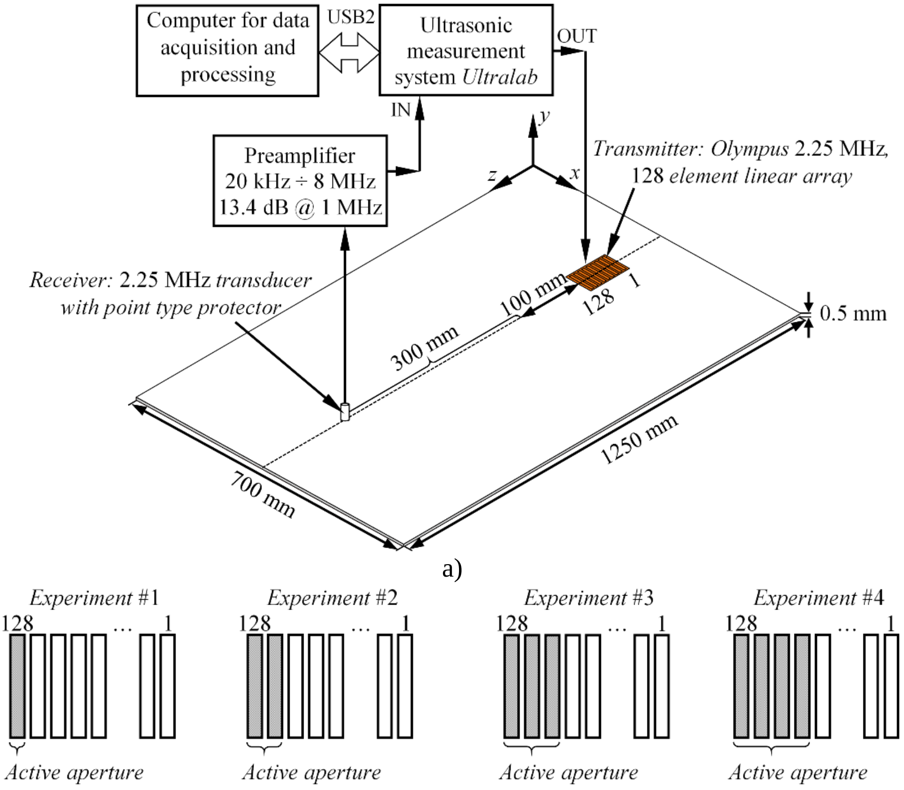

a)

b)

Fig. 2.5.1. The experimental set-up for investigation of source size influence on guided wave mode spectrum (a) and the array aperture configurations used throughout experiments (b)

According to the datasheet of the array, the width of each element was equal to 0.5 mm with an inter-element distance of 0.25 mm (pitch 0.75 mm). In such way, the active aperture in the experiment #1 was equal to 0.5 mm, while in each of the subsequent experiments – 1.25 mm, 2 mm and 2.75 mm. At the end of the experiments, in total four B-scan datasets were created, each at a different active aperture of the actuator. In this study, the S_0 mode was selected as the mode of interest. Thus, the frequency spectrum was estimated from each of the B-scans (namely $U_{\mathrm{S_0exp\#1}}(f)$, $U_{\mathrm{S_0exp\#2}}(f)$, $U_{\mathrm{S_0exp\#3}}(f)$, $U_{\mathrm{S_0exp\#4}}(f)$), employing the procedure described in section 2.3. In order to estimate the excitability functions, it was presumed, that the particle velocity is concentrated at the edges of each element. The example of the spatial particle velocity distribution in case four elements are excited at once (experiment #4) is presented in Fig. 2.5.2. The particle velocity distributions for other experiments were defined in the similar fashion, depending on how many elements were fired at the same time. In order to describe the phase velocities of the guided waves, the following material properties of an aluminium sample were defined: the Young's modulus: 72 GPa, the Poisson's ratio: 0.35, the density: 2,780 kg/m^3. In total, four excitability functions (referred as $H_{\mathrm{S_0\#1}}(f_k)$, $\mathrm{H}_{\mathrm{S_0\#2}}(f_k)$, $\mathrm{H}_{\mathrm{S_0\#3}}(f_k)$, $H_{\mathrm{S_0\#4}}(f_k)$) were estimated for each of the experiment.

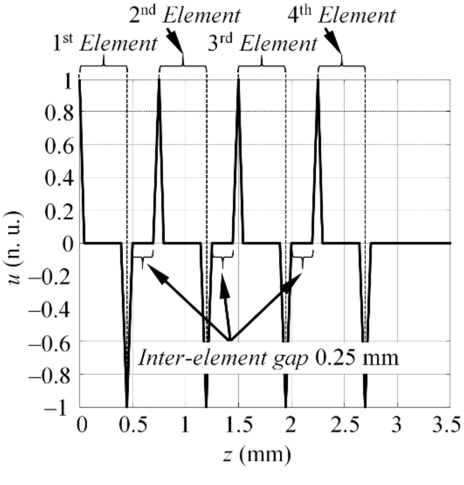

Fig. 2.5.2. The particle velocity distribution, which presumably excites the S_0 mode in case the four array elements are fired at the same time

The frequency spectrum ($U_{\mathrm{S_0exp\#1}}(f)$) and the excitability function ($H_{\mathrm{S_0\#1}}(f_k)$) of the S_0 mode in case one single element is fired (experiment #1) can be seen in Fig. 2.5.3a. The results show, that there is no zero harmonics in the spectrum of S_0 mode, which are caused by the type of excitation or the size of source if only one array element is fired. The results for experiment #2 can be seen in Fig. 2.5.3b. In the latter picture, the solid line represents the spectrum of S_0 mode ($U_{\mathrm{S_0exp\#2}}(f)$) in case two elements are fired at the same time. The excitability function ($H_{\mathrm{S_0\#2}}(f_k)$) is plotted in the dash-dot line, meanwhile the round-dot line is the product of: $U_{\mathrm{S_0exp\#1}}(f)$ and $H_{\mathrm{S_0\#2}}(f_k)$. The results for experiment #3 and experiment #4 are presented in a similar fashion, where the dotted line represents: $U_{S_0\text{exp}\#1}(f)\cdot H_{S_0\#3}(f_k)$ and $U_{S_0\text{exp}\#1}(f)\cdot H_{S_0\#4}(f_k)$ respectively. The results in Fig. 2.5.3b–d demonstrate the influence of the source size to the frequency response of the S_0 mode. It can be observed that the amount of zero values in the excitability function is related to the width of source.

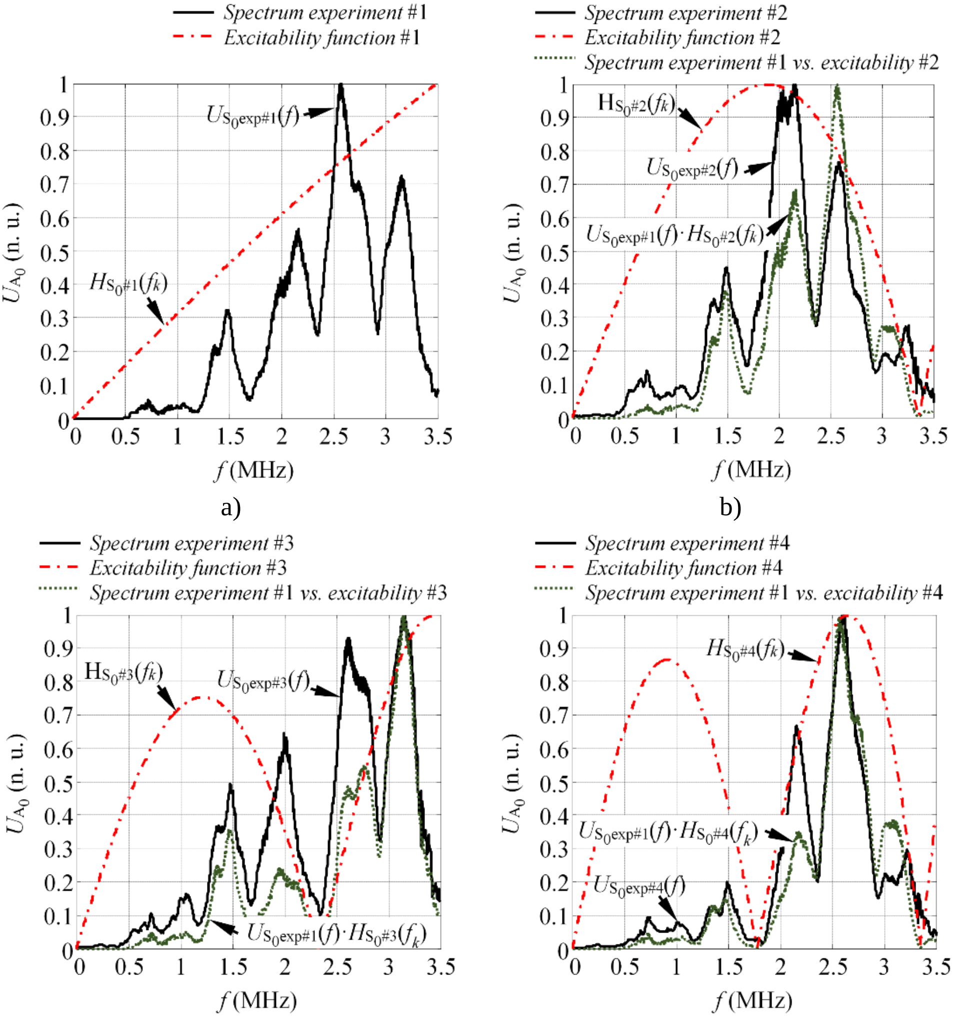

a) b) c) d)

Fig. 2.5.3. The influence of the source size to the frequency spectrum of S_0 mode on the 0.5 mm aluminium sample in case the active aperture is: 0.5 mm (experiment #1) (a), 1.25 mm (experiment #2) (b), 2 mm (experiment #3) (c) and 2.75 mm (experiment #4) (d)

2.6 Conclusions of Chapter 2

1. The source influence on the frequency response of guided waves was demonstrated and explained. It was shown with the numerical simulations and the experiments that the frequency response of each guided wave mode is a product of the spectrum of excitation pulse and the excitability function,

which itself depends on the type of excitation, material properties and size of source.

2. The novel excitability function estimation technique based on Fourier analysis of particle velocity distribution on the excitation area was proposed, which enables the response amplitude as a function of frequency separately for each GW mode to be estimated. The performance of the proposed technique was demonstrated for the fundamental A_0 and S_0 modes only, however the method itself can be used to predict the excitability functions of other modes as well.
3. The proposed technique can be applied to predict the frequency response of GW mode on any type of material (either isotropic structures, or multi-layered anisotropic composites) and under any type of excitation if the phase velocity dispersion curve and the particle velocity distribution of the wave source is known initially. The technique developed in this study can be further used as a tool to explain and predict differences in frequency bandwidths of each guided wave mode, which are excited using the same transducer. As the consequence, such tool may be beneficial in developing the high accuracy methods for guided wave signal analysis and mode decomposition.
4. The proposed excitability function estimation technique was validated with the appropriate numerical simulations and experiments on the GFRP and aluminium samples. The numerical and experimental results showed a good agreement with the theoretical predictions. It was proved that the excitability function is related to the wavelength of the guided wave, therefore the A_0 mode always has more frequency zones with amplitudes close to zero at the same frequency band compared to the S_0 mode.

3. ANALYTICAL MODEL FOR THE ANALYSIS OF THE GUIDED WAVE PROPAGATION IN THE OBJECTS WITH BOUNDARIES

3.1 The idea and concept of the proposed model

One of the major issues complicating the defect detection in SHM systems is distinguishing the wave propagation within the structure from the influence caused by damage or other sources. As the damage may produce unique wave propagation phenomenon, understanding wave propagation in a defect-free structure is of vital importance for the further signal processing and decision making. However, the GW signals even in the defect-free structures possess multimodal, dispersive and interferential behaviour, thus it is very easy to obtain the result similar to that presented in Chapter 1.1, Fig. 1.1.5. To be able to analyse and interpret such kind of data it is essential to know at least the arrival times and propagation paths of all possible modes that actually exist in the structure. Therefore, the analytical model was developed in this research with the general purpose of making the analysis of such complicated GW signals easier and faster compared to the existing solutions. The principal requirement for the model is to at least provide the rough values of the ToF and the map of propagation paths for separate GW mode packets, depending on the positions of virtual transmitters-receivers and bearing in mind the reflections from the object boundaries. Then by comparison of the experimental and the simulated data, possible GW modes can be identified according to the calculated ToF's. Meanwhile the wavepath analysis may indicate the positions of the likely defects since the presence of the damage usually can be observed by monitoring the changes of the waveform at specific time segments.

The model proposed in this study is based on the idea that instead of simulation of entire wave propagation, the positions of the wavefronts at discrete time instances are calculated only, according to the group velocity of the GW in the considered structure. In such a way, the transportation of the wave energy is considered, as it is assumed to be satisfactory to fulfil the principal requirement and makes the entire calculation routine significantly faster. The concept of the model is illustrated in Fig. 3.1.1.

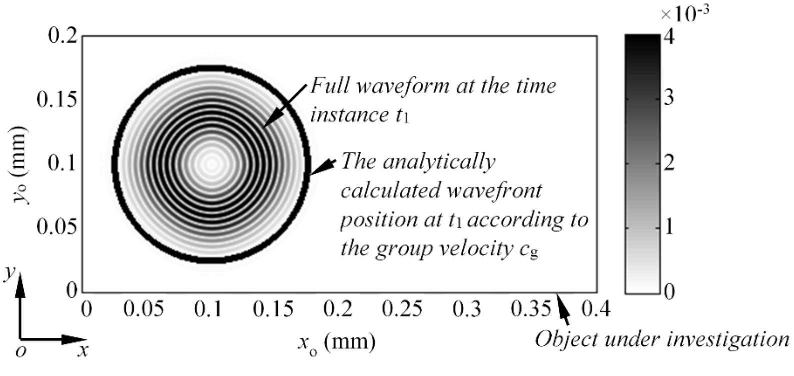

Fig. 3.1.1. The general idea of the proposed model: calculation of the wavefront positions at distinct time instances only (black solid line circle) instead of complete simulation of the wave propagation

In the remaining part of this section, the principle of the proposed model will be briefly revealed. The whole process of the calculation can be divided into the three main stages: ***pre-processing***, ***solution*** and ***post-processing***. This division was introduced for the sake of the process being clearer. In the stage of the ***pre-processing***, the object, material and virtual transducers have to be defined. The object under investigation is always assumed to be a flat, uniform thickness, rectangular 2D plate, with the bottom left corner positioned at the origin of the coordinate system (see Fig. 3.1.2). The size of the plate is defined by the length x_o and the width y_o. The model can be used to simulate the wave propagation on any type of material, which is characterized providing either the phase velocity dispersion curve, or both the dispersion curve and the directional dependence of the group velocity (*slowness profile*). Such directional and dispersive wave relationships themselves contain the information about the stiffness of the material. The required amount of input information about the material depends on the task which is being solved.

For the isotropic wave propagation, it is required to provide the dispersion curve of the phase velocity only, as the wave velocity is uniform in all directions and the slowness can be calculated using the well-known phase and group velocity relationship (see eq. 1.1.15 in Chapter 1.1). On the other hand, the anisotropic wave propagation possesses directional dependence of the wave velocity, so in general it may be required to know the dispersion curve of the phase velocity for each wave propagation angle. For the sake of simplicity, in case of anisotropic wave propagation, the proposed model requires the slowness profile $c_g(f_c, \alpha_m)$ at the central frequency of the excitation signal f_c and the dispersion curve of the phase velocity $c_p(f_{tr},\alpha_m)$ at 0° within the bandwidth of the excitation signal f_{tr}. Then the phase velocity dispersion curves for the rest of the angles are automatically generated using the provided slowness profile in corporation with the known phase and group velocity relationships.

The proposed model assumes that the wave front is generated from a single point within the object, which is described by the central coordinates (x_e,y_e), directivity pattern $D_e(\alpha_e)$ and excitability function $H(f,u,l)$. In general, the Lamb waves are usually generated at frequencies up to 250 kHz, possessing relatively large wavelengths (tens of millimetres and more). This means that in most cases the transmitters can be assumed as omnidirectional point sources (if the circumference of the source $2\pi a$ is less than one-half wavelength: $2\pi a/\lambda<0.5$, where a – is the radius of the source (245)). On the other hand, the introduction of the directivity patterns $D_e(\alpha_e)$ and the excitability function $H(f,u,l)$ additionally enables the excitation of the GW to be simulated by directional transmitters with a certain size and type of operation as well. This might be beneficial for higher frequency applications (i.e. when $2\pi a/\lambda>3$). The directivity pattern can be defined either by the trigonometrical or other mathematical function, which represents the wave energy as a function of angle α. The receivers in the proposed model are described by their central coordinates (x_r,y_r), orientation angle α_r, the directivity pattern $D_r(\alpha_r)$, the length l_1 and the width l_2. It was decided to include the length l_1 and the width l_2 of the receiver to implement the wavefront reception, which will be described later in this chapter. In general, the analytical model can contain an unlimited number of virtual transmitters and receivers, however the calculations are performed in series for one transmitter-receiver pair at the time. The summarized initial input information required to describe the object, transmitter and receiver in the proposed model is illustrated in Fig. 3.1.2.

The ***solution*** part of the proposed model itself consists of the four main stages: 1) calculation of the wavefront positions at different time instances; 2) estimation of the reflections from the object boundaries; 3) implementation of the wavefront "reception"; 4) prediction of the expected output waveform captured with the virtual receiver. In the following paragraphs each stage of the solution part will be briefly described.

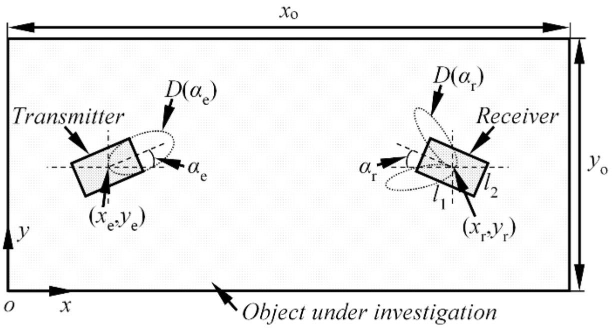

Fig. 3.1.2. The initial information required for the analytical model to describe the object, the transmitter and the receiver

Calculation of the wavefront positions at different time instances. The proposed model assumes that the wave is generated at the single point within the object and propagates in all directions. The pattern of the wavefront depends on the type of the considered material. The position of the wavefront at a discrete time instance can be described as a set of nodal points each defined by the coordinates (x_f,y_f) and the angle between the subsequent nodes $\Delta\alpha$. Mathematically the coordinates of the wavefront position (x_f,y_f) at the time instance t_k can be expressed by the following equations:

$$x_f(t_k,\alpha_m)=c_g(f_c,\alpha_m)\cdot t_k\cdot\cos(\alpha_m)+x_e, \tag{3.1.1}$$

$$y_f(t_k,\alpha_m)=c_g(f_c,\alpha_m)\cdot t_k\cdot\sin(\alpha_m)+y_e, \tag{3.1.2}$$

$$t_k=(k-1)\cdot\Delta t+t_p,\ k=1\div K,\ K=\frac{t_g-t_p}{\Delta t}+1, \tag{3.1.3}$$

$$\alpha_m=(m-1)\cdot\Delta\alpha,\ m=1\div M,\ M=\frac{2\pi}{\Delta\alpha}+1, \tag{3.1.4}$$

where $c_g(f_c,\alpha_m)$ is the slowness profile of the group velocity of the analysed mode in the considered structure; t_k is the discrete time instance at which wavefront position is being calculated; Δt is the step in time domain; t_p and t_g are the time instances, which denote the start and end of the calculation (t_p is equal to zero by default); α_m is the array of the wave front nodal angles; $\Delta\alpha$ is the angle between the subsequent wavefront nodes; x_e and y_e are the central coordinates of the transmitting point within the object.

The example of the calculated wavefront position at two distinct time instances t_1 = 28.5 µs and t_2 = 39.5 µs are illustrated in Fig. 3.1.3a and Fig. 3.1.3b. The calculation example is presented for the isotropic aluminium sample with dimensions of 400 mm × 200 mm. The value of the group velocity $c_g(f_c,\alpha_m)$ was set to 1,769 m/s, which corresponds to the group velocity of the A_0 mode on 1 mm thickness Al alloy 2024-T6 plate (the density: ρ = 2,780 kg/m^3, the Young's modulus: E = 72 GPa, the Poisson's ratio: υ = 0.35 (246)) at 100 kHz frequency. For the sake of better understanding, the background of Fig. 3.1.3a,b illustrates the solution of the same problem, obtained using the commercially available FE code. Such merging of the proposed and FE solutions has been presented to prove the adequacy of the developed model to the real world situations. Otherwise the FE code is not necessary for the model to work properly.

Estimation of the reflections from the object boundaries. When the wavefront propagates at least to one of the object boundaries, the coordinates of the nodal points that appear to be outside the object are mirrored with respect to the particular boundary in order to simulate the wave propagation in the opposite direction (see Fig. 3.1.3c). In general, the model allows the reflection from the boundaries possessing different geometries to be calculated, however for simplification purposes in this case it is assumed that the object under investigation is a four-sided shape that is made up of two pairs of parallel lines and that has four right angles of 90°. In such case the reflections from the object boundaries can be estimated as:

$$x_{\mathrm{f},m}(t_k) = \left|x_{\mathrm{f},m}(t_k)\right|, \forall m, x_{\mathrm{f},m}(t_k) < 0, \tag{3.1.5}$$

$$x_{\mathrm{f},m}(t_k) = x_\mathrm{o} - \left(x_{\mathrm{f},m}(t_k) - x_\mathrm{o}\right), \forall m, x_{\mathrm{f},m}(t_k) > x_\mathrm{o}, \tag{3.1.6}$$

$$y_{\mathrm{f},m}(t_k) = \left|y_{\mathrm{f},m}(t_k)\right|, \forall m, y_{\mathrm{f},m}(t_k) < 0, \tag{3.1.7}$$

$$y_{\mathrm{f},m}(t_k) = y_\mathrm{o} - \left(y_{\mathrm{f},m}(t_k) - y_\mathrm{o}\right), \forall m, y_{\mathrm{f},m}(t_k) > y_\mathrm{o}, \tag{3.1.8}$$

where $x_{\mathrm{f},m}(t_k)$ and $y_{\mathrm{f},m}(t_k)$ are the nodal points of the wavefront, which appear to be outside of the simulated object; t_k is the discrete time instance at which wavefront position is being calculated; x_o and y_o are the length and the width of the object under analysis. At this point, the wave reflection coefficient can be introduced in eq. 3.1.5–3.1.7, based on the surrounding medium of the sample. However, as the analysis of the wave amplitudes and their interference is not the primary task of the developed model, the reflection coefficients are excluded in the equations above. The principle of the estimation of wavefront reflection is illustrated in Fig. 3.1.3c. These results are again merged with the FE calculations on the same Al alloy 2024-T6 sample as in the previous case.

Implementation of the wavefront "reception". At the reception side the proposed model assumes that the virtual receiver is positioned somewhere within the object, at the coordinates $(x_\mathrm{r},y_\mathrm{r})$. It has the pre-described length l_1 and width l_2. In case the nodal points of the wavefront crosses the area of the virtual receiver L ($L = l_1 \cdot l_2$), the time instances t_{k_j} and the integral arbitrary amplitude values $A_\mathrm{e}(t_{k_j})$ are saved to an array $h_0(t)$. The arbitrary amplitude $A_\mathrm{e}(t_{k_j})$ represents the integral amplitude value of the wavefront received at the time instance t_{k_j}. It depends on the directivity pattern of the transmitter-receiver ($D_e(\alpha_e)$, $D_r(\alpha_r)$) and the amount of nodal points which appear to be within the area of the receiver at the particular time t_{k_j}. Thus, the array $h_0(t)$ can be mathematically expressed as a set of arbitrary amplitude values $A_e(t_{k_j})$ at distinct time instances t_{k_j}:

$$h_0(t) = \{A_e(t_{k_j}), \ldots, A_e(t_{k_N})\}, \tag{3.1.9}$$

where $j = 1,\ldots,N$ denotes the time instances, at which the wavefront is assumed to be captured by the virtual sensor ($k \leq j \leq K$). Using the wavefront reception approach described above, the arbitrary amplitude $A_e(t_{k_j})$ depends not only on the diffraction of the wave, but partially on the dimensions of the virtual receiver as well. However, this approach is assumed to be satisfactory if the ToF analysis is the main goal of the proposed model. The principle of the wavefront reception is illustrated in Fig. 3.1.3d.

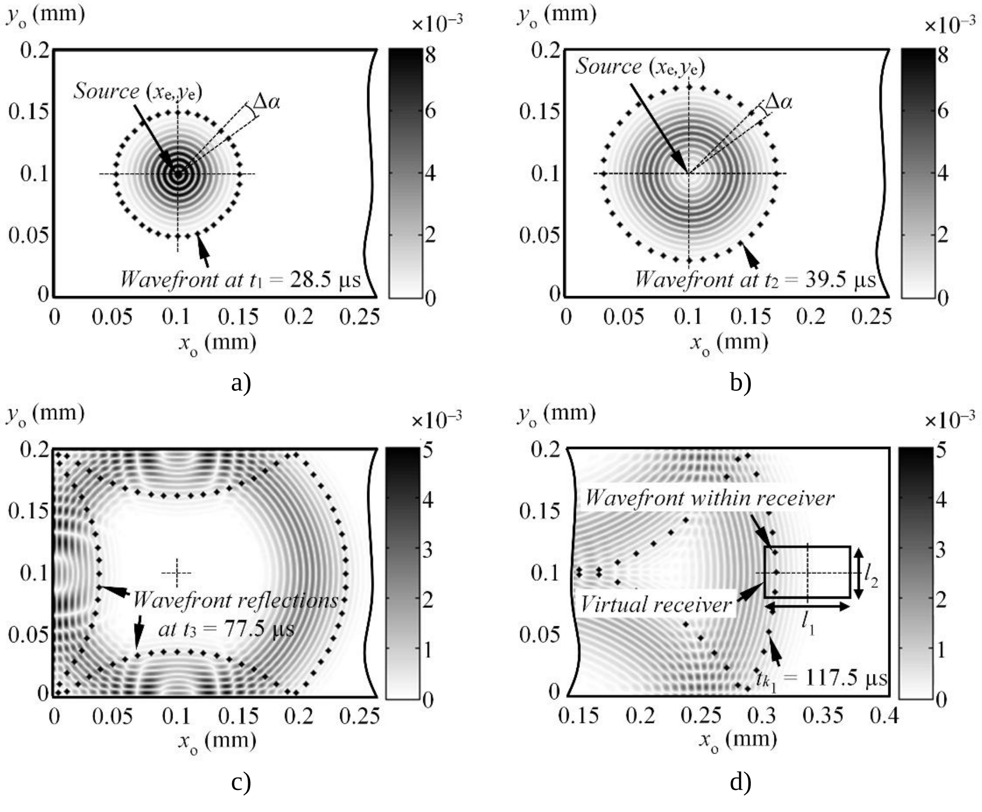

a) b)

c) d)

Fig. 3.1.3. A basic operational principle of the proposed model: calculated wavefront positions at different time instances t_1 = 28.5 μs and t_2 = 39.5 μs before the wavefront reflection (a,b); the illustration of the wavefront position at t_3 = 77.5 μs after reflection from the object boundaries (c), the implementation of wavefront “reception” with virtual sensor at t_{k_1} = 117.5 μs (d)

Prediction of the expected output waveform captured with the virtual receiver. In order to predict the waveform of a signal, passing through the medium, the impulse response of the system is required. For a non-dispersive wave propagation, the function $h_0(t)$ can be used to describe a system impulse response, since it contains the information about the wave arrival times and amplitudes under relatively wideband excitation. For the dispersive wave propagation, the impulse response can be expressed as the inverse Fourier transform of the frequency response of the system $H(\omega)$, which itself can be written as (247):

$$H(\omega)=A(\omega)e^{-j\theta(\omega)x}=e^{-\alpha(\omega)x}e^{\frac{-jx\omega}{c_{\mathrm{p}}(\omega)}}, \tag{3.1.10}$$

where $H(\omega)$ is the frequency response; $A(\omega)$ is the magnitude function; $\theta(\omega)$ is the phase angle per unit distance; $\alpha(\omega)$ is the attenuation function; $c_{\mathrm{p}}(\omega)$ is the phase velocity; x is the propagation distance. Once the wavefront propagation times t_{k_j} are known, the propagation distances x_{k_j} used in eq. 3.1.10 can be calculated using simple relation $x_{k_j} = t_{k_j} \cdot c_{\mathrm{g}}(f_{\mathrm{c}}, \alpha_{\mathrm{m}})$, where $c_{\mathrm{g}}(f_{\mathrm{c}}, \alpha_{\mathrm{m}})$ is the group velocity of the GW at central frequency f_{c} and the corresponding wavefront reception angle α_{m}. The variable $c_{\mathrm{p}}(\omega)$ in eq. 3.1.10 ($c_{\mathrm{p}}(\omega) = c_{\mathrm{p}}(f_{\mathrm{tr}},\alpha_{\mathrm{m}})$) denotes the dispersion curve of the phase velocity, which is related to the group velocity $c_{\mathrm{g}}(\omega)$ by eq. 1.1.15, presented in Chapter 1. Then the output signal $u_{k_j}(t_{k_j})$ for the particular received wavefront in the case of linear system can be calculated as a convolution of the input signal $u_{\mathrm{ref}}(t)$ and the systems impulse response. In case of non-dispersive and dispersive wave propagation, the output signal can be expressed using the following equations:

$$u_{k_j}\left(t_{k_j}\right)_{\mathrm{nd}} = u_{\mathrm{ref}}(t) \otimes h_0(t), \tag{3.1.11}$$

$$u_{k_j}\left(t_{k_j}\right)_{\mathrm{d}} = u_{\mathrm{ref}}(t) \otimes \mathrm{IFFT}\left|H_{k_j}(\omega)\right|, \tag{3.1.12}$$

where $\otimes$ denotes the convolution, which is an integral that expresses the amount of overlap between the two functions as one is shifted over another; IFFT defines the inverse Fourier transform; subscripts “nd” and “d” denotes the non-dispersive and dispersive wave propagation. Taking into account the values of an arbitrary amplitudes $A_{\mathrm{e}}(t_{k_j})$, the final output signal of the virtual receiver can be constructed as:

$$u_{\mathrm{r}}(t) = \sum_{k_j} u_{k_j}\left(t_{k_j}\right) \cdot A_e\left(t_{k_j}\right). \tag{3.1.13}$$

Using the abovementioned expressions, the proposed model enables the output of the virtual receiver to be predicted for different kind of structures, depending on the amount of dispersion, dimensions of an object and parameters of the virtual transducers. If filtering due to the size and the type of operation of the transmitter is taken into the account, the Fourier spectra of an input signal FFT($u_{\mathrm{ref}}(t)$) is multiplied by the excitability function $H(f,u,l)$ and the filtered input signal is obtained $u_{\mathrm{ref}}(t)$ employing the inverse Fourier transform. At the end of the solution stage, all the necessary data is saved to an array **M**, which contains the wavefront positions at each time instance and the corresponding angles of the wavefront nodal points α_m:

$$\mathbf{M} = \left[t_k, \mathbf{X}_{\mathrm{f}}(t_k, \alpha_m), \mathbf{Y}_{\mathrm{f}}(t_k, \alpha_m), \alpha_m\right], \tag{3.1.14}$$

where $\mathbf{X}_f(t_k,\alpha_m)$ and $\mathbf{Y}_f(t_k,\alpha_m)$ are the wavefront position matrices. Such approach enables the results of the solution to be analysed by different means, without repeating the calculation routine over and over.

At the ***post-processing*** stage of the proposed model, the ToF of the separate GW modes can be analysed once the t_{k_j} values are known from the array $h_0(t)$. Moreover, the likely output waveform of the virtual receiver $u_r(t)$ can be estimated from eq. 3.1.11 or eq. 3.1.12. Finally, since the angles of the wavefront nodal points α_m are known at each time instance t_k, the wave propagation paths at specific time intervals can be reconstructed. To sum up the main features of the proposed model can be outlined as follows:

- analysis of the ToF of the separate particular mode;
- calculation the wave propagation paths at specific time intervals;
- estimation of the likely output waveform of the virtual receiver.

It may seem that some of the features mentioned above can be easily estimated using other modelling methods such as the commercially available FE. However, the key point is that the model, provided in this research, enables the ToF of each mode to be analysed separately in real time, while the FE is slow and computationally expensive especially for large structures.

The current version of the model is limited to flat and rectangular structures. On the other hand, it can be used both for multi-layered, anisotropic and isotropic materials. It is noteworthy that the proposed model is highly customizable, since various parameters can be modified by the user. Hence, it is able to represent diverse real world situations and may act as a complimentary tool for the analysis of the complicated GW data. Currently, the main limitations of the developed model rely on the assumptions that:

- the object under investigation is a four-sided shape that is made up of two pairs of parallel lines and that has four right angles of 90°;
- at the normal or the oblique incidence of the wave neither the reflection coefficients nor mode conversion is considered;
- all modes of the GW are generated with the same efficiency and the arbitrary amplitude values $A_e(t_{k_j})$ depends on the directivity of the virtual transducers only.

Most of the abovementioned limitations were deliberately included in the proposed model in order to make it faster rather than precisely accurate. Regardless of all limitations it is an open source implementation, so many improvements can still be introduced at different stages of the solution.

3.2 Validation of the model employing FE method

In this chapter, the operation of the previously described model is validated and demonstrated employing the FE method. The aim of this research is to compare the performance of both FE and analytical techniques in terms of computational time and estimation of the ToF for different modes. In order to achieve the objectives, both the FE and analytical techniques will be employed to solve the same problem of transient wave propagation in isotropic and anisotropic plate-like structures. The few paragraphs below will briefly introduce the initial set-ups of FE and analytical models followed by the comparison of their performance. In this study, a propagation of the A_0 mode on an isotropic aluminium alloy 2024-T6 and anisotropic GFRP plates is considered.

Description of the FE model. As it was discussed in Chapter 1, the GW are the waves that require the boundary to propagate since it can be expressed as the result of interference between the longitudinal and shear waves. To obtain the correct dynamic solution of the dispersive wave propagation in 2D using the FE, the problem has to be either the plane-strain if the strain ε_z is normal to the *xy* plane and the shear strains γ_{xz}, γ_{yz} are equal to zero or the plane-stress if the normal stress σ_z and shear stresses τ_{xz}, τ_{yz} perpendicular to the *xy* plane are equal to zero (248). In other words, the plane-strain approximation assumes that the object is long in *z* direction and the loads act in the *xy* plane, so the cross-section of an object is considered only. In contrast, the plane-stress approximation assumes that the dimensions in *z* direction are small compared to the *x*, *y* dimensions, which in general means that the object is thin. In this case it was assumed that the plate is thin in *z* direction, so the problem is a plane-stress one.

To fulfil the scope of this study a 2D linear structural mechanics FE models are employed for an aluminium alloy (Al) 2024-T6 and anisotropic GFRP plates with dimensions of $x_o = 400$ mm, $y_o = 200$ mm. As the plane-stress solution requires the virtual thickness of an object, it was set equal to 1 mm for both cases. The plates in both cases were considered lossless. Throughout the simulations, a2D structural solid plane42 finite elements were used, which has four nodes each with two degrees of freedom (translations in the nodal *x* and *y* directions). The spatial size of the element was equal to 1 mm for the Al sample and 0.5 mm for the GFRP. This corresponds to the 10 and 14 nodes per wavelength respectively if the slowest A_0 mode at 100 kHz central frequency is considered. The spatial size of an element was set within the required ranges ($\lambda_{\min}/10 \leq l_e \leq \lambda_{\min}/20$) according to eq. 1.3.14 presented in Chapter 1.3.

The material properties used for the Al sample were the same as presented in the previous section 3.1. Meanwhile the properties of the GFRP plate for the 2D plane-stress problem were extracted from the stiffness matrix presented in Chapter 2. The excitation signal for both samples was a Gaussian envelope tone burst of 3 cycles and a central frequency of 100 kHz. Bandwidth of the excitation pulse at –6 dB level was equal to 53.8 kHz. The generation of the A_0 mode was performed by applying the normal out-of-plane nodal displacements at the *xy* plane. The excitation point was a single node located at the coordinates $x_e = 100$ mm, $y_e = 100$ mm. The integration step in time domain was 0.5 μs for both cases, which is 1/20 of the period at 100 kHz central frequency. The variable monitored in this study was a vertical displacement (*z*) at the surface of the specimen. For the ToF comparison a single node is selected at the coordinates $x_r = 300$ mm, $y_r = 100$ mm to represent the displacements at the location of the virtual receiver. The simulation included an implicit algorithm for solving the transient wave propagation.

Description of the analytical model. The analytical models used in this study were also described as a 2D rectangular Al and GFRP plates defined at the *xy* plane with dimensions of $x_o = 400$ mm, $y_o = 200$ mm. The material properties of an isotropic aluminium sample were defined by introducing the dispersion curve of the phase velocity $c_p(f_{tr},\alpha_m)$. Meanwhile, both slowness profile of the group velocity $c_g(f_c, \alpha_m)$ and the dispersion curve of the phase velocity $c_p(f_{tr},\alpha_m)$ at 0° angle were defined to describe the anisotropic structure of the GFRP. Since the propagation of the A_0 mode is considered in this study, the dispersion curves and slowness profiles were defined in each structure for A_0 mode only (see Fig. 3.2.1). The complete sketch of the model used in this study is presented in Fig. 3.2.2.

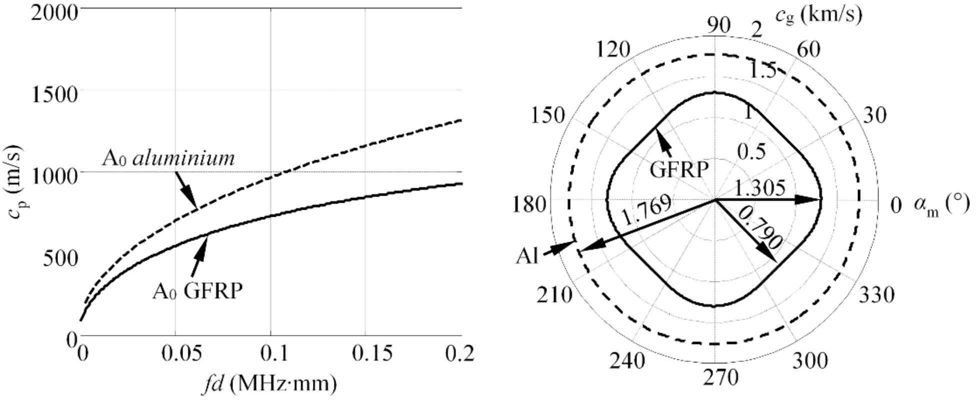

a) b)

Fig. 3.2.1. The phase velocity dispersion curves for A_0 mode in a traction-free aluminium and GFRP plates with a thickness of 1 mm at an angle α_m=0° (a), the slowness profile of the group velocity for A_0 mode propagating on aluminium (dashed line) and GFRP (solid line) samples (b)

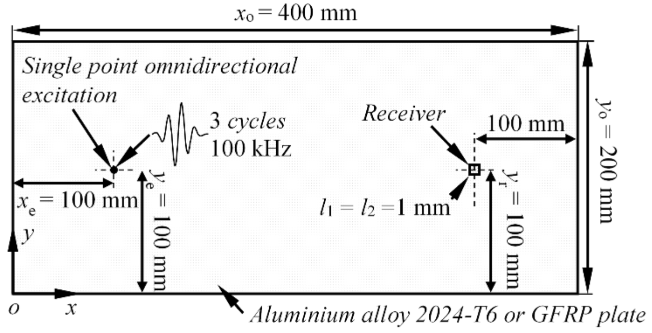

Fig. 3.2.2. The sketch of the model examined in this study with some initial input details

The wavefront in the analytical model was generated from one discrete point within the object, located at the same coordinates (x_e = 100 mm, y_e = 100 mm) as in the FE problem. The transmitter assumed to be an omnidirectional point source, as the dimensions of it is vanishing compared to the wavelength of the slowest A_0 mode. It was driven by the same Gaussian envelope tone burst of 3 cycles and a central frequency of 100 kHz as in the case of the FE model. Due to the assumptions made about the size and the directivity of the transmitter, no excitability function $H(f,u,l)$ was used at the transmission side. To implement the process of the wave "reception", the virtual receiver with dimensions of $l_1 = l_2 = 1$ mm was centred at the coordinates

x_r = 300 mm, y_r = 100 mm. The dimensions of the virtual receiver were set equal to the size of one element in the FE model. It was done deliberately to minimize the likely errors due to the time integration scheme used at the reception side in the analytical model. The directivity pattern of the receiver $D_r(\alpha_r)$ was neglected as well.

Comparison of the simulation results. The performance comparison of FE and analytical models is presented in this section. The purpose of it is to compare both models in terms of time delay between the estimated arrival of separate wave packets and the amount of time required for both techniques to solve the same task. In the following study, the FE model was used as a reference. The simulation results for the isotropic aluminium alloy 2024-T6 and GFRP samples are presented in Fig. 3.2.3 and Fig. 3.2.4 respectively.

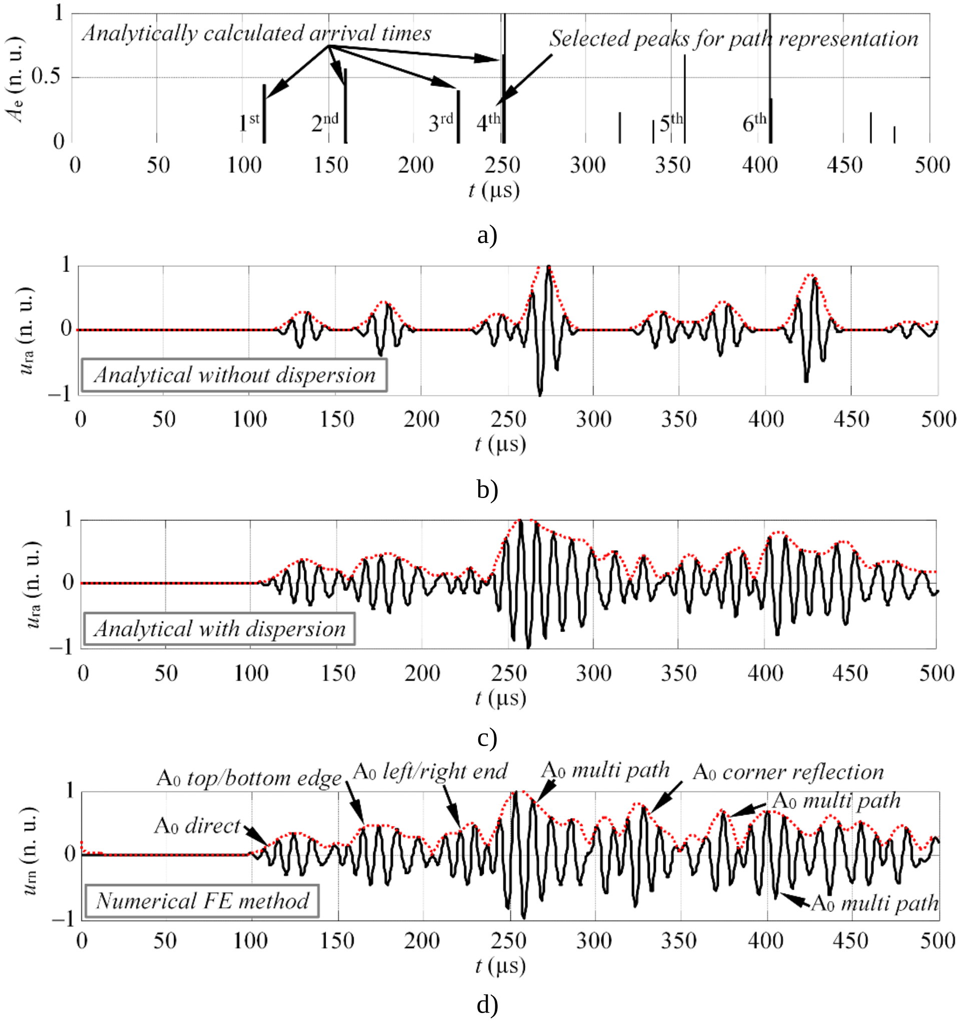

Fig. 3.2.3. The analytical and numerical calculations on the aluminium alloy 2024-T6 sample for the A_0 mode: time instances indicating the arrival of the wave packets (a), analytically predicted output of the virtual receiver for dispersion-free (b) and dispersive (c) wave propagation, the numerically calculated displacements using the FE method (d)

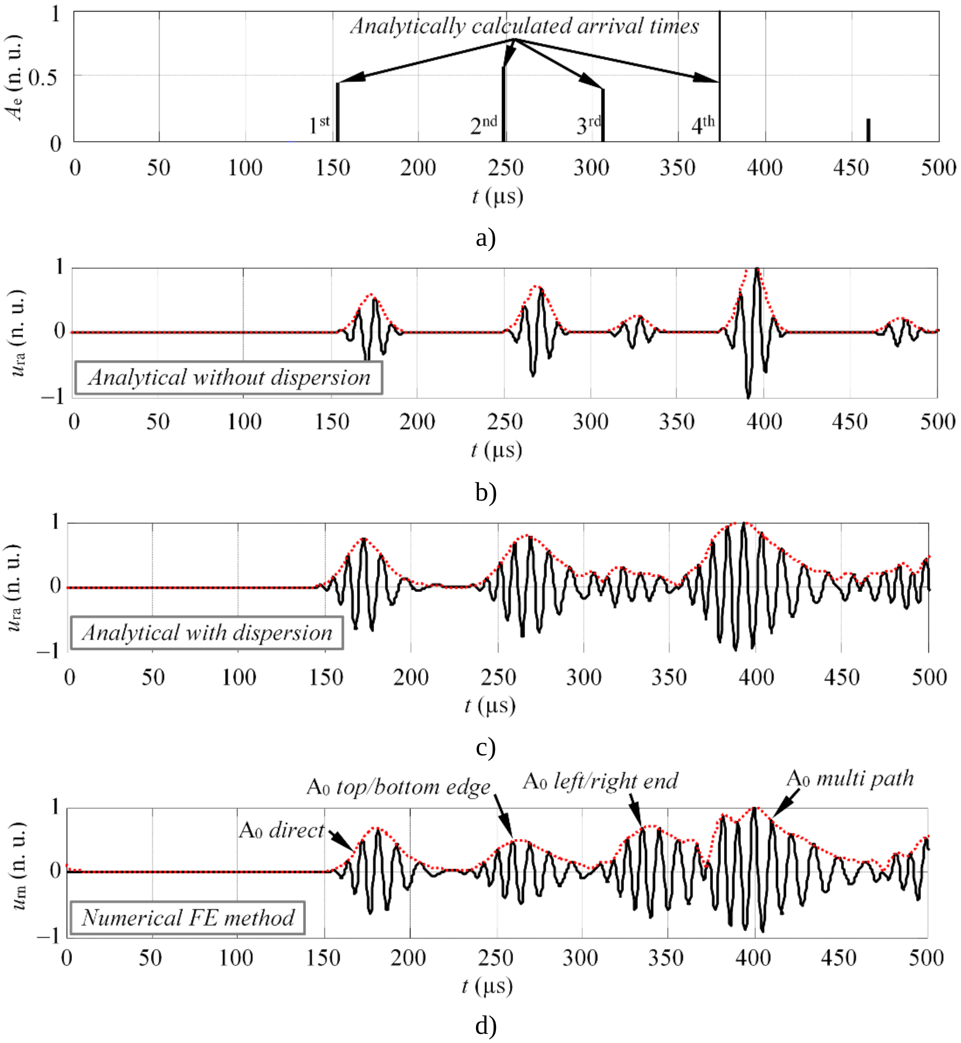

Fig. 3.2.4. The analytical and numerical calculations on the GFRP sample for the A_0 mode: time instances indicating the arrival of the wave packets (a), analytically predicted output of the virtual receiver for dispersion-free (b) and dispersive (c) wave propagation, the numerically calculated displacements using the FE method (d)

Each of the abovementioned figures (Fig. 3.2.3 and Fig. 3.2.4) consists of four subplots, where the three of them (a–c) represents the analytical calculations, meanwhile the last one is the result of the FE simulation. The first subplot in each figure (Fig. 3.2.3a, Fig. 3.2.4a) represents the analytically calculated array $h_0(t)$, which indicates the time instances t_{k_i} of the wavefront arrival and the corresponding integral arbitrary amplitude values $A_e(t_{k_i})$. The predicted outputs of the virtual receiver are presented in the second and the third subplots (Fig. 3.2.3b,c and Fig. 3.2.4b,c). The second subplot (Fig. 3.2.3b, Fig. 3.2.4b) was obtained using eq. 3.1.11, which describes the likely output of the virtual receiver in case dispersion is neglected.

Meanwhile the third subplot (Fig. 3.2.3c, Fig. 3.2.4c) is based on eq. 3.1.12, which takes into the account the dispersion of the phase velocity. The wavefront propagation paths at specific time intervals are illustrated at Fig. 3.2.5 (the selected peaks for path representation are numbered at Fig. 3.2.3a and Fig. 3.2.4a left of the appropriate bar).

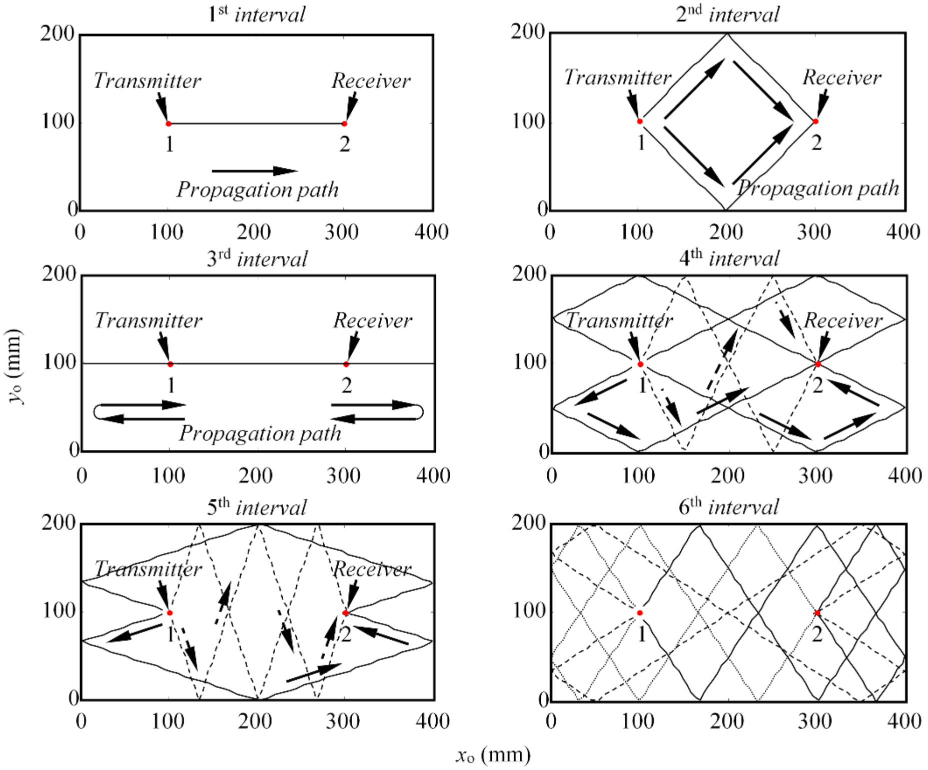

Fig. 3.2.5. The analytically calculated wave propagation paths of the A_0 mode at different time instances on the rectangular 400 mm × 200 mm sample

In order to quantitatively estimate a match between the analytical and numerical calculations, a short time cross-correlation function was used as the measure of similarity. This technique employs the comparison of two waveforms in a short time segments in which the signals can be assumed as quasi-stationary and the lag can be estimated separately for each reflection. Let’s assume that there are two waveforms $u_{\mathrm{ra}}(t)$ and $u_{\mathrm{rn}}(t)$, which describe the analytically and numerically calculated output waveforms of the virtual receiver respectively (Fig.3.2.3c, Fig.3.2.4c represents the $u_{\mathrm{ra}}(t)$, meanwhile Fig.3.2.3d, Fig.3.2.4d – $u_{\mathrm{rn}}(t)$). Then the similarity of the shape of two waveforms over time can be compared by calculating the maximum value of the normalized cross-correlation function at each window position (249):

$$x(\tau)=\frac{\sum_{t=-\Delta\tau}^{\Delta\tau} u_{\mathrm{rnw}}(t,\tau)\cdot u_{\mathrm{raw}}(t,\tau)}{\sqrt{k_1\cdot k_2}}, \tag{3.2.1}$$

$$k_1 = \sum_t u_{\mathrm{rnw}}(t,\tau)\cdot u_{\mathrm{rnw}}(t,\tau),\ k_2 = \sum_t u_{\mathrm{raw}}(t,\tau)\cdot u_{\mathrm{raw}}(t,\tau), \tag{3.2.2}$$

where $u_{\mathrm{rnw}}(t,\tau) = u_{\mathrm{rn}}(t)\cdot u_{\mathrm{w}}(t-\tau)$, $u_{\mathrm{raw}}(t,\tau) = u_{\mathrm{ra}}(t)\cdot u_{\mathrm{w}}(t-\tau)$ describes windowed waveforms obtained from numerical and analytical simulations respectively; $\tau = 0 \div (t_{\mathrm{m}}-\Delta\tau)$ is the shift of the time window; t_{m} is the total duration of the analysed signal; $\Delta\tau$ is the width of the time window; $u_{\mathrm{w}}(t)$ is the window function. This technique returns the single maximum value of the cross-correlation function at each window position, which is normalized at zero lag. In this case the width of the time window was set equal to 5 periods of the excitation signal (the duration of one cycle is 10 μs at 100 kHz). The maximum value of the cross-correlation function within the window itself represents the best similarity between the shape of two discrete time series, while its lag, relative to the centre of the window function $u_{\mathrm{w}}(t)$, indicates how much the waveforms $u_{\mathrm{ra}}(t)$ and $u_{\mathrm{rn}}(t)$ are delayed to each other. It means that the lag value can be used to estimate how precisely the arrival of the wave packets in the analytical model $u_{\mathrm{ra}}(t)$ matches with numerical calculations $u_{\mathrm{rn}}(t)$. In order to avoid the influence of noise and signals with small amplitudes, the result calculated with eq. 3.2.1 was additionally multiplied by the window function $w(t)$, which is expressed as:

$$w(t) = \begin{cases} 1 & x_{\mathrm{r}}(\tau) > 0.1\cdot\max(x_{\mathrm{r}}(\tau)) \\ 0 & x_{\mathrm{r}}(\tau) \leq 0.1\cdot\max(x_{\mathrm{r}}(\tau)) \end{cases}, \tag{3.2.3}$$

where $x_{\mathrm{r}}(\tau)$ represents the raw, unscaled short time cross-correlation. The match between the analytical and numerical calculations obtained using eq. 3.2.1 and eq. 3.2.3 is presented in Fig. 3.2.6. The left hand side of the figure represents the results for the aluminium sample, while the right hand side is devoted to the results from the GFRP sample. The results, presented in Fig. 3.2.6 indicate the four significant maximum values in each case, which in general indicates the wave packets possessing the best match (see the boxed time intervals in Fig. 3.2.6). For the aluminium sample, the good coincidence is obtained for the direct wave packet (Fig. 3.2.4: 1st interval), top/bottom reflections (Fig. 3.2.4: 2nd interval) and few multipath (Fig. 3.2.4: 4th and 5th intervals) wave packets. In addition, for the GFRP sample the good match for the left/right reflections is obtained as well.

In order to estimate the delay between the waveforms $u_{\mathrm{ra}}(t)$ and $u_{\mathrm{rn}}(t)$, the lag of the correlation maximum was measured at the positions indicating the best match. Therefore, in each case, four delay values were estimated. The time delay between the arrival times for different wave packets are summarized in Table 3.2.1. The “minus” sign in front of the delay value indicates that the analytically obtained arrival of the wave packet is delayed in respect of the numerical result. The accuracy of ToF in the proposed model depends on how precisely the slowness profile of the group velocity $c_{\mathrm{g}}(f_{\mathrm{c}}, \alpha_{\mathrm{m}})$ and the phase velocity dispersion curve $c_{\mathrm{p}}(f_{\mathrm{tr}},\alpha_{\mathrm{m}})$ is known initially. For the isotropic wave propagation, it is sufficient to know the phase velocity dispersion curve, since the slowness profile is uniform and can be calculated using the phase and group velocity relationships, presented earlier. On the other hand, for the anisotropic wave propagation, the phase velocity dispersion curve for each wave propagation angle must be known for the precise ToF estimation, which makes the solution of such problem a non-trivial one. However, the *a-priori* knowledge says that for most composites, despite of fibre orientation, the character of dispersion curve does not change much, especially at the low frequencies. The major changes are observed at the slope of the curve rather than in the shape of it. It means that if the dispersion curve of the phase velocity at 0° and the group velocities at all angles are known, the curve itself can be shifted vertically according to the phase-group velocity relationship to obtain the curve for non-zero propagation angle. Still, it is worth mentioning, that this is the assumption made in the model to reduce the amount of required input data required. Any error in defining the dispersion curve or the slowness will further introduce an error in ToF estimation.

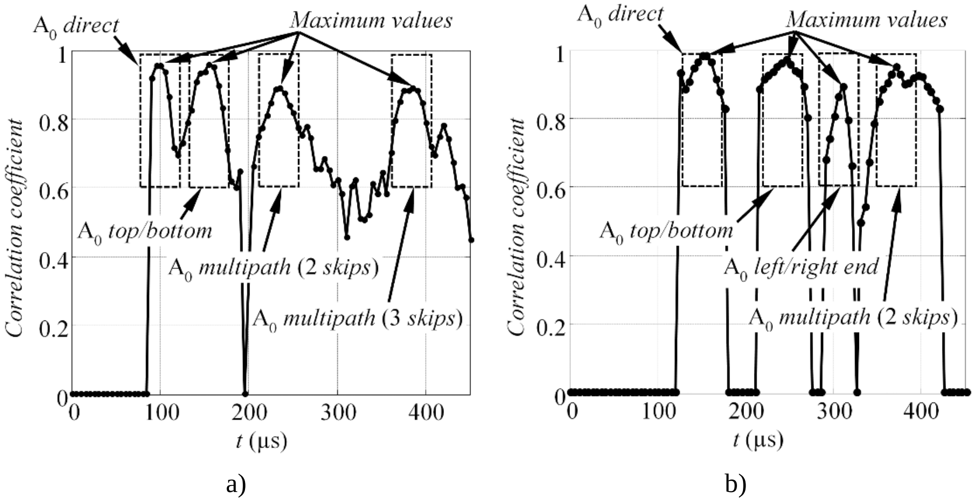

Fig. 3.2.6. The result of the short time cross-correlation between the analytical $u_{ra}(t)$ and numerical $u_{rn}(t)$ waveforms on the aluminium (a) and GFRP (b) sample

Table 3.2.1. The estimated mismatch of the wave packet arrival time between the analytical and numerical calculations for the aluminium and GFRP samples

A₀ mode, aluminium sample				**A₀ mode, GFRP sample**			
Wave packet	*Correlation coefficient*	*Window position,* (μs)	*Time delay,* (μs)	*Wave packet*	*Correlation coefficient*	*Window position,* (μs)	*Time delay,* (μs)
Direct	0.95	100.5	–6.5	Direct	0.97	155.5	8
Top/bottom	0.95	155.5	–3	Top/bottom	0.96	245.5	–6
Multipath (2 skips)	0.88	235.5	–9.5	Left/right end	0.89	310.5	10.5
Multipath (3 skips)	0.88	385.5	–8.5	Multipath (2 skips)	0.94	370.5	5

Finally, the performance of both analytical and FE approaches is compared in terms of the solution time. The FE solution was implemented using the ANSYS® implicit software (version 12.0), while for the analytical calculations the Matlab® environment (version 2013a, 8.1.0.604) was used. In all cases calculations were performed using the Intel® core i7-2700K computer with 32GB of random access memory. The time required for the solution was measured from the moment the problem is submitted to the complete return of the result. The study demonstrated that the numerical FE solution of the transient wave propagation in the aluminium sample takes roughly 27 minutes to complete. Meanwhile for the anisotropic GFRP plate 98 min are required to finish the task. Obviously, such solution time estimation is very rough. Moreover, the solution time of the FE method strongly relies on the density of the mesh, which is related to the type of problem and physical properties of the material. In contrast, the duration of the analytical solution is invariant to the type of the material. Hence, the result can be expected roughly in 10 seconds in either case, which is a tremendous improvement in terms of the solution time.

3.3 Experimental verification on the anisotropic GFRP plate

In this section, the ability of the analytical model to predict the propagation of the Lamb waves is experimentally verified. For this purpose, the experimental waveforms are compared to the analytically calculated in-plane and out-of-plane displacements of the A_0 and S_0 modes. The experiments have been carried out in a pitch-catch configuration on the 6-ply GFRP plate [biaxial: 0° and 90° / bias: ±45° / biaxial: 0° and 90°]$_S$ with dimensions x_o = 2,000 mm, y_o = 1,000 mm and 4 mm thickness (see Fig. 3.3.1).

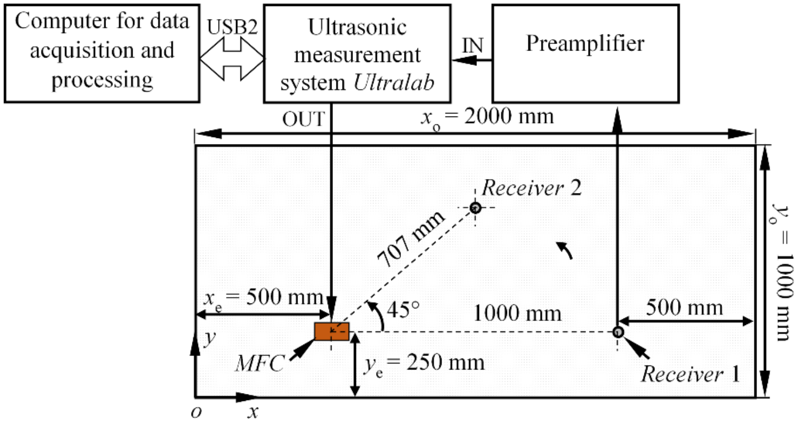

Fig. 3.3.1. The schematic diagram of the experiments for validation of the analytical model

The Lamb waves were generated using the MFC transducer centred at the coordinates x_e = 500 mm, y_e = 250 mm. It was bonded to the surface of the specimen using a thin layer of gasket maker. The emitter was excited by a 3 cycle square pulse with a central frequency of 50 kHz. According to the dispersion relationship, at this region the fundamental A_0 and S_0 modes exist in the structure. During the experiments two independent measurements were taken at different receiver positions. In the first measurement, the receiver was positioned along the wavepath in front of the transmitter at the coordinates x_r = 1,500 mm, y_r = 250 mm. The actuator-sensor distance was fixed to 1,000 mm. In the further experiment the same receiver was rotated by 45° counter clockwise and centred at the coordinates x_r = 1,000 mm, y_r = 750 mm. According to the Pythagorean theorem in this case the actuator-sensor distance was equal to 707 mm. The transmitter itself remained unmoved during both measurements. For the reception of the GW the round shape thickness mode receiver with a contact area of 10 mm and central frequency of 240 kHz was used (bandwidth of the transducer at –6 dB level is 340 kHz). To ensure better signal to noise ratio averaging by 8 times was used. The experiments were performed using the low frequency ultrasonic measurement system "*Ultralab*". The set-up of experiments is presented in Fig. 3.3.1.

The parameters of the analytical model were set to correspond to the experimental set-up. The dispersion curves of the phase velocity $c_p(f_{tr},\alpha_m)$ for the A_0 and S_0 modes at $\alpha_m = 0°$ and $\alpha_m = 45°$ propagation angles are presented in Fig. 3.3.2a. Meanwhile the slowness profiles $c_g(f_c, \alpha_m)$ for each mode can be observed from Fig. 3.3.2b. The directivity pattern of the MFC transmitter was estimated according to the *a-priori* knowledge and described by the following equation:

$$D_e(\alpha_e) = \left| \sin\left(\frac{\alpha_m + \pi}{2}\right)^{1.7} \right|. \tag{3.3.1}$$

Since the contact area of the receiver is comparable to the wavelength of the slowest A_0 mode, the omnidirectional directivity was used at the reception side. The comparison of the simulation and experimental data is presented in Fig. 3.3.3 for the 1st measurement and in Fig. 3.3.3 for the 2nd measurement. The results in Fig. 3.3.3 indicate that at the time range up to 740 μs the wave packets of S_0 mode can be observed only. The two wave packets of A_0 mode arrives approximately at 755 μs and 868 μs. Therefore, it is partly overlapped and distorted by the multipath reflections of the S_0 mode arriving at 743 μs and 842 μs. In the case of the second measurement (Fig. 3.3.4), the wave packet of the A_0 mode at 534 μs is overlapped with multipath reflection of S_0 mode, therefore it is barely observable in experiment.

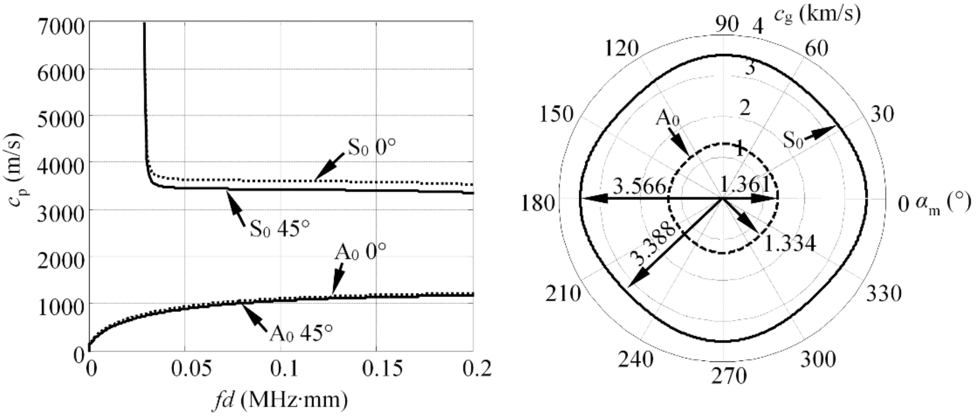

a) b)

Fig. 3.3.2. The phase velocity dispersion curves for A_0 and S_0 modes in GFRP plate at 0° and 45° wave propagation angle (a), the slowness profile of the group velocity for A_0 (dashed line) and S_0 (solid line) modes in the same structure (b)

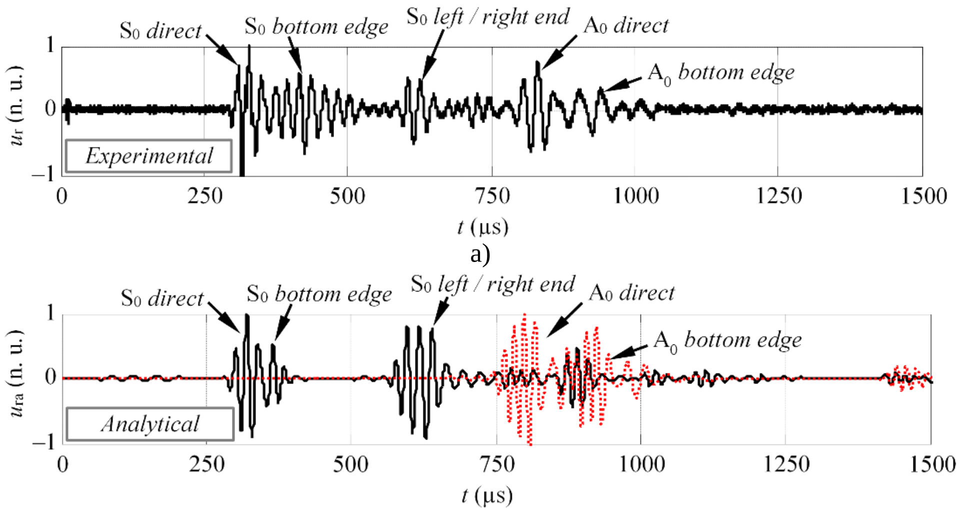

a)

b)

Fig. 3.3.3. The experimental waveform (a) versus the analytical prediction (b) on GFRP plate in case the receiver is positioned at $x_r = 1{,}500$ mm, $y_r = 250$ mm (corresponds to 0° wave propagation)

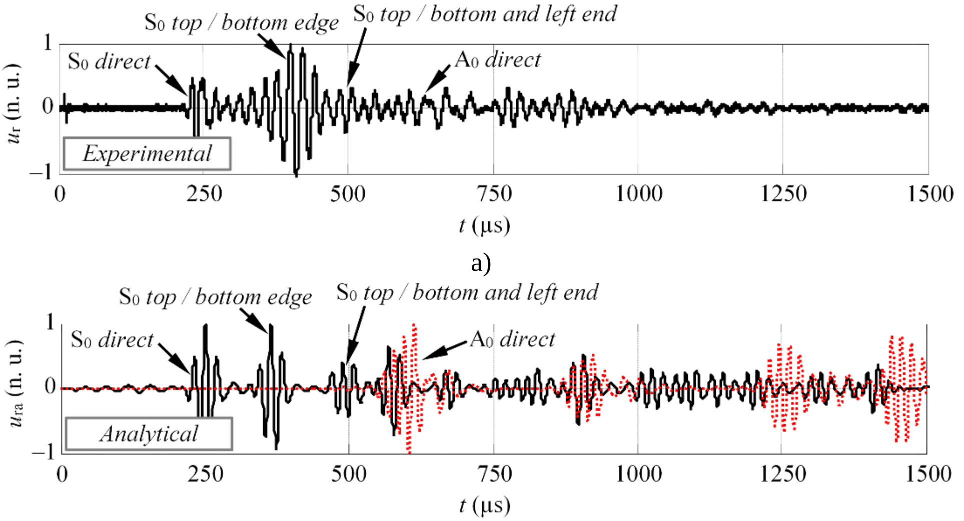

a)

b)

Fig. 3.3.4. The experimental waveform (a) versus the analytical prediction (b) on GFRP plate in case the receiver is positioned at $x_r = 1{,}500$ mm, $y_r = 250$ mm (corresponds to 45° wave propagation)

3.4 Conclusions of Chapter 3

1. The analytical model, which enables the better understanding, analysis and interpretation of the propagation of GW in plate-like structures has been developed. The proposed model allows the propagation of separate GW

mode packets in flat, rectangular structures with uniform thickness to be analysed, to calculate the arrival times of the wave packets after multiple reflections at a virtual receiver positioned anywhere on the object and to retrace the wave propagation paths at specific time intervals.

2. The proposed model was validated with the appropriate numerical simulations and experimental tests. The numerical and experimental results showed a good agreement with the analytical calculations both in isotropic aluminium and anisotropic GFRP samples. Also, the short time cross-correlation was employed to measure the match. The results demonstrated, that a good coincidence is obtained equally in terms of shape of the waveform and arrival times of wave packets after multiple reflections.
3. Some results in the research indicated that the major factor influencing the reliability of the analytical predictions is the initial knowledge of the wave velocity. In the perfect case scenario, the dispersion curves at each wave propagation angle would be beneficial for the model to work precisely. However, it was demonstrated that the slowness profile of the group velocity and the dispersion curve at 0° wave propagation angle may be sufficient to get the desired confidence of the model.
4. Compared to conventional FE model, the main advantage of the analytical technique is to significantly reduce the amount of time required to solve the transient wave propagation problem. Thus, it can be used as a real time tool.

4. GUIDED WAVE MODE IDENTIFICATION BASED ON PHASE VELOCITY ESTIMATION

4.1 Motivation and idea of the method for phase velocity estimation

The analytical model presented in the previous chapter demonstrated a great potential as the tool for GW signal analysis and mode identification. However, the study revealed that the accuracy of the solution strongly depends on how precisely the dispersion relationships are known initially, which is the fundamental characteristic of Lamb waves. In general, the thicknesses and material properties may vary going from one specimen to another, so it is crucial to estimate the actual velocities of GW modes to provide the proper analysis with certain confidence. Besides, the effects of mode conversion or interaction with the defect are not currently included in the proposed model, while various converted and reflected wave packets might appear within the experimental signals, which has to be further identified. Thus, the knowledge of actual velocity of the certain wave packet could provide a double benefit. On one hand it can give a more accurate velocity values for the analytical model, which itself would deliver a more reliable results in distinguishing the wave propagation within the structure from influence caused by damage. On the other hand, it could be used as a complimentary method to identify the unpredicted modes of GW in experimental signals, which might be a result of mode conversion and scattering in the presence of the defect. This leads to the demand of the methods to experimentally measure the velocities of separate GW mode packets.

If the wave packet of a single mode can be resolved separately from others, the conventional time-of-flight methods, such as zero-crossing or cross-correlation, might be used to evaluate the phase or group velocities (250). However, these methods are not accurate if the analysed signals are dispersive. For example, the zero-crossing method suffers from the phase uncertainty, especially at large propagation distances, as it become impossible to follow the same zero-crossing point of the elongating wave packet. Similarly, the conventional cross-correlation technique is not applicable to the signals, which consist of a number of dispersed and overlapped wave packets as well (251, 252). Besides, for dispersive waves it is required to estimate the velocity values at a variety of frequencies, so the time-frequency methods are often used as an alternative. Pialucha et al. (253) proposed to calculate the phase velocity from the maxima of amplitude spectrum of the signal reflected several times by the boundaries of the sample. However, the use of such approach is impracticable for complex structures, as it requires the edge reflected signals. In the low frequencies the resonance spectrum method (254) may be used to measure the phase velocities, which is based on the idea that the resonance occurs when the condition $2L = \lambda n$ is satisfied (where L is length of beam; λ is the wavelength; n is the harmonic number). Using the frequency sweep excitation, the phase velocity values c_p at the resonant frequencies f_n of the sample may be estimated according to the expression (254):

$$f_n = \frac{n c_\mathrm{p}}{2L}. \tag{4.1.1}$$

The abovementioned method is applicable at low frequencies only and requires high energy Lamb wave excitation to extract the natural frequencies of the structure. Another alternative is to use the two-dimensional FFT, which transfers the time-distance measurement to the frequency-wavenumber records at discrete frequencies, so the velocities of individual Lamb wave modes can be measured even if the time record is superimposed by multiple wave packets (152). However, the resolution 2D-FFT depends on the amount of time records measured at discrete distances. Therefore, this method is not applicable to the structural health monitoring systems, where a set of transducers are attached to permanent positions and point scanning devices with fine spatial step are not used.

In this study, the novel method to reconstruct the dispersion curve in a band of transducer, analysing the phase spectrum of the time series is proposed. The method exploits the sweep over excitation frequencies and uses a modified version of the phase spectrum method, which was initially proposed by Sachse (255) and later used by Schumacher (198). In the initial version of the phase spectrum method, the authors proposed to reconstruct the dispersion relationship in the whole bandwidth at once, using a wideband laser excitation. However, if the conventional contact transducers are used, the reconstruction bandwidth is certainly limited due to the type of excitation, vibration mode and size of the transducer. It means that in case of contact excitation of the GW, the frequency spectrum of the wave packet is limited and some frequency components are even absent. This makes it impracticable to use the conventional phase spectrum method to estimate the dispersion relationship directly. The method, proposed in this study is based on the idea that the transducer is driven by a square pulse at various central frequencies within its band and the phase velocities are reconstructed only at local maximum components of the Fourier spectra. In other words, this approach reconstructs the velocity values at the harmonics of the signal introduced by a square pulse. Changing the excitation frequency enables some intermediate velocity values to be collected, therefore the dispersion curve at wide band may be estimated and the likely errors due to the low values of some frequency components can be avoided. The algorithm of the proposed method can be summarized by the following steps:

1. The transducer is driven by a square pulse at a central frequency of f_1 and the waveforms $u_{\mathrm{r_1f_1}}(t)$ and $u_{\mathrm{r_2f_1}}(t)$ are registered with receivers r_1 and r_2, each positioned at a distances d_1 and d_2 from the source (see Fig. 4.1.1a for example).
2. The waveforms $u_{\mathrm{r_1f_1}}(t)$ and $u_{\mathrm{r_2f_1}}(t)$ are windowed using the tapered cosine window $w(t)$ to isolate the wave packets of particular mode (see Fig 4.1.1b):

   $$u_{\mathrm{r_1f_1w}}(t) = u_{\mathrm{r_1f_1}}(t)\cdot w(t),\quad u_{\mathrm{r_2f_1w}}(t) = u_{\mathrm{r_2f_1}}(t)\cdot w(t), \tag{4.1.2}$$

   where $u_{\mathrm{r_1f_1w}}(t)$ and $u_{\mathrm{r_2f_1w}}(t)$ represent the windowed versions of the waveforms $u_{\mathrm{r_1f_1}}(t)$ and $u_{\mathrm{r_2f_1}}(t)$ respectively.
3. Each waveform, $u_{\mathrm{r_1f_1w}}(t)$ and $u_{\mathrm{r_2f_1w}}(t)$, is shifted in the time domain by $-t_{\mathrm{m_1}}$ and $-t_{\mathrm{m_2}}$, to avoid the uncertainties in the phase unwrapping procedure. The waveforms are commonly shifted according to the centroid of signal (256),

but in case of moderate dispersion and propagation distance the time shift according to the maximum value of the Hilbert envelope is satisfactory as well:

$$u_{\mathrm{r_1f_1s}}(t)=u_{\mathrm{r_1f_1w}}\left(t+t_{\mathrm{m_1}}\right),\ u_{\mathrm{r_2f_1s}}(t)=u_{\mathrm{r_2f_1w}}\left(t+t_{\mathrm{m_2}}\right),\tag{4.1.3}$$

$$t_{\mathrm{m_1}}=\arg\left(\max_t\left[\mathrm{HT}\left(u_{\mathrm{r_1f_1w}}(t)\right)\right]\right),\ t_{\mathrm{m_2}}=\arg\left(\max_t\left[\mathrm{HT}\left(u_{\mathrm{r_2f_1w}}(t)\right)\right]\right),$$

where HT denotes the Hilbert transform; $t_{\mathrm{m_1}}$ and $t_{\mathrm{m_2}}$ are the time instances, which corresponds to the maximum of Hilbert envelope. The shift in time domain is illustrated in Fig. 4.1.2a.

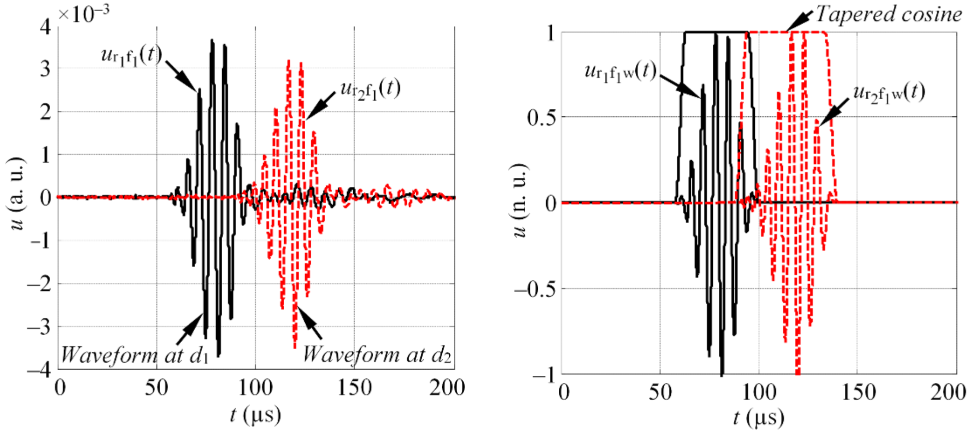

a) b)

Fig. 4.1.1. The example of waveform registered with receivers r_1 and r_2 at distances d_1 and d_2 (a), the illustration of waveform windowing to isolate the wave packet of single mode (b)

4. The complex frequency spectra of each time-shifted waveform $u_{\mathrm{r_1f_1s}}(t)$ and $u_{\mathrm{r_2f_1s}}(t)$ is obtained employing the Fourier transform:

$$U_{\mathrm{r_1f_1}}(jf)=\mathrm{FFT}\left[u_{\mathrm{r_1f_1s}}(t)\right],\ U_{\mathrm{r_2f_1}}(jf)=\mathrm{FFT}\left[u_{\mathrm{r_2f_1s}}(t)\right],\tag{4.1.4}$$

where FFT represents the fast Fourier transform.

5. The change in phase $\Delta\phi(f)$ between two waveforms, $u_{\mathrm{r_1f_1s}}(t)$ and $u_{\mathrm{r_2f_1s}}(t)$, is estimated for a given frequency band f (see Fig 4.1.2b):

$$\Delta\phi(f)=\left(\alpha_{\mathrm{r_1f_1}}(f)-\alpha_{\mathrm{r_2f_1}}(f)\right),\tag{4.1.5}$$

$$\alpha_{\mathrm{r_1f_1}}(f)=\arctan\left[\frac{\mathrm{Im}\left(U_{\mathrm{r_1f_1}}(f)\right)}{\mathrm{Re}\left(U_{\mathrm{r_1f_1}}(f)\right)}\right],\ \alpha_{\mathrm{r_2f_1}}(f)=\arctan\left[\frac{\mathrm{Im}\left(U_{\mathrm{r_2f_1}}(f)\right)}{\mathrm{Re}\left(U_{\mathrm{r_2f_1}}(f)\right)}\right],$$

Note that the phases $\alpha_{\mathrm{r_1f_1}}(f)$ and $\alpha_{\mathrm{r_2f_1}}(f)$ are calculated in a range of $-\pi\ldots\pi$ radians. If the true phase of the particular frequency is less than $-\pi$ radians it will be represented below the π radians. It means that some discontinuities will appear in case the phase goes beyond the $\pm\pi$ radian limit. Therefore, the phases $\alpha_{\mathrm{r_1f_1}}(f)$ and $\alpha_{\mathrm{r_2f_1}}(f)$ has to be unwrapped.

6. The phase velocity as a function of frequency is calculated at particular frequencies f_{k,f_1} using a modified version of the phase spectrum method:

$$c_{\mathrm{p}}\left(f_{k,\mathrm{f}_1}\right)=\frac{2\pi f_{k,\mathrm{f}_1} d}{\Delta\phi\left(f_{k,\mathrm{f}_1}\right)-2\pi f_{k,\mathrm{f}_1}\left(t_{\mathrm{m}_1}-t_{\mathrm{m}_2}\right)}, \tag{4.1.6}$$

where f_{k,f_1} are the frequencies that corresponds to the local maxima of the Fourier spectra $|U_{\mathrm{r}_1\mathrm{f}_1}(jf)|$; d is the separation distance between the receivers r_1 and r_2 ($d = d_2 - d_1$). The frequency selection for phase velocity estimation is illustrated in Fig. 4.1.2c.

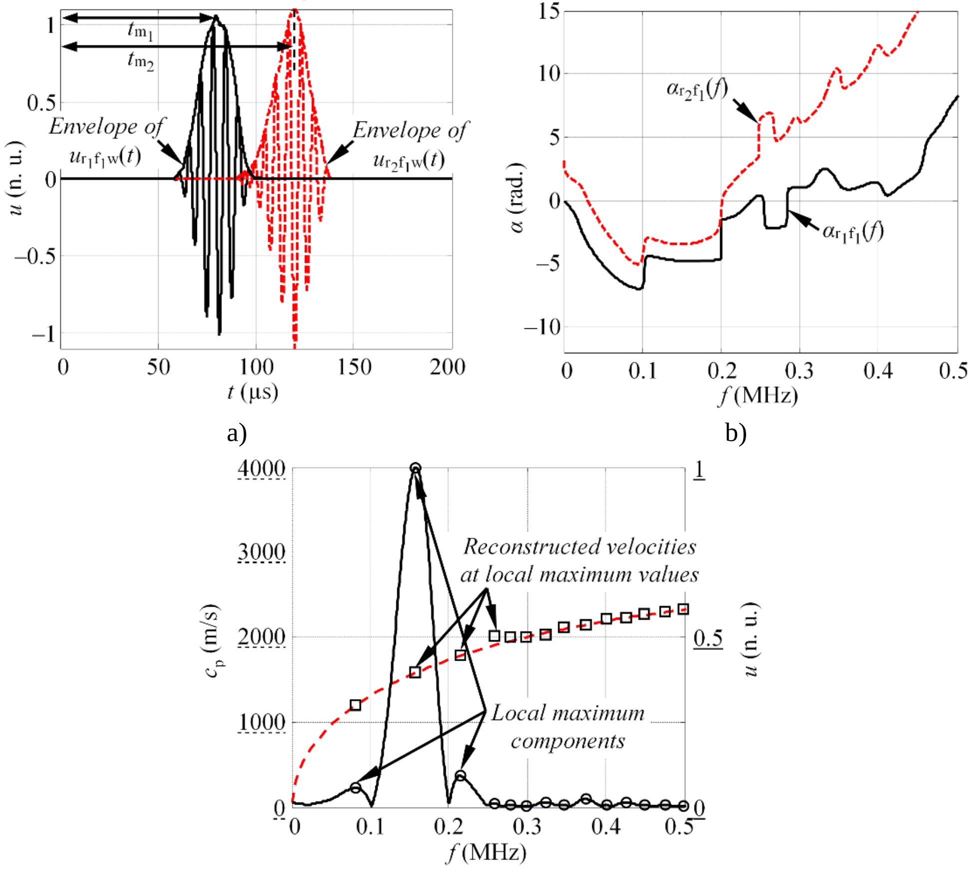

a)

b)

c)

Fig. 4.1.2. The illustration of the shift of waveform in time domain to the maximum value of the Hilbert envelope (a), the phase spectra of the waveforms registered at distances d_1 and d_2 (b), the normalized magnitude spectra of the waveform captured with receiver r_1 with the local maximum frequency values (circle markers), at which the phase velocity values are estimated (square markers) (dashed line represents the theoretical DC) (c)

7. The intermediate values of the phase velocities at other frequencies are obtained by changing the excitation frequency to f_2 and repeating the whole

routine described above. The final result is obtained by combining the calculations at different excitation frequencies $f_1 \ldots f_m$:

$$c_{\mathrm{p}}(f)=\left\{c_{\mathrm{p}}\left(f_{k,\mathrm{f}_1}\right), c_{\mathrm{p}}\left(f_{k,\mathrm{f}_2}\right),\ldots,c_{\mathrm{p}}\left(f_{k,\mathrm{f}_m}\right)\right\}. \tag{4.1.7}$$

where m is the number of excitation frequencies used to drive the emitter.

The method presented above is applicable to flat structures with uniform thicknesses, which can be multi-layered, anisotropic or isotropic. In contrast to the conventional phase spectrum method, it provides better accuracy of velocity estimation and enables errors to be avoided, which are caused by the low values of some frequency components in the spectrum of analysed wave packet.

4.2 Experimental validation of the proposed method

In this chapter, the proposed phase velocity estimation method is validated with the appropriate experiments. For this purpose, the phase velocity values, extracted with the developed method are compared with the theoretical calculations, which were considered as a reference. In this study, the velocities of the S_0 mode on the aluminium sample will be analysed.

The experiments were carried out on the aluminium alloy 2024-T6 sample, which was 2 mm thick, 650 mm wide and 1,250 mm long. The well-known isotropic material was deliberately selected for this study, in order to be able to compare the experimental results with the theoretically estimated values. The S_0 mode was launched into the structure by attaching the thickness mode transducer to the edge of the Al plate as it is shown on Fig. 4.2.1. For the reception, two transducers r_1 and r_2 possessing the same characteristics were bonded perpendicularly to the upper surface of the specimen at distances d_1 = 450 mm and d_2 = 550 mm from the source (see Fig.4.2.1).

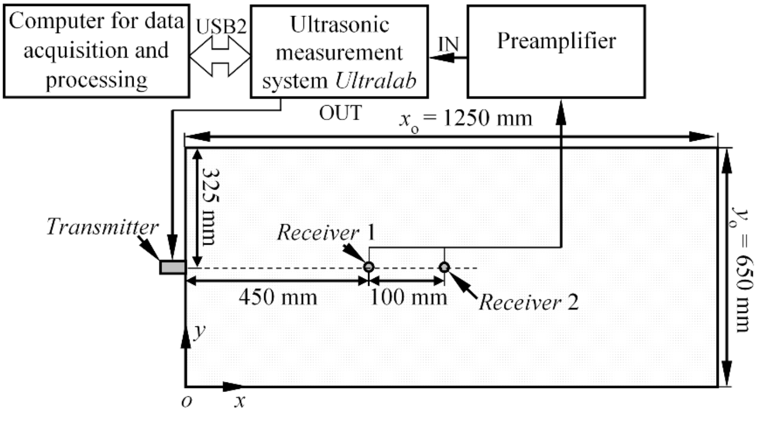

Fig. 4.2.1. The schematic diagram of the experimental set-up for validation of phase velocity estimation method

In this research, the transducers with a central frequency of 240 kHz and a bandwidth of 340 kHz at –6 dB level was used. The frequency response of the probe can be seen in Fig. 4.2.2a. To reconstruct the dispersion curve under the wide band, two different scenarios employing the square pulse excitation were used as follows: $n_1 = 3$ cycles, $f_1 = 150$ kHz and $n_2 = 3$ cycles, $f_2 = 200$ kHz. Such excitation frequencies were deliberately selected according to the magnitude spectrum of excitation pulse, which can be seen in Fig. 4.2.2b. The results presented in the figure demonstrate that a minor shift of excitation frequency (from 150 kHz to 200 kHz) enables local maximum amplitudes of the magnitude spectra to be obtained at different frequencies in contrast to 150k Hz excitation. Moreover, the local maximum values in case of 200 kHz excitation mostly correspond to the local minimum frequencies of 150 kHz excitation. Thus, excitation under the selected frequencies enables a larger variety of reconstruction frequencies to be obtained as well as the phase velocity values. In this case it was presumed that the selected excitation frequencies will provide a sufficient amount of velocity values. Meanwhile in other cases, more excitation frequencies may be used exploiting the whole bandwidth of the transducer.

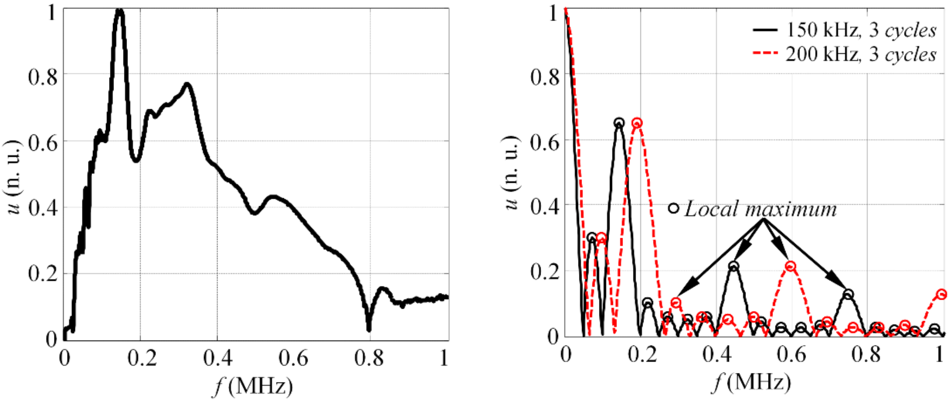

a)

b)

Fig. 4.2.2. The frequency response of the thickness mode transducer used for the experiments (a), the magnitude spectra of 3 cycles 150 kHz (solid line) and 3 cycles 200 kHz (dashed line) square excitation pulse (b)

The experimental waveforms of the S_0 mode at distances d_1 and d_2 under the $f_1 = 150$ kHz and $f_2 = 200$ kHz excitation are presented in Fig. 4.2.3a,b respectively. The magnitude spectra $|U_{r_1 f_1}(jf)|$ and $|U_{r_2 f_2}(jf)|$ of the windowed S_0 mode wave packet can be seen in Fig. 4.2.3c. The frequencies at which the phase velocity values were extracted are indicated with circle markers. Finally, the reconstructed dispersion curve of the phase velocity for the S_0 mode along with theoretical estimation is shown on Fig. 4.2.3d. The theoretical dispersion curve was calculated employing the SAFE method and material properties of aluminium 2024-T6 listed in the previous chapter.

The results in Fig. 4.2.3d show, that the phase velocities are reconstructed quite accurately in the frequency band up to 0.8 MHz. According to the frequency response of the transducer used in this study (see Fig. 4.2.2a), the technique enables the phase velocities in the –20 dB level bandwidth of the actuator to be reconstructed. In this study, a total of 52 velocity values were extracted at a band up to 1 MHz. It is noteworthy that the general reliability of the phase spectrum method depends on proper selection of the time window to crop the wave packet of the single mode for

FFT. Therefore, if the proposed method is used to experimentally estimate the actual dispersion relationship of the unknown structure, the degree of separation between the receivers r_1, r_2 and object boundaries has to be sufficient to achieve the good isolation between modes. On the other hand, if the goal is to estimate the dispersion relationship, in most cases it is satisfactory to analyse the first arrival of each mode only, which is usually separated to an adequate extent. Once the dispersion relationship of each mode are known, it can be passed to the analytical model, which may be further used to distinguish the wave propagation within the structure from influence caused by damage.

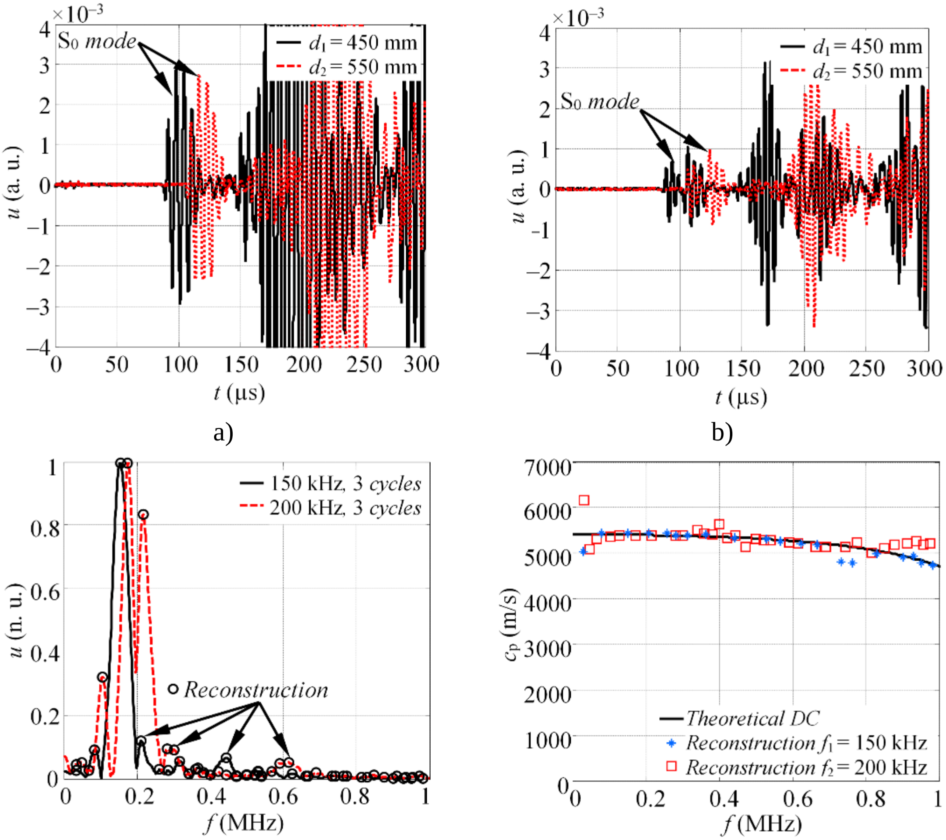

a)

b)

c)

d)

Fig. 4.2.3. The experimental waveforms of S_0 mode at distances d_1 and d_2 in case of 150 kHz (a) and 200 kHz (b) excitation, the magnitude spectra of windowed S_0 mode at different excitation frequencies (c), the combined reconstruction of dispersion relations (d)

In order to estimate the agreement of the results with theoretical phase velocities, the standard deviation (STD) was used as a measure of spread. Mathematically it can be expressed:

$$\sigma = \sqrt{\frac{1}{N-1}\sum_{i=1}^{N}\left|A_i - \mu\right|^2}, \qquad (4.2.1)$$

where A is the deviation of estimated velocity values from the theoretical DC ($A = c_p(f) – c_{pe}(f)$, where $c_p(f)$ are the theoretical velocities; $c_{pe}(f)$ are the extracted velocities); μ is the mean of A. According to eq. 4.2.1 the estimated variation of calculated phase velocity values is $\sigma = 161.2$ m/s. This leads to the conclusion that 40 out of 52 velocity values (77%) are within the standard deviation (see Fig. 4.2.4).

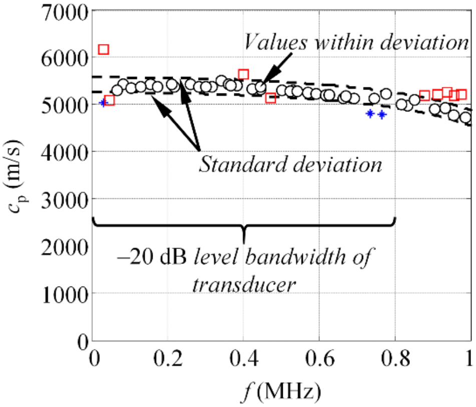

Fig. 4.2.4. The graphic representation of standard deviation showing the spread of estimated phase velocity values

The major advantage of this technique over the conventional phase spectrum method initially proposed by Sachse (255) is the ability to reconstruct the dispersion relationship in a wide band using relatively narrowband transducers. This is especially beneficial if contact type transducers and square pulse excitation are used, as it delivers some additional distortions in magnitude spectra due to operation mode, type of excitation and size of transducer. Thus the conventional method cannot be used directly, while the excitation at different frequencies and reconstruction only at local maximum components of Fourier spectra enables more precise velocity values to be obtained in wide band. It was determined that the conventional phase spectrum method (255) would provide the approximate deviation of $\sigma = 452$ m/s for the abovementioned experiment.

4.3 Verification of the phase velocity method employing the converted modes

In the upcoming section, the numerical validation of the proposed phase velocity method will be presented. The major focus will be given to the method performance in case the analysed signal is surrounded by the wave packets of other modes. To achieve the purpose of this study, the phase velocities of converted A_0 mode will be analysed, which arrive later than the direct S_0 mode.

To fulfil the scope of this research, the 3D finite element model of isotropic aluminium alloy 2024-T6 plate (600 mm × 200 mm × 2 mm) is considered. The top view of the analysed structure is presented on Fig. 4.3.1. The S_0 mode was initially launched into the structure by applying the tangential in-plane nodal displacements to the shortest edge of the Al plate. To generate the converted A_0 mode, the vertical 36 mm wide (along x axis) crack type defect with depth of 66% of the plate thickness was introduced by duplicating the nodes of the mesh. It was shown by the various researchers, that if a crack is not symmetrical to the middle plane of the plate according to the thickness, the mode conversion takes place upon the wave interaction with the notch and both S_0 and A_0 modes are expected as the reflected and transmitted waves (257). The defect was centred with respect to the short edge of the sample and situated at the distance of 200 mm from source of Lamb waves (see Fig. 4.3.1).

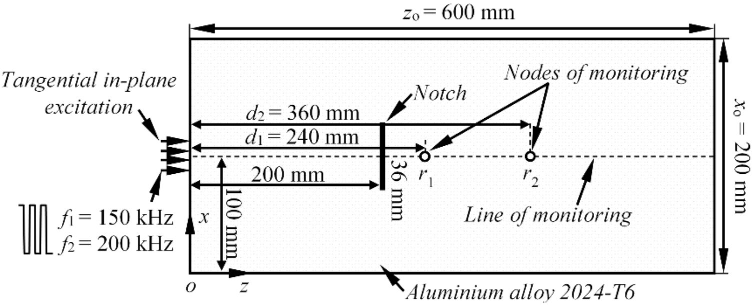

Fig. 4.3.1. Illustration of the set-up of numerical aluminium plate FE model with the notch

Throughout the simulations, 3D solid64 finite elements were used, which are defined by eight nodes having three degrees of freedom at each node. Once again two different scenarios employing the square pulse excitation were used as it was described in the previous section. At first the excitation pulse consisted of $n_1 = 3$ cycles with central frequency of $f_1 = 150$ kHz. Meanwhile in the second case, the Lamb waves were excited with $n_2 = 3$ cycles at $f_2 = 200$ kHz. The average mesh size was equal to 0.8 mm, which corresponds to 13 nodes per wavelength for the slowest A_0 mode at f_1 and 11 nodes per wavelength at f_2. The integration step in time domain was 0.33 µs and 0.25 µs respectively, which produces a 1/20 of the period both at f_1 and at f_2. The variable monitored in this study was a vertical component of particle velocity (y) along the centreline of the sample. The waveforms for the phase velocity estimation were selected along the centreline of the sample at distances $d_1 = 240$ mm and $d_2 = 360$ mm. The B-scan images of the longitudinal (z) and vertical component (y) of the particle velocity, showing the S_0 and converted A_0 modes are presented in Fig. 4.3.2a,b.

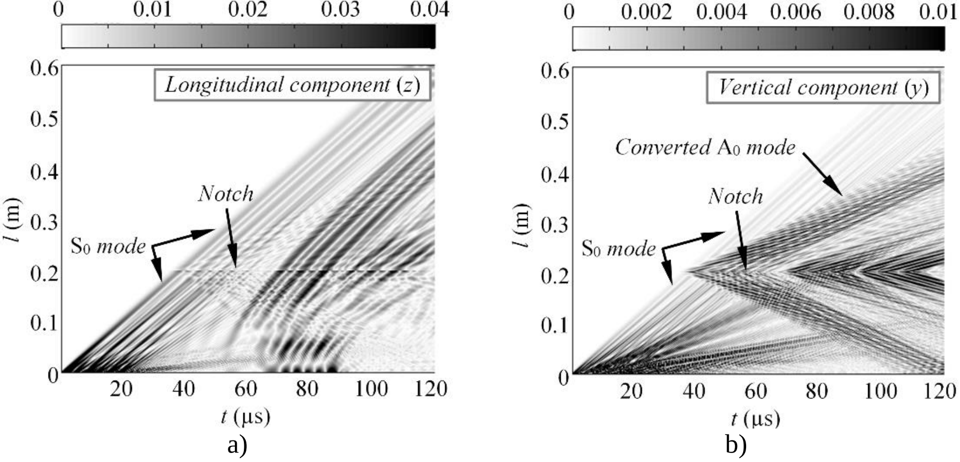

a) b)

Fig. 4.3.2. The longitudinal (a) and vertical (b) component of particle velocity along the centreline of the sample in case of 150 kHz excitation

The simulated waveforms of the converted A_0 modes at distances d_1 and d_2 in case of f_1 = 150 kHz and f_2 = 200 kHz excitation are presented in Fig. 4.3.3a,b. The selected time windows to cut the wave packet of single mode are indicated with vertical dashed lines. The magnitude spectra of windowed A_0 mode at frequencies f_1 and f_2 along with indicated reconstruction frequencies can be seen on Fig. 4.3.3c. Finally, the comparison of estimated DC with the theoretical calculations is shown on Fig. 4.3.3d. The results demonstrate a good match between the estimated results and theoretical phase velocities. The standard deviation of the reconstructed velocities is equal to σ = 47.3 m/s according to eq. 4.2.1. Overall the 32 velocity values were extracted, while 20 (63%) of them were within the standard deviation.

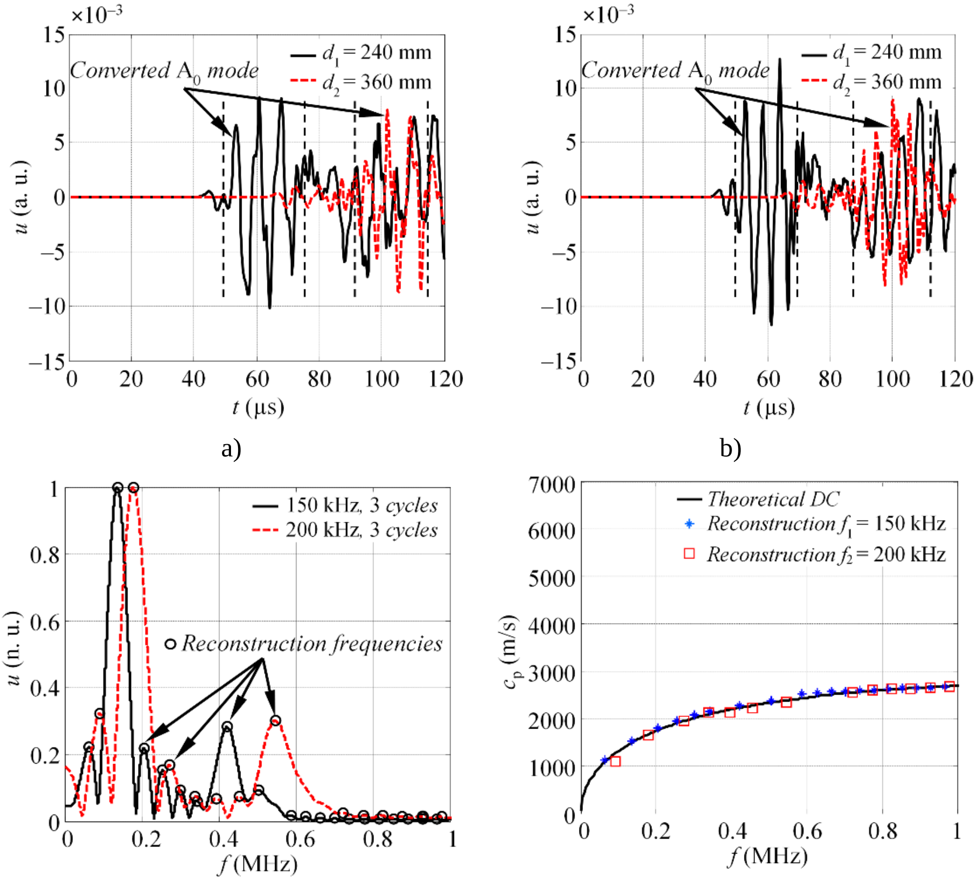

a)

b)

c)

d)

Fig. 4.3.3. The simulated waveforms of converted A_0 mode at distances d_1 and d_2 in case of 150 kHz (a) and 200 kHz (b) excitation, the magnitude spectra of windowed A_0 mode at different excitation frequencies (c), the combined reconstruction of phase velocity dispersion curve along with the theoretical estimation (d)

As it was mentioned previously, if the proposed method is used to determine the dispersion relationship of unknown structure, it is recommended to analyse the first arrival. In such case the proper selection of time window is not a very serious problem as the modes tend to be well isolated. If the proposed method is used to identify unpredicted modes, which are likely due to the presence of some defects, then the start and stop points may be selected employing the analytical model presented in the previous chapter. As it was demonstrated, the analytical model enables the wave propagation to be analysed in the defect-free structure. Thus, the comparison between analytical predictions and experimental measurements may give an idea where the time window should be positioned.

The proposed method implicitly assumes that only one mode is present at the selected time window. Therefore, it is not so effective if more than one mode shares the same frequency and time range. On the other hand, it is attractive from the SHM point of view, since two measurement locations are required only for the phase velocity reconstruction.

4.4 Analysis of the experimental multimodal signals in anisotropic structure

In this section, the performance of the proposed phase spectrum method is validated qualitatively by analysing the experimental multimodal signals in an anisotropic structure. For this purpose, the same GFRP plate and set-up previously presented in Chapter 3, section 3.3 was used. Two waveforms were recorded along the wavepath (0° propagation) at the distances $d_1 = 773$ mm and $d_2 = 895$ mm from the source of Lamb waves (see Fig. 3.3.1). In this case the measurements were recorded at a single excitation frequency $f = 100$ kHz. The proposed phase velocity estimation method was used to extract velocities of four wave packets: direct S_0, bottom reflected S_0, left-top edge reflected S_0 and direct A_0 mode. The experimentally obtained waveforms at the distances d_1 and d_2 are presented in Fig. 4.4.1a,b. The start and stop points of time windows used to crop the wave packets are indicated by dashed squares.

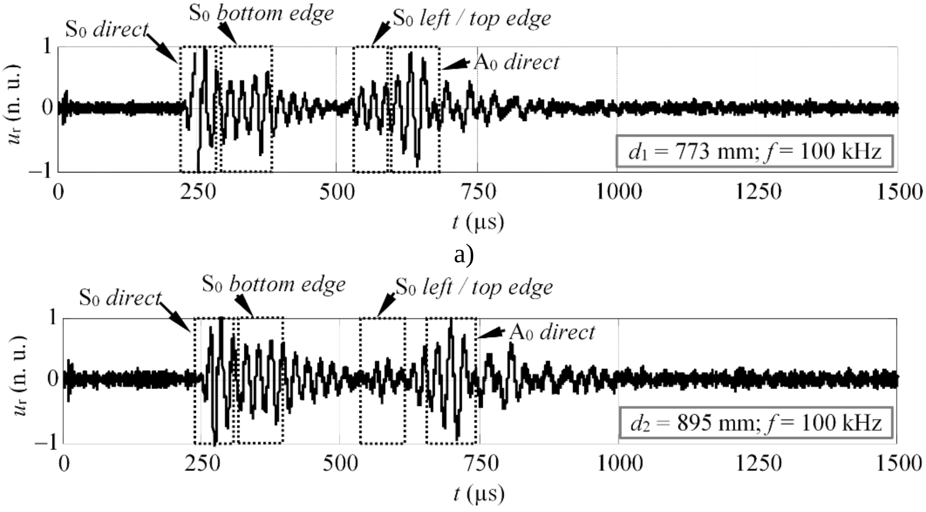

a)

b)

Fig. 4.4.1. The experimental waveforms obtained on GFRP sample along the wavepath at distances d_1 (a) and d_2 (b)

The reconstructed phase velocities of different reflections can be seen in Fig. 4.4.2a–d. The standard deviations for each case of reconstruction are summarized in Table 4.4.1. Note, the reconstructed velocity values below the cut-off frequency of S_0 mode were not considered in the calculations of STD.

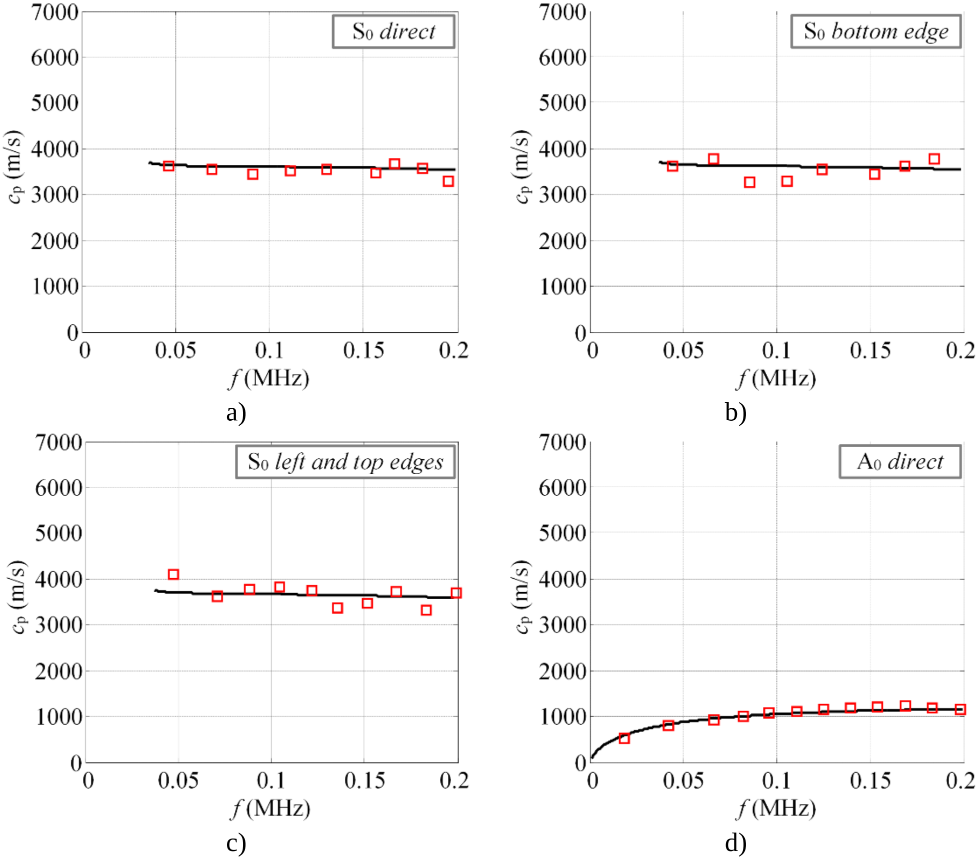

Fig. 4.4.2. The reconstructed phase velocities of the S_0 and A_0 modes: S_0 direct (a), S_0 bottom edge reflected (b), S_0 left and top edge reflected (c), A_0 direct (d)

Table 4.4.1. The standard deviation of the estimated phase velocities for different GW mode packets

Type of mode	*Standard deviation, σ* (m/s)
S_0 direct	97.4
S_0 bottom edge	202.7
S_0 left and top edge	224.5
A_0 direct	51.5

The results presented above (Fig. 4.4.2) were found to be in quite good agreement with theoretical calculations. Thus, the proposed technique can be used with a certain reliability to extract the phase velocities of GW. The results show, that the velocities of direct modes are closer to theoretical values in comparison to the reflected ones. The average deviation for the direct modes is approximately 75 m/s, while for the reflected modes – 213 m/s. Several factors may influence the reliability of the results though. First of all, the selected time windows in Fig. 4.4.1a,b (dashed squares) may give an idea that this procedure is not very straightforward, especially for the reflected modes. As it turns out, in some cases part of the wave packet has to be cropped to get better velocity estimation. Another important factor is the propagation distance, which varies for modes arriving at different directions. It means that the variable *d* has to be predefined for each wave packet separately. If the propagation distance is not known in advance, an additional error will be obtained. The study revealed that the proposed velocity estimation technique gives an approximate experimental error of 4% in comparison to theoretical predictions. Meanwhile, for the incident modes, the error is always less than a 2.5%. For example, the 2D FFT method (152) gives an error of approximately of 1%. However, to achieve such accuracy, the authors used a set of 64 time series, spatially sampled at 1 mm.

4.5 Conclusions of Chapter 4

1. The modified method for phase velocity estimation based on existing phase spectrum techniques was developed. The proposed method enables the dispersion relationship in the –20 dB level bandwidth of the transducer to be reconstructed, employing the time series measured at two distinct locations. Thus it can be effectively used in SHM systems as the tool to estimate the actual velocity of GW modes in the structure and to identify unknown reflections.
2. In contrast to the conventional phase spectrum technique, the proposed method is applicable to the narrowband transducers, maintaining the wide reconstruction bandwidth and accurate velocity values. This is achieved by reconstructing the velocities at harmonics of magnitude spectra only and by driving the actuator at several different frequencies.
3. The proposed phase velocity estimation technique is applicable to flat structures with uniform thicknesses, which can be multi-layered, anisotropic or isotropic, including complex geometries.
4. The proposed technique was validated with the numerical simulations and the experiments both on metallic and composite structures. It was determined that experimentally the velocities are estimated with an average spread of 4%, compared to the theoretical predictions. The incident modes are reconstructed more accurately (with deviation up to 2.5%), while the reflected modes are spread out over a wider range of values, up to 6%. For the numerical signals, the estimated velocities were even closer to theoretical ones, producing an average deviation of 2%.
5. The method developed in this research implicitly assumes that only a single mode is present in the selected time window. If more than one wave packet shares the same time and frequency content, the proper velocity reconstruction becomes impossible. On the other hand, the method demonstrated a good performance estimating the velocities of isolated, dispersive signals and might be effectively used in SHM systems, unlike the conventional zero-crossing and cross-correlation techniques.

5. A METHOD FOR DAMAGE DETECTION AND FEATURE EXTRACTION IN COMPOSITE STRUCTURES

5.1 Motivation and background of the proposed method

Once the behaviour of GW in the investigated defect-free structure can be fully explained, the next step forward is to detect the damage and to extract its features. The identification of damage can be described as a four step process that involves the information about the existence, location, type and severity of the defect. The detection and localisation of damage does not necessarily require the reference data from the damaged structure, meanwhile for characterisation of defect, the data from both undamaged and damaged structures is usually mandatory. For example, the presence of a defect can be identified by using the time reversal method (202), while the location of it can be determined using various imaging approaches, described in section 1.5. In most of the current SHM applications, the detection of damage simply relies on the algebraic difference between the current time trace and the reference baseline. It is assumed that subtraction allows the structural features to be removed, leaving the influence of damage. However, as those time traces are recorded at different environmental conditions and wear stages of the structure, such simple approach to detect the damage is not reliable, unless the additional compensation strategies, such as optimal baseline subtraction or baseline signal stretch (59) are applied. Moreover, such technique can only tell the existence of damage. Many authors have also used other approaches to detect and localise the damage as well, such as analysis of natural frequencies, mode shapes or wavelet post-processing. However, only a few of them are taking a step further to develop the indicators suitable to describe the features of damage, such as size and depth. This information is substantial for complete identification of damage, as well as for the prognosis of strength and lifetime of the structure. The lack of damage features makes the SHM systems ineffective, as not every imperfection present in the structure can be treated as critical.

Among the attempts to describe the features of the damage, a lot of attention has been paid to assess delamination type defects, as they are common in composite structures. For example, Guo and Cawley (258) investigated the reflection and transmission of S_0 mode signals as a function of defect positioning through the thickness of the laminate. They found that the presence of delamination affects the reflected signal of the S_0 mode rather than the direct one. Similarly, Birt (259) studied the dependencies between the magnitude of the reflected S_0 mode and the width of the delamination. Furthermore, Tan et al. (260) scanned the receiver along the delaminated area and found that the greater sensitivity is obtained in the case of a defect situated close to the surface. The research listed above formed an initial background for development of algorithms to characterize the damage. However, currently there are no widely known approaches that may be used to describe the remote delamination type defects, employing the time series captured at a few permanent locations. In this study, the SHM method to detect the delamination type defects and to extract the size and depth of it is proposed. It is a baseline method, based on the delay time estimation and constructive/destructive interference of the A_0

mode, which propagates through delaminated area. In this case, the baseline is referred as a database of analytically calculated relationships between the parameters of A_0 mode and the features of damage, which is compared to the experimental data in order to describe the delamination. The proposed method employs the A_0 mode, which ensures adequate sensitivity to such defects, since it possess a dominant out-of-plane component and smaller wavelength in contrast to the symmetrical modes. The proposed technique features one side access and can provide the information about the existence, depth and size of the damage employing a few time traces measured at a series of different excitation frequencies. In the upcoming few paragraphs, the general interaction of A_0 mode with the delamination type defect will be briefly explained, followed by description of the proposed technique to detect and describe the damage.

Let's assume we have the composite plate with length l and thickness h as shown in Fig. 5.1.1. It will be analysed in a 2D approach, which means that the plate is infinite along the y axis. As it was mentioned previously, in SHM systems the transducers are attached to permanent positions on the structure and in contrast to conventional NDT, and surface scanning is not used. Hence, in this case, the considered problem will be analysed between two permanent positions on the structure – the source point at which the A_0 mode is being introduced and the monitoring point, located beyond the damage. Consider that the delamination type defect is present in the analysed structure, which is l_1 wide and situated at a distances of l_0 and l_2 from the source and monitoring point respectively, at the depth of h_1 in respect to the top surface. The sketch of the discussed example is presented in Fig. 5.1.1.

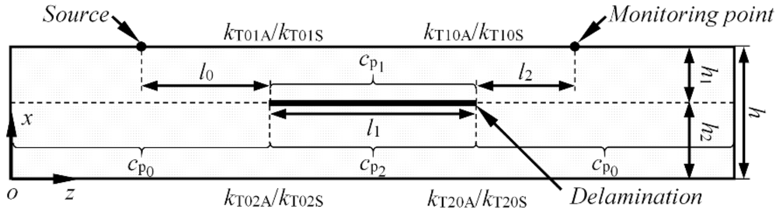

Fig. 5.1.1. The schematic diagram of considered example of the composite plate with delamination type damage

In general, upon the interaction of the A_0 mode with the delamination type defect, the reflection, transmission and mode conversion occurs at each end of the damage. In such way, at the leading edge of the damage, the initial A_0 mode reflects back and splits into the wave packets that accordingly propagate above and below the defect. Moreover, mode conversion occurs at the leading edge, therefore part of the energy transforms into the S_0 mode as well (see Fig. 5.1.2a). Similarly, at the trailing edge of the damage, both A_0 and S_0 modes are reflecting back, propagating forward and converting to each other (see Fig. 5.1.2b). The brief explanation of the GW interaction with a delamination type defect is graphically illustrated at Fig. 5.1.2. To simplify the task, in this study the directly transmitted wave packets of A_0 mode at the monitoring point are analysed only.

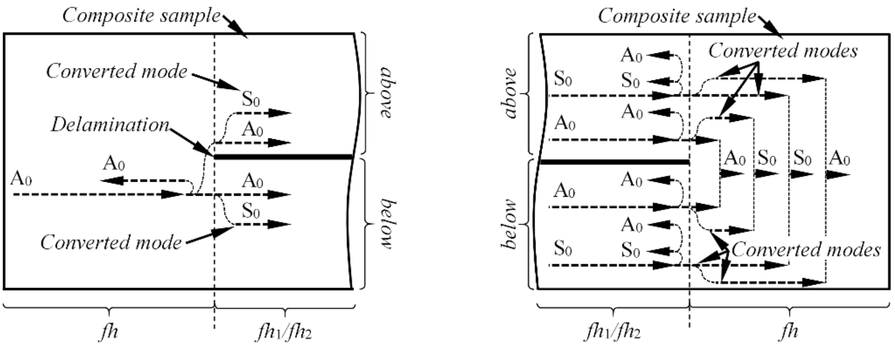

a) b)

Fig. 5.1.2. The graphic representation of A0 mode interaction with delamination type defect at the leading (a) and trailing edge (b)

Based on the parameters of the transmitted A0 mode, such as propagation time and magnitude, the special indicators will be estimated to assess the size and the depth of the defect. Mathematically the first arrival of A0 mode at the monitoring point can be expressed as:

$$
\begin{aligned}
U_{\mathrm{IA}_0}(\omega) &= U_{\mathrm{sA}_0}(\omega)\cdot H\left(\omega, c_{\mathrm{p_0A_0}}, l_0\right)\cdot k_{\mathrm{T01A}}\cdot H\left(\omega, c_{\mathrm{p_1S_0}}, l_1\right)\cdot k_{\mathrm{T10S}}\cdot H\left(\omega, c_{\mathrm{p_0A_0}}, l_2\right)+\\
&+U_{\mathrm{sA}_0}(\omega)\cdot H\left(\omega, c_{\mathrm{p_0A_0}}, l_0\right)\cdot k_{\mathrm{T02A}}\cdot H\left(\omega, c_{\mathrm{p_2S_0}}, l_1\right)\cdot k_{\mathrm{T20S}}\cdot H\left(\omega, c_{\mathrm{p_0A_0}}, l_2\right)=\\
&=\left(U_{\mathrm{sA}_0}(\omega)\cdot H\left(\omega, c_{\mathrm{p_0A_0}}, L-l_1\right)\right)\cdot\begin{pmatrix} k_{\mathrm{T01A}}\cdot H\left(\omega, c_{\mathrm{p_1S_0}}, l_1\right)\cdot k_{\mathrm{T10S}}+\\ +k_{\mathrm{T02A}}\cdot H\left(\omega, c_{\mathrm{p_2S_0}}, l_1\right)\cdot k_{\mathrm{T20S}}\end{pmatrix},
\end{aligned}
\tag{5.1.1}
$$

$$
H\left(\omega, c_{\mathrm{pA}_0}, l\right)=e^{-\alpha(\omega)x}e^{\frac{-jl\omega}{c_{\mathrm{pA_0}}(\omega)}},
\tag{5.1.2}
$$

where $U_{\mathrm{sA}_0}(\omega)$ is the frequency representation of the A0 mode upon its introduction into the structure; $H(\omega)$ is the frequency response of the analysed system; $\alpha(\omega)$ is the attenuation function; $c_p(\omega)$ is the phase velocity; l is the propagation distance; L is the separation between the source and the monitoring point ($L = l_0 + l_1 + l_2$); k_{T01A}, k_{T02A}, k_{T10S} and k_{T20S} are the transmission coefficients for the A0 and S0 modes at the leading and trailing edges of the delamination respectively for the layer above and below the defect. The wave packet described by eq. 5.1.1 is A0 mode, which is a superposition of the signals, traveling above and below the damage, that converts to S0 mode at the leading edge and back to A0 at the trailing edge of the defect. Due to this reason, this wave packet $U_{\mathrm{IA}_0}(\omega)$ arrives earlier compared to the direct transmission of the A0 mode, as the S0 mode possess greater phase velocities at low frequencies ($c_{\mathrm{p_1S_0}}>c_{\mathrm{p1A0}}$ and $c_{\mathrm{p_2S_0}}>c_{\mathrm{p_2A_0}}$). Consequently, the direct transmission of A0 mode can be written as:

$$
\begin{aligned}
U_{\mathrm{IIA}_0}(\omega) &= U_{\mathrm{sA}_0}(\omega)\cdot H\left(\omega, c_{\mathrm{p_0A_0}}, l_0\right)\cdot k_{\mathrm{T01A}}\cdot H\left(\omega, c_{\mathrm{p_1A_0}}, l_1\right)\cdot k_{\mathrm{T10A}}\cdot H\left(\omega, c_{\mathrm{p_0A_0}}, l_2\right)+\\
&+U_{\mathrm{sA}_0}(\omega)\cdot H\left(\omega, c_{\mathrm{p_0A_0}}, l_0\right)\cdot k_{\mathrm{T02A}}\cdot H\left(\omega, c_{\mathrm{p_2A_0}}, l_1\right)\cdot k_{\mathrm{T20A}}\cdot H\left(\omega, c_{\mathrm{p_0A_0}}, l_2\right)=\\
&=\left(U_{\mathrm{sA}_0}(\omega)\cdot H\left(\omega, c_{\mathrm{p_0A_0}}, L-l_1\right)\right)\cdot\begin{pmatrix} k_{\mathrm{T01A}}\cdot H\left(\omega, c_{\mathrm{p_1A_0}}, l_1\right)\cdot k_{\mathrm{T10A}}+\\ +k_{\mathrm{T02A}}\cdot H\left(\omega, c_{\mathrm{p_2A_0}}, l_1\right)\cdot k_{\mathrm{T20A}}\end{pmatrix}.
\end{aligned}
\tag{5.1.3}
$$

The first part of eq. 5.1.1 and eq. 5.1.3 ($U_{\mathrm{sA}_0}(\omega)\cdot H(\omega,c_{\mathrm{p}_0\mathrm{A}_0},L-l_1)$) describe the wave propagation in a defect free area, meanwhile the second part represent the converted S_0 wave propagation in case of eq. 5.1.2 and direct A_0 wave propagation in case of eq. 5.1.3 within the defect. In a similar way the transmitted S_0 modes at the monitoring point can be expressed as well:

$$\begin{aligned}
U_{\mathrm{IS}_0}(\omega) &= U_{\mathrm{sA}_0}(\omega)\cdot H\left(\omega,c_{\mathrm{p}_0\mathrm{A}_0},l_0\right)\cdot k_{\mathrm{T01A}}\cdot H\left(\omega,c_{\mathrm{p}_1\mathrm{S}_0},l_1\right)\cdot k_{\mathrm{T10S}}\cdot H\left(\omega,c_{\mathrm{p}_0\mathrm{S}_0},l_2\right)+\\
&+U_{\mathrm{sA}_0}(\omega)\cdot H\left(\omega,c_{\mathrm{p}_0\mathrm{A}_0},l_0\right)\cdot k_{\mathrm{T02A}}\cdot H\left(\omega,c_{\mathrm{p}_2\mathrm{S}_0},l_1\right)\cdot k_{\mathrm{T20S}}\cdot H\left(\omega,c_{\mathrm{p}_0\mathrm{S}_0},l_2\right)=\\
&=\left(U_{\mathrm{sA}_0}(\omega)\cdot H\left(\omega,c_{\mathrm{p}_0\mathrm{A}_0},l_0\right)\cdot H\left(\omega,c_{\mathrm{p}_0\mathrm{S}_0},l_2\right)\right)\cdot\begin{pmatrix}k_{\mathrm{T01A}}\cdot H\left(\omega,c_{\mathrm{p}_1\mathrm{S}_0},l_1\right)\cdot k_{\mathrm{T10S}}+\\+k_{\mathrm{T02A}}\cdot H\left(\omega,c_{\mathrm{p}_2\mathrm{S}_0},l_1\right)\cdot k_{\mathrm{T20S}}\end{pmatrix},
\end{aligned}\tag{5.1.4}$$

$$\begin{aligned}
U_{\mathrm{IIS}_0}(\omega) &= U_{\mathrm{sA}_0}(\omega)\cdot H\left(\omega,c_{\mathrm{p}_0\mathrm{A}_0},l_0\right)\cdot k_{\mathrm{T01A}}\cdot H\left(\omega,c_{\mathrm{p}_1\mathrm{A}_0},l_1\right)\cdot k_{\mathrm{T10A}}\cdot H\left(\omega,c_{\mathrm{p}_0\mathrm{S}_0},l_2\right)+\\
&+U_{\mathrm{sA}_0}(\omega)\cdot H\left(\omega,c_{\mathrm{p}_0\mathrm{A}_0},l_0\right)\cdot k_{\mathrm{T02A}}\cdot H\left(\omega,c_{\mathrm{p}_2\mathrm{A}_0},l_1\right)\cdot k_{\mathrm{T20A}}\cdot H\left(\omega,c_{\mathrm{p}_0\mathrm{S}_0},l_2\right)=\\
&=\left(U_{\mathrm{sA}_0}(\omega)\cdot H\left(\omega,c_{\mathrm{p}_0\mathrm{A}_0},l_0\right)\cdot H\left(\omega,c_{\mathrm{p}_0\mathrm{S}_0},l_2\right)\right)\cdot\begin{pmatrix}k_{\mathrm{T01A}}\cdot H\left(\omega,c_{\mathrm{p}_1\mathrm{A}_0},l_1\right)\cdot k_{\mathrm{T10A}}+\\+k_{\mathrm{T02A}}\cdot H\left(\omega,c_{\mathrm{p}_2\mathrm{A}_0},l_1\right)\cdot k_{\mathrm{T20A}}\end{pmatrix},
\end{aligned}\tag{5.1.5}$$

where $U_{\mathrm{IS}_0}(\omega)$ and $U_{\mathrm{IIS}_0}(\omega)$ are the wave packets which convert to S_0 mode at the leading and trailing edge of the damage respectively. In general, the S_0 mode has a weak out-of-plane component at low frequencies, therefore in this study the direct transmissions of the A_0 mode, described by eq. 5.1.1 and eq. 5.1.3 were considered only. For the sake of simplicity, all the reflections and repetitive transmissions were not taken into the account. The interaction of the A_0 mode with a delamination type defect is illustrated in Fig. 5.1.3, which represents the B-scan of vertical (a) and longitudinal (b) components of particle velocity, obtained along the top surface of the 4 mm thickness GFRP sample, with the geometry corresponding to the one presented in Fig. 5.1.1. Note that only the wave packets $U_{\mathrm{IA}_0}(\omega)$ and $U_{\mathrm{IIA}_0}(\omega)$ will be analysed further to detect and describe the damage.

An approach to estimate the existence of a defect. Based on the concept of guided wave interaction with delamination type defect, several observations may be outlined, which enables the damage to be detected and described. The results in Fig. 5.1.3 show that after the interaction with a delamination type defect, four directly transmitted wave packets can be captured at the monitoring point, situated beyond the damage: two weak S_0 modes ($U_{\mathrm{IS}_0}(t)$ and $U_{\mathrm{IIS}_0}(t)$) and two dominant A_0 modes ($U_{\mathrm{IA}_0}(t)$ and $U_{\mathrm{IIA}_0}(t)$, see Fig.5.1.3a,b). It is obvious that if the structure is defect free, only the direct A_0 or boundary reflected modes will be observed. Meanwhile, in the presence of delamination, the converted A_0 mode ($U_{\mathrm{IA}_0}(t)$) appears in the structure and arrives even faster than the direct A_0 one ($U_{\mathrm{IIA}_0}(t)$), due to the conversion to S_0 mode at the defective area (see Fig.5.1.3a). Thus, in order to detect the presence of damage it is proposed to monitor the appearance of converted A_0 mode $U_{\mathrm{IA}_0}(t)$ in front of the direct arrival $U_{\mathrm{IIA}_0}(t)$. The converted A_0 mode $U_{\mathrm{IA}_0}(t)$ can be detected using the short time cross-correlation technique between the current time trace and the excitation signal.

The technique was previously described in Chapter 3, section 3.2, mathematically it can be expressed as:

$$x(\tau)=\frac{\sum\limits_{t=-\Delta\tau}^{\Delta\tau} u_{\mathrm{e}}(t,\tau)\cdot u_{\mathrm{ref}}(t)}{\sqrt{k_1\cdot k_2}}, \tag{5.1.6}$$

where $u_{\mathrm{e}}(t,\tau)$ is the current time trace, captured from the structure; $u_{\mathrm{ref}}(t)$ is the reference excitation signal. In the absence of a defect, only the direct arrival $U_{\mathrm{IIA}_0}(t)$ will be detected using eq. 5.1.6. Meanwhile in the presence of delamination, two wave packets of same mode ($U_{\mathrm{IA}_0}(t)$ and $U_{\mathrm{IIA}_0}(t)$) will be observed next to each other.

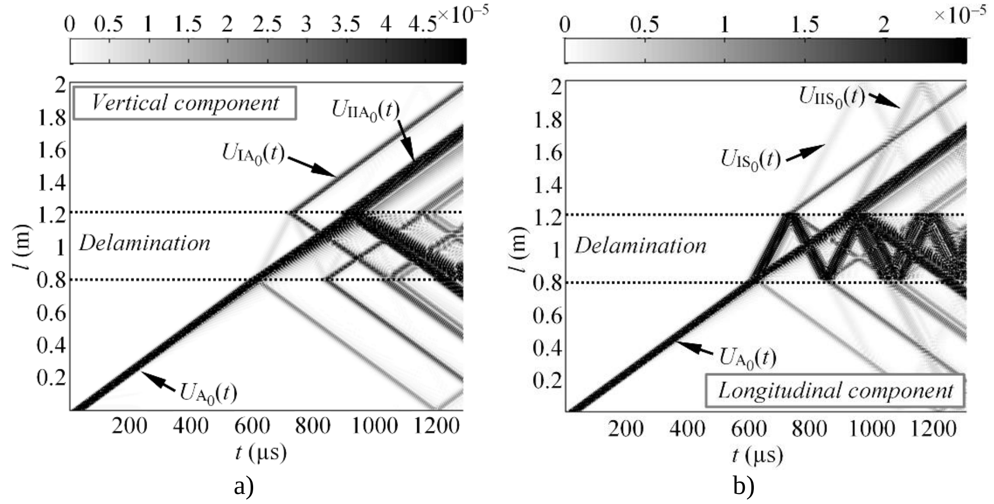

Fig. 5.1.3. The illustration of A_0 mode interaction with delamination: the B-scan images of vertical (a) and longitudinal (b) component of particle velocity along the top surface of the 4 mm thickness GFRP sample

The proposed approach to detect the existence of delamination is relatively simple and in general invariant to environmental conditions, as the likely temperature shifts will alter the arrival of all wave packets assuming that no temperature gradient is present in the structure. On the other hand, the proposed approach has some challenges to cope with as well. If the size of defect is relatively small compared to the wavelength, the converted $U_{\mathrm{IA}_0}(t)$ and the direct $U_{\mathrm{IIA}_0}(t)$ modes may be completely or partly overlapped in time domain. Thus, there is a minimum size of the detectable defect, which is a function of frequency and group velocities of A_0 and S_0 modes. It is presumed that the existence of a defect can be detected if the converted mode $U_{\mathrm{IA}_0}(t)$ is fully separated from the direct arrival $U_{\mathrm{IIA}_0}(t)$. It is noteworthy that in some cases, the converted A_0 mode might be concealed due to low signal to noise ratio or interference with other reflected modes from structural boundaries as well. Hence, the abovementioned points have to be considered during design of the monitoring system.

Method to estimate the depth of defect. In order to extract the depth of damage, the approach based on excitation of A_0 mode at different frequencies and constructive/destructive interference is proposed. As it was shown by eq. 5.1.3 the wave packet of direct A_0 mode is a superposition of the waves traveling at the layers below and above the damage. If the delamination is asymmetrical ($h_1 \neq h_2$) the phase velocities at these layers are different as well ($c_{p_1} \neq c_{p_2}$). The proof of change in the phase velocity upon the interaction with the defect can be seen in the zoomed B-scan image of the vertical component of the particle velocity, which is presented in Fig. 5.1.4. Beyond the defect, the modes from the different layers interfere with each other resulting in the single transmitted A_0 mode $U_{IIA_0}(t)$. The magnitude of this mode is proportional to the result of interference, which can be either in-phase, out-of-phase or intermediate, depending on the parameters of the defect. In general, the length and depth of the defect are related to each other and both of them influence the behaviour of GW simultaneously. However, some wave parameters, such as amplitude may appear to be more suitable to extract the depth, while others, like delay time – to estimate the length of the defect. Thus the idea of the proposed method to estimate the depth of damage relies on magnitude measurements of the direct A_0 mode $U_{IIA_0}(t)$ at different excitation frequencies (f_1, f_2, … f_n). Note, that technique is only valid if delamination is asymmetrical $h_1 \neq h/2 \neq h_2$.

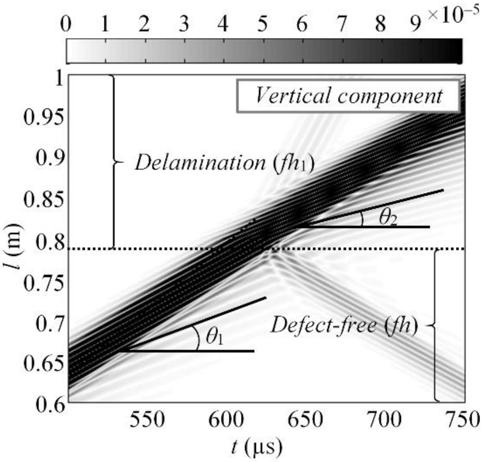

Fig. 5.1.4. The zoomed region of the B-scan image of vertical component of particle velocity, showing the change in phase velocity upon the interaction with defect

The proposed methodology to estimate the depth of delamination requires a baseline dataset, which would represent the analytical prediction of magnitude variation both due to the excitation frequency, depth and size of damage. Then the experimental measurements can be compared with the baseline data looking for best match. It is presumed that the baseline whose variation best matches the experiments is the one which gives the closest definition of damage depth in the structure. The step by step procedure of the damage depth estimation can be outlined as follows:

1. The emitter E is driven at frequency f_1, to introduce the A_0 mode in the investigated structure.
2. The time trace $U_{A_0}(t)$ is received with the sensor R_{ref}, which represents the structure without the damage. Meanwhile the other receiver R_i captures the

time history $U_{\mathrm{IIA}_0}(t)$, which represents the response of structure at monitoring point, beyond the likely defective area ($i = 1 \dots N$, N – is the number of receivers, depending on the implemented arrangement).

3. The ratio $U_{\mathrm{A}_0\exp f_1}$ of peak-to-peak amplitudes of waveforms $U_{\mathrm{A}_0}(t)$ and $U_{\mathrm{IIA}_0}(t)$ is estimated at the excitation frequency f_1.
4. The same procedure is repeated over for all available excitation frequencies $f = (f_1, f_2, \dots f_n)$. As the consequence, the experimental dataset $U_{\mathrm{A}_0\exp}(f) = \{f, U_{\mathrm{A}_0\exp f_1}, U_{\mathrm{A}_0\exp f_2}, \dots, U_{\mathrm{A}_0\exp f_n}\}$ is collected.
5. The experimental dataset $U_{\mathrm{A}_0\exp}(f)$ is compared to the prescribed database of analytical predictions $U_{\mathrm{A}_0\mathrm{ref}}(f,h,x)$ referred as the baseline (where h, x – are the depth and the length of damage respectively). Based upon this concept, the goal is to select the baseline that is the closest to the experimental data. The criteria to characterize the similarity of two datasets include the mean and standard deviation are as follows:

$$h_{\min_1} = \arg\min_h\left(\left|\operatorname*{mean}_x\left(u_{\mathrm{mean}}(h,x)\right)\right|\right),$$
$$u_{\mathrm{mean}}(h,x) = \operatorname*{mean}_f\left(U_{\mathrm{A}_0\mathrm{ref}}(f,h,x) - U_{\mathrm{A}_0\exp}(f)\right), \tag{5.1.7}$$

$$h_{\min_2} = \arg\min_h\left(u_{\mathrm{std}}(h,x)\right),$$
$$u_{\mathrm{std}}(h,x) = \operatorname*{std}_f\left(U_{\mathrm{A}_0\mathrm{ref}}(f,h,x) - U_{\mathrm{A}_0\exp}(f)\right), \tag{5.1.8}$$

   where $h_{\min_1}$ and $h_{\min_2}$ are the values that correspond to the delamination depth where the baseline best matches the experimental dataset; $U_{\mathrm{A}_0\mathrm{ref}}(f,h,x)$ is the analytically calculated baseline dataset; $U_{\mathrm{A}_0\exp}(f)$ is the experimental dataset; h and x are the depth and length of delamination respectively; mean and std denotes the mean value and the standard deviation.
6. If the structure is defect-free, there will be no variation in the ratio $U_{\mathrm{A}_0\exp}(f)$. Meanwhile if the variation in the magnitude ratio is observed, it can be related to the depth of the defect.

In the *in-situ* applications, the magnitude of the time series can be altered due to the attenuation and external factors such as transducer bonding, environmental, operational conditions etc. The proposed approach enables the influence of the most external factors to be eliminated, as the two signals recorded at the same time on the same structure are divided at locations before and after interaction with the defect. In most cases the ratio of the latter time series should be invariant to the external factors. As soon as the depth of the defect is known, the length of it can be estimated further, using the approach described in the next paragraph.

Technique to assess the length of defect. If the depth of the defect is known, the size of it can be estimated from the delay between the direct $U_{\mathrm{IIA}_0}(t)$ and converted $U_{\mathrm{IA}_0}(t)$ A_0 modes, which can be denoted as Δt_{A_0}. As mentioned above the A_0 mode converts to the S_0 at the leading edge of the delamination. Due to this phenomenon, the converted A_0 mode $U_{\mathrm{IA}_0}(t)$ arrives first compared to the direct one $U_{\mathrm{IIA}_0}(t)$, because the S_0 mode possess a velocity greater than the A_0 one. The separation Δt_{A_0} between the direct and converted A_0 modes is proportional to the excitation frequency and propagation path of S_0 mode, which itself is actually determined by the length of the defect (Fig. 5.1.5 for complete understanding). Thus, the delay time between wave packets $U_{IA_0}(t)$ and $U_{IIA_0}(t)$ at discrete excitation frequencies should be estimated in order to extract the length of damage. The time delay between two neighbouring wave packets can be estimated according to:

$$\Delta t_{A_0} = \arg\max_t \left[\mathrm{HT}\left(U_{IIA_0}(t)\right) \right] - \arg\max_t \left[\mathrm{HT}\left(U_{IA_0}(t)\right) \right] , \tag{5.1.9}$$

where $U_{IA_0}(t)$ and $U_{IIA_0}(t)$ are the wave packets of converted and direct A_0 mode respectively, and HT denotes the Hilbert transform. In most cases it should be sufficient to measure a delay at a single frequency only, especially if no major dispersion is present at the used frequency band.

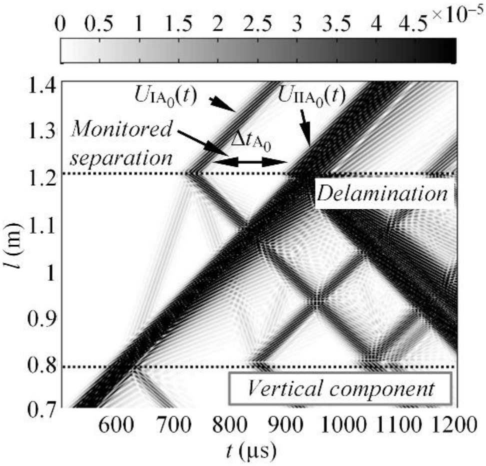

Fig. 5.1.5. The zoomed in region of the B-scan image of vertical component of particle velocity, showing separation between converted and direct A_0 modes beyond the defect

It is noteworthy that for the reliable operation of the method, again the direct and converted modes have to be separated to an adequate extent. Thus, there is a minimum size of defect that can be evaluated using this approach. Furthermore, it is important to bear in mind that in real-world situations the temperature shifts may alter the phase and group velocities of GW. If the influence of temperature appears to be different for asymmetrical and symmetrical modes, the delay Δt_{A_0} may vary as well.

5.2 Analytical estimation of the baseline dataset

As mentioned previously, the proposed technique to estimate the depth and size of delamination relies on a baseline, which means that the experimental signals must be compared to the model based analytical predictions to extract the features of the damage. In this chapter, the techniques to calculate the baseline datasets, which include the theoretical dependencies required to assess the depth and the length of the defect, will be introduced. Two separate baseline datasets will be estimated, one for damage depth and the other for size assessment.

In order to extract the depth of damage, the analytical dependencies between the magnitude of the transmitted A$_0$ mode $U_{\mathrm{A_0ref}}(f,h,x)$, excitation frequency ($f$) and depth ($h$) at fixed defect lengths (x) will be calculated. Meanwhile for damage size description, the separation in time domain between the converted $U_{\mathrm{IA_0}}(t)$ and direct $U_{\mathrm{IIA_0}}(t)$ A$_0$ modes as a function of defect length (x) and excitation frequency (f) will be estimated for the particular known depth (h). The baseline datasets have to be calculated for each investigated material separately including all possible excitation scenarios, defect sizes and through-thickness positions. In this study, for a better understanding, the estimation of baseline datasets will be demonstrated employing the 2D GFRP plate. To achieve the purpose of the baseline estimation, the analytical approach to predict waveform that passes through a medium will be implemented and described in the following paragraphs.

Technique to calculate the baseline dataset for defect depth assessment. To assess the depth of defect, the theoretical dataset of analytically predicted magnitude variations versus frequency at particular depths and defect lengths is required. In general, the goal is to analytically predict the part of eq. 5.1.3 that describes the propagation of A$_0$ mode within the defect area. Eq. 5.1.3 can be written in a short form as:

$$\begin{aligned} U_{\mathrm{IIA_0}}(\omega) &= \left(U_{\mathrm{sA_0}}(\omega)\cdot H\left(\omega, c_{\mathrm{p_0A_0}}, L-l_1\right)\right)\cdot\begin{pmatrix} k_{\mathrm{T01A}}\cdot H\left(\omega, c_{\mathrm{p_1A_0}}, l_1\right)\cdot k_{\mathrm{T10A}} + \\ + k_{\mathrm{T02A}}\cdot H\left(\omega, c_{\mathrm{p_2A_0}}, l_1\right)\cdot k_{\mathrm{T20A}} \end{pmatrix} = \\ &= U_{\mathrm{A_0}}(\omega)\cdot\left(U_{\mathrm{A_0ad}}(\omega) + U_{\mathrm{A_0bd}}(\omega)\right), \end{aligned} \tag{5.2.1}$$

where $U_{\mathrm{A_0ad}}(\omega)$ and $U_{\mathrm{A_0bd}}(\omega)$ represent the propagation of the A$_0$ mode above and below the delamination respectively. The sum of wave packets $U_{\mathrm{A_0ad}}(\omega)$ and $U_{\mathrm{A_0bd}}(\omega)$ determine the amplitude of transmitted A$_0$ mode $U_{\mathrm{IIA_0}}(\omega)$. The waveforms $U_{\mathrm{A_0ad}}(t)$ and $U_{\mathrm{A_0bd}}(t)$ can be predicted analytically according to the theory of linear acoustics, which states that the output waveform of the system is the convolution of the input signal and system impulse response. Consequently, each of the signals $U_{\mathrm{A_0ad}}(t)$ and $U_{\mathrm{A_0bd}}(t)$ can be expressed by the equations:

$$U_{\mathrm{A_0ad}}(t, x_k, h_{1m}, f_l) = k_{\mathrm{T01A}}\cdot k_{\mathrm{T10A}}\cdot\mathrm{Re}\left\{\mathrm{FT}^{-1}\left\{\mathrm{FT}\left(u_{\mathrm{ref}}(t, f_l)\right)\cdot\left|e^{-\alpha(f)x_k}e^{\frac{-jx_k f}{c_p(fh_{1m})}}\right|\right\}\right\}, \tag{5.2.2}$$

$$U_{\mathrm{A_0bd}}(t, x_k, h_{2m}, f_l) = k_{\mathrm{T02A}}\cdot k_{\mathrm{T20A}}\cdot\mathrm{Re}\left\{\mathrm{FT}^{-1}\left\{\mathrm{FT}\left(u_{\mathrm{ref}}(t, f_l)\right)\cdot\left|e^{-\alpha(f)x_k}e^{\frac{-jx_k f}{c_p(fh_{2m})}}\right|\right\}\right\}, \tag{5.2.3}$$

where $u_{\mathrm{ref}}(t, f_l)$ is the theoretical input signal at a particular excitation frequency ($l = 1 \div M$, where M is the total number of frequencies used to drive the emitter); $\alpha(f)$ is the attenuation function; x_k is the propagation path that is equal to the length of the defect ($k = 1 \div N$, where N is the total number of length incrementations); $c_{\mathrm{p}}(f,h_{1\mathrm{m}})$

and $c_p(f,h_{2m})$ are the phase velocities for the layer above (h_{1m}) and below the defect (h_{2m}), which depend on the amount of defect asymmetry; FT denotes the Fourier transform. The equations listed above enables the waveforms to be predicted, which exist at different frequency-thickness regions and propagates the distance equal to the length of the defect. The in-phase or out-of-phase sum of these signals define the magnitude of the transmitted A_0 mode $U_{A_0\mathrm{ref}}(x_k,h_{1m},h_{2m},f_l)$ at excitation frequency f_l:

$$U_{A_0}(x_k,h_{1m},h_{2m},f_l)=\max_t\left(U_{A_0\mathrm{ad}}(t,x_k,h_{1m},f_l)+U_{A_0\mathrm{bd}}(t,x_k,h_{2m},f_l)\right)- \\ -\min_t\left(U_{A_0\mathrm{ad}}(t,x_k,h_{1m},f_l)+U_{A_0\mathrm{bd}}(t,x_k,h_{2m},f_l)\right) \qquad (5.2.4)$$

Eq. 5.2.2–5.2.4 can be used to predict the magnitude of the directly transmitted A_0 mode at different defect depths, lengths and excitation frequencies by changing the appropriate parameters ($c_p(f,h_{1m})$, $c_p(f,h_{2m})$, x_k and f_l) in eq. 5.2.2 and eq. 5.2.3.

To illustrate the estimation of baseline dataset, let's consider the GFRP plate of thickness $h = 4$ mm, with the delamination type defects situated at the various depths as follows: $h_{1m} = mh/8$, $h_{2m} = h–h_{1m}$, where $m = 1, 2,…,3$. Assume that the excitation frequency of the incident A_0 mode varies starting from 50 kHz to 200 kHz with increments of 1 kHz. The graphic illustration of the magnitude of A_0 mode $U_{A_0\mathrm{ref}}(x_k,h_{1m},h_{2m},f_l)$ as the function of excitation frequency f_l at the discrete depths $h_{1m} = mh/8$, $h_{2m} = h–h_{1m}$ are illustrated in Fig. 5.2.1 and Fig. 5.2.2. The results are presented at the fixed defect lengths of $x_1 = 50$ mm, $x_2 = 70$ mm, $x_3 = 90$ mm and $x_4 = 110$ mm. The results demonstrate that the magnitude variation of transmitted A_0 mode depends both on the depth and length of the defect. However, as one might observe, the estimation of defect length is not so straightforward from these amplitude relationships. For example, if the defect is 0.5 mm below the surface, the magnitude variation versus frequency is almost identical at defect lengths of $x_3 = 90$ mm and $x_4 = 110$ mm (see Fig. 5.2.2). On the other hand, at any of the defect lengths the observed variations due to the depth are always different. It means that the amplitude variation is mostly suitable to estimate the depth rather than the length.

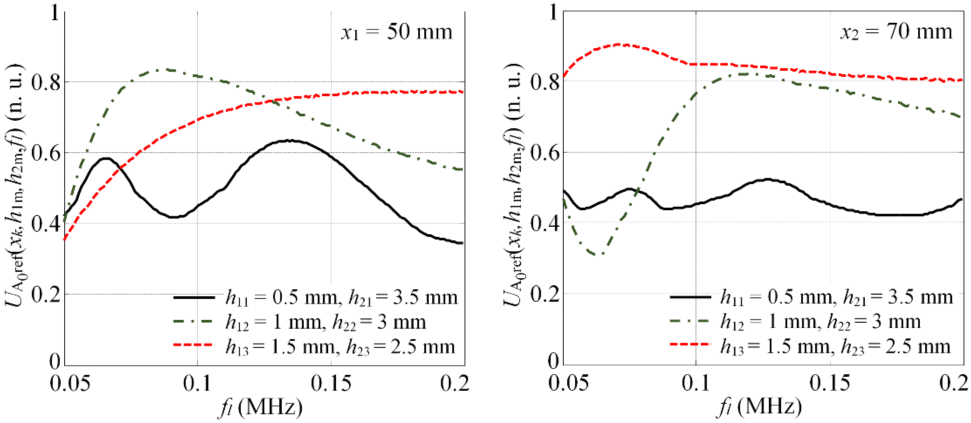

a) b)

Fig. 5.2.1. The magnitude variation of the transmitted A_0 mode versus frequency at different defect depths in case the length of defect is equal to $x_1 = 50$ mm (a) and $x_2 = 70$ mm (b)

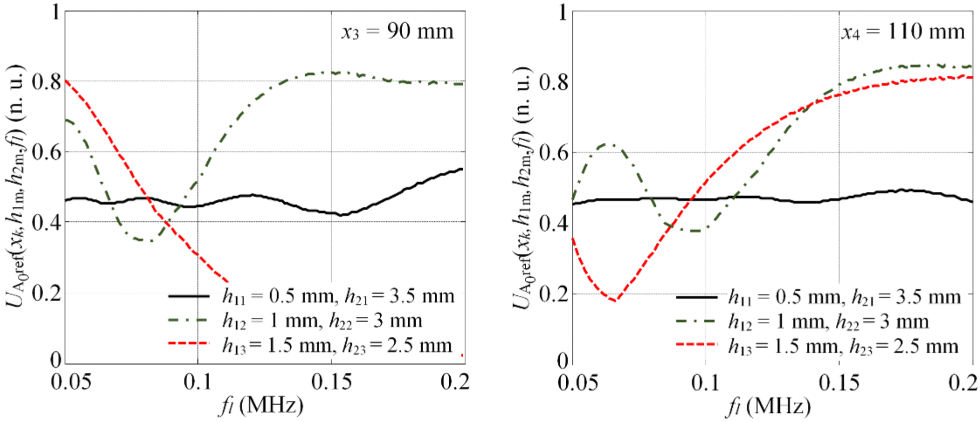

a) b)

Fig. 5.2.2. The magnitude variation of the transmitted A_0 mode versus frequency at different defect depths in case the length of defect is equal to x_3 = 90 mm (a) and x_4 = 110 mm (b)

***Technique to calculate the baseline dataset for assessment of defect length*.** Once the depth of the defect is known, the length of it can be estimated analysing the delay Δt_{A_0} between the direct and converted A_0 modes. As in the previous case, the damage size estimation requires a baseline, which would represent the delay Δt_{A_0} versus defect length x_k at a particular frequency and damage depth. The closest match will represent the actual length of the damage. The delay time is proportional to the difference in group velocities of A_0 and S_0 modes. The arrival time of the direct t_{A_0} and converted t_{A_0c} A_0 mode can be estimated using the simple relations:

$$t_{A_0}(x_k, f_l) = \frac{x_k}{c_{gA_0}(f_l, h)}, \quad t_{A_0c}(x_k, f_l) = \frac{x_k}{c_{gS_0}(f_l, h)}, \tag{5.2.5}$$

where $c_{gA_0}(f_l,h)$, $c_{gS_0}(f_l,h)$ are the group velocities of the A_0 and S_0 modes at particular depth h and excitation frequency f_l. Then the delay Δt_{A_0} as the function of frequency and defect length can be expressed as:

$$\Delta t_{A_0}(x_k, f_l) = t_{A_0c}(x_k, f_l) - t_{A_0}(x_k, f_l). \tag{5.2.6}$$

If again the 4 mm thickness GFRP plate is considered with the known defect depth of 1 mm below the surface (h_{12} = 1 mm, h_{22} = 3 mm), the arrival time of direct $t_{A_0}(x_k,f_l)$ and converted $t_{A_0c}(x_k,f_l)$ mode will be determined by the velocity at thicker layer h_{22}, as it possess greater velocity. Then the dispersion curves of A_0 and S_0 modes at that particular thickness will look like that presented in Fig. 5.2.3a. The results in Fig.5.2.3a demonstrate, that at low frequency-thickness values, the velocities of both modes can be similar. Meanwhile, increasing with the frequency, the velocities remain separated by almost the same amount. As an example, in this case the delays may be measured at the excitation frequencies f_1 = 50 kHz, f_2 = 70 kHz, f_3 = 190 kHz. The estimated length-delay relations at depth h_{12} = 1 mm, h_{22} = 3 mm and frequencies f_1, f_2 and f_3 are presented on Fig. 5.2.3b. As in the previous case, the experimentally obtained delay values at different frequencies are compared with the analytically predicted baseline looking for the best similarity.

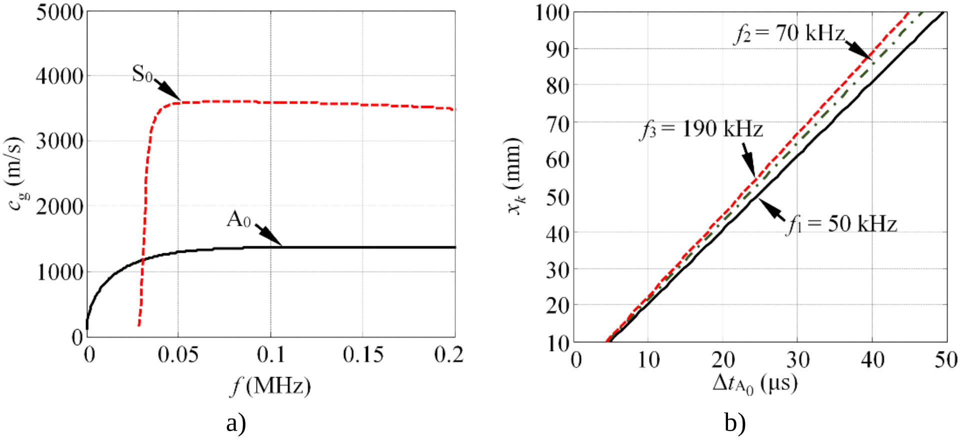

Fig. 5.2.3. The group velocity dispersion curves of the A_0 and S_0 modes on 3 mm GFRP plate (a), the estimated delay values between the direct and converted A_0 modes as a function of defect length and excitation frequency (b)

5.3 Numerical and experimental verification of baseline estimation technique

In the following chapter the analytical technique presented in the previous section, which can be used to estimate the amplitude variations due to the excitation frequency, length and depth of the defect is verified with the appropriate numerical simulations and experiments on the GFRP and aluminium samples. The goal of this validation is to prove that the assumptions made earlier, as well as the estimated amplitude variations correspond to the real-world situations. To achieve the purpose of this study, the numerically and experimentally estimated amplitude variations due to the increasing length of the defect at constant excitation frequency and depth are compared to the analytical predictions calculated with eq. 5.2.4. It is presumed that if a good match is achieved at one particular defect depth and excitation frequency, then the analytical results can be treated as trustworthy for the rest of the frequencies and depths as well. In the upcoming paragraphs, the numerical model and experimental set-up used for the validation will be briefly described followed by the appropriate comparison of the results.

Numerical validation of the baseline dataset. To fulfil the scope of this study, a total number of 50 2D linear structural mechanics FE models were employed for an anisotropic GFRP plate with the dimensions of x = 2,000 mm, y = 4 mm. In this case it was presumed that the object is long in the z direction and the loads act in the xy plane, so the problem to solve was a plane-strain one. In each of the 50 models, delamination type defects were introduced 1.5 mm below the surface (h_1 = 1.5 mm, h_2 = 2.5 mm) by separating the appropriate nodes of the mesh. The length of the delamination x varied from 10 mm to 500 mm with increment of 10 mm, yielding a total number of 50 numerical models. The delamination was centred horizontally along the x axis of the investigated sample. Throughout the simulations, 2D structural solid plane42 finite elements were used. The spatial size of the element was equal to 0.5 mm, which corresponds to the 26 nodes per wavelength if the slowest A_0 mode at 80 kHz central frequency is considered. The excitation signal in all cases was a Gaussian envelope tone burst of 3 cycles and a central frequency of 80 kHz. The A_0 mode was introduced by applying the normal out-of-plane nodal displacements to the edge of the sample. The integration step in time domain was 0.625 μs, which is 1/20 of the period at 80 kHz central frequency. The sketch of the numerical model used in this study is presented in Fig. 5.3.1.

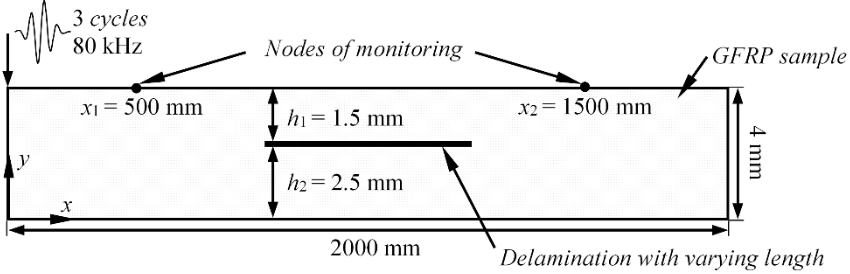

Fig. 5.3.1. The sketch of the numerical model used for validation of analytical predictions

The variable monitored in this study was a vertical displacements (y) at the nodal locations before (x_1 = 500 mm, y_1 = 4 mm) and beyond (x_2 = 1,500 mm, y_2 = 4 mm) the defect (see Fig. 5.3.1). The peak-to-peak amplitude ratio of A_0 mode at these nodal points was compared to the analytical predictions estimated with eq. 5.2.4. In the analytical calculations (eq. 5.2.2 and eq. 5.2.3), the DC of 1.5 mm and 2.5 mm GFRP plate was used to define the phase velocities for the layer above (h_{1m}) and below the defect (h_{2m}). The theoretical input signal $u_{\mathrm{ref}}(t, f_l)$ was a Gaussian envelope tone burst of 3 cycles and a central frequency of 80 kHz. The length of the defect ranged from 1 mm, to 500 mm with increments of 10 mm. Attenuation $\alpha(f)$ and coefficients k_{T01A}, k_{T10A}, k_{T02A} and k_{T20A} were ignored. The numerically and analytically estimated amplitude variations due to the change of defect length in case the delamination is positioned 1.5 mm below surface can be seen in Fig. 5.3.3a, which is presented at the end of this section. The solid line in the results presented below stands for analytical predictions, meanwhile the dashed line represents the numerical simulations.

Experimental verification of the baseline dataset. In addition to the numerical calculations, the experiments on a custom made aluminium alloy plate with dimensions of 1250 mm × 600 mm × 5 mm were carried out as well. A special aluminium sample with an artificial air gap was produced in order to obtain the response adequate to that with the delamination type defect. Such simple and well known material was deliberately selected for simplicity of controlling the size and properties of the artificial defect. In the production of the sample, two aluminium sheets with thicknesses of 2 mm and 3 mm were bonded together, to produce a total thickness of 5 mm. The air gap at the interface of the sheets was introduced at particular locations of the sample by machining a thin wedge shaped groove. The lateral dimensions of the air gap were ranging from 35 mm to 335 mm, which enabled the delamination type defect of variable size to be simulated. The sketch of the experimental set-up used for validation purposes is presented in Fig. 5.3.2.

The experimental investigation was performed using low frequency ultrasonic transducers (130 kHz) operating in a thickness mode. The transducers were arranged in a pitch-catch configuration and attached perpendicularly to the surface of the sample to introduce A_0 mode. To achieve reliable and uniform acoustic contact between the transducer and the specimen, special spring type adjusters were used. The transmitter and receiver were linked together and scanned along the short edge of artificial defect as it is shown in Fig. 5.3.2. The results of experiment, the set of waveforms at different defect lengths, was collected. The peak-to-peak amplitude of each time trace was compared to the reference time history captured at the same basis on the defect free region.

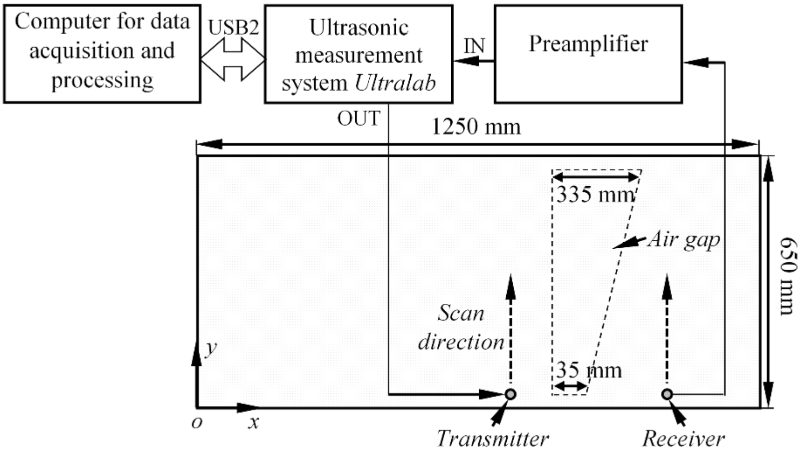

Fig. 5.3.2. The illustration of experimental set-up used to validate the analytical predictions

For the analytical predictions, the DC of 2 mm and 3 mm aluminium plate was used to define the phase velocities for the layers above (h_{1m}) and below (h_{2m}) the defect in eq. 5.2.2 and eq. 5.2.3. The theoretical input signal $u_{\text{ref}}(t, f_l)$ was a Gaussian envelope tone burst of 3 cycles and a central frequency of 130 kHz. As in the previous case, the attenuation $\alpha(f)$ and coefficients k_{T01A}, k_{T10A}, k_{T02A} and k_{T20A} were ignored. The length of the defect x_k varied from 1 mm, to 400 mm with increments of 1 mm. The experimentally and analytically estimated amplitude variations due to the change of defect length can be seen in Fig. 5.3.3b. Again, the solid and the dashed lines represents the analytical and experimental results respectively.

The results presented Fig. 5.3.3 demonstrate a quite good agreement between the numerical, experimental and analytical predictions, especially below the defect lengths of 200 mm. The numerical calculations (Fig. 5.3.2a) demonstrated good agreement between the values of amplitude ratio U_{A_0}, meanwhile, the experimental estimations (Fig. 5.3.2b) showed a good match in terms of periodicity of local extrema in the ratio U_{A_0}. Hence, it can be presumed that the analytically calculated baselines can be used with some certain confidence to detect the defects smaller than 200 mm. The mismatch in the amplitude ratio between the analytical and experimental estimations, which can be observed in Fig. 5.3.2b, may be due to the ignored transmission coefficients in eq. 5.2.2 and eq. 5.2.3. These coefficients depend on the material, frequency, depth of defect and conversion of energy to other modes, thus they have to be estimated each time prior to the investigation of any structure. The estimation of actual values of coefficients k_{T01A}, k_{T10A}, k_{T02A} and k_{T20A} is not very straightforward, as they are different at the leading and trailing edges of the damage. Thus, the estimation of k values was out of the scope of this study. In the following section, the procedure of detecting and describing the damage will be demonstrated with the numerical models that contain delaminations of different size and depth.

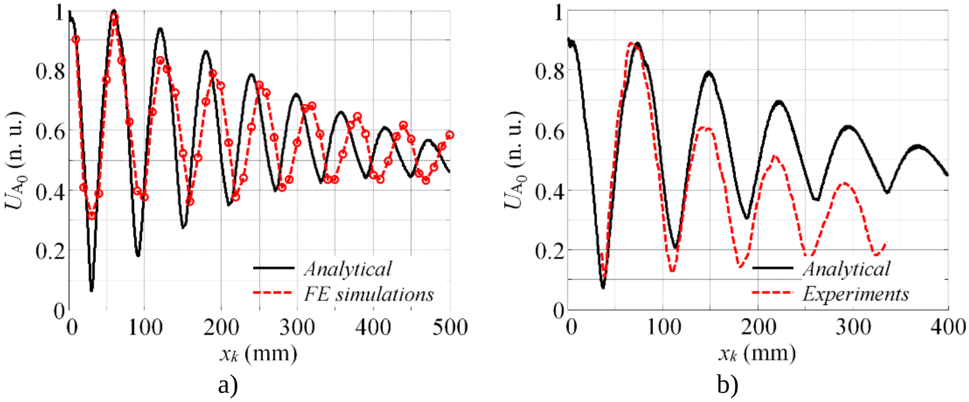

Fig. 5.3.3. The amplitude variation due to the size of defect: the analytical predictions along with numerical verification on the GFRP sample (a), the analytical estimations together with experimental validation on the aluminium sample (b)

5.4 Numerical validation of performance of the proposed method

In the following chapter, the procedure on how the defects can be detected and distinguished from each other will be demonstrated utilising the proposed method. For this purpose, two separate 2D GFRP numerical models both with dimensions of 2,000 mm × 4 mm will be considered. For the sake of better understanding, let's denote them as "sample No. 1" and "sample No. 2". Each of the considered models contain delaminations of different sizes and through-thickness locations. In "sample No. 1", the $x_1 = 70$ mm wide delamination is introduced 1 mm below the top surface ($h_{11} = 1$ mm, $h_{21} = 3$ mm). Meanwhile, "sample No. 2" has a defect of $x_2 = 90$ mm, located at a depth of 1.5 mm ($h_{12} = 1.5$ mm, $h_{22} = 2.5$ mm). In both cases the delamination was centred horizontally along the x axis of the investigated sample. The sketch of the considered cases is presented in Fig. 5.4.1.

Throughout the simulations, 2D structural solid plane42 finite elements were used. In each of the investigated cases the frequency sweep excitation employing the Gaussian envelope tone burst of 3 cycles was used. The excitation frequencies ranged from $f_1 = 50$ kHz to $f_n = 200$ kHz with increments of 10 kHz. Hence, 16 different excitation frequencies were used for each of the considered models. The spatial size of the element in all cases was constant and equal to 0.5 mm, which corresponds from 37 to 12 nodes per wavelength for the slowest A_0 in a frequency range of f_1, f_2, …, f_n. The A_0 mode was introduced into the structure by applying the normal out-of-plane nodal displacements to the edge of sample in the same way as it was demonstrated in

Fig. 5.3.1. The integration step in time domain varied from 1 μs for the lowest excitation frequency $f_1 = 50$ kHz, to 0.25 μs for $f_n = 200$ kHz. The variable monitored in this study was a vertical displacements (y) at the nodal locations r_1 ($x_1 = 750$ mm, $y_1 = 4$ mm) and r_2 ($x_2 = 1250$ mm, $y_2 = 4$ mm), where r_1 is the waveform before the defect, meanwhile r_2 is the waveform after interaction with the defect. In the following sections estimations of the existence, depth and size of the defect will be demonstrated.

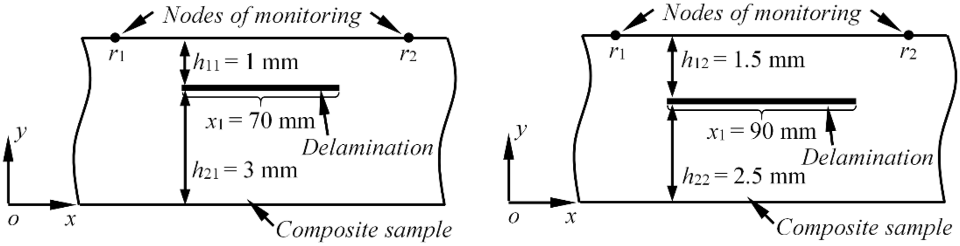

a) b)

Fig. 5.4.1. The graphic representation of investigated cases: “sample No. 1” with 70 mm wide delamination located 1 mm below the surface (a), “sample No. 2” with delamination of 90 mm at depth of 1.5 mm (b)

Defect detection. As it was mentioned previously, in order to detect the existence of a defect, it is proposed to monitor the appearance of converted A_0 $U_{IA_0}(\omega)$ mode, which arrives faster than the direct A_0 $U_{IIA_0}(\omega)$. In this case both defects can be reliably found at the frequencies of 130 kHz and above. However, for the sake of simplicity, the results will be presented for the frequency $f_9 = 130$ kHz only. The vertical component of the particle velocity at nodal point r_2 for both of investigated samples is presented in Fig. 5.4.2a,b. The short-time cross-correlation between the current time trace and the excitation signal (see eq. 5.1.6) is presented in Fig. 5.4.3c,d.

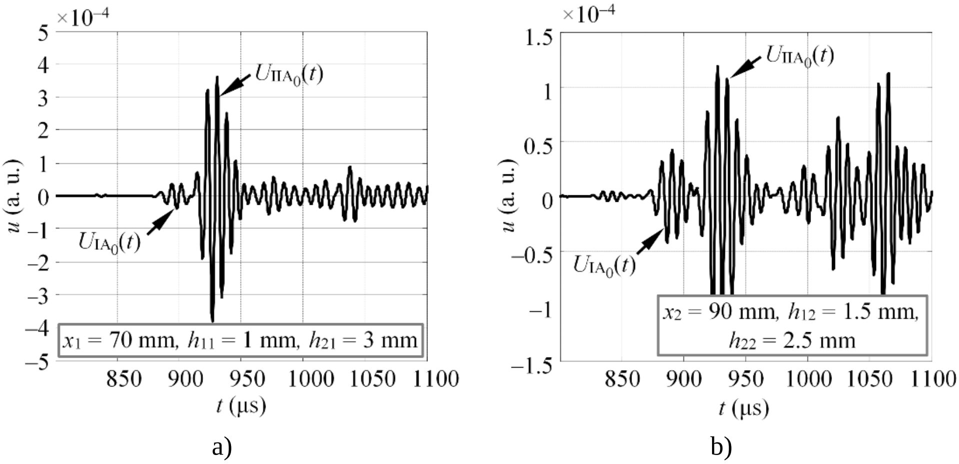

a) b)

Fig. 5.4.2. The vertical component of the particle velocity at nodal point r_2 beyond the defect for “sample No. 1” (a), “sample No. 2” (b)

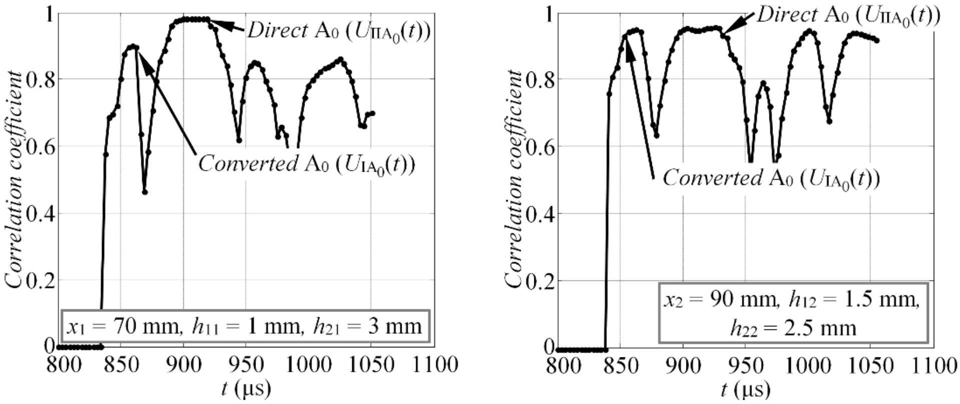

a) b)

Fig. 5.4.3. The short-time cross-correlation between the current time trace and the excitation signal for "sample No. 1" (a) and "sample No. 2" (b)

The results above demonstrate, that in both cases the converted A_0 mode can be easily detected using the frequency of $f_9 = 130$ kHz and the correlation coefficient threshold of 0.8 and above, if the estimated arrival of the direct A_0 mode is known. The magnitude of converted $U_{\text{IA}_0}(\omega)$ mode is –10 dB for "sample No. 1" and –4 dB for "sample No. 2" relative to the direct arrival $U_{\text{IIA}_0}(t)$. For the proposed technique to function properly, it is recommended to estimate the short-time cross-correlation for each excitation frequency to reliably detect the likely appearance of $U_{\text{IA}_0}(t)$ mode.

Estimation of defect depth. In order to estimate the depth of the defect, the procedure described in section 5.1 is employed. The analytical baseline is calculated according to eq. 5.2.2–5.2.4 for the defect lengths x_1 = 10 mm, x_2 = 11 mm, …, x_N = 100 mm and defect depths h_{11} = 0.5 mm, h_{12} = 1 mm, h_{13} = 1.5 mm for the same set of excitation frequencies (f_1 = 50 kHz, f_2 = 60 kHz, …, f_n = 200 kHz). Then the h_{min_1} and h_{min_2} are calculated using eq. 5.1.7 and eq. 5.1.8 to estimate the depth of damage. The graphic illustration of $u_{\text{mean}}(h,x)$ and $u_{\text{std}}(h,x)$ at different lengths and depths is presented in Fig. 5.4.4.

The criteria to estimate the actual depth of defect is based on the selection of the average $u_{\text{mean}}(h,x)$ value which is closest to zero and the minimum of $u_{\text{std}}(h,x)$ (see eq. 5.1.7 and eq. 5.1.8). The estimated h_{min_1} and h_{min_2} values for "sample No. 1" and "sample No. 2" at different depths are summarized in Table 5.4.1.

The results presented in Table 5.4.1 show that values of h_{min_1} and h_{min_2} may be used to discriminate the depth of damage. For example, it can be observed that for "sample No. 1" (Fig. 5.4.4a,b) h_{min_1} is close to zero for the depth h_{12} = 1 mm (dash-dot line in Fig. 5.4.4a), meanwhile h_{min_2} has a minimum at the same depth as well (dash-dot line in Fig. 5.4.4b). Hence, the estimated depth of delamination for "sample No. 1" is 1 mm, which corresponds to the actual depth of the damage. Similar observations may be made for "sample No. 2". The h_{min_1} and h_{min_2} possess the lowest values at the depth h_{13} = 1.5 mm (dashed line in Fig. 5.4.4c,d), which is in agreement with the actual depth of damage. As one might observe, the values presented in

Table 5.4.1 are relatively close to each other, however they indicate the correct depth of delamination in both cases, despite the investigated sample being very thin (4 mm) and the excitation frequencies were quite low (up to 200 kHz, wavelength of A_0 mode up to 6.1 mm).

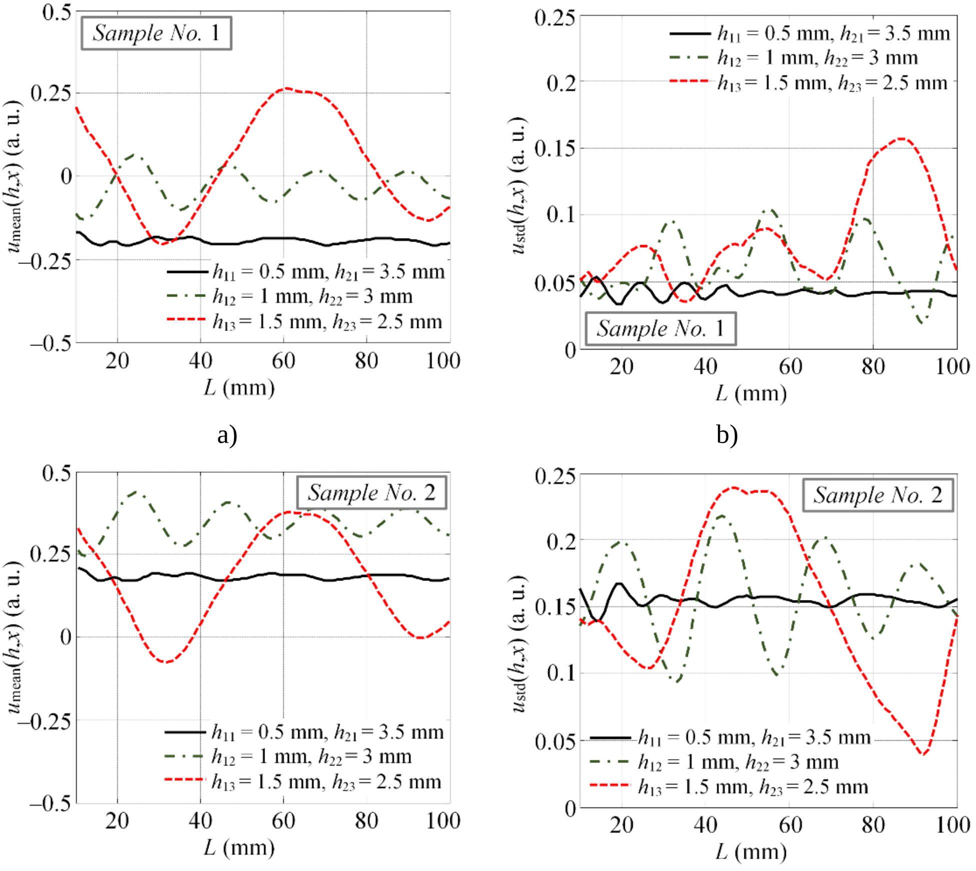

a) b)

c) d)

Fig. 5.4.4. The mean and deviation values of difference between the experimental and analytical baseline: the results for “sample No. 1” with defect located 1 mm below the surface (a,b), the results for “sample No. 2” with delamination situated at depth of 1.5 mm (c,d)

Table 5.4.1. The $h_{\min_1}$ and $h_{\min_2}$ values for “sample No. 1” and “sample No. 2” which are used as a criterion to estimate the depth of delamination

	Sample No. 1		**Sample No. 2**	
	$h_{\min_1}$	$h_{\min_2}$	$h_{\min_1}$	$h_{\min_2}$
h_{11} = 0.5 mm, h_{21} = 3.5 mm	0.195	0.033	0.179	0.137
h_{12} = 1 mm, h_{22} = 3 mm	**0.03**	**0.018**	0.344	0.091
h_{13} = 1.5 mm, h_{23} = 2.5 mm	0.034	0.035	**0.158**	**0.036**

Evaluation of the defect length. As the depth of defect for both samples is known, the length is estimated by measuring the delay between the converted $U_{\mathrm{IA}_0}(t)$ and direct $U_{\mathrm{IIA}_0}(t)$ A_0 mode. The delays are measured according to the maximum envelope values of each wave packet, using eq. 5.1.9. In this particular case due to a large amount of data, the delay values are estimated at a single excitation frequency f_9 = 130 kHz and then compared to the analytical baselines calculated by eq. 5.2.6 to extract the length of the damage.

The vertical component of the particle velocity at nodal point r_2 for “sample No. 1” and “sample No. 2” are presented in Fig. 5.4.5a,b. The picture shows the wave packets of converted $U_{\mathrm{IA}_0}(t)$ and direct $U_{\mathrm{IIA}_0}(t)$ A_0 mode, along with the estimated delay values according to the Hilbert envelope. The analytically estimated delay versus the length of the defect at depth h_{12} = 1 mm for “sample No. 1” and h_{13} = 1.5 mm for “sample No. 2” can be seen in Fig. 5.4.5c,d respectively.

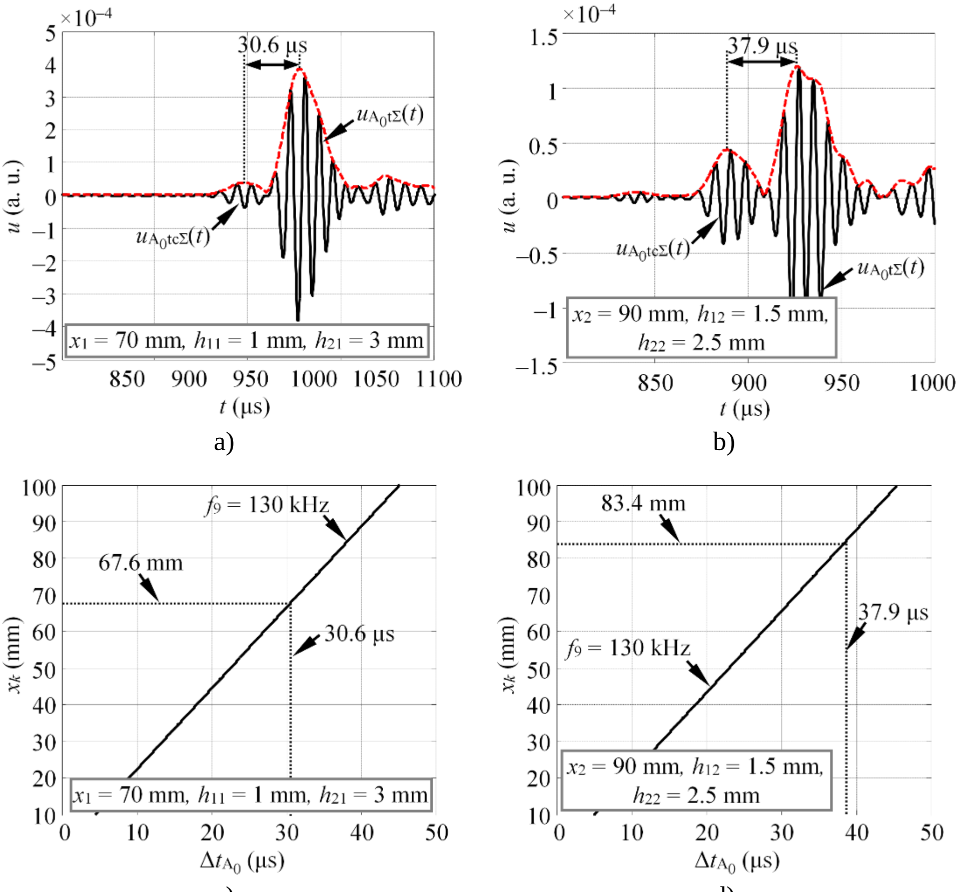

a) b)

c) d)

Fig. 5.4.5. The vertical component of the particle velocity at the nodal point r_2 for “sample No. 1” (a) and “sample No. 2” (b) showing the converted and direct A_0 modes along with an estimated delay values and the analytically obtained delay versus defect length for “sample No. 1” (c) and “sample No. 2” (d), showing the estimated size of damage

The results demonstrate that the estimated delay values correspond to the defect length of 67.6 mm for “sample No. 1”, meanwhile for “sample No. 2” the delay indicates the length of 83.4 mm. The results demonstrate that the average error in the length estimation is approximately 5% relative to the actual size. The amount of error depends on the proper selection of dispersion relations required for analytical predictions, as well as the accuracy of delay estimation from the experimental data.

5.5 Conclusions of Chapter 5

1. The model based baseline method to detect and describe the delamination type defect was proposed, exploiting the frequency sweep excitation, mode conversion and constructive/destructive interference of the A_0 mode. The proposed technique features one side access and can provide the information about the existence, depth and size of the damage even at a relatively narrow frequency bandwidth.
2. The proposed method is limited to the detection of delamination type defects on flat, uniform thickness structures only, where the defect is located anywhere but in the middle across the thickness of the sample. On the other hand, it can be used to detect and describe the damage on both isotropic and multi-layered anisotropic structures, possessing complicated geometries.
3. The special analytical method to create a baseline dataset, required to extract the depth and length of defect was developed. The baseline dataset enables the amplitude and delay time variation due to the size, depth of defect and frequency of excitation for any 2D investigated structure to be predicted. Furthermore, the analytically calculated baselines were validated with appropriate numerical simulations and experiments showing a good agreement, especially for the defects smaller than 200 mm.
4. The performance of the proposed method was demonstrated and verified detecting and describing two delamination type defects of different lengths and depths. It was demonstrated, that the depth of the damage can be estimated analysing the amplitude variations of the transmitted A_0 mode, meanwhile the size can be extracted from the delay time between the wave packets of converted and direct A_0 modes. The results of numerical validation demonstrated that the size of defect can be reconstructed with an error of approximately 5%.
5. The study revealed several limitations of the proposed method as well. First of all, the wave packets of converted and direct A_0 modes have to be separated from each other in time domain in order to be able to detect and estimate the size of damage. Furthermore, for correct damage depth estimation it is important to carefully set the values of transmission and reflection coefficients k at the leading and trailing edges of the defect. The actual values of these coefficients depend on material, frequency, depth of the defect and energy conversion to other modes. Finally, the error in the damage depth and length estimation is directly proportional to the error in setting the phase velocity, which is required for calculation of the baseline.

6. A TECHNIQUE TO SIMULATE THE RESPONSE OF DELAMINATION TYPE DEFECTS

6.1 Motivation and background of the proposed technique

The design of any structural health monitoring system is a multi-step process that involves: the definition of damage that has to be detected; choice of the physical measurands and damage sensitive features; formulation and validation of the developed methods and installation to the in-service structures. Currently there are many ultrasonic SHM methods available, which are capable of detecting defects of different kinds employing various physical measurands and signal processing techniques. Most of them are well tested and have demonstrated a feasibility in the controlled laboratory environments, which presumably reproduces the real-world conditions. The vast majority of the laboratory studies involve detection of defects, such as cracks, corrosion or delaminations. To get the response of the defect, special samples are usually produced by introducing some special artificial inserts in the structure of an object. In such way, the developed SHM system can be tested and validated. However, the progress of these methods towards the in-field use is still limited, as the laboratory and real-world environments are never the same. Due to this reason, upon the installation of any SHM system, it has to be somehow re-validated, with the general purpose to make sure that the performance of it is the same as it is supposed to be. During the implementation phase of the SHM system, it is usually scaled, going from the compact laboratory samples, to the real structures, hence the confirmation test of correctness of the system design becomes an important feature. However, the in-service structures can no longer be damaged or affected by any other means that are usually available in the laboratory environment. Moreover, during the exploitation of the monitoring system, most parts of it including the transducers, bonding and hardware tend to degrade, thus performance of the in-service SHM systems have to be checked periodically as well. In contrast to SHM, the conventional NDE systems are always calibrated first, employing known calibration blocks, prior to testing of the in-field structures. Whereas the calibration of the SHM system is an open and challenging task, since currently there are no available calibration standards. Thus, the verification of the SHM systems is usually limited to the proof of simple functioning.

The aim of this study was to develop a theoretical calibration method that would be suitable to proof the performance and to test the sensitivity of the in-field SHM systems. The method proposed in this research has a general purpose to non-destructively imitate the response of a delamination type defect. In such a way, the performance of the in-service SHM system can be tested and the sensitivity to the defects of different sizes can be estimated without damaging the structure. The idea of the proposed method relies on the hypothesis, that the effect of wave trapping inside the delaminated area with some limitations can be reproduced with the artificial calibration block of certain geometry and size attached to the surface of the structure. For the sake of better understanding, let's again analyse the structure, which is presented in Fig. 6.1.1. Assume that the analysed structure holds the delamination type defect of width l_1, the edges of which are situated at the distances l_0 and l_2 in respect to the source of guided waves and the monitoring point respectively.

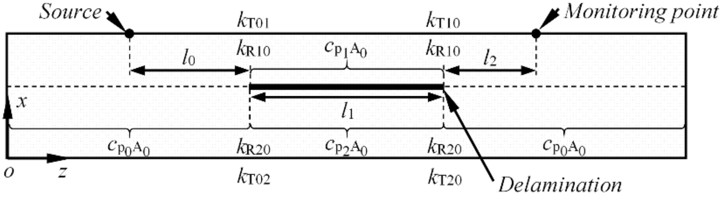

Fig. 6.1.1. The sketch of the analysed problem of guided wave interaction with delamination

If the A_0 mode is introduced into the structure, the directly transmitted wave packet $U_{d_IA_0}(\omega)$ at the monitoring point can be expressed mathematically as the superposition of two wave packets, traveling above and below the damage:

$$\begin{aligned}
&U_{d_IA_0}(\omega)=U_{sA_0}(\omega)\cdot H\left(\omega,c_{p_0A_0},l_0\right)\cdot k_{T01}\cdot H\left(\omega,c_{p_1A_0},l_1\right)\cdot k_{T10}\cdot H\left(\omega,c_{p_0A_0},l_2\right)+\\
&+U_{sA_0}(\omega)\cdot H\left(\omega,c_{p_0A_0},l_0\right)\cdot k_{T02}\cdot H\left(\omega,c_{p_2A_0},l_1\right)\cdot k_{T20}\cdot H\left(\omega,c_{p_0A_0},l_2\right)=\\
&=\left(U_{sA_0}(\omega)\cdot H\left(\omega,c_{p_0A_0},L-l_1\right)\right)\cdot\\
&\cdot\left(k_{T01}\cdot H\left(\omega,c_{p_1A_0},l_1\right)\cdot k_{T10}+k_{T02}\cdot H\left(\omega,c_{p_2A_0},l_1\right)\cdot k_{T20}\right),
\end{aligned}\tag{6.1.1}$$

$$H\left(\omega,c_{pA_0},l\right)=e^{-\alpha(\omega)x}e^{\frac{-jl\omega}{c_{pA_0}(\omega)}},\tag{6.1.2}$$

where $U_{sA_0}(\omega)$ is the frequency representation of the A_0 mode upon its introduction into the structure; $H(\omega,c_p,l)$ is the frequency response of the analysed system; $\alpha(\omega)$ is the attenuation function; $c_p(\omega)$ is the phase velocity; l is the propagation distance; L is the separation between the source and the monitoring point ($L = l_0 + l_1 + l_2$); k_{T01}, k_{T02}, k_{T10} and k_{T20} are the transmission coefficients at the leading and trailing edges of the delamination for the layers above and below the damage respectively; k_{R10} and k_{R20} are the reflection coefficients in the layers above and below the damage, which are required to describe the trapped wave. The first part of eq. 6.1.1 ($U_{sA_0}(\omega)\cdot H(\omega,c_{p_0A_0},L-l_1)$) represent the propagation of the A_0 mode in the defect free area, meanwhile the second part ($k_{T01}\cdot H(\omega,c_{p_1A_0},l_1)\cdot k_{T10}+k_{T02}\cdot H(\omega,c_{p_2A_0},l_1)\cdot k_{T20}$) describe the transmission below and above the damage. Upon the interaction of the A_0 mode with the delamination, the wave packet of A_0 mode gets trapped inside the defect by reflecting back and forth multiple times. Due to this reason, the decaying repetitive transmissions of the A_0 mode will be observed at the monitoring point as well. Thus, similarly to eq. 6.1.1, the first repetitive transmission or in other words the second wave packet of A_0 mode $U_{d_{II}A_0}(\omega)$ at the monitoring point can be described as:

$$\begin{aligned}
&U_{d_{II}A_0}(\omega)=U_{sA_0}(\omega)\cdot H\left(\omega,c_{p_0A_0},l_0\right)\cdot k_{T01}\cdot H\left(\omega,c_{p_1A_0},l_1\right)\cdot k_{R10}\cdot H\left(\omega,c_{p_1A_0},l_1\right)\cdot\\
&\cdot k_{R01}\cdot H\left(\omega,c_{p_1A_0},l_1\right)\cdot k_{T10}\cdot H\left(\omega,c_{p_0A_0},l_2\right)+U_{sA_0}(\omega)\cdot H\left(\omega,c_{p_0A_0},l_0\right)\cdot k_{T02}\cdot\\
&\cdot H\left(\omega,c_{p_2A_0},l_1\right)\cdot k_{R20}\cdot H\left(\omega,c_{p_2A_0},l_1\right)\cdot k_{R02}\cdot H\left(\omega,c_{p_2A_0},l_1\right)\cdot k_{T20}\cdot H\left(\omega,c_{p_0A_0},l_2\right).
\end{aligned}\tag{6.1.3}$$

Such repetitive wave transmission behaviour happens until the transmitted wave packet is completely attenuated. If N_g repetitive transmissions of the A_0 mode are considered, then eq. 6.1.3 can be re-written in a form as follows:

$$U_{\mathrm{dA_0}}(\omega)=\left(U_{\mathrm{sA_0}}(\omega)\cdot H\left(\omega,c_{\mathrm{p_0A_0}},L-l_1\right)\right)\cdot$$
$$\cdot\sum_{N=0}^{N_{\mathrm{g}}}\left(\begin{array}{l}\left(k_{\mathrm{T01}}\cdot k_{\mathrm{T10}}\cdot k_{\mathrm{R10}}^{2N}\cdot H\left(\omega,c_{\mathrm{p_1A_0}},(2N+1)\cdot l_1\right)\right)+\\ +\left(k_{\mathrm{T02}}\cdot k_{\mathrm{T20}}\cdot k_{\mathrm{R20}}^{2N}\cdot H\left(\omega,\mathrm{c}_{\mathrm{p_2A_0}},(2N+1)\cdot l_1\right)\right)\end{array}\right). \tag{6.1.4}$$

Note that eq. 6.1.1 and eq. 6.1.4 describe the repetitive wave transmission only in the absence of mode conversion, which inevitably happens at each end of the defect. The main purpose of this study is to develop a method to reproduce such repetitive wave transmission at the monitoring point defined by eq. 6.1.4 ($N \geq 1$), without damaging the structure. It is noteworthy that it is impossible to non-destructively reproduce direct A_0 mode transmissions defined by eq. 6.1.1, which is delayed due to presence of damage. However, it will be demonstrated later that the method proposed in this research enables the transmission of subsequent wave packets to be reproduced in terms of ToF as it was described in eq. 6.1.4 ($N \geq 1$). For the graphic illustration of the goal of this study, assume that the A_0 mode is introduced into the 2 m long and 4 mm thick GFRP plate with the 150 mm delamination situated 1.5 mm below the surface. The typical B-scan image along the surface of the sample will look like that presented in Fig. 6.1.2a. The results in the latter figure demonstrate that multiple reflections of A_0 mode are inside the delaminated area, which produces the multiple transmissions beyond the defect as well. The received signal at the distance of 1.25 m on the surface of the sample is presented in Fig. 6.1.2b. This picture illustrates the aim of this study, which is to reproduce multiple repetitive transmissions ($U_{\mathrm{d_{II}A_0}}(t)$, …, $U_{\mathrm{d_{Ng}A_0}}(t)$) of the A_0 mode (see wave packets in square dashed boxes), yet without intervention into the structure.

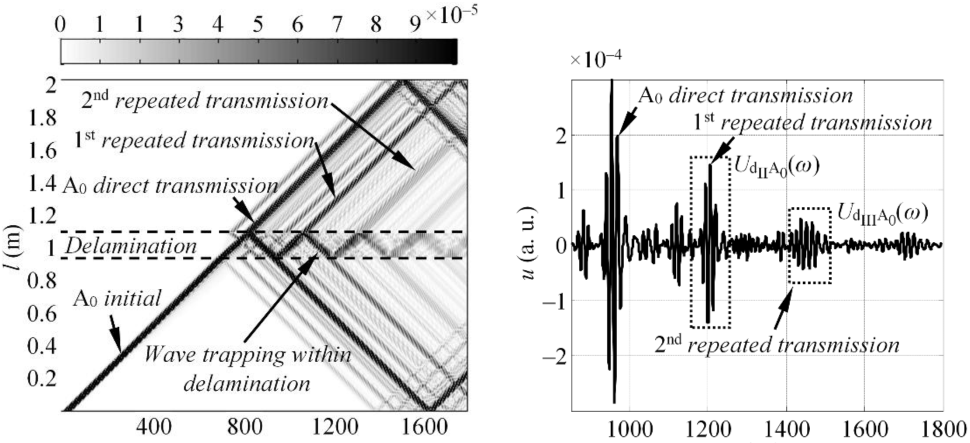

a) b)

Fig. 6.1.2. The B-scan image of the vertical component of the particle velocity on GFRP plate. The 150 mm long delamination is situated 1.5 mm below the top surface (a) and the appropriate signal acquired on the surface of the sample at the distance of 1,250 mm, showing the wave packets that are intended to be non-destructively reproduced (b)

Note, that in general the mechanism of guided wave interaction with delamination is much more complicated, as the mode conversion occurs after each wave reflection (see intermediate reflections in Fig. 6.1.2b). However, in this study, the analysis is limited to the repetitive transmission of the A_0 mode only, neglecting the conversion to other modes. Moreover, the reproduction of the shape or the amplitude of the wave packet was out of the scope of this study, as the main focus will be given to the estimation of the correct ToF, which itself is related with the length of the damage.

The sketch of the proposed configuration for non-destructive imitation of "trapped" wave behaviour is presented in Fig. 6.1.3. The proposed configuration consists of two rectangular blocks of any material, attached to the surface of the sample, where each of them is devoted to imitate the wave propagation at the layer above and below the damage respectively.

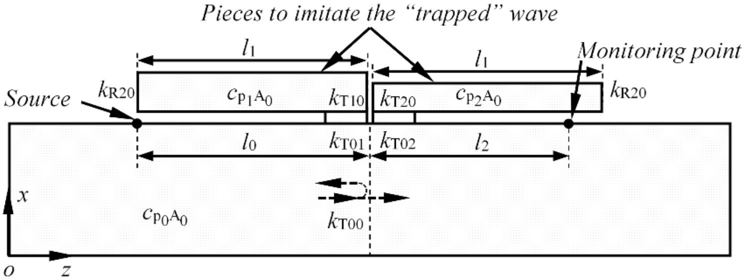

Fig. 6.1.3. The proposed configuration for non-destructive imitation of the "trapped" wave behaviour, which is presumably adequate to the structural damage

To prove the point of this study, let's mathematically describe the wave transmission for the structure presented above. The directly transmitted wave packet at the monitoring point can be expressed as:

$$U_{\mathrm{I_IA_0}}(\omega)=U_{\mathrm{sA_0}}(\omega)\cdot H\left(\omega,c_{\mathrm{p_0A_0}},L\right)\cdot k_{\mathrm{T00}}, \tag{6.1.5}$$

where L is the separation between the source and the monitoring point ($L = l_0 + l_2$). As it can be observed from Fig. 6.1.3 and eq. 6.1.5, the direct wave propagates in a defect free structure, thus $U_{\mathrm{D_IA_0}}(\omega)$ will never be equal to $U_{\mathrm{I_IA_0}}(\omega)$ ($U_{\mathrm{D_IA_0}}(\omega) \neq U_{\mathrm{I_IA_0}}(\omega)$). It means that the proposed configuration cannot be used to reproduce the directly transmitted wave, which is delayed due to the presence of the damage. On the other hand, the 1st repetitive transmission at the monitoring point for the proposed configuration can be expressed as:

$$\begin{aligned}
U_{\mathrm{I_{II}A_0}}(\omega)&=U_{\mathrm{sA_0}}(\omega)\cdot H\left(\omega,c_{\mathrm{p_0A_0}},l_0+l_2\right)\cdot k_{\mathrm{T01}}\cdot H\left(\omega,c_{\mathrm{p_1A_0}},2l_1\right)\cdot k_{\mathrm{R20}}\cdot k_{\mathrm{T10}}+\\
&+U_{\mathrm{sA_0}}(\omega)\cdot H\left(\omega,c_{\mathrm{p_0A_0}},l_0+l_2\right)\cdot k_{\mathrm{T02}}\cdot H\left(\omega,c_{\mathrm{p_2A_0}},2l_1\right)\cdot k_{\mathrm{R20}}\cdot k_{\mathrm{T20}}=\\
&=\left(U_{\mathrm{sA_0}}(\omega)\cdot H\left(\omega,c_{\mathrm{p_0A_0}},l_0+l_2\right)\right)\cdot\left(\begin{aligned}H\left(\omega,c_{\mathrm{p_1A_0}},2l_1\right)\cdot k_{\mathrm{T01}}\cdot k_{\mathrm{R20}}\cdot k_{\mathrm{T10}}+\\ H\left(\omega,c_{\mathrm{p_2A_0}},2l_1\right)\cdot k_{\mathrm{T02}}\cdot k_{\mathrm{R20}}\cdot k_{\mathrm{T20}}\end{aligned}\right).
\end{aligned} \tag{6.1.6}$$

In order to prove that trapped wave phenomenon can be imitated with the proposed configuration, let's now analyse and mathematically compare the cases that are graphically illustrated in Fig. 6.1.4. In this case, only the first repeated transmission in the structure with a defect and the structure with a beam attached to the surface is considered. For the sake of simplicity, the wave propagation in the layer above the damage and one beam is taken into the account only.

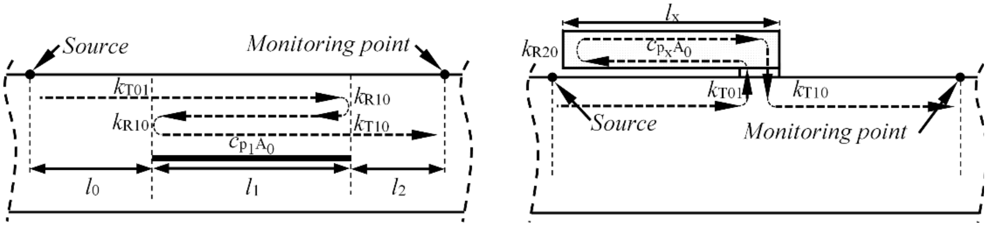

a) b)

Fig. 6.1.4. The investigated case to proof the adequacy of the proposed configuration to the structural damage in terms of wave trapping: the defective structure (a) and the structure with a beam attached to the surface (b)

Hence, the first repeated transmission ($N = 1$) at the monitoring point for the defective structure (Fig. 6.1.4a) can be expressed as:

$$U_{\mathrm{d_{II}A_0}}(\omega)=U_{\mathrm{sA_0}}(\omega)\cdot H\left(\omega,c_{\mathrm{p_0A_0}},L-l_1\right)\cdot H\left(\omega,c_{\mathrm{p_1A_0}},3\cdot l_1\right)\cdot K_{\Pi_\mathrm{d}},\tag{6.1.7}$$

where $K_{\Pi_\mathrm{d}} = k_{\mathrm{T01}}\cdot k_{\mathrm{T10}}\cdot(k_{\mathrm{R10}})^2$. Taking into the account eq. 6.1.2, the expression 6.1.7 can be rearranged into:

$$U_{\mathrm{d_{II}A_0}}(\omega)=U_{\mathrm{sA_0}}(\omega)\cdot H\left(\omega,c_{\mathrm{p_0A_0}},L\right)\cdot \frac{H\left(\omega,c_{\mathrm{p_1A_0}},3\cdot l_1\right)}{H\left(\omega,c_{\mathrm{p_0A_0}},l_1\right)}\cdot K_{\Pi_\mathrm{d}}.\tag{6.1.8}$$

In a similar fashion, the first repeated reflection for the structure presented in Fig. 6.1.4b can be written as:

$$U_{\mathrm{I_{II}A_0}}(\omega)=U_{\mathrm{sA_0}}(\omega)\cdot H\left(\omega,c_{\mathrm{p_0A_0}},L\right)\cdot H\left(\omega,c_{\mathrm{p_xA_0}},2\cdot l_\mathrm{x}\right)\cdot K_{\Pi_\mathrm{I}},\tag{6.1.9}$$

where $K_{\Pi_\mathrm{I}} = k_{\mathrm{T01}}\cdot k_{\mathrm{T10}}\cdot k_{\mathrm{R20}}$, l_x and $c_{\mathrm{p_xA_0}}$ are the length and the phase velocity of a beam, attached to the surface of the structure. From eq. 6.1.8 and 6.1.9 it follows that in terms of the trapped wave behaviour, the imitation of the defect is adequate to the defective case if:

$$H\left(\omega,c_{\mathrm{p_xA_0}},2\cdot l_\mathrm{x}\right)=\frac{H\left(\omega,c_{\mathrm{p_1A_0}},3\cdot l_1\right)}{H\left(\omega,c_{\mathrm{p_0A_0}},l_1\right)}.\tag{6.1.10}$$

The left side of eq. 6.1.10 represent the defect imitation case, meanwhile the right side describe the defective case. Using eq. 6.1.10, the parameters of the beam (length and phase velocity) can be calculated, which makes it adequate to the layer above the damage. If the beam attached to the surface of the sample is made of different material, then the parameters of it have to be matched to the properties of the structure in the appropriate layer within the delamination. From eq. 6.1.10 it can be written that:

$$\frac{2\cdot l_\mathrm{x}}{c_{\mathrm{p_xA_0}}}=\frac{3\cdot l_1}{c_{\mathrm{p_1A_0}}}-\frac{l_1}{c_{\mathrm{p_0A_0}}}.\tag{6.1.11}$$

The equation above can be rearranged into the form of:

$$\frac{c_{\mathrm{p_xA_0}}}{l_\mathrm{x}} = \frac{2 \cdot c_{\mathrm{p_1A_0}} \cdot c_{\mathrm{p_0A_0}}}{l_1 \cdot \left(3 \cdot c_{\mathrm{p_0A_0}} - c_{\mathrm{p_1A_0}}\right)}. \tag{6.1.12}$$

Consider that carbon steel is selected as the material of a beam. If the phase velocity dispersion relationships are known ($c_{\mathrm{p_xA_0}} = c_{\mathrm{p_{steel}}}$), then the parameters of a beam can be estimated by minimizing a function:

$$F\left(l_\mathrm{x}, d\right) = \sum_{f=f_1}^{f_\mathrm{g}} \left| \left(\frac{2 \cdot c_{\mathrm{p_1A_0}} \cdot c_{\mathrm{p_0A_0}}}{l_1 \cdot \left(3 \cdot c_{\mathrm{p_0A_0}} - c_{\mathrm{p_1A_0}}\right)} - \frac{c_{\mathrm{p_{steel}}}}{l_\mathrm{x}} \right) \right|, \tag{6.1.13}$$

where d is the thickness of the attached beam. In a similar way, the parameters of the second beam, which describe the wave propagation below the damage can be defined as well. As the consequence, the proposed set-up can be used as a tool to imitate the presence of damage, as it enables repeated transmissions of A_0 mode to be reproduced. The proposed method is limited to reproduce trapped wave behaviour only, since neither the directly transmitted wave nor the mode conversion are considered in this case. On the other hand, such construction can be positioned anywhere on the investigated structure and may be beneficial as a tool for testing the correctness of developed damage detection methods upon SHM system installation to an in-service structure. The parameters of the attached beams (length, thickness) can be related to the depth and size of the structural damage, hence defects of various sizes can be reproduced without intervention into the material.

6.2 Numerical validation of the proposed technique

In this section, the proposed method to reproduce the trapped wave behaviour will be validated with the numerical finite element simulations. To complete the goal of this verification, two numerical models will be compared, where one of them includes the structural damage, while the other one is the beam attached to the surface. The waveforms at specific locations on both structures will be compared in terms of ToF and the adequacy of the proposed set-up will be estimated. In the following paragraphs, the employed numerical models will be briefly described. The propagation of the A_0 mode in a 2D GFRP plate with dimensions of 2,000 mm × 4 mm was considered in this validation.

Description of numerical model for the defective sample. The numerical model of the defective sample consists of 150 mm long delamination type defect situated 1.5 mm below the top surface of the sample. The defect was virtually produced by separating appropriate nodes in the mesh of the FE model. The parameters of the model, such as the size of an element, excitation signal, material properties and integration step in time domain were the same as described in section 5.3. The variable monitored in this study was a vertical component of the particle velocity (y) along the top surface of the structure.

Description of numerical model of the structure with the attached beams. In this case, the defect free 2D GFRP sample was considered, with the beams attached to the surface of the structure. To check the adequacy of proposed set-up two separate models were created here. In the first model one beam adjusted to be adequate to the layer below the damage (possessing the thickness of 2.5 mm) was attached to the surface only. Meanwhile in the second model, two beams were bonded to the surface, where each of them correspond to the layer below and above the defect. Note that all the parameters of the GFRP, such as the excitation, numerical integration and so on were the same as in the previous model, except that two beams were bonded to the surface instead of separating the nodes in the mesh. The carbon steel was selected as the material of the beam with the following properties: the Young's modulus: 212.8 GPa, the Poisson's ratio: 0.287, the density: 7,800 kg/m^3. The parameters of the beams were calculated using eq. 6.1.13. As the consequence it was estimated that the carbon steel beams with dimensions 358.8 mm × 6 mm and 358.8 mm × 9.4 mm may be adequate to the 150 mm long delamination, situated in the GFRP sample 1.5 mm below the top surface. The first beam represents the 150 mm × 1.5 mm layer in the GFRP, while the second beam corresponds to the layer with dimensions of 150 mm × 2.5 mm. Thus in the first model, the beam with dimensions of 358.8 mm × 9.4 mm was attached to the surface only. Whereas in the second model two beams were bonded at a time. The sketch of the considered cases in this study are presented in Fig. 6.2.1. To ensure the acoustic contact between the beam and the structure, a one element layer of elastic fluid was used with the properties: the Young's modulus: 0.75 kPa, the Poisson's ratio: 0.49, the density: 1,000 kg/m^3. The length of the contact area between the GFRP and steel beam was set to 2 mm.

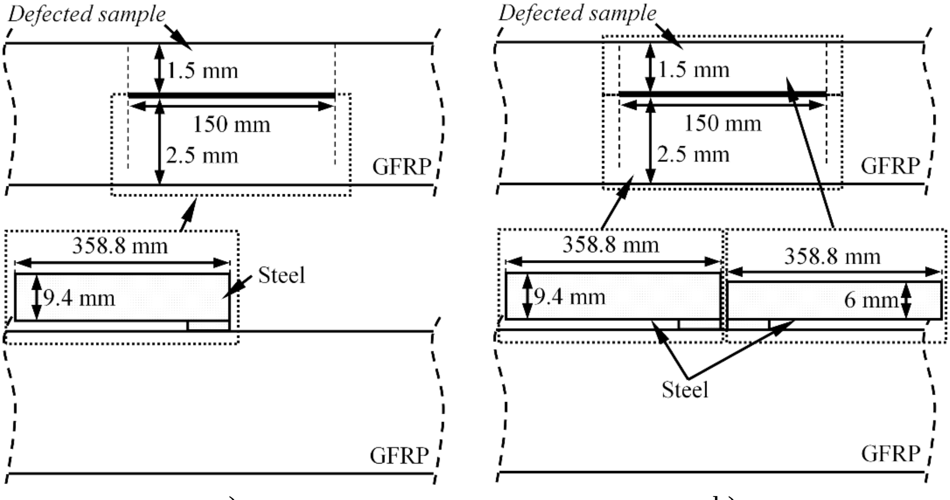

a) b)

Fig. 6.2.1. The sketch of considered numerical models for verification of proposed method: one beam set-up, which corresponds to the layer below the damage (a) and two beam set-up which each represents the layer above and below the defect (b)

In this case the variable monitored in this study was again a vertical component (y) of the particle velocity along the surface of the sample. The B-scan images of the vertical component of the particle velocity in case of structural damage and attached single beam (as it was shown in Fig. 6.2.1a) are presented in Fig. 6.2.2a and

Fig. 6.2.2b respectively. The results indicate, that multiple repetitive transmissions of the A_0 mode are observed in both cases. At the first sight it may seem that the B-scan images presented below are completely different as many more wave packets can be observed in the case of structural damage. However, in case of SHM system the end user does not operate with the B-scan data, since the transducers are bonded to the permanent positions. It will be demonstrated later that the time series for both of the investigated cases can be very close to each other at some monitoring points on the structure, of course with some limitations.

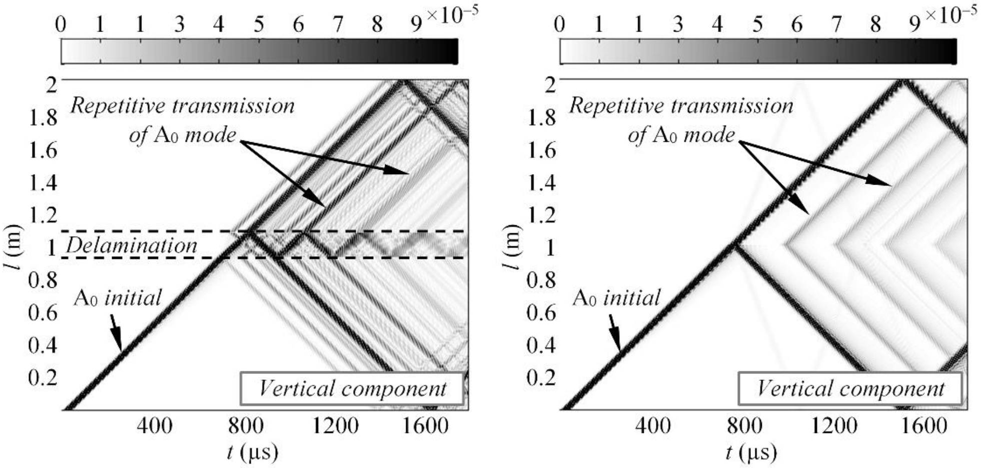

a) b)

Fig. 6.2.2. The B-scan image of the vertical component of the particle velocity along the top surface of the sample in case of structural damage (a) and the single beam attached to the surface (b)

As the main goal of this study is to reproduce the wave “trapping” in terms of ToF between the subsequent wave packets, the waveforms at monitoring points located on the surface of the sample at coordinates x_1 = 1,250 mm, y_1 = 4 mm were further compared. The graphic illustration of the time series from the defective sample and the one with a single beam on the surface is presented in Fig. 6.2.3a. Meanwhile Fig. 6.2.3b represents the comparison in case two beams are attached at a time. The results in Fig. 6.2.3 show that the repetitive transmissions of the A_0 mode arrive faster if the single beam is attached to the surface only compared to the case of structural defect. On the other hand, it can be observed that if two beams are bonded at a time the arrival time of repetitive reflections is almost identical in both cases.

In order to mathematically measure the match between the two-time series, presented in Fig. 6.2.3, the cross-correlation technique, described in section 3.1 by eq. 3.2.1 and eq. 3.2.3 was employed. Throughout the calculations of the short time cross-correlation, the width of time window was equal to 5 periods of the excitation signal. The delay between the two wave packets was estimated by measuring the lag of correlation function at the window position indicating the best match. The match between the signal from the damaged structure and the sample with the attached single beam is presented in Fig. 6.2.4a. Similarly, the comparison for the damaged structure and two beams bonded at a time can be seen in Fig. 6.2.4b. The estimated delay values for both cases are summarized in Table 6.2.1. The results in Table 6.2.1 indicate that in case a single beam is attached to the surface, the wave packets of the first and second repetitive A_0 mode transmission arrives faster by approximately 25μs compared to the damaged structure. If two beams are attached simultaneously, the ToF in both cases are almost identical. Furthermore, the correlation itself is better for the two beam set-up as well. Thus it can be concluded, that the proposed set-up enables the trapped wave behaviour to be quite accurately reproduced in terms of the arrival time of each repetitive transmission.

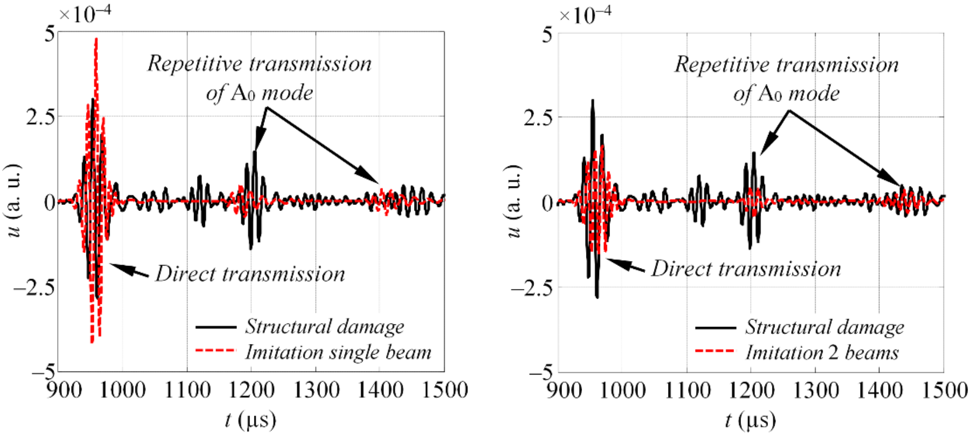

a) b)

Fig. 6.2.3. The comparison of the time series in the defective structure and the sample with the attached beams in case single (a) and two beams (b) are mounted to the structure

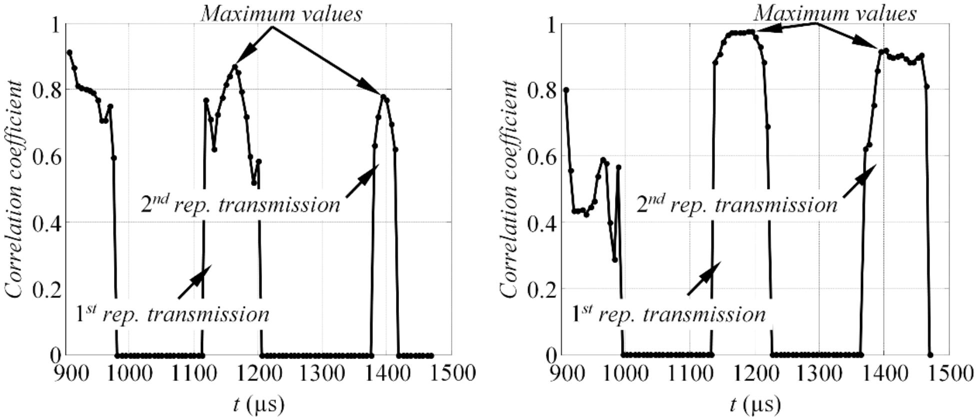

a) b)

Fig. 6.2.4. The short time cross-correlation between the waveform obtained from the damaged structure and the one from the structure with the single (a) and two beams (b)

As one might observe, the mismatch in terms of ToF may increase for each subsequent repetitive transmission, however, in most cases it is sufficient to obtain at least two repetitive reflections to estimate the size of the damage. In addition, the proposed set-up enables the amplitudes of the repetitive transmissions to be equalized as well by adjusting the coupling material and contact area between the beam and the structure in the proposed set-up. In this particular case the steel beam was bonded to the GFRP using an elastic fluid as a coupler and 2 mm contact area. However, if transmission and reflection coefficients K_{Π_d} (see eq. 6.1.7) are known, the contact area and the coupling can be selected in the way that $K_{\Pi_\mathrm{d}} = K_{\Pi_\mathrm{I}}$. Then the amplitude of reflected transmissions in the case of attached beams should be close to the response amplitude from the structural damage, thus the sensitivity to the defect can be estimated using the proposed approach.

Table 6.2.1. The estimated mismatch of the wave packet arrival time between the damaged structure and the one with single and two beams attached to the surface

Wave packet	**Defective sample vs single beam**			**Defective sample vs two beams**		
	Correlation coefficient	*Window position,* (μs)	*Time delay,* (μs)	*Correlation coefficient*	*Window position,* (μs)	*Time delay,* (μs)
1st repetitive transmission	0.86	1,163	22.5	0.98	1,188	0
2nd repetitive transmission	0.77	1,394	26.88	0.92	1,401	1.875

6.3 Conclusions of Chapter 6

1. The technique to non-destructively imitate the delamination type defect was proposed, which reproduces the trapped wave behaviour with beam structures attached to the surface of the sample. The technique developed in this research can be used as a tool to proof the correctness of the performance of the SHM systems upon installation to an in-service structure, without damaging it.
2. It was mathematically demonstrated that under the certain circumstances the proposed set-up may be adequate to the structural damage in terms of ToF between the repetitive trapped wave transmissions. It was also shown that the beams can be produced from any material and related to the parameters of the structural damage such as the length and the depth. As a consequence, the proposed method enables the sensitivity of the SHM system to defects of different sizes to be evaluated.
3. The proposed technique was validated by the numerical simulations, comparing the wave propagation in the sample holding structural delamination and the same material with the attached beams. It was demonstrated that if two beams are bonded to the surface at a time, where each of them represents the appropriate structural layer above and below the damage, the ToF of the repeated transmissions of A_0 mode are almost identical in both cases.
4. The method proposed in this research is limited to the imitation of trapped wave behaviour as it cannot be used to reproduce the direct transmission and the appropriate mode conversion at each end of the defect.

GENERAL CONCLUSIONS

1. In this thesis, the set of novel ultrasonic signal analysis and interpretation methods, which are mandatory in order to properly analyse the complex behaviour of GW, to extract the features of detected damage and to validate the monitoring system, were proposed. The methods developed in this research, aim to solve the most essential problems in the field of guided wave structural health monitoring.
2. The source influence on the frequency response of guided wave modes was demonstrated and explained. It was shown with the numerical simulations and the experiments that the frequency response of each guided wave mode is a product of the spectrum of the excitation pulse and the excitability function, which itself depends on the loading type, material properties and size of source. A novel excitability function estimation technique based on Fourier analysis of particle velocity distribution on the excitation area was proposed, which enables the response amplitude as a function of frequency to be estimated separately for each mode under any type of complex surface loading. The technique developed in this study was validated with the appropriate numerical simulations and experiments and can be further used as a tool to explain and predict differences in frequency bandwidths of each guided wave mode.
3. The analytical model, which enables the propagation of GW in plate-like structures to be better understood, analysed and interpreted has been developed. The proposed model allows the propagation of separate GW mode packets in the plate-like rectangular structures to be analysed, to calculate the arrival times of the wave packets after multiple reflections at virtual receivers positioned anywhere on the object and to retrace the wave propagation paths at specific time intervals. It was demonstrated that the proposed model offers tremendous improvements in terms of solution time of transient wave propagation problems, compared to the commonly used FE method and proves high accuracy in terms of ToF of different wave packets if the initial phase and group velocities are properly defined.
4. The method for phase velocity estimation based on the phase spectrum technique was developed. The proposed method enables the dispersion relations in the –20 dB level bandwidth of the transducer to be reconstructed, employing the time series measured at two distinct locations. In contrast to the conventional phase spectrum technique, the proposed method is applicable to the narrowband transducers, maintaining the wide reconstruction bandwidth and accurate velocity estimation. It was determined that experimentally the velocities are estimated with an average spread of 4%, compared to the theoretical predictions. The incident modes are reconstructed more accurately (with a deviation up to 2.5%), while the reflected modes are spread out over a wider range of values, up to 6%. Due to the abovementioned reasons the proposed method can be effectively used in SHM systems as the tool to estimate the actual velocity of GW modes in the structure and to identify unknown reflections.

5. The model based baseline method to detect and describe the delamination type defect was proposed, exploiting the frequency sweep excitation, mode conversion and constructive/destructive interference of the A_0 mode. It was shown that the magnitude of the direct transmission of the A_0 mode appeared to be significantly sensitive to the depth of damage, meanwhile the delay time between the direct and converted transmission of A_0 mode can be reliably used for damage size extraction. The investigations revealed that the proposed features of A_0 mode can tell the depth and the size of damage with an error of approximately 5% even in relatively thin structures, at wavelengths that are at least twice the thickness of the investigated structures.
6. The technique to non-destructively imitate the delamination type defect in terms of wave trapping inside the defect was proposed, which uses the two-beam structure attached to the surface of the sample, where each of them represents wave propagation in the layer above and below the defect. The proposed set-up was mathematically validated showing that under certain circumstances it may be adequate to the structural damage in terms of ToF between the repetitive A_0 wave transmissions. This technique can be used as a tool to proof the correctness of the performance of the SHM systems upon installation to an in-service structure, without structural intervention.

GUIDELINES FOR FUTURE WORK

The methods proposed in this research creates a framework of the guided wave based structural health monitoring system, that can be used in practical applications. However, some further improvements could be made that would increase the practical adaptability:

- The proposed baseline method to detect and describe the delamination type defects demonstrated good performance and sensitivity to the features of the defect on the 2D model, however, it should be tested and verified further using the 3D FE technique and experiments on the sample with natural structural damage.
- It is expected, that the proposed damage detection method could be applied to detect the multiple parallel delaminations as well, since they are common consequence of impact damage.
- The developed damage detection technique requires the transducer arrangement and data collection schemes, that would allow adequate surface coverage to be ensured and reliable detection of the defects on the in-service structures.
- Further developments could be made for the proposed non-destructive defect imitation technique, which demonstrated good feasibility on the FE model, yet it has not been validated experimentally.

It is anticipated that the abovementioned research areas will be addressed during the post-doc internship.

REFERENCES

1. SHIWA, M. and KISHI, T. Encyclopedia of Materials: Science and Technology (Second Edition) Veyssière, K.H. Jürgen Buschow Robert W. Cahn Merton C. Flemings Bernhard Ilschner Edward J. Kramer Subhash Mahajan Patrick ed., Oxford: Elsevier, 2005 *NDT-Based Assessment of Damage: An Overview*, pp. 1-8 ISBN 9780080431529.
2. KATUNIN, A., DRAGAN, K. and DZIENDZIKOWSKI, M. Damage Identification in Aircraft Composite Structures: A Case Study using various Non-Destructive Testing Techniques. *Composite Structures*, 9/1, 2015, vol. 127. pp. 1-9 ISSN 0263-8223.
3. FEIO, A. and MACHADO, J.S. In-Situ Assessment of Timber Structural Members: Combining Information from Visual Strength Grading and NDT/SDT Methods – A Review. *Construction and Building Materials*, 2015 ISSN 0950-0618.
4. MCCANN, D.M. and FORDE, M.C. Review of NDT Methods in the Assessment of Concrete and Masonry Structures. *NDT & E International*, 3, 2001, vol. 34, No.. 2. pp. 71-84 ISSN 0963-8695.
5. SHOKRIEH, M.M. and GHANEI MOHAMMADI, A.R. Residual Stresses in Composite Materials M.M. SHOKRIEH ed., Woodhead Publishing, 2014 *3 - Non-Destructive Testing (NDT) Techniques in the Measurement of Residual Stresses in Composite Materials: An Overview*, pp. 58-75 ISBN 9780857092700.
6. ILIOPOULOS, S., et al. Detection and Evaluation of Cracks in the Concrete Buffer of the Belgian Nuclear Waste Container using Combined NDT Techniques. *Construction and Building Materials*, 3/1, 2015, vol. 78. pp. 369-378 ISSN 0950-0618.
7. YANG, B. and SUN, D. Testing, Inspecting and Monitoring Technologies for Wind Turbine Blades: A Survey. *Renewable and Sustainable Energy Reviews*, 6, 2013, vol. 22. pp. 515-526 ISSN 1364-0321.
8. HELLIER, C. *Handbook of Non-destructive Evaluation, Second Edition.* McGraw-Hill Professional, 08/21; 2015/09, 2012 ISBN 0071777148.
9. KESSLER, S.S., SPEARING, S.M. and SOUTIS, C. Damage Detection in Composite Materials using Lamb Wave Methods. *Smart Materials and Structures*, 2002, vol. 11, No.. 2. pp. 269-278.
10. CROXFORD, A.J., WILCOX, P.D., DRINKWATER, B.W. and KONSTANTINIDIS, G. Strategies for Guided-Wave Structural Health Monitoring. *Proceedings of the Royal Society of London A: Mathematical, Physical and Engineering Sciences*, 11/08, 2007, vol. 463, No. 2087. pp. 2961-2981.
11. HUTSON, D. *Structural Sensing, Health Monitoring, and Performance Evaluation.* Taylor & Francis, 09/21; 2015/09, 2011 ISBN 978-0-7503-0919-6.
12. BALAGEAS, D. Structural Health Monitoring ISTE, 2010 *Introduction to Structural Health Monitoring*, pp. 13-43 ISBN 9780470612071.
13. OCHÔA, P., INFANTE, V., SILVA, J.M. and GROVES, R.M. Detection of Multiple Low-Energy Impact Damage in Composite Plates using Lamb Wave Techniques. *Composites Part B: Engineering*, 10, 2015, vol. 80. pp. 291-298 ISSN 1359-8368.
14. SU, Z. and YE, L. *Identification of Damage using Lamb Waves: From Fundamentals to Applications.* Springer-Verlag London, 2009 ISBN 978-1-84882-783-7.

15. RAGHAVAN, A. and CESNIK, C.E.S. Review of Guided-Wave Structural Health Monitoring. *The Shock and Vibration Digest*, 2007, vol. 39, No.. 2. pp. 91-114 ISSN 0583-1024.
16. DELRUE, S. and VAN DEN ABEELE, K. Detection of Defect Parameters using Nonlinear Air-Coupled Emission by Ultrasonic Guided Waves at Contact Acoustic Nonlinearities. *Ultrasonics*, 12, 2015, vol. 63. pp. 147-154 ISSN 0041-624X.
17. CLARKE, T., CAWLEY, P., WILCOX, P.D. and CROXFORD, A.J. Evaluation of the Damage Detection Capability of a Sparse-Array Guided-Wave SHM System Applied to a Complex Structure Under Varying Thermal Conditions. *Ultrasonics, Ferroelectrics, and Frequency Control, IEEE Transactions On*, 2009, vol. 56, No. 12. pp. 2666-2678 ISSN 0885-3010.
18. CAWLEY, P. *Practical Guided Wave Inspection and Applications to Structural Health Monitoring.* Brisbane, Australia ed. Proceedings of the 5th Australasian Congress on Applied Mechanics (ACAM 2007), 2007, 2007 ISBN 0 8582 5862 5.
19. ROSE, J.L. Ultrasonic Guided Waves in Structural Health Monitoring. *Key Engineering Materials*, 2004, vol. 270-273. pp. 14-21 ISSN 1662-9795.
20. MICHAELS, J.E., DAWSON, A.J., MICHAELS, T.E. and RUZZENE, M. *Approaches to Hybrid SHM and NDE of Composite Aerospace Structures.* San Diego, California, USA ed. Proc. SPIE 9064, Health Monitoring of Structural and Biological Systems, 2014, 2014 DOI doi:10.1117/12.2045172.
21. OSTIGUY, P., QUAEGEBEUR, N. and MASSON, P. Non-Destructive Evaluation of Coating Thickness using Guided Waves. *NDT & E International*, 12, 2015, vol. 76. pp. 17-25 ISSN 0963-8695.
22. ALLEYNE, D.N., PAVLAKOVIC, B., LOWE, M.J.S. and CAWLEY, P. Rapid, Long Range Inspection of Chemical Plant Pipework using Guided Waves. *AIP Conference Proceedings*, 2001, vol. 557, No. 1. pp. 180-187. Available from: http://scitation.aip.org/content/aip/proceeding/aipcp/10.1063/1.1373757 DOI http://dx.doi.org/10.1063/1.1373757.
23. KANG, T., et al. Enhancement of Detecting Defects in Pipes with Focusing Techniques. *NDT & E International*, 3, 2011, vol. 44, No. 2. pp. 178-187 ISSN 0963-8695.
24. WANG, X., TSE, P.W., MECHEFSKE, C.K. and HUA, M. Experimental Investigation of Reflection in Guided Wave-Based Inspection for the Characterization of Pipeline Defects. *NDT & E International*, 6, 2010, vol. 43, No. 4. pp. 365-374 ISSN 0963-8695.
25. COBB, A.C., KWUN, H., CASERES, L. and JANEGA, G. Torsional Guided Wave Attenuation in Piping from Coating, Temperature, and Large-Area Corrosion. *NDT & E International*, 4, 2012, vol. 47. pp. 163-170 ISSN 0963-8695.
26. CASTAINGS, M. and BACON, C. Finite Element Modeling of Torsional Wave Modes Along Pipes with Absorbing Materials. *The Journal of the Acoustical Society of America*, 2006, vol. 119, No. 6. pp. 3741-3751. Available from: http://scitation.aip.org/content/asa/journal/jasa/119/6/10.1121/1.2197807 DOI http://dx.doi.org/10.1121/1.2197807.
27. YANG, F., et al. Experimental and Numerical Studies of the Oblique Defects in the Pipes using a Chaotic Oscillator Based on Ultrasonic Guided Waves. *Journal of Sound and Vibration*, 7/7, 2015, vol. 347. pp. 218-231 ISSN 0022-460X.

28. WILLEY, C.L., SIMONETTI, F., NAGY, P.B. and INSTANES, G. Guided Wave Tomography of Pipes with High-Order Helical Modes. *NDT & E International*, 7, 2014, vol. 65. pp. 8-21 ISSN 0963-8695.

29. LØVSTAD, A. and CAWLEY, P. The Reflection of the Fundamental Torsional Guided Wave from Multiple Circular Holes in Pipes. *NDT & E International*, 11, 2011, vol. 44, No. 7. pp. 553-562 ISSN 0963-8695.

30. LEINOV, E., LOWE, M.J.S. and CAWLEY, P. Investigation of Guided Wave Propagation and Attenuation in Pipe Buried in Sand. *Journal of Sound and Vibration*, 7/7, 2015, vol. 347. pp. 96-114 ISSN 0022-460X.

31. WU, F. and CHANG, F. Debond Detection using Embedded Piezoelectric Elements for Reinforced Concrete Structures - Part II: Analysis and Algorithm. *Structural Health Monitoring*, March 01, 2006, vol. 5, No. 1. pp. 17-28.

32. SHARMA, A., SHARMA, S., SHARMA, S. and MUKHERJEE, A. Ultrasonic Guided Waves for Monitoring Corrosion of FRP Wrapped Concrete Structures. *Construction and Building Materials*, 10/15, 2015, vol. 96. pp. 690-702 ISSN 0950-0618.

33. LU, Y., LI, J., YE, L. and WANG, D. Guided Waves for Damage Detection in Rebar-Reinforced Concrete Beams. *Construction and Building Materials*, 10, 2013, vol. 47. pp. 370-378 ISSN 0950-0618.

34. FARHIDZADEH, A. and SALAMONE, S. Reference-Free Corrosion Damage Diagnosis in Steel Strands using Guided Ultrasonic Waves. *Ultrasonics*, 3, 2015, vol. 57. pp. 198-208 ISSN 0041-624X.

35. RIZZO, P. and DI SCALEA, F.L. Feature Extraction for Defect Detection in Strands by Guided Ultrasonic Waves. *Structural Health Monitoring*, September 01, 2006, vol. 5, No. 3. pp. 297-308.

36. BALTAZAR, A., HERNANDEZ-SALAZAR, C.D. and MANZANARES-MARTINEZ, B. Study of Wave Propagation in a Multiwire Cable to Determine Structural Damage. *NDT & E International*, 11, 2010, vol. 43, No. 8. pp. 726-732 ISSN 0963-8695.

37. RAIŠUTIS, R., et al. Ultrasonic Guided Wave-Based Testing Technique for Inspection of Multi-Wire Rope Structures. *NDT & E International*, 3, 2014, vol. 62. pp. 40-49 ISSN 0963-8695.

38. XU, J., WU, X. and SUN, P. Detecting Broken-Wire Flaws at Multiple Locations in the Same Wire of Pre-stressing Strands using Guided Waves. *Ultrasonics*, 1, 2013, vol. 53, No. 1. pp. 150-156 ISSN 0041-624X.

39. LOVEDAY, P.W. and LONG, C.S. Laser Vibrometer Measurement of Guided Wave Modes in Rail Track. *Ultrasonics*, 3, 2015, vol. 57. pp. 209-217 ISSN 0041-624X.

40. COCCIA, S., et al. Numerical and Experimental Study of Guided Waves for Detection of Defects in the Rail Head. *NDT & E International*, 1, 2011, vol. 44, No. 1. pp. 93-100 ISSN 0963-8695.

41. LEE, C.M., ROSE, J.L. and CHO, Y. A Guided Wave Approach to Defect Detection Under Shelling in Rail. *NDT & E International*, 4, 2009, vol. 42, No. 3. pp. 174-180 ISSN 0963-8695.

42. LI, F., et al. Propagation of Guided Waves in Pressure Vessel. *Wave Motion*, 1, 2015, vol. 52. pp. 216-228 ISSN 0165-2125.

43. JIANGONG, Y., BIN, W., HONGLI, H. and CUNFU, H. Characteristics of Guided Waves in Anisotropic Spherical Curved Plates. *Wave Motion*, 3, 2007, vol. 44, No. 4. pp. 271-281 ISSN 0165-2125.

44. LU, Y., YE, L., SU, Z. and YANG, C. Quantitative Assessment of Through-Thickness Crack Size Based on Lamb Wave Scattering in Aluminium Plates. *NDT & E International*, 1, 2008, vol. 41, No. 1. pp. 59-68 ISSN 0963-8695.

45. RATHOD, V.T. and ROY MAHAPATRA, D. Ultrasonic Lamb Wave Based Monitoring of Corrosion Type of Damage in Plate using a Circular Array of Piezoelectric Transducers. *NDT & E International*, 11, 2011, vol. 44, No. 7. pp. 628-636 ISSN 0963-8695.

46. EREMIN, A.A., GLUSHKOV, E.V., GLUSHKOVA, N.V. and LAMMERING, R. Evaluation of Effective Elastic Properties of Layered Composite Fibre-Reinforced Plastic Plates by Piezoelectrically Induced Guided Waves and Laser Doppler Vibrometry. *Composite Structures*, 7, 2015, vol. 125. pp. 449-458 ISSN 0263-8223.

47. MUSTAPHA, S. and YE, L. Propagation Behaviour of Guided Waves in Tapered Sandwich Structures and Debonding Identification using Time Reversal. *Wave Motion*, 9, 2015, vol. 57. pp. 154-170 ISSN 0165-2125.

48. PUTKIS, O., DALTON, R.P. and CROXFORD, A.J. The Anisotropic Propagation of Ultrasonic Guided Waves in Composite Materials and Implications for Practical Applications. *Ultrasonics* ISSN 0041-624X.

49. CASTAINGS, M., SINGH, D. and VIOT, P. Sizing of Impact Damages in Composite Materials using Ultrasonic Guided Waves. *NDT & E International*, 3, 2012, vol. 46. pp. 22-31 ISSN 0963-8695.

50. RAIŠUTIS, R., KAŽYS, R., ŽUKAUSKAS, E. and MAŽEIKA, L. Ultrasonic Air-Coupled Testing of Square-Shape CFRP Composite Rods by Means of Guided Waves. *NDT & E International*, 11, 2011, vol. 44, No. 7. pp. 645-654 ISSN 0963-8695.

51. DENG, Q. and YANG, Z. Propagation of Guided Waves in Bonded Composite Structures with Tapered Adhesive Layer. *Applied Mathematical Modelling*, 11, 2011, vol. 35, No. 11. pp. 5369-5381 ISSN 0307-904X.

52. MASSEREY, B., RAEMY, C. and FROMME, P. High-Frequency Guided Ultrasonic Waves for Hidden Defect Detection in Multi-Layered Aircraft Structures. *Ultrasonics*, 9, 2014, vol. 54, No. 7. pp. 1720-1728 ISSN 0041-624X.

53. PUTHILLATH, P. and ROSE, J.L. Ultrasonic Guided Wave Inspection of a Titanium Repair Patch Bonded to an Aluminium Aircraft Skin. *International Journal of Adhesion and Adhesives*, 10, 2010, vol. 30, No. 7. pp. 566-573 ISSN 0143-7496.

54. FROMME, P. and SAYIR, M.B. Detection of Cracks at Rivet Holes using Guided Waves. *Ultrasonics,* 5, 2002, vol. 40, No. 1–8. pp. 199-203 ISSN 0041-624X.

55. SU, Z., YE, L. and LU, Y. Guided Lamb Waves for Identification of Damage in Composite Structures: A Review. *Journal of Sound and Vibration*, 8/22, 2006, vol. 295, No. 3–5. pp. 753-780 ISSN 0022-460X.

56. MIRAHMADI, S.J. and HONARVAR, F. Application of Signal Processing Techniques to Ultrasonic Testing of Plates by S0 Lamb Wave Mode. *NDT & E International*, 1, 2011, vol. 44, No. 1. pp. 131-137 ISSN 0963-8695.

57. WORDEN, K., FARRAR, C.R., MANSON, G. and PARK, G. The Fundamental Axioms of Structural Health Monitoring. *Proceedings of the Royal Society of London A: Mathematical, Physical and Engineering Sciences*, The Royal Society, 2007, vol.

463, No. 2082. pp. 1639-1664. Available from: http://rspa.royalsocietypublishing.org/content/463/2082/1639.abstract DOI 10.1098/rspa.2007.1834.

58. KONSTANTINIDIS, G., DRINKWATER, B.W. and WILCOX, P.D. The Temperature Stability of Guided Wave Structural Health Monitoring Systems. *Smart Materials and Structures*, 2006, vol. 15, No. 4. pp. 967 ISSN 0964-1726.
59. CROXFORD, A.J., MOLL, J., WILCOX, P.D. and MICHAELS, J.E. Efficient Temperature Compensation Strategies for Guided Wave Structural Health Monitoring. *Ultrasonics*, 4, 2010, vol. 50, No. 4–5. pp. 517-528 ISSN 0041-624X.
60. KONSTANTINIDIS, G., WILCOX, P.D. and DRINKWATER, B.W. An Investigation into the Temperature Stability of a Guided Wave Structural Health Monitoring System using Permanently Attached Sensors. *Sensors Journal, IEEE*, 2007, vol. 7, No. 5. pp. 905-912 ISSN 1530-437X.
61. CLARKE, T., SIMONETTI, F. and CAWLEY, P. Guided Wave Health Monitoring of Complex Structures by Sparse Array Systems: Influence of Temperature Changes on Performance. *Journal of Sound and Vibration*, 6/7, 2010, vol. 329, No. 12. pp. 2306-2322 ISSN 0022-460X.
62. LU, Y. and MICHAELS, J.E. A Methodology for Structural Health Monitoring with Diffuse Ultrasonic Waves in the Presence of Temperature Variations. *Ultrasonics*, 10, 2005, vol. 43, No. 9. pp. 717-731 ISSN 0041-624X.
63. CHEN, X., MICHAELS, J.E., LEE, S.J. and MICHAELS, T.E. Load-Differential Imaging for Detection and Localization of Fatigue Cracks using Lamb Waves. *NDT & E International*, 10, 2012, vol. 51. pp. 142-149 ISSN 0963-8695.
64. JATA, K.V., KUNDU, T. and PARTHASARATHY, T.A. Advanced Ultrasonic Methods for Material and Structure Inspection ISTE, 2007 *An Introduction to Failure Mechanisms and Ultrasonic Inspection*, pp. 1-42 ISBN 9780470612248.
65. ROSE, J.L. A Baseline and Vision of Ultrasonic Guided Wave Inspection Potential. *Journal of Pressure Vessel Technology*, July 26, 2002, vol. 124, No. 3. pp. 273-282.
66. GIURGIUTIU, V. Structural Health Monitoring with Piezoelectric wafer active sensors V. GIURGIUTIU ed., Burlington: Academic Press, 2008 *6 - Guided Waves*, pp. 185-238 ISBN 9780120887606.
67. ROSE, J.L. *Ultrasonic Waves in Solid Media.* Cambridge University Press, 2004 ISBN 978-0521548892.
68. VIKTOROV, I.A. *Rayleigh and Lamb Waves: Physical Theory and Applications.* Springer, 2013 ISBN 978-1489956835.
69. ROSE, J.L. *Ultrasonic Guided Waves in Solid Media.* Cambridge University Press, 2014 ISBN 9781107273610. DOI http://dx.doi.org/10.1017/CBO9781107273610.
70. ACHENBACH, J. *Wave Propagation in Elastic Solids.* North Holland, 1987 ISBN 978-0720403251.
71. FRANK PAI, P., DENG, H. and SUNDARESAN, M.J. Time-Frequency Characterization of Lamb Waves for Material Evaluation and Damage Inspection of Plates. *Mechanical Systems and Signal Processing*, 10, 2015, vol. 62–63. pp. 183-206 ISSN 0888-3270.
72. OSTACHOWICZ, W., KUDELA, P., KRAWCZUK, M. and ZAK, A. Guided Waves in Structures for SHM John Wiley & Sons, Ltd, 2012 *Introduction to the Theory of Elastic Waves*, pp. 1-46 ISBN 9781119965855.

73. BEN, B.S., BEN, B.A., VIKRAM, K.A. and YANG, S.H. Damage Identification in Composite Materials using Ultrasonic Based Lamb Wave Method. *Measurement*, 2, 2013, vol. 46, No. 2. pp. 904-912 ISSN 0263-2241.
74. ENSMINGER, D. and BOND, L.J. *Ultrasonics: Fundamentals, Technologies, and Applications, Third Edition.* CRC Press, 2011 ISBN 978-0-8247-5889-9.
75. HAYASHI, T., SONG, W. and ROSE, J.L. Guided Wave Dispersion Curves for a Bar with an Arbitrary Cross-Section, a Rod and Rail Example. *Ultrasonics*, 5, 2003, vol. 41, No. 3. pp. 175-183 ISSN 0041-624X.
76. HAYASHI, T., TAMAYAMA, C. and MURASE, M. Wave Structure Analysis of Guided Waves in a Bar with an Arbitrary Cross-Section. *Ultrasonics*, 1, 2006, vol. 44, No. 1. pp. 17-24 ISSN 0041-624X.
77. BARTOLI, I., MARZANI, A., LANZA DI SCALEA, F. and VIOLA, E. Modelling Wave Propagation in Damped Waveguides of Arbitrary Cross-Section. *Journal of Sound and Vibration*, 8/22, 2006, vol. 295, No. 3–5. pp. 685-707 ISSN 0022-460X.
78. MU, J. and ROSE, J.L. Guided Wave Propagation and Mode Differentiation in Hollow Cylinders with Viscoelastic Coatings. *The Journal of the Acoustical Society of America*, 2008, vol. 124, No. 2. pp. 866-874. Available from: http://scitation.aip.org/content/asa/journal/jasa/124/2/10.1121/1.2940586 DOI http://dx.doi.org/10.1121/1.2940586.
79. ROKHLIN, S.I. and WANG, L. Stable Recursive Algorithm for Elastic Wave Propagation in Layered Anisotropic Media: Stiffness Matrix Method. *The Journal of the Acoustical Society of America*, 2002, vol. 112, No. 3. pp. 822-834. Available from: http://scitation.aip.org/content/asa/journal/jasa/112/3/10.1121/1.1497365 DOI http://dx.doi.org/10.1121/1.1497365.
80. CHIMENTI, D., ROKHLIN, S. and NAGY, P. *Physical Ultrasonics of Composites.* Oxford University Press, 2011 ISBN 978-0-19-507960-9.
81. WANG, L. and ROKHLIN, S.I. Stable Reformulation of Transfer Matrix Method for Wave Propagation in Layered Anisotropic Media. *Ultrasonics*, 10, 2001, vol. 39, No. 6. pp. 413-424 ISSN 0041-624X.
82. LOWE, M.J.S. Matrix Techniques for Modelling Ultrasonic Waves in Multi-layered Media. *Ultrasonics, Ferroelectrics, and Frequency Control, IEEE Transactions On*, 1995, vol. 42, No. 4. pp. 525-542 ISSN 0885-3010.
83. DEMČENKO, A. and MAŽEIKA, L. Calculation of Lamb Waves Dispersion Curves in Multi-Layered Planar Structures. *Ultragarsas*, 2002, vol. 3, No. 44. pp. 15-17 ISSN 1392-2114.
84. LEMPRIERE, B.M. Ultrasound and Elastic Waves B.M. LEMPRIERE ed., Burlington: Academic Press, 2003 *3 - Wave Propagation Concepts*, pp. 25-44 ISBN 9780124433458.
85. PRAKASH, R. *Non-Destructive Testing Techniques.* New age international, 2010 ISBN 978-81-224-2588-8.
86. CHEEKE, J. *Fundamentals and Applications of Ultrasonic Waves.* CRC Press, 2012 ISBN 9781439854945.
87. FENG, F., SHEN, J. and LIN, S. Scattering Matrices of Lamb Waves at Irregular Surface and Void Defects. *Ultrasonics*, 8, 2012, vol. 52, No. 6. pp. 760-766 ISSN 0041-624X.

88. HARHAD, N., et al. Propagation of Lamb Waves in an Immersed Periodically Grooved Plate: Experimental Detection of the Scattered Converted Backward Waves. *Ultrasonics*, 3, 2014, vol. 54, No. 3. pp. 860-866 ISSN 0041-624X.

89. BENMEDDOUR, F., GRONDEL, S., ASSAAD, J. and MOULIN, E. Study of the Fundamental Lamb Modes Interaction with Asymmetrical Discontinuities. *NDT & E International*, 7, 2008, vol. 41, No. 5. pp. 330-340 ISSN 0963-8695.

90. BENMEDDOUR, F., GRONDEL, S., ASSAAD, J. and MOULIN, E. Study of the Fundamental Lamb Modes Interaction with Symmetrical Notches. *NDT & E International*, 1, 2008, vol. 41, No. 1. pp. 1-9 ISSN 0963-8695.

91. XU, K., TA, D., SU, Z. and WANG, W. Transmission Analysis of Ultrasonic Lamb Mode Conversion in a Plate with Partial-Thickness Notch. *Ultrasonics*, 1, 2014, vol. 54, No. 1. pp. 395-401 ISSN 0041-624X.

92. SICARD, R., CHAHBAZ, A. and GOYETTE, J. Guided Lamb Waves and L-SAFT Processing Technique for Enhanced Detection and Imaging of Corrosion Defects in Plates with Small Depth-to Wavelength Ratio. *Ultrasonics, Ferroelectrics, and Frequency Control, IEEE Transactions On*, 2004, vol. 51, No. 10. pp. 1287-1297 ISSN 0885-3010.

93. CHEN, J., SU, Z. and CHENG, L. Identification of Corrosion Damage in Submerged Structures using Fundamental Anti-Symmetric Lamb Waves. *Smart Materials and Structures*, 2009, vol. 19, No. 1.

94. SHKERDIN, G. and GLORIEUX, C. Lamb Mode Conversion in a Plate with a Delamination. *The Journal of the Acoustical Society of America*, 2004, vol. 116, No. 4. pp. 2089-2100. Available from: http://scitation.aip.org/content/asa/journal/jasa/116/4/10.1121/1.1784435 DOI http://dx.doi.org/10.1121/1.1784435.

95. HU, N., SHIMOMUKAI, T., YAN, C. and FUKUNAGA, H. Identification of Delamination Position in Cross-Ply Laminated Composite Beams using S0 Lamb Mode. *Composites Science and Technology*, 5, 2008, vol. 68, No. 6. pp. 1548-1554 ISSN 0266-3538.

96. CHAKRAPANI, S.K. and DAYAL, V. The Interaction of Rayleigh Waves with Delaminations in Composite Laminates. *The Journal of the Acoustical Society of America*, 2014, vol. 135, No. 5. pp. 2646-2653. Available from: http://scitation.aip.org/content/asa/journal/jasa/135/5/10.1121/1.4869684 DOI http://dx.doi.org/10.1121/1.4869684.

97. RHEE, S., LEE, J. and LEE, J. The Group Velocity Variation of Lamb Wave in Fibre Reinforced Composite Plate. *Ultrasonics*, 12, 2007, vol. 47, No. 1–4. pp. 55-63 ISSN 0041-624X.

98. CHIMENTI, D.E. Guided Waves in Plates and their use in Materials Characterization. *Applied Mechanics Reviews*, May 1, 1997, vol. 50, No. 5. pp. 247-284.

99. WANG, L. and YUAN, F.G. Group Velocity and Characteristic Wave Curves of Lamb Waves in Composites: Modelling and Experiments. *Composites Science and Technology*, 6, 2007, vol. 67, No. 7–8. pp. 1370-1384 ISSN 0266-3538.

100. GIURGIUTIU, V. Tuned Lamb Wave Excitation and Detection with Piezoelectric Wafer Active Sensors for Structural Health Monitoring. *Journal of Intelligent Material Systems and Structures*, April 01, 2005, vol. 16, No. 4. pp. 291-305.

101. WU, T. and UME, I.C. Fundamental Study of Laser Generation of Narrowband Lamb Waves using Superimposed Line Sources Technique. *NDT & E International*, 5, 2011, vol. 44, No. 3. pp. 315-323 ISSN 0963-8695.

102. MICHAELS, J.E., LEE, S.J., CROXFORD, A.J. and WILCOX, P.D. Chirp Excitation of Ultrasonic Guided Waves. *Ultrasonics*, 1, 2013, vol. 53, No. 1. pp. 265-270 ISSN 0041-624X.

103. RAGHAVAN, A. and CESNIK, C.E.S. Guided-Wave Signal Processing using Chirplet Matching Pursuits and Mode Correlation for Structural Health Monitoring. *Smart Materials and Structures*, 2007, vol. 16, No. 2 ISSN 0964-1726.

104. YEUM, C.M., SOHN, H. and IHN, J.B. Lamb Wave Mode Decomposition using Concentric Ring and Circular Piezoelectric Transducers. *Wave Motion*, 6, 2011, vol. 48, No. 4. pp. 358-370 ISSN 0165-2125.

105. HARLEY, J.B. and MOURA, J.M.F. Sparse Recovery of the Multimodal and Dispersive Characteristics of Lamb Wavesa). *The Journal of the Acoustical Society of America*, 2013, vol. 133, No. 5. pp. 2732-2745. Available from: http://scitation.aip.org/content/asa/journal/jasa/133/5/10.1121/1.4799805 DOI http://dx.doi.org/10.1121/1.4799805.

106. PRUELL, C., KIM, J.-., QU, J. and JACOBS, L.J. A Nonlinear-Guided Wave Technique for Evaluating Plasticity-Driven Material Damage in a Metal Plate. *NDT & E International*, 4, 2009, vol. 42, No. 3. pp. 199-203 ISSN 0963-8695.

107. HUANG, J.Y. Multiple Cracks Subjected to Guided Waves. *Theoretical and Applied Fracture Mechanics*, 6, 2011, vol. 55, No. 3. pp. 213-221 ISSN 0167-8442.

108. DJILI, S., et al. Notch Detection in Copper Tubes Immersed in Water by Leaky Compressional Guided Waves. *NDT & E International*, 3, 2013, vol. 54. pp. 183-188 ISSN 0963-8695.

109. CHAKRAPANI, S.K., BARNARD, D. and DAYAL, V. Non-destructive Evaluation of Helicopter Rotor Blades using Guided Lamb Modes. *Ultrasonics*, 3, 2014, vol. 54, No. 3. pp. 826-833 ISSN 0041-624X.

110. WILCOX, P.D., LOWE, M.J.S. and CAWLEY, P. Mode and Transducer Selection for Long Range Lamb Wave Inspection. *Journal of Intelligent Material Systems and Structures*, August 01, 2001, vol. 12, No. 8. pp. 553-565.

111. WILCOX, P., LOWE, M. and CAWLEY, P. The Effect of Dispersion on Long-Range Inspection using Ultrasonic Guided Waves. *NDT & E International*, 1, 2001, vol. 34, No. 1. pp. 1-9 ISSN 0963-8695.

112. SCHUBERT, K.J. and HERRMANN, A.S. On Attenuation and Measurement of Lamb Waves in Viscoelastic Composites. *Composite Structures*, 12, 2011, vol. 94, No. 1. pp. 177-185 ISSN 0263-8223.

113. MUSTAPHA, S. and YE, L. Leaky and Non-Leaky Behaviours of Guided Waves in CF/EP Sandwich Structures. *Wave Motion*, 9, 2014, vol. 51, No. 6. pp. 905-918 ISSN 0165-2125.

114. LONG, R., LOWE, M. and CAWLEY, P. Attenuation Characteristics of the Fundamental Modes that Propagate in Buried Iron Water Pipes. *Ultrasonics*, 9, 2003, vol. 41, No. 7. pp. 509-519 ISSN 0041-624X.

115. LIU, T., VEIDT, M. and KITIPORNCHAI, S. Single Mode Lamb Waves in Composite Laminated Plates Generated by Piezoelectric Transducers. *Composite Structures*, 0, 2002, vol. 58, No. 3. pp. 381-396 ISSN 0263-8223.

116. MAŽEIKA, L., KAŽYS, R. and MACIULEVIČIUS, A. Optimization of Transducer Arrays Parameters for Efficient Excitation of Lamb Waves. *Ultragarsas*, 2007, vol. 62, No. 4 ISSN 1392-2114.
117. BADCOCK, R.A. and BIRT, E.A. The use of 0-3 Piezocomposite Embedded Lamb Wave Sensors for Detection of Damage in Advanced Fibre Composites. *Smart Materials and Structures*, 2000, vol. 9, No. 3. pp. 291 ISSN 0964-1726.
118. MONKHOUSE, R.S.C., et al. The Rapid Monitoring of Structures using Interdigital Lamb Wave Transducers. *Smart Materials and Structures*, 2000, vol. 9, No. 3 ISSN 0964-1726.
119. SU, Z. and YE, L. Selective Generation of Lamb Wave Modes and their Propagation Characteristics in Defective Composite Laminates. *Proceedings of the Institution of Mechanical Engineers, Part L: Journal of Materials Design and Applications*, April 01, 2004, vol. 218, No. 2. pp. 95-110.
120. GLUSHKOV, E.V., GLUSHKOVA, N.V., KVASHA, O.V. and LAMMERING, R. Selective Lamb Mode Excitation by Piezoelectric Coaxial Ring Actuators. *Smart Materials and Structures*, 2010, vol. 19, No. 3 ISSN 0964-1726.
121. PHILTRON, J.H. and ROSE, J.L. Mode Perturbation Method for Optimal Guided Wave Mode and Frequency Selection. *Ultrasonics*, 9, 2014, vol. 54, No. 7. pp. 1817-1824 ISSN 0041-624X.
122. LANZA DISCALEA, F., et al. Health Monitoring of UAV Wing Skin-to-Spar Joints using Guided Waves and Macro Fibre Composite Transducers. *Journal of Intelligent Material Systems and Structures*, April 01, 2007, vol. 18, No. 4. pp. 373-388.
123. SALAS, K.I. and CESNIK, C.E.S. Guided Wave Excitation by a CLoVER Transducer for Structural Health Monitoring: Theory and Experiments. *Smart Materials and Structures*, 2009, vol. 18, No. 7 ISSN 0964-1726.
124. XU, B. and GIURGIUTIU, V. Single Mode Tuning Effects on Lamb Wave Time Reversal with Piezoelectric Wafer Active Sensors for Structural Health Monitoring. *Journal of Non-destructive Evaluation*, 2007, vol. 26, No. 2. pp. 123 ISSN 0195-9298.
125. GIURGIUTIU, V. and ZAGRAI, A.N. Characterization of Piezoelectric Wafer Active Sensors. *Journal of Intelligent Material Systems and Structures*, December 01, 2000, vol. 11, No. 12. pp. 959-976.
126. GIURGIUTIU, V. Structural Damage Detection with Piezoelectric Wafer Active Sensors. *Journal of Physics: Conference Series*, 2011, vol. 305, No. 1 ISSN 1742-6596.
127. NA, J.K., BLACKSHIRE, J.L. and KUHR, S. Design, Fabrication, and Characterization of Single-Element Interdigital Transducers for NDT Applications. *Sensors and Actuators A: Physical*, 12/3, 2008, vol. 148, No. 2. pp. 359-365 ISSN 0924-4247.
128. MAMISHEV, A.V., et al. Interdigital Sensors and Transducers. *Proceedings of the IEEE*, 2004, vol. 92, No. 5. pp. 808-845 ISSN 0018-9219.
129. BELLAN, F., et al. A New Design and Manufacturing Process for Embedded Lamb Waves Interdigital Transducers Based on Piezopolymer Film. *Sensors and Actuators A: Physical*, 9/23, 2005, vol. 123–124. pp. 379-387 ISSN 0924-4247.
130. JIN, J., QUEK, S.T. and WANG, Q. Design of Interdigital Transducers for Crack Detection in Plates. *Ultrasonics*, 5, 2005, vol. 43, No. 6. pp. 481-493 ISSN 0041-624X.

131. GRONDEL, S., et al. Design of Optimal Configuration for Generating A0 Lamb Mode in a Composite Plate using Piezoceramic Transducers. *The Journal of the Acoustical Society of America*, 2002, vol. 112, No. 1. pp. 84.
132. SEUNG, B.K. and HOON, S. Instantaneous Reference-Free Crack Detection Based on Polarization Characteristics of Piezoelectric Materials. *Smart Materials and Structures*, 2007, vol. 16, No. 6. pp. 2375 ISSN 0964-1726.
133. FROMME, P., WILCOX, P.D., LOWE, M.J.S. and CAWLEY, P. On the Development and Testing of a Guided Ultrasonic Wave Array for Structural Integrity Monitoring. *Ultrasonics, Ferroelectrics, and Frequency Control, IEEE Transactions On*, 2006, vol. 53, No. 4. pp. 777-785 ISSN 0885-3010.
134. BORIGO, C., ROSE, J.L. and YAN, F. A Spacing Compensation Factor for the Optimization of Guided Wave Annular Array Transducers. *The Journal of the Acoustical Society of America*, 2013, vol. 133, No. 1. pp. 127-135. Available from: http://scitation.aip.org/content/asa/journal/jasa/133/1/10.1121/1.4770238 DOI http://dx.doi.org/10.1121/1.4770238.
135. Wenhao Zhu and ROSE, J.L. Lamb Wave Generation and Reception with Time-Delay Periodic Linear Arrays: A BEM Simulation and Experimental Study. *Ultrasonics, Ferroelectrics, and Frequency Control, IEEE Transactions On*, 1999, vol. 46, No. 3. pp. 654-664 ISSN 0885-3010.
136. LI, J. and ROSE, J.L. Implementing Guided Wave Mode Control by use of a Phased Transducer Array. *Ultrasonics, Ferroelectrics, and Frequency Control, IEEE Transactions On*, 2001, vol. 48, No. 3. pp. 761-768 ISSN 0885-3010.
137. PAVLAKOVIC, B., LOWE, M., ALLEYNE, D. and CAWLEY, P. Review of Progress in Quantitative Non-destructive Evaluation D.O. THOMPSON and D.E. CHIMENTI eds., Springer US, 1997 *Disperse: A General Purpose Program for Creating Dispersion Curves*, pp. 185-192 ISBN 978-1-4613-7725-2.
138. MAL, A.K. Wave Propagation in Layered Composite Laminates Under Periodic Surface Loads. *Wave Motion*, 6, 1988, vol. 10, No. 3. pp. 257-266 ISSN 0165-2125.
139. GUO, N. and CAWLEY, P. The Interaction of Lamb Waves with Delaminations in Composite Laminates. *The Journal of the Acoustical Society of America*, 1993, vol. 94, No. 4. pp. 2240-2246. Available from: http://scitation.aip.org/content/asa/journal/jasa/94/4/10.1121/1.407495 DOI http://dx.doi.org/10.1121/1.407495.
140. RAIŠUTIS, R., ŽUKAUSKAS, E. and MAŽEIKA, L. Application of Analytical and Semi--Analytical Modelling Methods for Investigation of Ultrasonic Guided Waves Propagation in Composites. *Ultragarsas*, 2011, vol. 66, No. 2 ISSN 1392-2114.
141. LOVEDAY, P.W. and LONG, C.S. Time Domain Simulation of Piezoelectric Excitation of Guided Waves in Rails using Waveguide Finite Elements. *Proc. SPIE 6529, Sensors and Smart Structures Technologies for Civil, Mechanical, and Aerospace Systems*, 2007.
142. HUTTON, D.V. *Fundamentals of Finite Element Analysis.* McGraw-Hill Science, 2004 ISBN 978-0072922363.
143. GRAVENKAMP, H., BIRK, C. and SONG, C. Simulation of Elastic Guided Waves Interacting with Defects in Arbitrarily Long Structures using the Scaled Boundary Finite Element Method. *Journal of Computational Physics*, 8/15, 2015, vol. 295. pp. 438-455 ISSN 0021-9991.

144. OSTACHOWICZ, W., KUDELA, P., KRAWCZUK, M. and ZAK, A. *Guided Waves in Structures for SHM: The Time-Domain Spectral Element Method.* United Kingdom: John Wiley & Sons, 2012 ISBN 978-0-470-97983-9.

145. SUN, J.S., LEE, K.H. and LEE, H.P. Comparison of Implicit and Explicit Finite Element Methods for Dynamic Problems. *Journal of Materials Processing Technology*, 9/7, 2000, vol. 105, No. 1–2. pp. 110-118 ISSN 0924-0136.

146. MOSER, F., JACOBS, L.J. and QU, J. Modelling Elastic Wave Propagation in Waveguides with the Finite Element Method. *NDT & E International*, 6, 1999, vol. 32, No. 4. pp. 225-234 ISSN 0963-8695.

147. BARTOLI, I., LANZA DI SCALEA, F., FATEH, M. and VIOLA, E. Modelling Guided Wave Propagation with Application to the Long-Range Defect Detection in Railroad Tracks. *NDT & E International*, 7, 2005, vol. 38, No. 5. pp. 325-334 ISSN 0963-8695.

148. HAYASHI, T. and KAWASHIMA, K. Multiple Reflections of Lamb Waves at a Delamination. *Ultrasonics*, 5, 2002, vol. 40, No. 1–8. pp. 193-197 ISSN 0041-624X.

149. TERRIEN, N., et al. A Combined Finite Element and Modal Decomposition Method to Study the Interaction of Lamb Modes with Micro-Defects. *Ultrasonics*, 3, 2007, vol. 46, No. 1. pp. 74-88 ISSN 0041-624X.

150. BENMEDDOUR, F., TREYSSÈDE, F. and LAGUERRE, L. Numerical Modelling of Guided Wave Interaction with Non-Axisymmetric Cracks in Elastic Cylinders. *International Journal of Solids and Structures*, 3/1, 2011, vol. 48, No. 5. pp. 764-774 ISSN 0020-7683.

151. NIETHAMMER, M., JACOBS, L.J., QU, J. and JARZYNSKI, J. Time-Frequency Representation of Lamb Waves using the Reassigned Spectrogram. *The Journal of the Acoustical Society of America*, 2000, vol. 107, No. 5. pp. L19-L24. Available from: http://scitation.aip.org/content/asa/journal/jasa/107/5/10.1121/1.428894 DOI http://dx.doi.org/10.1121/1.428894.

152. ALLEYNE, D. and CAWLEY, P. A Two-Dimensional Fourier Transform Method for the Measurement of Propagating Multimode Signals. *The Journal of the Acoustical Society of America*, 1991, vol. 89, No. 3. pp. 1159-1168. Available from: http://scitation.aip.org/content/asa/journal/jasa/89/3/10.1121/1.400530 DOI http://dx.doi.org/10.1121/1.400530.

153. SHI, Z.Y., LAW, S.S. and XU, X. Identification of Linear Time-Varying Mdof Dynamic Systems from Forced Excitation using Hilbert Transform and EMD Method. *Journal of Sound and Vibration*, 4/10, 2009, vol. 321, No. 3–5. pp. 572-589 ISSN 0022-460X.

154. KAŽYS, R., TUMŠYS, O. and PAGODINAS, D. Ultrasonic Detection of Defects in Strongly Attenuating Structures using the Hilbert–Huang Transform. *NDT & E International*, 9, 2008, vol. 41, No. 6. pp. 457-466 ISSN 0963-8695.

155. CHEN, G., CHEN, J. and DONG, G.M. Chirplet Wigner–Ville Distribution for Time–frequency Representation and its Application. *Mechanical Systems and Signal Processing*, 12, 2013, vol. 41, No. 1–2. pp. 1-13 ISSN 0888-3270.

156. XU, X., SHI, Z.Y. and YOU, Q. Identification of Linear Time-Varying Systems using a Wavelet-Based State-Space Method. *Mechanical Systems and Signal Processing*, 1, 2012, vol. 26. pp. 91-103 ISSN 0888-3270.

157. KUTTIG, H., NIETHAMMER, M., HURLEBAUS, S. and JACOBS, L.J. Model-Based Analysis of Dispersion Curves using Chirplets. *The Journal of the Acoustical Society of America*, 2006, vol. 119, No. 4. pp. 2122-2130. Available from: http://scitation.aip.org/content/asa/journal/jasa/119/4/10.1121/1.2177587 DOI http://dx.doi.org/10.1121/1.2177587.

158. LI, J. and LIU, S. The Application of Time-Frequency Transform in Mode Identification of Lamb Waves. *17th World Conference on Non-destructive Testing*, 2008.

159. FENG, Z., LIANG, M. and CHU, F. Recent Advances in Time–frequency Analysis Methods for Machinery Fault Diagnosis: A Review with Application Examples. *Mechanical Systems and Signal Processing*, 7/5, 2013, vol. 38, No. 1. pp. 165-205 ISSN 0888-3270.

160. KIM, C. and PARK, K. Mode Separation and Characterization of Torsional Guided Wave Signals Reflected from Defects using Chirplet Transform. *NDT & E International*, 9, 2015, vol. 74. pp. 15-23 ISSN 0963-8695.

161. NIETHAMMER, M., JACOBS, L.J., QU, J. and JARZYNSKI, J. Time-Frequency Representations of Lamb Waves. *The Journal of the Acoustical Society of America*, 2001, vol. 109, No. 5. pp. 1841.

162. KOTTE, O., NIETHAMMER, M. and JACOBS, L.J. Lamb Wave Characterization by Differential Reassignment and Non-Linear Anisotropic Diffusion. *NDT & E International*, 3, 2006, vol. 39, No. 2. pp. 96-105 ISSN 0963-8695.

163. HONG, J.C., SUN, K.H. and KIM, Y.Y. Dispersion-Based Short Time Fourier Transform Applied to Dispersive Wave Analysis. *J.Acoust.Soc.Am.*, 2005, vol. 117, No. 5. pp. 2949.

164. LE TOUZE, G., NICOLAS, B., MARS, J.I. and LACOUME, J.-. Matched Representations and Filters for Guided Waves. *Signal Processing, IEEE Transactions On*, 2009, vol. 57, No. 5. pp. 1783-1795 ISSN 1053-587X.

165. SIQUEIRA, M.H.S., GATTS, C.E.N., DA SILVA, R.R. and REBELLO, J.M.A. The use of Ultrasonic Guided Waves and Wavelets Analysis in Pipe Inspection. *Ultrasonics*, 5, 2004, vol. 41, No. 10. pp. 785-797 ISSN 0041-624X.

166. BORGHETTI, A., et al. Continuous-Wavelet Transform for Fault Location in Distribution Power Networks: Definition of Mother Wavelets Inferred from Fault Originated Transients. *Power Systems, IEEE Transactions On*, 2008, vol. 23, No. 2. pp. 380-388 ISSN 0885-8950.

167. LIU, Y., LI, Z. and GONG, K. Detection of a Radial Crack in Annular Structures using Guided Circumferential Waves and Continuous Wavelet Transform. *Mechanical Systems and Signal Processing*, 7, 2012, vol. 30. pp. 157-167 ISSN 0888-3270.

168. LIU, Y., LI, Z. and ZHANG, W. Crack Detection of Fibre Reinforced Composite Beams Based on Continuous Wavelet Transform. *Non-destructive Testing and Evaluation*, 03/01, 2010, vol. 25, No. 1. pp. 25-44 ISSN 1058-9759.

169. LE, T. and ARGOUL, P. Continuous Wavelet Transform for Modal Identification using Free Decay Response. *Journal of Sound and Vibration*, 10/6, 2004, vol. 277, No. 1–2. pp. 73-100 ISSN 0022-460X.

170. QIU, Z., LEE, C.-., XU, Z.H. and SUI, L.N. A Multi-Resolution Filtered-X LMS Algorithm Based on Discrete Wavelet Transform for Active Noise Control.

Mechanical Systems and Signal Processing, 1, 2016, vol. 66–67. pp. 458-469 ISSN 0888-3270.

171. GRABOWSKA, J., PALACZ, M. and KRAWCZUK, M. Damage Identification by Wavelet Analysis. *Mechanical Systems and Signal Processing*, 10, 2008, vol. 22, No. 7. pp. 1623-1635 ISSN 0888-3270.
172. RIZZO, P., SORRIVI, E., LANZA DI SCALEA, F. and VIOLA, E. Wavelet-Based Outlier Analysis for Guided Wave Structural Monitoring: Application to Multi-Wire Strands. *Journal of Sound and Vibration*, 10/23, 2007, vol. 307, No. 1–2. pp. 52-68 ISSN 0022-460X.
173. LEE, I., et al. Evaluation of Rock Bolt Integrity using Fourier and Wavelet Transforms. *Tunnelling and Underground Space Technology*, 3, 2012, vol. 28. pp. 304-314 ISSN 0886-7798.
174. KERBER, F., et al. Attenuation Analysis of Lamb Waves using the Chirplet Transform. *EURASIP Journal on Advances in Signal Processing*, 2010, vol. 2010, No. 5.
175. YANG, Y., PENG, Z.K., ZHANG, W.M. and MENG, G. Frequency-Varying Group Delay Estimation using Frequency Domain Polynomial Chirplet Transform. *Mechanical Systems and Signal Processing*, 5/3, 2014, vol. 46, No. 1. pp. 146-162 ISSN 0888-3270.
176. HU, G. and ZHU, F.F. An Improved Chirplet Transform and its Application for Harmonics Detection. *Circuits and Systems*, 2011, vol. 2, No. 3. pp. 107.
177. PROSSER, W.H., SEALE, M.D. and SMITH, B.T. Time Frequency Analysis of the Dispersion of Lamb Waves. *J.Acoust.Soc.Am.*, 1999, vol. 105, No. 5. pp. 2669 ISSN 0001-4966.
178. KAVALLIERATOU, E., FAKOTAKIS, N. and KOKKINAKIS, G. Skew Angle Estimation in Document Processing using Cohen's Class Distributions. *Pattern Recognition Letters*, 11, 1999, vol. 20, No. 11–13. pp. 1305-1311 ISSN 0167-8655.
179. PACHORI, R.B. and NISHAD, A. Cross-Terms Reduction in the Wigner–Ville Distribution using Tunable-Q Wavelet Transform. *Signal Processing*, 3, 2016, vol. 120. pp. 288-304 ISSN 0165-1684.
180. ZENG, W., WANG, H., TIAN, G. and HU, G. Application of Laser Ultrasound Imaging Technology in the Frequency Domain Based on Wigner–Ville Algorithm for Detecting Defect. *Optics & Laser Technology*, 11, 2015, vol. 74. pp. 72-78 ISSN 0030-3992.
181. TANG, B., LIU, W. and SONG, T. Wind Turbine Fault Diagnosis Based on Morlet Wavelet Transformation and Wigner-Ville Distribution. *Renewable Energy*, 12, 2010, vol. 35, No. 12. pp. 2862-2866 ISSN 0960-1481.
182. RODRÍGUEZ, M.A., SAN EMETERIO, J.L., LÁZARO, J.C. and RAMOS, A. Ultrasonic Flaw Detection in NDE of Highly Scattering Materials using Wavelet and Wigner–Ville Transform Processing. *Ultrasonics*, 4, 2004, vol. 42, No. 1–9. pp. 847-851 ISSN 0041-624X.
183. MALLAT, S.G. and ZHANG, Z. Matching Pursuits with Time-Frequency Dictionaries. *Signal Processing, IEEE Transactions On*, 1993, vol. 41, No. 12. pp. 3397-3415 ISSN 1053-587X.
184. XU, B., GIURGIUTIU, V. and YU, L. Lamb Waves Decomposition and Mode Identification using Matching Pursuit Method. *Proc. SPIE 7292, Sensors and Smart*

Structures Technologies for Civil, Mechanical, and Aerospace Systems, 2009, vol. 7292.

185. LIU, B., LING, S.F. and GRIBONVAL, R. Bearing Failure Detection using Matching Pursuit. *NDT & E International*, 6, 2002, vol. 35, No. 4. pp. 255-262 ISSN 0963-8695.
186. YANG, H., MATHEW, J. and MA, L. Fault Diagnosis of Rolling Element Bearings using Basis Pursuit. *Mechanical Systems and Signal Processing*, 3, 2005, vol. 19, No. 2. pp. 341-356 ISSN 0888-3270.
187. Wang Yuemin, Zhu Longxiang, Luo Fan and Sun Fengrui. *Guided Waves Modes Identification in Pipes Detection by Application of the Matching Pursuit Method.* 2011 DOI 10.1109/ICEMI.2011.6037945.
188. HUANG, N.E., et al. The Empirical Mode Decomposition and the Hilbert Spectrum for Nonlinear and Non-Stationary Time Series Analysis. *Proceedings of the Royal Society of London A: Mathematical, Physical and Engineering Sciences*, The Royal Society, 1998, vol. 454, No. 1971. pp. 903-995. Available from: http://rspa.royalsocietypublishing.org/content/454/1971/903.abstract DOI 10.1098/rspa.1998.0193.
189. LIN, L. and CHU, F. Feature Extraction of AE Characteristics in Offshore Structure Model using Hilbert–Huang Transform. *Measurement*, 1, 2011, vol. 44, No. 1. pp. 46-54 ISSN 0263-2241.
190. FRANK PAI, P. Time–frequency Analysis for Parametric and Non-Parametric Identification of Nonlinear Dynamical Systems. *Mechanical Systems and Signal Processing*, 4, 2013, vol. 36, No. 2. pp. 332-353 ISSN 0888-3270.
191. QUEK, S.T., TUA, P.S. and WANG, Q. Detecting Anomalies in Beams and Plate Based on the Hilbert–Huang Transform of Real Signals. *Smart Materials and Structures*, 2003, vol. 12, No. 3. pp. 447 ISSN 0964-1726.
192. WU, F. and QU, L. An Improved Method for Restraining the End Effect in Empirical Mode Decomposition and its Applications to the Fault Diagnosis of Large Rotating Machinery. *Journal of Sound and Vibration*, 7/22, 2008, vol. 314, No. 3–5. pp. 586-602 ISSN 0022-460X.
193. SUN, B., et al. Time-Frequency Signal Processing for Gas-Liquid Two Phase Flow through a Horizontal Venturi Based on Adaptive Optimal-Kernel Theory. *Chinese Journal of Chemical Engineering*, 4, 2011, vol. 19, No. 2. pp. 243-252 ISSN 1004-9541.
194. LEE, S.K. and WHITE, P.R. Higher Order Time Frequency Analysis and its Application to Fault Detection in Rotating Machinery. *Mechanical Systems and Signal Processing*, 7, 1997, vol. 11, No. 4. pp. 637-650 ISSN 0888-3270.
195. POULIMENOS, A.G. and FASSOIS, S.D. Parametric Time-Domain Methods for Non-Stationary Random Vibration Modelling and Analysis — A Critical Survey and Comparison. *Mechanical Systems and Signal Processing*, 5, 2006, vol. 20, No. 4. pp. 763-816 ISSN 0888-3270.
196. CHENG, J., YANG, Y. and YANG, Y. A Rotating Machinery Fault Diagnosis Method Based on Local Mean Decomposition. *Digital Signal Processing*, 3, 2012, vol. 22, No. 2. pp. 356-366 ISSN 1051-2004.
197. LIANG, M. and SOLTANI BOZCHALOOI, I. An Energy Operator Approach to Joint Application of Amplitude and Frequency-Demodulations for Bearing Fault Detection.

Mechanical Systems and Signal Processing, 7, 2010, vol. 24, No. 5. pp. 1473-1494 ISSN 0888-3270.

198. SCHUMACHER, N.A., BURGER, C.P. and GIEN, P.H. A Laser-based Investigation of Higher-order Modes in Transient Lamb Waves. *The Journal of the Acoustical Society of America*, 1993, vol. 93, No. 5. pp. 2981-2984. Available from: http://scitation.aip.org/content/asa/journal/jasa/93/5/10.1121/1.405817 DOI http://dx.doi.org/10.1121/1.405817.
199. PROSSER, W.H. and GORMAN, M.R. Plate Mode Velocities in Graphite/Epoxy Plates. *J.Acoust.Soc.Am.*, 1994, vol. 96, No. 2. pp. 902.
200. ANASTASI, R.F. and MADARAS, E.I. *Aging Wire Insulation Assessment by Phase Spectrum Examination of Ultrasonic Guided Waves.* San Diego, CA; United States ed. SPIE's 8th International Symposium on NDE for Health Monitoring and Diagnostics, 2-6 Mar. 2003, 2003.
201. DAI, D. and HE, Q. Structure Damage Localization with Ultrasonic Guided Waves Based on a Time–frequency Method. *Signal Processing*, 3, 2014, vol. 96, Part A. pp. 21-28 ISSN 0165-1684.
202. SOHN, H., Hyun Woo Park, LAW, K.H. and FARRAR, C.R. Combination of a Time Reversal Process and a Consecutiv Outlier Analysis for Baseline-Free Damage Diagnosis. *Journal of Intelligent Material Systems and Structures*, April 01, 2007, vol. 18, No. 4. pp. 335-346.
203. PARK, H.W., KIM, S.B. and SOHN, H. Understanding a Time Reversal Process in Lamb Wave Propagation. *Wave Motion*, 11, 2009, vol. 46, No. 7. pp. 451-467 ISSN 0165-2125.
204. GANGADHARAN, R., MURTHY, C.R.L., GOPALAKRISHNAN, S. and BHAT, M.R. Time Reversal Technique for Health Monitoring of Metallic Structure using Lamb Waves. *Ultrasonics*, 12, 2009, vol. 49, No. 8. pp. 696-705 ISSN 0041-624X.
205. MICHAELS, J.E. and MICHAELS, T.E. *Enhanced Differential Methods for Guided Wave Phased Array Imaging using Spatially Distributed Piezoelectric Transducers.* American Institute Of Physics, 2006 ISBN 0-7354-0312-0.
206. MICHAELS, J.E. and MICHAELS, T.E. Guided Wave Signal Processing and Image Fusion for in Situ Damage Localization in Plates. *Wave Motion*, 6, 2007, vol. 44, No. 6. pp. 482-492 ISSN 0165-2125.
207. GIURGIUTIU, V. and BAO, J. Embedded-Ultrasonics Structural Radar for in Situ Structural Health Monitoring of Thin-Wall Structures. *Structural Health Monitoring*, June 01, 2004, vol. 3, No. 2. pp. 121-140.
208. PUREKAR, A.S., PINES, D.J., SUNDARARAMAN, S. and ADAMS, D.E. Directional Piezoelectric Phased Array Filters for Detecting Damage in Isotropic Plates. *Smart Materials and Structures*, 2004, vol. 13, No. 4. pp. 838 ISSN 0964-1726.
209. YU, L. and GIURGIUTIU, V. In-Situ Optimized PWAS Phased Arrays for Lamb Wave Structural Health Monitoring. *Journal of Mechanics of Materials and Structures*, 2007, vol. 2, No. 3. pp. 459.
210. YU, L. and GIURGIUTIU, V. In Situ 2-D Piezoelectric Wafer Active Sensors Arrays for Guided Wave Damage Detection. *Ultrasonics*, 4, 2008, vol. 48, No. 2. pp. 117-134 ISSN 0041-624X.
211. WILCOX, P.D. Omni-Directional Guided Wave Transducer Arrays for the Rapid Inspection of Large Areas of Plate Structures. *Ultrasonics, Ferroelectrics, and*

Frequency Control, IEEE Transactions On, 2003, vol. 50, No. 6. pp. 699-709 ISSN 0885-3010.

212. VISHNUVARDHAN, J., MURALIDHARAN, A., KRISHNAMURTHY, C.V. and BALASUBRAMANIAM, K. Structural Health Monitoring of Anisotropic Plates using Ultrasonic Guided Wave STMR Array Patches. *NDT & E International*, 4, 2009, vol. 42, No. 3. pp. 193-198 ISSN 0963-8695.
213. RAJAGOPALAN, J., BALASUBRAMANIAM, K. and KRISHNAMURTHY, C.V. A Phase Reconstruction Algorithm for Lamb Wave Based Structural Health Monitoring of Anisotropic Multi-layered Composite Plates. *J.Acoust.Soc.Am.*, 2006, vol. 119, No. 2. pp. 872.
214. MURALIDHARAN, A., BALASUBRAMANIAM, K. and KRISHNAMURTHY, C.V. A Migration Based Reconstruction Algorithm for the Imaging of Defects in a Plate using a Compact Array. *Smart Structures and Systems*, 2008, vol. 4, No. 4. pp. 449.
215. KUDELA, P., OSTACHOWICZ, W. and ŻAK, A. Damage Detection in Composite Plates with Embedded PZT Transducers. *Mechanical Systems and Signal Processing*, 8, 2008, vol. 22, No. 6. pp. 1327-1335 ISSN 0888-3270.
216. OSTACHOWICZ, W., KUDELA, P., MALINOWSKI, P. and WANDOWSKI, T. Damage Localisation in Plate-Like Structures Based on PZT Sensors. *Mechanical Systems and Signal Processing*, 8, 2009, vol. 23, No. 6. pp. 1805-1829 ISSN 0888-3270.
217. WANDOWSKI, T., MALINOWSKI, P. and OSTACHOWICZ, W.M. Damage Detection with Concentrated Configurations of Piezoelectric Transducers. *Smart Materials and Structures*, 2011, vol. 20, No. 2 ISSN 0964-1726.
218. WANDOWSKI, T., MALINOWSKI, P.H. and OSTACHOWICZ, W.M. Circular Sensing Networks for Guided Waves Based Structural Health Monitoring. *Mechanical Systems and Signal Processing*, 1, 2016, vol. 66–67. pp. 248-267 ISSN 0888-3270.
219. GIRIDHARA, G., et al. Rapid Localization of Damage using a Circular Sensor Array and Lamb Wave Based Triangulation. *Mechanical Systems and Signal Processing*, 11, 2010, vol. 24, No. 8. pp. 2929-2946 ISSN 0888-3270.
220. SOLODOV, I., BAI, J., BEKGULYAN, S. and BUSSE, G. A Local Defect Resonance to Enhance Acoustic Wave-Defect Interaction in Ultrasonic Non-destructive Evaluation. *Applied Physics Letters*, 2011, vol. 99, No. 21. pp. 211911. Available from: http://scitation.aip.org/content/aip/journal/apl/99/21/10.1063/1.3663872 DOI http://dx.doi.org/10.1063/1.3663872.
221. DELRUE, S. and VAN DEN ABEELE, K. Three-Dimensional Finite Element Simulation of Closed Delaminations in Composite Materials. *Ultrasonics*, 2, 2012, vol. 52, No. 2. pp. 315-324 ISSN 0041-624X.
222. SOLODOV, I., DERUSOVA, D. and RAHAMMER, M. Thermosonic Chladni Figures for Defect-Selective Imaging. *Ultrasonics*, 7, 2015, vol. 60. pp. 1-5 ISSN 0041-624X.
223. TUA, P.S., QUEK, S.T. and WANG, Q. Detection of Cracks in Plates using Piezo-Actuated Lamb Waves. *Smart Materials and Structures*, 2004, vol. 13, No. 4. pp. 643 ISSN 0964-1726.
224. PAGET, C.A., SÉBASTIEN, G., LEVIN, K. and DELEBARRE, C. Damage Assessment in Composites by Lamb Waves and Wavelet Coefficients. *Smart Materials and Structures*, 2003, vol. 12, No. 3. pp. 393 ISSN 0964-1726.

225. DOUKA, E., LOUTRIDIS, S. and TROCHIDIS, A. Crack Identification in Plates using Wavelet Analysis. *Journal of Sound and Vibration*, 2/6, 2004, vol. 270, No. 1–2. pp. 279-295 ISSN 0022-460X.

226. BAID, H., SCHAAL, C., SAMAJDER, H. and MAL, A. Dispersion of Lamb Waves in a Honeycomb Composite Sandwich Panel. *Ultrasonics*, 2, 2015, vol. 56. pp. 409-416 ISSN 0041-624X.

227. MORENO, E., GALARZA, N., RUBIO, B. and OTERO, J.A. Phase Velocity Method for Guided Wave Measurements in Composite Plates. *Physics Procedia,* 2015, vol. 63. pp. 54-60 ISSN 1875-3892.

228. SREEKUMAR, P., RAMADAS, C., ANAND, A. and JOSHI, M. Attenuation of Ao Lamb Mode in Hybrid Structural Composites with Nanofillers. *Composite Structures,* 11/15, 2015, vol. 132. pp. 198-204 ISSN 0263-8223.

229. YU, J.G., RATOLOJANAHARY, F.E. and LEFEBVRE, J.E. Guided Waves in Functionally Graded Viscoelastic Plates. *Composite Structures*, 10, 2011, vol. 93, No. 11. pp. 2671-2677 ISSN 0263-8223.

230. REN, B. and LISSENDEN, C.J. Ultrasonic Guided Wave Inspection of Adhesive Bonds between Composite Laminates. *International Journal of Adhesion and Adhesives*, 9, 2013, vol. 45. pp. 59-68 ISSN 0143-7496.

231. SHERAFAT, M.H., et al. Structural Health Monitoring of a Composite Skin-Stringer Assembly using within-the-Bond Strategy of Guided Wave Propagation. *Materials & Design*, 1/15, 2016, vol. 90. pp. 787-794 ISSN 0264-1275.

232. CASTAINGS, M., HOSTEN, B. and FRANÇOIS, D. The Sensitivity of Surface Guided Modes to the Bond Quality between a Concrete Block and a Composite Plate. *Ultrasonics*, 4, 2004, vol. 42, No. 1–9. pp. 1067-1071 ISSN 0041-624X.

233. CASTAINGS, M. and HOSTEN, B. Ultrasonic Guided Waves for Health Monitoring of High-Pressure Composite Tanks. *NDT & E International*, 12, 2008, vol. 41, No. 8. pp. 648-655 ISSN 0963-8695.

234. CAMINERO, M.A., et al. Analysis of Adhesively Bonded Repairs in Composites: Damage Detection and Prognosis. *Composite Structures*, 1, 2013, vol. 95. pp. 500-517 ISSN 0263-8223.

235. PAVLOPOULOU, S., et al. Continuous Debonding Monitoring of a Patch Repaired Helicopter Stabilizer: Damage Assessment and Analysis. *Composite Structures*, 9/1, 2015, vol. 127. pp. 231-244 ISSN 0263-8223.

236. HABIB, F., MARTINEZ, M., ARTEMEV, A. and BROTHERS, M. Structural Health Monitoring of Bonded Composite Repairs – A Critical Comparison between Ultrasonic Lamb Wave Approach and Surface Mounted Crack Sensor Approach. *Composites Part B: Engineering*, 4, 2013, vol. 47. pp. 26-34 ISSN 1359-8368.

237. STASZEWSKI, W.J., MAHZAN, S. and TRAYNOR, R. Health Monitoring of Aerospace Composite Structures – Active and Passive Approach. *Composites Science and Technology*, 9, 2009, vol. 69, No. 11–12. pp. 1678-1685 ISSN 0266-3538.

238. SOHN, H., et al. Delamination Detection in Composites through Guided Wave Field Image Processing. *Composites Science and Technology*, 6/15, 2011, vol. 71, No. 9. pp. 1250-1256 ISSN 0266-3538.

239. GRONDEL, S., ASSAAD, J., DELEBARRE, C. and MOULIN, E. Health Monitoring of a Composite Wingbox Structure. *Ultrasonics*, 4, 2004, vol. 42, No. 1–9. pp. 819-824 ISSN 0041-624X.

240. ROGGE, M.D. and LECKEY, C.A.C. Characterization of Impact Damage in Composite Laminates using Guided Wavefield Imaging and Local Wavenumber Domain Analysis. *Ultrasonics*, 9, 2013, vol. 53, No. 7. pp. 1217-1226 ISSN 0041-624X.

241. SU, Z. and YE, L. Lamb Wave-Based Quantitative Identification of Delamination in CF/EP Composite Structures using Artificial Neural Algorithm. *Composite Structures*, 0, 2004, vol. 66, No. 1–4. pp. 627-637 ISSN 0263-8223.

242. RAMADAS, C., BALASUBRAMANIAM, K., JOSHI, M. and KRISHNAMURTHY, C.V. Characterisation of Rectangular Type Delaminations in Composite Laminates through B- and D-Scan Images Generated using Lamb Waves. *NDT & E International*, 5, 2011, vol. 44, No. 3. pp. 281-289 ISSN 0963-8695.

243. LANZA DI SCALEA, F., MATT, H. and BARTOLI, I. The Response of Rectangular Piezoelectric Sensors to Rayleigh and Lamb Ultrasonic Waves. *The Journal of the Acoustical Society of America*, 2007, vol. 121, No. 1. pp. 175-187. Available from: http://scitation.aip.org/content/asa/journal/jasa/121/1/10.1121/1.2400668 DOI http://dx.doi.org/10.1121/1.2400668.

244. MANKA, M., et al. Lamb Wave Transducers made of Piezoelectric Macro-Fibre Composite. *Structural Control and Health Monitoring*, 2013, vol. 20, No. 8. pp. 1138-1158 ISSN 1545-2263.

245. BERANEK, L.L. *Acoustics.* American Institute of Physics, 1986 ISBN 978-0883184943.

246. BIRKS, A.S. and GREEN, R. *Non-Destructive Testing Handbook.* P. MCINTIRE ed., Second edition ed. American Society for Non-Destructive testing, 1991 ISBN 0-931403-04-9.

247. HE, P. Simulation of Ultrasound Pulse Propagation in Lossy Media Obeying a Frequency Power Law. *Ultrasonics, Ferroelectrics, and Frequency Control, IEEE Transactions On*, 1998, vol. 45, No. 1. pp. 114-125 ISSN 0885-3010.

248. LIU, G.R. and QUEK, S.T. *The Finite Element Method, Second Edition: A Practical Course.* 2nd Edition ed. Butterworth-Heinemann, 2013 ISBN 978-0080983561.

249. SAMAITIS, V. and MAŽEIKA, L. Investigation of Diffuse Lamb Wave Sensitivity to the Through-Thickness Notch in Structural Health Monitoring of Composite Objects. *Electronics and Electrical Engineering*, 2014, vol. 20, No. 3. pp. 48 ISSN 1392-1215.

250. ANDRIA, G., ATTIVISSIMO, F. and GIAQUINTO, N. Digital Signal Processing Techniques for Accurate Ultrasonic Sensor Measurement. *Measurement*, 9, 2001, vol. 30, No. 2. pp. 105-114 ISSN 0263-2241.

251. BOSSY, E., TALMANT, M. and LAUGIER, P. Effect of Bone Cortical Thickness on Velocity Measurements using Ultrasonic Axial Transmission: A 2D Simulation Study. *J.Acoust.Soc.Am.*, 2002, vol. 112, No. 1. pp. 297.

252. QUEIRÓS, R., MARTINS, R.C., GIRÃO, P.S. and CRUZ SERRA, A. *A New Method for High Resolution Ultrasonic Ranging in Air.* Proceedings of the XVIII IMEKO World Congress Metrology for a Sustainable Development, September, 17 – 22, 2006, Rio de Janeiro, Brazil ed.

253. PIALUCHA, T., GUYOTT, C.C.H. and CAWLEY, P. An Amplitude Spectrum Method for the Measurement of Phase Velocity. *Ultrasonics*, 1989, vol. 27. pp. 270–279.

254. DÍAZ VALDÉS, S.H. and SOUTIS, C. Real-Time Non-Destructive Evaluation of Fibre Composite Laminates using Low-Frequency Lamb Waves. *The Journal of the Acoustical Society of America*, 2002, vol. 111, No. 5. pp. 2026-2033. Available from: http://scitation.aip.org/content/asa/journal/jasa/111/5/10.1121/1.1466870 DOI http://dx.doi.org/10.1121/1.1466870.

255. SACHSE, W. and PAO, Y. On the Determination of Phase and Group Velocities of Dispersive Waves in Solids. *Journal of Applied Physics*, 1978, vol. 49, No. 8. pp. 4320-4327. Available from: http://scitation.aip.org/content/aip/journal/jap/49/8/10.1063/1.325484 DOI http://dx.doi.org/10.1063/1.325484.

256. ROKHLIN, S.I., LEWIS, D.K., GRAFF, K.F. and ADLER, L. Real-time Study of Frequency Dependence of Attenuation and Velocity of Ultrasonic Waves during the Curing Reaction of Epoxy Resin. *The Journal of the Acoustical Society of America*, 1986, vol. 79, No. 6. pp. 1786-1793. Available from: http://scitation.aip.org/content/asa/journal/jasa/79/6/10.1121/1.393240 DOI http://dx.doi.org/10.1121/1.393240.

257. CASTAINGS, M., LE CLEZIO, E. and HOSTEN, B. Modal Decomposition Method for Modelling the Interaction of Lamb Waves with Cracks. *The Journal of the Acoustical Society of America*, 2002, vol. 112, No. 6. pp. 2567-2582. Available from: http://scitation.aip.org/content/asa/journal/jasa/112/6/10.1121/1.1500756 DOI http://dx.doi.org/10.1121/1.1500756.

258. GUO, N. and CAWLEY, P. Lamb Wave Reflection for the Quick Non-Destructive Evaluation of Large Composite Laminates. *Materials Evaluation*, 1994, vol. 52, No. 3. pp. 404-411 ISSN 0025-5327.

259. BIRT, E.A. Damage Detection in Carbon-Fibre Composites using Ultrasonic Lamb Waves. *Insight*, 1998, vol. 40, No. 5. pp. 335.

260. TAN, K.S., GUO, N., WONG, B.S. and TUI, C.G. Experimental Evaluation of Delaminations in Composite Plates by the use of Lamb Waves. *Composites Science and Technology*, 1995, vol. 53, No. 1. pp. 77-84 ISSN 0266-3538.

LIST OF RESEARCH PUBLICATIONS

Articles published in journals belonging to scientific international databases

Indexed in the Web of Science with Impact Factor

1. **Samaitis, V.**; Mažeika, L. Investigation of diffuse Lamb wave sensitivity to the through-thickness notch in structural health monitoring of composite objects // Elektronika ir elektrotechnika = Electronics and Electrical Engineering. Kaunas: KTU. ISSN 1392-1215. 2014, Vol. 20, No. 3, p. 48-51. [Science Citation Index Expanded (Web of Science); INSPEC; Computers & Applied Sciences Complete; Central & Eastern European Academic Source] [IF (E): 0,561 (2014)].
2. Raišutis, R.; Kažys, R.; Mažeika, L.; Žukauskas, E.; **Samaitis, V.**; Jankauskas, A. Ultrasonic guided wave-based testing technique for inspection of multi-wire rope structures // NDT & E international. Oxford: Elsevier Science. ISSN 0963-8695. 2014, Vol. 62, p. 40-49. [Science Citation Index Expanded (Web of Science); Academic Search Premier; Chemical Abstracts (CAplus); Compendex; Science Direct] [IF (E): 2,225 (2014)].
3. Raišutis, R.; Žukauskas, E.; **Samaitis, V.**; Jankauskas, A.; Draudvilienė, L.; Griškevičius, P.; Juzėnas, K. Analysis of ultrasonic guided waves propagation in complex composite structures // International journal of structural stability and dynamics. Singapore: World Scientific Publishing Co. ISSN 0219-4554. 2014, vol. 14, iss. 8, Article No. 1440024, p. [1-19]. [Science Citation Index Expanded (Web of Science); Current Contents (Engineering, Computing & Technology); Scopus] [IF (E): 0,764 (2014)].
4. Raišutis, R.; Kažys, R.; Mažeika, L.; Žukauskas, E.; **Samaitis, V.**; Draudvilienė, L.; Vladišauskas, A. An adjustment-free NDT technique for defect detection in multi-layered composite constructions using ultrasonic guided waves // International journal of structural stability and dynamics. Singapore: World Scientific Publishing Company. ISSN 0219-4554. 2014, vol. 14, iss. 8, Article No. 1440025, p. [1-15]. [Science Citation Index Expanded (Web of Science); Current Contents (Engineering, Computing & Technology); Scopus] [IF (E): 0,764 (2014)].

Articles in other peer reviewed research publications

Articles published in conference proceedings

1. Raišutis, R.; Kažys, R.; Žukauskas, E.; **Samaitis, V.**; Draudvilienė, L.; Vladišauskas, A. The contact type NDT technique for defect detection in multi-layered composite constructions using ultrasonic guided waves // Application of contemporary non-destructive testing in engineering: conference proceedings of the 12th international conference of The Slovenian Society for Non-Destructive Testing, Portorož, 4-6 September 2013, Slovenia. Ljubljana: Slovenian Society for Non-Destructive Testing, 2013, ISBN 9789619353707. p. [1-7].
2. Raišutis, R.; Mažeika, L.; **Samaitis, V.**; Jankauskas, A.; Mayorga, P.; Garcia, A.; Correa, M.; Neal, B. Application of ultrasonic guided waves for investigation of composite constructional components of tidal power plants // Application of contemporary non-destructive testing in engineering: conference proceedings of the 12th international conference of The Slovenian Society for Non-Destructive Testing,

Portorož, 4-6 September 2013, Slovenia. Ljubljana: Slovenian Society for Non-Destructive Testing, 2013, ISBN 9789619353707. p. [1-8].

3. Raišutis, R.; Žukauskas, E.; **Samaitis, V.**; Jankauskas, A.; Draudvilienė, L.; Griškevičius, P.; Juzėnas, K. Application of ultrasonic guided waves for investigation of composite constructions made of honeycomb materials // Mechatronic systems and materials: abstracts of the 11th international conference, MSM 2015, 7-9 July 2015, Kaunas, Lithuania / Editors: I. Skiedraitė, R. Rimašauskienė, L. Zubrickaitė, E. Drafašius. Kaunas: Kauno technologijos universitetas. ISSN 1822-8283. 2015, p. 29-30.

Abstracts in scientific conferences

1. **Samaitis, V.**; Mažeika, L. Novel NDT technique for detection of delamination type defects in structural health monitoring of composites, “19th World Conference on Non-Destructive Testing WCNDT”, Munich, Germany, 2016.06.13–17.
2. Raišutis, R.; Žukauskas, E.; **Samaitis, V.**; Jankauskas, A.; Draudvilienė, L.; Griškevičius, P.; Juzėnas, K. Application of ultrasonic guided waves for investigation of composite constructions made of honeycomb materials, “11th international conference on Mechatronic systems and materials”, Kaunas, Lithuania, 2015.07.07–09.
3. Mažeika, L.; **Samaitis, V.**; Kažys, R.; Wilkinson, A.; Deere, M. Application of the SAFT at low frequencies for detection of the concentrated defect in sprinkler pipe, “6th International Conference on Emerging Technologies in Non-Destructive Testing”, Brussels, Belgium, 2015.05.27–29.
4. **Samaitis, V.**; Mažeika, L. Investigation of spatial filtering effects on generation and mode identification of ultrasonic guided waves, “11th International Conference on Non-Destructive Testing ECNDT”, Prague, Czech Republic, 2014.10.06–10.
5. Raišutis, R.; Kažys, R.; Mažeika, L.; Žukauskas, E.; **Samaitis, V.**; Draudvilienė, L.; Vladišauskas, A. Application of ultrasonic guided waves for testing and structure health monitoring of honeycomb based composite constructions, “11th International Conference on Non-Destructive Testing ECNDT”, Prague, Czech Republic, 2014.10.06–10.
6. **Samaitis, V.**; Mažeika, L. Influence of dimensions of the transducers on guided wave mode identification in structural health monitoring of composite objects, “11th International Conference on Condition Monitoring and Machinery Failure Prevention Technologies”, Manchester, United Kingdom, 2014.07.09–13.
7. Raišutis, R.; Žukauskas, E.; **Samaitis, V.**; Jankauskas, A.; Draudvilienė, L.; Griškevičius, P.; Juzėnas, K. Analysis of ultrasonic guided waves propagation in Honeycomb composite structures, International seminar “Nonlinear and Multiscale Dynamics of Smart Materials in Energy Harvesting”, Lublin, Poland, 2014.02.17–18.
8. **Samaitis, V.**; Mažeika, L.; Raišutis, R. Application of diffuse guided waves for detection of originating defects in structural health monitoring of composite objects, International seminar “Nonlinear and Multiscale Dynamics of Smart Materials in Energy Harvesting”, Lublin, Poland, 2014.02.17–18.
9. Mažeika, L.; Raišutis, R.; Kažys, R.; **Samaitis, V.**; Jankauskas, A. Structural health monitoring of wind turbine blades using ultrasonic guided waves, “International Symposium on Piezocomposite Applications”, Dresden, Germany, 2013.09.19–20.

10. Raišutis, R.; Mažeika, L.; **Samaitis, V.**; Jankauskas, A.; Maragoya, P.; Garcia, A.; Correa, M.; Neal, B. Application of ultrasonic guided waves for investigation of composite constructional components of tidal power plants, “12th International Conference on Application of Contemporary Non-destructive testing in Engineering”. Portoroz, Slovenia, 2013.09.04–06.
11. Raišutis, R.; Kažys, R.; Mažeika, L.; Žukauskas, E.; **Samaitis, V.**; Draudvilienė, L.; Vladišauskas, A. The contact type NDT technique for defect detection in multi-layered composite constructions using ultrasonic guided waves, “12th International Conference on Application of Contemporary Non-destructive testing in Engineering”. Portoroz, Slovenia, 2013.09.04–06.
12. **Samaitis, V.**; Mažeika, L.; Raišutis, R.; Kažys, R. Application of diffuse guided waves for detection of originating defects in structural health monitoring of composite objects, “The Tenth International Conference on Condition Monitoring and Machinery Failure Prevention Technologies”, Krakow, Poland, 2013.07.18–20.
13. **Samaitis, V.**; Mažeika, L. Investigation of diffuse Lamb wave sensitivity to the through-thickness notch in structural health monitoring of composite objects, “17th International Conference on Electronics 2013”, Palanga, Lithuania, 2013.07.17–19.
14. Raišutis, R.; Kažys, R.; Mažeika, L.; Žukauskas, E.; **Samaitis, V.**; Jankauskas, A. Investigation of propagation of ultrasonic guided waves along twisted multi-wire ropes. “International Congress on Ultrasonics ICU2013”. Singapore. 2013.05.02–05.
15. **Samaitis, V.**; Mažeika, L.; Raišutis, R.; Kažys, R. Application of ultrasonic guided waves for monitoring of the constructional components made of multi-layered composites. “The 19th International Congress on Sound and Vibration”. Vilnius, Lithuania, 2012.07.08–12.

Study literature

Textbooks, handbooks and manuals

1. Jasiūnienė, E.; Žukauskas, E.; **Samaitis, V**. Ultragarsinių matavimų laboratoriniai darbai: mokomoji knyga / Kauno technologijos universitetas. Prof. K. Baršausko ultragarso mokslo institutas. Kaunas: Technologija, 2013. 91 p. ISBN 9786090208359.

ACKNOWLEDGEMENT

I would like to express my sincere gratitude to my advisor Prof. Liudas Mažeika for the continuous support, patience, advices, inspiration and immense knowledge. A special heart-felt gratitude go to my family for all of the sacrifices that they have made on my behalf: to my mother Dalia, father Rimantas, sister Dovilė, my little niece Monika and my beloved wife Dovilė. Your unconditional love and support, encouragement, optimism and belief in me was more valuable than you could ever imagine.

SL344. 2016-08-17, 19 leidyb. apsk. l. Tiražas 12 egz. Užsakymas 277.
Išleido Kauno technologijos universitetas, K. Donelaičio g. 73, 44249 Kaunas
Spausdino leidyklos „Technologija“ spaustuvė, Studentų g. 54, 51424 Kaunas